Endogenous tagging using CRISPR/Cas9 to study protein localization across human cell types

Mathieu Husser

A Thesis

In the Department of

Biology

Presented in Partial Fulfillment of the Requirements

For the Degree of

Doctor of Philosophy (Biology)

At Concordia University

Montréal, Québec, Canada

August 2023

CONCORDIA UNIVERSITY

School of Graduate Studies

This is to certify that the thesis prepared

By: Mathieu Husser
Entitled: Endogenous tagging using CRISPR/Cas9 to study protein localization across human cell types

and submitted in partial fulfillment of the requirements for the degree of

Doctor of Philosophy (Biology)

complies with the regulations of the University and meets the accepted standards with respect to originality and quality.

Signed by the final examining committee:

_____Chair
Dr.

_____Thesis Supervisor
Dr. Alisa Piekny

_____Thesis Supervisor
Dr. Vincent Martin

_____Examiner
Dr. Michael Sacher

_____Examiner
Dr. Malcolm Whiteway

_____External Examiner
Dr. Brandon Helfield

_____External Examiner
Dr. Anna Jezierski

Approved by _____
Dr. Robert Weladji, Graduate Program Director

August 2023 _____
Dr. Pascale Sicotte, Dean
Faculty of Arts and Science

ABSTRACT

Endogenous tagging using CRISPR/Cas9 to study protein localization across human cell types

Mathieu Husser, Ph.D.

Concordia University, 2023

Gene editing technologies have facilitated the genetic manipulation of cells to study proteins by generating knockouts, point mutations and endogenous tags. Amongst precise edits, endogenous tags provide valuable tools to study protein localization in live cells. However, precise gene editing is inefficient in mammalian cells, and generating edited cell lines is time-consuming. Therefore, most studies of cellular processes in human cells rely on other methods such as over-expression, and use cancerous or transformed cell lines that are easy to manipulate. For example, cytokinesis, the physical separation of a cell into two daughter cells at the end of mitosis, is mainly understood in the context of cancerous HeLa cells. In this thesis, I present tools and protocols to tag proteins endogenously in multiple human cell lines, which enables the study of cytokinesis proteins in their native cellular context. I first generated endogenous tags using CRISPR/Cas9 (clustered regularly interspaced short palindromic repeats; CRISPR-associated protein 9) to study protein localization during cytokinesis in different human cell lines. By characterizing cytokinesis parameters, I found that cytokinesis occurs differently in different cell lines, suggesting that the underlying mechanisms regulating cytokinesis differ with cell type. I then engineered an iPS cell line that facilitates large-scale endogenous tagging by taking advantage of a split mNeonGreen protein where the tagging fragment is short. Endogenous tagging with this system is efficient and can be scaled up for high-throughput editing and screening. This work provides new tools to study

protein localization during cytokinesis and other cellular processes in human cells. It also enables comparative studies of cellular processes across human cell types to understand cellular function on the scale of all human cell types.

ACKNOWLEDGEMENTS

I want to thank my PhD supervisors, Drs. Alisa Piekny and Vincent Martin for their guidance and support throughout this project. I am extremely thankful for the opportunity to learn from you both by undertaking this collaboration. Most of all, thank you for allowing me to be creative and independent in my research. I would also like to acknowledge the support of my committee members, Dr. Michael Sacher and Dr. Malcolm Whiteway, for their invaluable feedback.

Thank you to all the members of the Piekny and Martin labs who contributed to my work in one way or another. I especially want to thank the co-authors who contributed to the work shown in this thesis: Dr. Imge Özügergin, Nhat Pham, Dr. Chris Law, Flavia Araujo, Noha Skaik and Tiziana Resta.

For their help with equipment use and data analysis, thank you to Dr. Chris law from the CMCI, and Nick Gold, Angela Quach, Flavia Araujo and Dr. Smita Amarnath from the Genome Foundry. Thank you also to Andrew Cormier and Omeeda Naoum for their contribution to the cloning of several expression vectors. Finally, thank you to the McGill Flow Cytometry Innovation Platform for the use of their cell sorter.

For their guidance and feedback on iPSC culture and editing, thank you to Dr. Knut Woltjen and his lab, and to several members of the National Research Council of Canada, including Drs. Anna Jezierski, Scott McComb and Simon Drouin.

Thank you to the funding sources that supported my studies and this research: Concordia University, the FRQNT, the SynBioApps program, NSERC Discovery and the National Research Council of Canada.

DEDICATIONS

I want to dedicate this thesis to the two joys of my life: my wife Imge (also known as Dr. Özügergin) and our soon-to-be nugget (maybe a doctor one day but no pressure). Thank you for supporting me and making me a better person every day. I can't wait to see what life has in store for our family.

I also want to take the time to thank the teachers who first sparked my passion for Biology: Mme Maura, who showed me a movie of mitosis for the first time; Mme Chonis, who first taught me about genetics; and Dr. Stirling, who taught my first university genetics course. Thank you also to the non-biology teachers who contributed to putting me on this path, especially Mrs. Canadas and Mr. Raskauskas.

I also want to thank the mentors and the friends I made in the lab during my university years. Thank you to my first mentors in research, Lauren and Dave, as well as the Hyasynth team. Thank you to Adithi, Kevin and Thiban for being awesome iGEM teammates. Thank you also to all the lab members and friends who made the lab a fun place to work. Special shoutout to Mo, Mike, Meghan and Jaya from the Martin lab, and Kevin and Nhat from the Piekny lab.

Finally, thank you to my family, who has been there from day one (believe it or not). You supported me moving to Canada to find my passion and I am very excited for you to see it finally work out!

CONTRIBUTION OF AUTHORS

Chapter 1: Introduction

Part of this chapter is adapted from the manuscript written by Alisa Piekny, Vincent Martin, Noha Skaik and Mathieu Husser. Imge Özügergin provided the images of a *C. elegans* embryo shown in Figure 1.4.

Chapter 2: Cytokinetic diversity in mammalian cells is revealed by the characterization of endogenous anillin, Ect2 and RhoA

Alisa Piekny and Vincent Martin supervised the project and edited the manuscript. Imge Özügergin performed experiments and data analysis, and wrote part of the manuscript. This contribution applies to Figures 2.3, 2.4, 2.5, 2.6, S2.4 and S2.5. Tiziana Resta generated the double- and triple-tagged cell lines shown in Figure S2.2, and was supervised by Mathieu Husser. Andrew Cormier and Mathieu Husser designed and cloned the Golden Gate vector used in Figures 2.2 and S2.3. Mathieu Husser performed experiments and data analysis, wrote the manuscript and prepared figures. This contribution applies to all figures.

Chapter 3: Endogenous tagging using split mNeonGreen in human iPSCs for live imaging studies

Vincent Martin and Alisa Piekny supervised the project and edited the manuscript. Nhat Pham performed the microscopy experiments shown in Figures 3.3, 3.4, S3.3 and S3.5. Chris Law set up and ran the CARE neural network for image restoration used in Figures 3.4 and S3.5. Flavia

Araujo set up and ran the basecalling and demultiplexing of the Nanopore sequencing reads used in Figure 3.2 and 3.3. Mathieu Husser performed experiments and data analysis, wrote the manuscript and prepared figures. This contribution applies to all figures.

TABLE OF CONTENTS

LIST OF FIGURES

LIST OF TABLES

LIST OF SUPPLEMENTARY FIGURES

LIST OF SUPPLEMENTARY TABLES

LIST OF ABBREVIATIONS

201B7	Human iPS cell line derived from healthy dermal fibroblasts
53BP1	p53-binding protein 1
AAV	Adeno-associated virus
AAVS1	Adeno-associated virus integration site 1
ACTB	Actin beta gene
AIR-1	Aurora/Ipl1 related kinase 1, *C. elegans* ortholog of Aurora A kinase
AIR-2	Aurora/Ipl1 related kinase 1, *C. elegans* ortholog of Aurora B kinase
Alt-EJ	Alternative end-joining
Alt-NHEJ	Alternative non-homologous end-joining
AmpR	Ampicillin resistance gene
ANI-1	*C. elegans* ortholog of anillin
ANLN	Anillin gene
ANOVA	Analysis of variance
bGH	Bovine growth hormone poly-adenylation signal
BHK-21	Baby hamster kidney cell line
BMP	Bone morphogenetic protein
bp	Base pair
BRCA1	Breast cancer type 1 susceptibility protein
BRCA2	Breast cancer type 2 susceptibility protein
BRCT	BRCA1 C-terminus
C-terminus	Carboxyl terminus
CAAX	Cysteine (C), two aliphatic amino acids (A) and any amino acid (X)
CAG	Promoter composed of the CMV enhancer, chicken β-actin promoter and first intron, and rabbit β-globin splicing acceptor
CARE	Content-aware image restoration
Cas	CRISPR-associated protein
Cas12	CRISPR-associated protein 12
Cas14	CRISPR-associated protein 14
Cas9	CRISPR-associated protein 9

CCM-3	Cerebral cavernous malformation 3
CCR5	C-C Motif Chemokine Receptor 5 gene
CCS	Cosmic calf serum
Cdk1	Cyclin-dependent kinase 1
CLYBL	Citramalyl-CoA lyase gene
cNHEJ	Canonical non-homologous end-joining
CRISPR	Clustered regularly interspaced short palindromic repeats
CRISPRa	CRISPR activation
CRISPRi	CRISPR interference
crRNA	CRISPR RNA
CtIP	CtBP-interacting protein
CYK-1	Cytokinesis defect 1, *C. elegans* ortholog of mDia1
Cyk4	Cytokinesis defect 4 (Gene: RACGAP1)
DH	Dbl homology
DH5α	*Escherichia coli* cloning strain
DMEM	Dulbecco's modified Eagle medium
DMSO	Dimethyl sulfoxide
DNA	Deoxyribonucleic acid
DNA-PK	DNA-dependent protein kinase
DNA-PKcs	DNA-dependent protein kinase catalytic subunit
DNA2	DNA replication ATP-dependent helicase/nuclease 2
dPCR	Digital PCR
DSB	Double-stranded break
dsDNA	Double-stranded DNA
dsODN	Double-stranded oligodeoxynucleotide
E-cadherin	Epithelial cadherin protein (Gene: CDH1)
Ect2	Epithelial cell transforming 2 (Gene: ECT2)
EDTA	Ethylenediaminetetraacetic acid
EGFP/eGFP	Enhanced green fluorescent protein
EMEM	Eagle's minimum essential medium
ER2925	*Escherichia coli* methylation-deficient strain

ERM	Ezrin/Radixin/Moesin
ESC	Embryonic stem cells
EXO1	Exonuclease 1
F-actin	Filamentous actin
FACS	Fluorescence-activated cell sorting
FBS	Fetal bovine serum
FCS	Fluorescence correlation spectroscopy
FOXA2	Forkhead box protein A2
G-banding	Giemsa banding
G2	Growth phase 2
GAP	GTPase-activating protein
GCK-1	Germinal center kinase 1
GEF	Guanine nucleotide exchange factor
GFP	Green fluorescent protein
gRNA	Guide RNA
GTP	Guanosine triphosphate
GTPase	Guanosine triphosphatase
H2BC11	Histone H2B type 1-J gene
HCT116	Human colorectal carcinoma cell line
HDR	Homology-directed repair
HEK293	Human embryonic kidney cell line
HeLa	Human cervical cancer cell line taken from Henrietta Lacks
HEPES	4-(2-Hydroxyethyl)piperazine-1-ethane-sulfonic acid
HepG2	Human hepatocellular carcinoma cell line
hPSC	Human pluripotent stem cells
HR	Homologous recombination
hTERT	Human telomerase reverse transcriptase gene
HypaCas9	Hyper-accurate Cas9 variant
iPSC	Induced pluripotent stem cells
K-ras	Kirsten rat sarcoma viral oncogene homolog
kb	Kilobase

KIF23	Kinesin family member 23, referred to as MKLP1
KIF2C	Kinesin Family Member 2C, referred to as MCAK
KRT14	Type I cytoskeletal keratin 14 gene
KRT18	Type I cytoskeletal keratin 18 gene
KRT5	Type II cytoskeletal keratin 5 gene
Ku70	70 kDa subunit of Ku antigen
Ku80	86 kDa subunit of Ku antigen
LED	Light-emitting diode
LET-502	Lethal 502, *C. elegans* ortholog of ROCK
MCAK	Mitotic centromere-associated kinesin
MDCK	Madin–Darby canine kidney cell line
mDia1	Diaphanous-related formin 1
mEGFP	Monomeric enhanced green fluorescent protein
MgcRacGAP	Male germ cell Rac GTPase activating protein, referred to as Cyk4
MKLP1	Mitotic kinesin-like protein 1
MMEJ	Microhomology-mediated end-joining
mNG	mNeonGreen
$mNG2_{1-10}$	mNeonGreen2 beta strands 1-10
$mNG2_{11}$	mNeonGreen2 beta strand 11
MP-GAP	M phase GTPase activating protein
MRN	MRE11–RAD50–NBS1
mRNA	Messenger ribonucleic acid
MYH10	Non-muscle myosin heavy chain IIB gene
N-terminus	Amino terminus
NA	Numerical aperture
NANOG	Homeobox protein NANOG
NCAM	Neural cell adhesion molecule (Gene: NCAM1)
NDS	Normal donkey serum
NES	Nestin gene
NGS	Next-generation sequencing
NHEJ	Non-homologous end-joining

NLS	Nuclear localization signal
NMY-2	*C. elegans* ortholog of non-muscle myosin heavy chain II
ns	Not significant
NU7441	Small molecule inhibitor of DNA-PK
OCT3/4	Octamer-binding transcription factor 3/4
ORF	Open reading frame
PAM	Protospacer-adjacent motif
PAR	Abnormal embryonic partitioning of cytoplasm
PAR-6	Abnormal embryonic partitioning of cytoplasm 6 protein
PAX6	Paired box 6 protein
PBS	Phosphate-buffered saline
PCR	Polymerase chain reaction
PDB	Protein Data Bank
PDCD10	Programmed cell death 10 protein
PE	Prime editing
pegRNA	Prime editing guide RNA
Pen-Strep	Penicillin and streptomycin antibiotics
PFA	Paraformaldehyde
PH	Pleckstrin homology
PI(4,5)P2	Phosphatidylinositol (4,5)-bisphosphate
PLCγ	Phospholipase C gamma
Plk1	Polo-like kinase 1
PLST-1	*C. elegans* ortholog of Plastin 1
PP1	Protein phosphatase 1
PPP1R12C	Protein Phosphatase 1 Regulatory Subunit 12C gene
PPP1R7	Protein phosphatase 1 regulatory subunit 7
PRC1	Protein regulator of cytokinesis 1
Puro	Puromycin resistance gene
qPCR	Quantitative PCR
RAD18	E3 ubiquitin-protein ligase RAD18
RAD51	DNA repair protein RAD51 homolog 1

RAD52	DNA repair protein RAD52 homolog
Ran	Ras-related nuclear protein
RanGAP	Ran GTPase activating protein
RanQ69L	GTPase-deficient Ran mutant
RCC1	Regulator of chromosome condensation 1
RHO-1	*C. elegans* ortholog of RhoA
RhoA	Ras homolog family member A (Gene: RHOA)
RNP	Ribonucleoprotein
ROCK	Rho-associated protein kinase
ROSA26	Reverse orientation splice acceptor 26
RPA	Replication protein A
RPE-1	Retinal pigment epithelial cell line
RT-qPCR	Reverse transcriptase quantitative PCR
S	Synthesis phase
S2	*Drosophila melanogaster* Schneider 2 cell line
SA	Splicing acceptor
SaCas9	*Staphylococcus aureus* Cas9
SB431542	Small molecule inhibitor of TGF-β receptors
SCR7	Small molecule inhibitor of DNA ligase IV
SD	Standard deviation
Sds22	Suppressor of Dis2 mutant 2, *Drosophila* ortholog of PPP1R7
sgRNA	Single guide RNA
SK-MEL-2	Human melanoma cell line
SMAD	Small mothers against Decapentaplegic
smNG2-P	Split mNeonGreen2 parental cell line
SNR	Signal-to-noise ratio
SOE	Splicing by overlap extension
SOX2	SRY-box transcription factor 2
SpCas9	*Streptococcus pyogenes* Cas9
ssDNA	Single-stranded DNA
ssODN	Single-stranded oligodeoxynucleotide

SSTR	Single-stranded templated repair
STK24, 25, 26	Serine/threonine-protein kinase 24, 25, 26
T2A	*Thosea asigna* virus 2A peptide
TagBFP	Tag blue fluorescent protein
TagRFP-T	Tag red fluorescent protein S158T
TBXT	T-box transcription factor T gene
TCA	Trichloroacetic acid
TGF-β	Transforming growth factor beta
TIDE	Tracking of indels by decomposition
TPX2	Targeting protein for *Xenopus* kinesin-like 2 protein
TPXL-1	*C. elegans* ortholog of TPX2
TRA-1-60	Tumor-related antigen 1-60
tracrRNA	Trans-activating CRISPR RNA
TUBA1B	Tubulin alpha 1b gene
TUBB3	Tubulin beta-3 chain gene
UNC-59	Uncoordinated 59, *C. elegans* ortholog of Septin 7
WT	Wild-type
WTC-11	Human iPS cell line
Y-27632	Small molecule inhibitor of ROCK
ZO-1	Zonula occludens 1 protein
β-glo	Rabbit β-globin poly-adenylation signal

CHAPTER 1

Introduction

Adapted from: Husser, M. C., Skaik, N., Martin, V. J. J., & Piekny, A. (2021, Apr 15). CRISPR-Cas tools to study gene function in cytokinesis. *J Cell Sci, 134*(8).

1.1 Preamble

Recent advances in gene editing have revolutionized our ability to manipulate genomes. Gene editing tools can be used to generate gene knockouts or introduce point mutations or knock-ins at precise genomic locations to help study how cells function. However, precision gene editing is challenging in cultured mammalian cells. In this thesis, I aimed to use gene editing tools to facilitate the study of proteins in human cells. I focused on endogenous tagging to visualize proteins of interest at endogenous expression levels in live cells. In this chapter, I review the use of common gene editing tools and their limitations in mammalian cells. I also discuss the use of gene editing to generate endogenous tags to study proteins function in mammalian cells, with a focus on cytokinesis. This literature review provides the rationale for the work presented in Chapters 2 and 3, where I generated a number of endogenously-tagged human and mammalian cell lines and used them to study cytokinesis across multiple cell types.

1.2 Gene editing using CRISPR/Cas9

1.2.1 CRISPR/Cas9

Gene editing technologies rely on the ability to introduce DNA damage at specific genomic sites and take advantage of DNA repair pathways to introduce the desired changes. Early gene

editing tools consisted of site-specific nucleases or nucleases fused to DNA-binding domains engineered to target desired genomic sites (generally 500 bp to 1 kb; Adli, 2018). However, these tools were difficult to reprogram to target new genomic sites (Gupta & Musunuru, 2014). Since their development in 2012, CRISPR/Cas (clustered regularly interspaced short palindromic repeats; CRISPR-associated proteins) tools have revolutionized gene editing thanks to their ability to be easily reprogrammed to target any desired genomic site (Jinek et al., 2012). The most widely used CRISPR system for gene editing is derived from *Streptococcus pyogenes*, where its primary function is to confer bacterial immunity against viruses (Wiedenheft et al., 2012). This system consists of an RNA-guided endonuclease (SpCas9; generally referred to as Cas9) in complex with a gRNA (guide RNA; Jinek et al., 2012; Wiedenheft et al., 2012). In the native system, gRNAs are made up of a crRNA (CRISPR RNA), which directs Cas9 enzyme to a specific target site, and tracrRNA (trans-activating CRISPR RNA) that mediates interactions with Cas9 (Jinek et al., 2012). To facilitate their use for gene editing, the crRNA has been fused with the tracrRNA for their expression as a single molecule referred to as sgRNA (single guide RNA; Jinek et al., 2012). The sgRNA contains a 20-nucleotide spacer sequence that recognizes a complementary target sequence (also called protospacer; Fig. 1.1). Cas9 is directed to the genomic target site by the sgRNA, where Cas9 cleaves the target dsDNA (double-stranded DNA), resulting in a double-stranded break (DSB; Fig. 1.1). Cas9 also requires a PAM site (protospacer-adjacent motif; NGG sequence for SpCas9) to be directly adjacent to the protospacer sequence for cleavage (Fig. 1.1). Cas9 typically generates blunt DSBs 3 base pairs (bp) upstream of the PAM site within the protospacer sequence (Fig. 1.1; Jinek et al., 2012). This tool can be reprogrammed to target any site that is adjacent to a PAM site by changing the sgRNA spacer sequence (Fig. 1.1; Cong et al., 2013; Jinek et al., 2012; Mali et al., 2013; Pickar-Oliver & Gersbach, 2019).

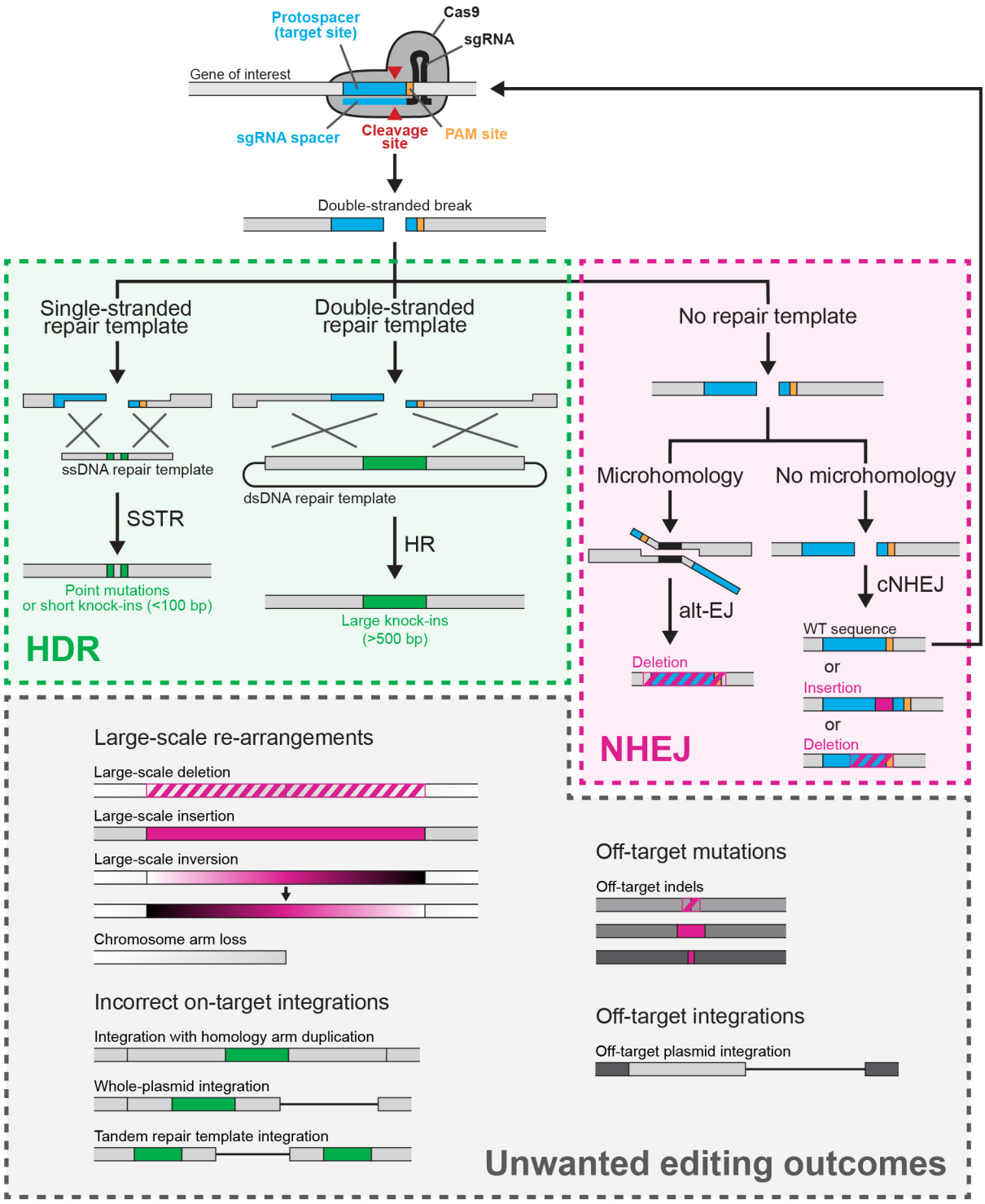

Figure 1.1. Gene editing using CRISPR/Cas9. Schematic representation of Cas9 targeting and DNA repair to introduce different mutations. Cas9 locates the target site (protospacer) dictated by the sgRNA spacer sequence. Cas9 generates a DSB at the target site, which can be repaired using a repair template by HDR (green box, left) or without by NHEJ (pink box, right). In HDR, after

end resection, SSTR can repair DSBs using a homologous ssDNA repair template, while HR can repair the DSB using a homologous dsDNA repair template. Both strategies will introduce mutations from the repair templates in a precise manner at the target site. In NHEJ, the free DNA ends are ligated ends back together, which can result in the introduction of indel mutations around the DSB site. Alt-EJ can also repair DSBs using microhomologies on either side of the break, resulting in short deletions. Finally, gene editing using CRISPR/Cas9 can also lead to unwanted mutations (grey box, bottom), including on-target large-scale re-arrangements or incorrect integrations, or off-target indel mutations or random integrations.

1.2.2 Other CRISPR systems for gene editing

Many CRISPR systems have been identified in bacteria, archaea and viruses, which have been classified based on their components, organisation and sequence similarity (Makarova et al., 2020). Type II and V CRISPR systems are often used for gene editing as they rely on a single effector enzyme to target DNA and sometimes RNA (Cas9 in type II systems and Cas12 in type V systems). Meanwhile, type I, III and IV CRISPR systems rely on multi-protein effector complexes, and type VI systems exclusively target RNA. *Staphylococcus aureus* Cas9 (SaCas9) has been used as a smaller alternative to SpCas9 (1053 amino acids compared to 1368 amino acids for SpCas9), which allows it to be packaged into AAV (adeno-associated virus) vectors that carry up to 5 kb of cargo (Friedland et al., 2015). SpCas9 and SaCas9 have similar activity, but SaCas9 recognizes NNGRRT PAM sequences (Friedland et al., 2015). Other small Cas9 enzymes have been characterized, which cover a range of PAM sites but are less well characterized (Anzalone et al., 2020). Type V systems use Cas12 as an effector enzyme and mainly target DNA (Anzalone et al., 2020; Makarova et al., 2020). Amongst Cas12 enzymes, Cas12a derived from *Acidaminococcus sp. BV3L6* and *Lachnospiraceae bacterium ND2006* have been more popular for gene editing (Friedland et al., 2015). Cas12a enzymes are similar in size to Cas9 (1307 and 1228 amino acids, respectively) and require T-rich PAM sequences (TTTN and TTTV, respectively). Moreover, Cas12a can process crRNA arrays (pre-crRNA) into individual crRNAs

that function as gRNAs without a tracrRNA (Paul & Montoya, 2020). This facilitates multiplexed gene editing where multiple gRNAs are delivered in one array and processed into individual crRNAs by Cas12a before editing (Campa et al., 2019). Cas12a also generates staggered DSBs with 4 -5 bp overhangs, as opposed to the blunt DSBs generated by Cas9. The characterization of different CRISPR/Cas systems with different PAM sites provides more options for target site selection. However, the *S. pyogenes* CRISPR/Cas9 system is most characterized system for gene editing, with many datasets, tools and protocols that can be used to inform new editing experiments.

1.2.3 DNA damage repair pathways

Gene editing tools induce DNA damage and take advantage of DNA repair pathways to introduce desired mutations. DSBs are typically repaired by NHEJ (non-homologous end-joining) or HDR (homology-directed repair; Yeh et al., 2019). Canonical NHEJ (cNHEJ) repairs DSBs by ligating two blunt ends together (Fig 1.1). Free DNA ends are first recognized by the Ku70/Ku80 protein complex, which recruits DNA-PKcs (DNA-dependent protein kinase catalytic subunit) to form the DNA-PK complex. This complex then recruits several proteins, including DNA ligase IV, to ligate the ends back together (Yeh et al., 2019). The protein 53BP1 is also recruited to DSB sites and inhibits competing repair pathways (Shibata, 2017). Although cNHEJ generally repairs DSBs correctly, nucleotides can be removed or added to the DNA ends before ligation, resulting in short insertions or deletions (indel mutations; Fig 1.1; Mali et al., 2013). Another pathway called alternative end-joining (Alt-EJ; also referred to as alt-NHEJ or MMEJ) can repair DSBs using short microhomologies (5-25 bp) on either side of the break, causing the loss of intervening sequence to form short deletions (Yeh et al., 2019). In the Alt-EJ pathway, short-range end

resection of the free 5' ends is carried out by the MRN (MRE11–RAD50–NBS1) complex, which is activated by CtIP and BRCA1. End resection exposes microhomologies that can anneal together. Any remaining flaps are then removed by an endonuclease, gaps are filled by polymerase θ, and DNA ligase I or III ligate the break (Yeh et al., 2019). BRCA1 is antagonized by 53BP1, which prevents resection during cNHEJ (Ackerson et al., 2021). The competition between 53BP1 and BRCA1 establishes the decision point between cNHEJ, which requires blunt DNA ends, and Alt-EJ or HDR, which require resected ssDNA (single-stranded DNA) ends. Indel mutations resulting from Alt-EJ and cNHEJ are broadly classified as NHEJ mutations. Indel mutations introduced within the coding sequence of a gene can result in frame-shifts and gene loss-of-function (Cong et al., 2013). Because NHEJ is the predominant repair pathway in most animal cells, it is the easiest way to generate loss-of-function mutations. Alternatively, DSBs can be repaired by HDR (homology-directed repair), which employs a repair template homologous to the damaged region (Wright et al., 2018). Homologous sister chromatids are generally used for HDR, so this pathway is only active in S and G2 phases of the cell cycle. For precision gene editing, synthetic repair templates can be provided to repair the DSB and introduce the desired mutations (Fig. 1.1; Verma et al., 2017). Repair templates are designed to carry the desired mutations flanked by homology arms that match the sequence on either side of the DSB. During HDR, short-range end resection by the MRN complex is followed by long-range resection performed by the EXO1 or DNA2 nucleases, which generates ssDNA tails that are stabilized by RPA proteins (Yeh et al., 2019). Different HDR pathways are involved in the repair of DNA damage using ssDNA or dsDNA repair templates. SSTR (single-stranded templated repair) uses a ssDNA repair template and requires short homology arms for repair (40-80 bp; Fig. 1.1). For this reason, ssODNs (single-stranded oligodeoxyribonucleotides) are used to introduce point mutations and small knock-ins (<100 bp;

Fig. 1.1; Glaser et al., 2016; Yu et al., 2016). During SSTR, RAD52 mediates the annealing of a free ssDNA tail, either generated by end resection or directly released by Cas9, to a homologous ssODN molecule (Yeh et al., 2019). The DNA end is then extended by replicating the ssODN before dissociating, and the DNA ends are ligated together. ssODNs are generally short (<200 bp), so dsDNA repair templates (referred to as dsODNs; double-stranded oligodeoxynucleotides) are required to carry larger integrations (>200 bp). HR (homologous recombination) uses dsODNs for repair and requires long homology arms (generally 500 bp to 1 kb). HR comprises multiple related pathways that result in the repair of DNA breaks by replicating a homologous repair template (Wright et al., 2018). RPA proteins are first displaced by BRCA2 and replaced with RAD51, which directs the search for homologous sequences (Yeh et al., 2019). When a homologous sequence is found, strand invasion occurs, and the free DNA end is extended by polymerase δ. The other DSB end may undergo strand capture and be extended from the repair template as well. Finally, the extended DSB ends can anneal and are ligated by DNA ligase I (Yeh et al., 2019). HDR can be used to introduce precise mutations using repair templates, but it is far less efficient than NHEJ in mammalian cells, making precision gene editing challenging to achieve.

1.3 Challenges of gene editing

1.3.1 Delivery

Despite the advantages of CRISPR/Cas9 over other gene editing tools, several bottlenecks limit its widespread use. The methods employed to deliver CRISPR components and repair templates into cells can be inefficient and/or toxic. The most common approach is to transfect cells with plasmids expressing Cas9 and a sgRNA, where different sgRNA spacers can easily be cloned to target specific sites. However, these plasmids are generally large (>8 kb), which results in low

transfection efficiency and high toxicity. On the other hand, the transfection of Cas9 mRNA or purified Cas9/sgRNA RNP (ribonucleoprotein) complexes results in higher editing efficiency and lower toxicity compared to plasmid delivery (Kagita et al., 2021; Kim et al., 2014; Liang et al., 2015). mRNA molecules are less toxic than plasmid DNA, and only need to be delivered to the cytosol for expression (Sinclair et al., 2023). Meanwhile, Cas9/sgRNA binding can be inhibited by intracellular RNA molecules, so pre-assembled Cas9/sgRNA RNP complexes are more active than Cas9 and sgRNAs expressed intracellularly (Kagita et al., 2021; Kim et al., 2014). To maximize the delivery of CRISPR components, electroporation methods are preferred as they provide high transfection efficiency and low toxicity (Ghetti et al., 2021; Xu et al., 2021). Viral transduction is also highly efficient, but some viral vectors have restrictions in cargo size and/or can integrate into the genome (Asmamaw Mengstie, 2022). Importantly, viral delivery also requires the generation of viral particles prior to editing. Today, the electroporation of Cas9/sgRNA RNP complexes, along with the delivery of repair templates either by co-electroporation or by AAV transduction is the gold standard for gene editing in cultured mammalian cells.

1.3.2 Targeting efficiency

The efficiency of gene editing using CRISPR/Cas9 is also affected by how efficiently Cas9 cuts DNA at the target site. Cutting efficiency (or targeting efficiency) is dependent on sgRNA expression and RNP complex formation (Kagita et al., 2021; Mefferd et al., 2015), spacer sequence (Xu et al., 2015) and chromatin accessibility at the target site (Horlbeck et al., 2016; Kuscu et al., 2014; Wu et al., 2014). The targeting efficiency of Cas9/sgRNA complexes is determined by the ability to introduce indel mutations at a target site, as measured by T7 endonuclease I or Surveyor

assays, TIDE (tracking of indels by decomposition) analysis of Sanger sequencing data, or next-generation sequencing (Sentmanat et al., 2018). Models have been built to predict sgRNA targeting efficiency based on large-scale sgRNA screens (Concordet & Haeussler, 2018; Cui et al., 2018; Doench et al., 2016; Hsu et al., 2013; Stemmer et al., 2015). Some tools also predict Cas9 off-target sites based on similarity with the sgRNA target across the genome (Cui et al., 2018). Although these tools are useful for design, sgRNA activity can vary and multiple sgRNAs may need to be tested to find one sgRNA with high cutting efficiency at a desired target site. Using pre-assembled Cas9/sgRNA RNP complexes can improve cutting efficiency as described earlier (Kagita et al., 2021; Kim et al., 2014). Moreover, chemical modifications can be added to chemically synthesized sgRNAs to increase their stability and prevent their degradation, thereby increasing their efficiency (Allen et al., 2020; Hendel et al., 2015).

1.3.3 Efficiency of precise DNA repair

Although HDR is required to introduce precise mutations using CRISPR/Cas9, this process is inefficient in mammalian cells. In human cells, HDR activity is restricted to the S and G2 phases of the cell cycle (Yeh et al., 2019). Moreover, repair by NHEJ is much faster than HDR (as fast as 10 minutes for NHEJ and 7 hours for HDR), and NHEJ proteins inhibit end resection, which is required for HDR (Fu et al., 2021; Mao et al., 2008; Yeh et al., 2019). Strategies to increase the frequency of repair by HDR include synchronizing cells in G2 phase using small molecules (Lin et al., 2014a; Maurissen & Woltjen, 2020), enriching a population of cells in G2 phase by FACS (fluorescence-activated cell sorting; Yang et al., 2016), or restricting Cas9 activity to the G2 phase (Gutschner et al., 2016; Matsumoto et al., 2020). These strategies can increase the frequency of HDR by up to 6-fold, but some cell types are not easily amenable to synchronizing strategies, and

variable effects have been reported in different cell lines (Lin et al., 2014a; Maurissen & Woltjen, 2020; Yang et al., 2016). Another approach is to use small molecule that inhibit NHEJ (Chen et al., 2022; Chu et al., 2015; Maruyama et al., 2015; Maurissen & Woltjen, 2020; Riesenberg et al., 2023; Schimmel et al., 2023; Yeh et al., 2019). For example, the small molecules SCR7 and NU7441 inhibit DNA ligase IV and DNA-PKcs, respectively, and can increase the frequency of HDR repair by 2- to 3-fold (Maurissen & Woltjen, 2020; Robert et al., 2015; Shams et al., 2022). The knockdown of NHEJ and Alt-EJ proteins, including Ku70, Ku80, DNA ligase IV and DNA-PKcs has also been shown to increase the frequency of HDR by up to 3-fold, which can be further increased by targeting multiple proteins simultaneously (Chu et al., 2015; Paulsen et al., 2017; Riesenberg et al., 2023; Robert et al., 2015). Similarly, the expression of HDR activators such as CtIP, RAD18, EXO1 and RAD52, or a dominant-negative 53BP1 protein, increases the frequency of HDR by up to 3-fold (Canny et al., 2018; Hackley, 2021; Nakade et al., 2018; Nambiar et al., 2019; Paulsen et al., 2017; Shams et al., 2022). Other strategies have been devised to increase the frequency of HDR, including melting or crosslinking dsDNA repair templates before transfection (Ghanta & Mello, 2020; Ghasemi et al., 2023), or co-targeting the repair template to the target site along with Cas9 (Aird et al., 2018). However, the efficacy of these strategies varies between different loci and in different cell lines. Overall, using NHEJ inhibitors is the easiest method to increase the frequency of precise repair by HDR. A new CRISPR/Cas9-based tool termed Prime Editing (PE) was recently developed, where a Cas9 nickase is used to generate single-stranded nicks and is fused to a reverse transcriptase to copy desired edits from the 3’ end of the sgRNA (termed pegRNA; Prime Editing gRNA) into the nicked target site (Anzalone et al., 2019). PE relies on different DNA repair pathways and has demonstrated higher editing efficiency with less unwanted by-products than HDR (Anzalone et al., 2019; Ferreira da Silva et al., 2022). However,

although PE provides high editing efficiency to introduce precise point mutations, it does not work efficiently for integrations larger than 30 bp (Koeppel et al., 2023). Further work is required to increase the efficiency of precise repair by HDR, and to develop new tools that can introduce a range of mutations efficiently.

1.3.4 Unwanted editing outcomes

Another challenge with CRISPR/Cas9 editing is that Cas9 can generate DSBs at off-target sites that closely match the sgRNA target. This can result in the introduction of unwanted indel mutations at off-target sites (Fig. 1.1; Zhang et al., 2015). To alleviate this, sgRNA design software often generates off-target scores that consider the number of putative off-target sites across the genome of interest, and their similarity to the sgRNA target site (Cui et al., 2018). A good sgRNA should have few predicted off-target sites with low scores or low similarities to the sgRNA target. Several Cas9 variants have been engineered to have increased specificity by reducing the frequency of off-target cutting (Slaymaker & Gaudelli, 2021). One of these variants, HypaCas9, was engineered to enhance its proofreading mechanism, thereby reducing the frequency of cleavage at mismatched target sites (Chen et al., 2017). Such variants have higher specificity, measured as the ratio of on-target mutations to off-target cutting, but may also display reduced on-target activity compared to WT Cas9 (Kim et al., 2023; Vakulskas et al., 2018). Alternatively, using a Cas9 nickase variant to target two adjacent sites on opposite strands of the DNA will result in on-target editing without significant off-target mutations (Ran et al., 2013a). In this approach, two adjacent nicks generate a staggered DSB that can be repaired by NHEJ or HDR. Meanwhile, off-target cleavage would likely only occur with one of the sgRNAs, resulting in a single-stranded nick that is easily repaired in an error-free manner (Ran et al., 2013a).

Another concern is that DNA molecules used for editing (plasmids expressing Cas9 and/or sgRNAs and repair templates) can be randomly integrated into the genome (Arias-Fuenzalida et al., 2017; Burgio & Teboul, 2020; Hanss et al., 2019; Lim et al., 2023; Roberts et al., 2017; Saito et al., 2017; Tanaka et al., 2022; Zelensky et al., 2017). Off-target integrations can go undetected if they can have no visible effect on the cells. However, they can result in ectopic transgene expression or disrupt endogenous genes when the integration occurs within a gene. Linear dsDNA is more prone to random integration than plasmids or ssDNA molecules (Lim et al., 2023). Random integrations can also be detected after isolating clones by using specific PCR screening strategies, measuring integration copy number, or by unbiased sequencing (Dawes et al., 2020; Roberts et al., 2017; Schjeide & Puschel, 2023; Yan et al., 2020).

Amongst other unwanted outcomes of gene editing, large-scale rearrangements can occur around the Cas9 target site (Burgio & Teboul, 2020). Specifically, kilobase- to megabase-scale deletions, insertions, inversions and translocations can occur around the sgRNA target site during editing (Fig. 1.1; Birling et al., 2017; Boroviak et al., 2017; Burgio & Teboul, 2020; Cullot et al., 2019; Kosicki et al., 2018; Leibowitz et al., 2021; Liu et al., 2021; Owens et al., 2019; Park et al., 2022; Weisheit et al., 2020; Zuccaro et al., 2020). Such large-scale re-arrangements are particularly deleterious because they can go undetected by PCR, which is commonly used for screening. While it is unclear how frequent these rearrangements are across different loci and cell types, they can be detected using different methods, including specific PCR detection strategies, copy number quantification, long-range sequencing, or whole-genome sequencing (Burgio & Teboul, 2020; Cullot et al., 2019; Kosicki et al., 2018; Zuccaro et al., 2020).

Finally, incorrect integrations of exogenous DNA can also occur at the Cas9 target site (Burgio & Teboul, 2020; Erbs et al., 2023; Medert et al., 2023; Roberts et al., 2017; Skryabin et

al., 2020; Tanaka et al., 2022). Incorrect integrations can include entire plasmids, repair templates with duplicated homology arms, or repair template concatemers, among others (Fig. 1.1). Some incorrect integrations can be misidentified as correct integrations. It is unclear how frequently these incorrect integrations occur across different loci and cell lines but they can be identified using specific PCR strategies, by measuring copy number, or by long-range sequencing or unbiased sequencing (Burgio & Teboul, 2020; Erbs et al., 2023; Medert et al., 2023).

1.3.5 Clonal isolation

After editing, clonal cell populations often need to be recovered to obtain a homogeneous cell population for downstream experiments. Methods for clonal isolation include limiting dilution, colony picking (Cerbini et al., 2015b; Haupt et al., 2018; Kime et al., 2016; Ye et al., 2021), and high-throughput approaches such as FACS (fluorescence-activated cell sorting) or single-cell dispensing (Giuliano et al., 2019; Takahashi & Miyaoka, 2023). Specifically, FACS enables the isolation of many clones at once by sorting individual cells into each well of 96- or 384-well plates. Cells can be sorted based on fluorescence or indiscriminately, recovered and screened for the desired edit. However, clonal isolation can be challenging as the rate of single-cell recovery can be low depending on the cell line. For example, healthy human cells like stem cells are programmed to undergo apoptosis upon loss of adherence to an extracellular matrix or to other cells (Wang et al., 2009; Watanabe et al., 2007). When cells show poor single-cell recovery, protocols can be optimized to increase recovery by using specific media, extracellular matrix components, or additives such as growth factors or apoptosis inhibitors (Bhargava et al., 2022; Chen & Pruett-Miller, 2018; Singh, 2019; Tristan et al., 2023). Alternatively, successive rounds of dilution and screening for the enrichment of edited cells can be carried out to obtain nearly pure

cell populations while avoiding single-cell isolation (Deneault et al., 2018). Even though single-cell recovery is inefficient for mammalian cells, it is essential to recover clones that can be screened for the desired edits.

1.4 Knock-ins and endogenous tags

1.4.1 Design of knock-in experiments

CRISPR/Cas9 can be used to generate gene knock-ins where exogenous DNA sequences are integrated precisely into the genome. The most common types of knock-ins are gene expression cassettes and endogenous tags. Expression cassettes comprise a promoter and a gene of interest. Endogenous tags are protein tags (fluorescent proteins, enzymatic reporters or epitope tags) that are inserted into and in frame with endogenous genes to allow detection or purification of a protein of interest. Precise knock-ins are usually generated via the HDR pathway. Short knock-ins (<200 bp) can be made using ssODN repair templates, which requires short homology arms (40-80 bp; Yang et al., 2013; Yu et al., 2016). ssODNs can be purchased commercially and provide higher editing efficiency compared to dsODNs (Eroglu et al., 2023; Glaser et al., 2016; Richardson et al., 2016). Although long ssODNs can be used for larger knock-ins, they are more difficult to generate (Eroglu et al., 2023; Inoue et al., 2021). Larger knock-ins (>200 bp) are commonly made using dsODNs that carry the integration flanked with large homology arms (generally 500 bp to 1 kb; Zhang et al., 2017). Since the cloning of dsODNs can be tedious and the efficiency of integration by HDR is low, several groups have taken advantage of NHEJ-based ligation to generate knock-ins. For this approach, a linear dsDNA repair template is simply ligated into the DSB by NHEJ (Bukhari & Muller, 2019). This approach uses repair templates made up of only the integration with no homology arms, which are easier to assemble. Moreover, NHEJ-based ligation provides

higher knock-in efficiencies than HDR (He et al., 2016). However, integration of the repair template by NHEJ can only occur at the DSB site, whereas HDR offers the flexibility of making integrations within a short distance of the DSB site (usually within 20 nucleotides, with lower efficiency at a greater distance; Artegiani et al., 2020; Paquet et al., 2016). The linear dsDNA fragment can also be ligated in either of two orientations (He et al., 2016; Sawatsubashi et al., 2018; Zeng et al., 2020). Moreover, NHEJ-based ligations can occur with errors, resulting in indel mutations at the integration junctions (Artegiani et al., 2020; He et al., 2016; Manna et al., 2019; Sawatsubashi et al., 2018; Shi et al., 2023; Zeng et al., 2020). Finally, off-target integrations are more frequent when using linear dsDNA repair templates (Lim et al., 2023; Sawatsubashi et al., 2018). Several approaches have been devised to overcome these limitations, including the use of cleavable vectors to deliver linear fragments only when Cas9 is active (Sawatsubashi et al., 2018; Suzuki et al., 2016; Zeng et al., 2020), frame selection strategies to ligate tags in frame with a gene (Artegiani et al., 2020; Shi et al., 2023), and re-excision of incorrectly oriented integrations (Manna et al., 2019). Despite these improvements, NHEJ-based knock-ins are error-prone, and HDR remains the preferred pathway for precise knock-ins in mammalian cells.

1.4.2 Safe-harbor sites for expression cassette knock-ins

Expression cassette knock-ins require integration sites that allow for stable transgene expression, referred to as safe-harbor sites (Pavani & Amendola, 2020). Although recent work has identified new potential safe-harbor sites (Aznauryan et al., 2022; Pellenz et al., 2019), few sites have been characterized and regularly used as safe-harbors in the human genome. The most widely used safe-harbor site in the human genome is the AAVS1 locus (Adeno-associated virus integration site 1), which lies in the first intron of the PPP1R12C gene on chromosome 19. This

site was discovered as an integration site for adeno-associated viruses (Kotin et al., 1990), and was subsequently used for transgene integration and expression (Bharucha et al., 2021; Oceguera-Yanez et al., 2016; Smith et al., 2008; Stellon et al., 2022). Most importantly, it has been shown that transgenes integrated at the AAVS1 locus are not subject to the loss of expression by epigenetic silencing during long-term culturing or cell differentiation (Luo et al., 2014; Oceguera-Yanez et al., 2016; Ogata et al., 2003; Shin et al., 2020; Smith et al., 2008). Other safe harbor sites have been found amongst viral integration sites or in large-scale screens, and characterized for their ability to support high and stable transgene expression, including the CLYBL, ROSA26 and CCR5 loci (Aznauryan et al., 2022; Cerbini et al., 2015a; Shin et al., 2020). The ROSA26 locus has been extensively used for knock-ins in mice (Abe et al., 2011), and has been characterized as a safe-harbor locus in other mammals (Yuan et al., 2021).

1.5 Tools to study protein localization

1.5.1 Transgene over-expression

In human cells, protein localization is most commonly studied by transfecting a plasmid that carries the gene coding for a protein of interest fused to a fluorescent protein for visualization (Kim & Eberwine, 2010). Strong promoters are often used to drive transgene expression, resulting in high over-expression in cells. Expression vectors can be transfected transiently, where they are delivered into cells for transient expression, but are not maintained by the cells and are eliminated after a few days. Most experiments are carried out 24 to 48 hours after transfection, and expression is extremely variable as each cell gets a different number of plasmid copies to drive expression. Additionally, transfection can transiently alter cell physiology and gene expression (Fus-Kujawa et al., 2021; Jacobsen et al., 2009). Alternatively, stable transfection can be achieved by selecting

for an antibiotic resistance marker carried by the expression vector (Kechad & Hickson, 2017; Kim & Eberwine, 2010). Mammalian cells can randomly integrate exogenous dsDNA into their genome at low frequency, so stable cell lines expressing the desired transgenes can be selected and isolated (Spector & Goldman, 2010). In this case, transgene expression is less variable as every cell has the same random integration. Cells with stable over-expression can also be generated by integrating an expression cassette using site-specific recombinases in a cell line that carries recombination sites (Spitzer et al., 2013). However, stable cell lines can be subject to loss of expression by epigenetic silencing (Cabrera et al., 2022). Moreover, over-expression can alter cell physiology and induce artefacts of protein localization and cellular behavior by saturating the cells with one protein (Gibson et al., 2013; Ratz et al., 2015; Rizzo et al., 2009; Roberts et al., 2017). As an alternative to over-expression, chemically inducible promoters can be used to titrate transgene expression to a desired level and induce expression only when needed (Adriaans et al., 2019; Manukyan et al., 2015; Zanin et al., 2013).

1.5.2 Fixed immunofluorescence

Endogenous proteins can be visualized by staining cells with fluorescently labelled antibodies (Donaldson, 2015). Since antibodies have high affinity for specific epitopes, staining tends to be highly specific. Antibodies can also be raised against antigens with specific post-translational modifications or proteins in a specific conformation (Keller et al., 2019; Yuce et al., 2005). However, immunofluorescence requires cells to be chemically fixed and permeabilized to allow the antibodies to reach the intracellular space, which can introduce artefacts and variable patterns depending on the chemical used (Huebinger et al., 2018; Irgen-Gioro et al., 2022; Yonemura et al., 2004). Moreover, fixation precludes the imaging of cells over time, providing

only a static view over a cell's lifetime. Additionally, staining efficiency and background signal can vary between samples (Pina et al., 2022).

1.5.3 Endogenous tags

Endogenous tags also allow for the visualization of protein localization in cells. For this, a protein tag is inserted into the genome in frame with a gene of interest (Fig. 1.2). Fluorescent proteins are commonly used for endogenous tagging as they allow for measurements of protein expression and localization (Bukhari & Muller, 2019; Husser et al., 2022). Fluorescent protein tags are often added to the start or the end of an open reading frame to generate an N-terminal or C-terminal fusion, respectively, but can also be inserted within proteins. The sites chosen for fusion should consider accessibility for molecular interactions regions and regions that need to be post-translationally modified. Linkers can be added to increase the distance between the tag and protein of interest and to ensure that the tag does not interfere with folding (Chen et al., 2013; Roberts et al., 2017). Most fluorescent protein-coding genes are ≈700 bp in size, requiring large repair templates for integration by HDR, which are often delivered as dsODNs (linear dsDNA or plasmids), or non-integrative AAV vectors (Fig. 1.2; Gaj et al., 2017). Although endogenous tagging with fluorescent proteins in mammalian cells is inefficient, tagged cells can easily be screened by fluorescence microscopy or flow cytometry (Fig. 1.2; Bukhari & Muller, 2019).

Endogenous tagging with fluorescent proteins enables the study of target proteins at endogenous levels in live, unperturbed cells (Bukhari & Muller, 2019; Dambournet et al., 2014). While the localization of endogenously-tagged proteins generally agrees with transient transfection and fixed immunofluorescence, studies have shown that endogenous tags provide less

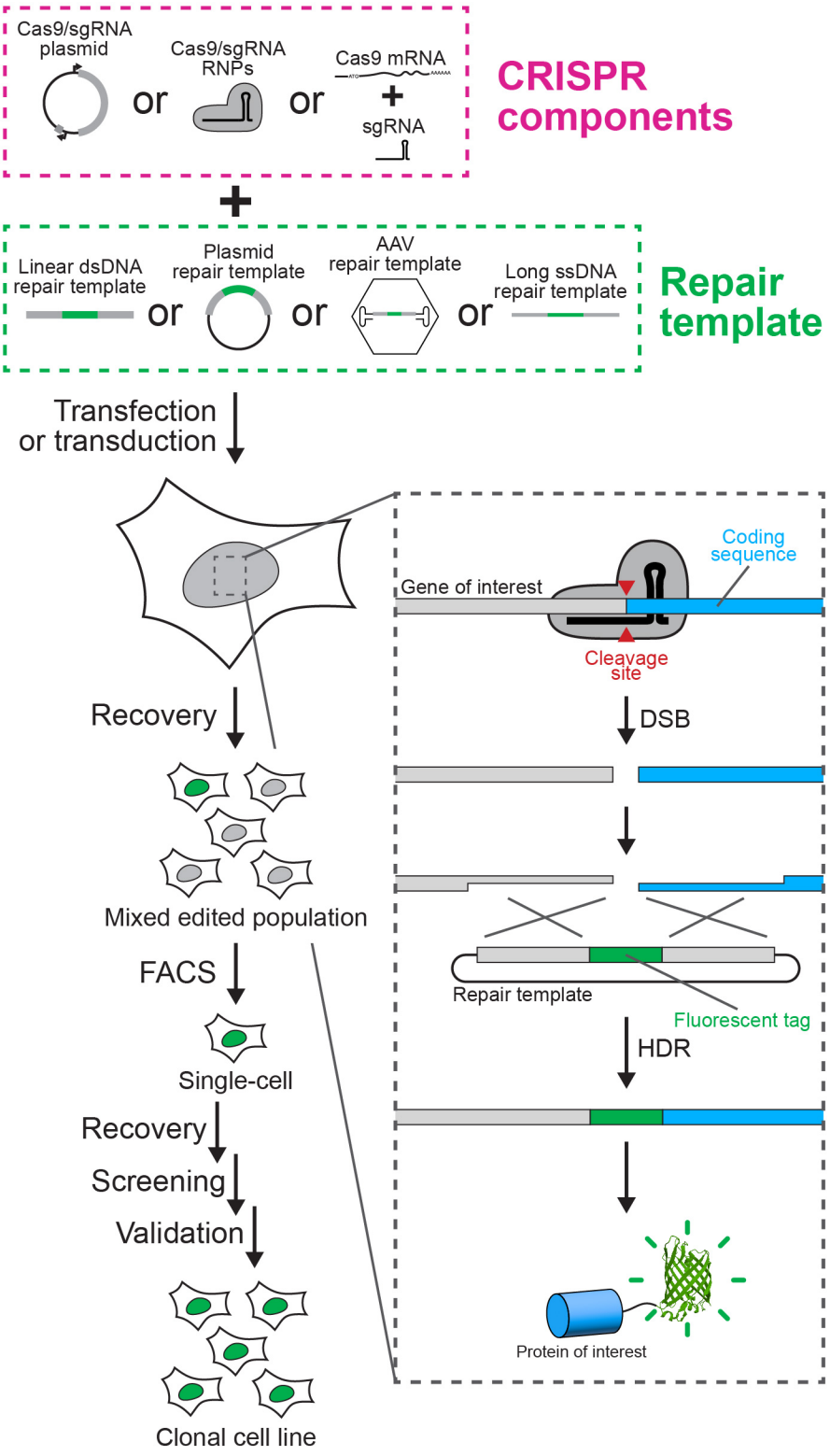

Figure 1.2. Endogenous tagging workflow. Schematic representation of the workflow for endogenous tagging in human cells. CRISPR components are delivered as plasmids, RNP

complexes or Cas9 mRNA with purified sgRNA, and repair templates are delivered as linear DNA, plasmids or AAV particles. After co-delivery of CRISPR components and a repair template, the endogenous tag can be integrated at the target site by HDR (inset, right), and the cells will express the tagged protein. Tagged cells can be isolated by FACS, recovered, screened and validated to obtain a clonal endogenously tagged cell line.

variable and more accurate measurements of protein levels and behavior (Doyon et al., 2011; Grassart et al., 2014; Mahen et al., 2014; Ratz et al., 2015; Strohmeier et al., 2021). Specifically, an early study of clathrin-mediated endocytosis using gene editing showed that over-expression of clathrin light chain A slowed down endocytosis, whereas endogenous tagging of clathrin light chain A recapitulated WT endocytosis dynamics in SK-MEL-2 cells [human melanoma cell line; (Doyon et al., 2011)]. In a comparative study of over-expressed and endogenously-tagged Aurora B kinase in HeLa cells, Mahen et al. (2014) measured the concentration and diffusion coefficient of the tagged protein around chromatin during mitosis. They found that endogenously-tagged Aurora B kinase is highly enriched at chromatin, while over-expression saturates chromatin-binding sites and leads to the accumulation of Aurora B kinase in the cytosol. Moreover, the diffusion coefficient of Aurora B kinase decreased during mitosis in endogenously tagged cell lines but remained the same throughout the cell cycle when over-expressed. These studies demonstrate that quantitative measurements of native protein behavior require endogenous protein levels. Although endogenous tags provide these advantages, as described earlier, the generation of endogenously tagged cell lines is inefficient and time-consuming. Endogenous tagging also requires the fusion of a protein of interest with a protein tag, which may affect the folding, activity, or interactions of the protein of interest. Moreover, functional point mutations are more difficult to introduce endogenously, which limits their use for functional studies. Comparatively, functional protein mutants are easy to generate and study using expression vectors. Therefore, studies of

cellular processes in human cells will benefit from combining the reliability of endogenous tags with the feasibility of transgene transfection and fixed immunofluorescence.

1.6 Cytokinesis

1.6.1 Overview

Cytokinesis occurs at the end of mitosis to physically separate a cell into two daughter cells. A RhoA (Ras homolog family member A)-dependent actomyosin contractile ring is assembled at the equatorial cortex during anaphase and ingresses to pinch in the membrane between the segregating chromosomes (Fig. 1.3A). The contractile ring is spatiotemporally controlled by multiple spindle-dependent and -independent pathways to ensure that cells inherit the correct fate determinants and genetic content (Fig. 1.3B). Failure to do so can cause changes in ploidy or cell fate, which can lead to the development of diseases, including cancer (D'Avino et al., 2015; Fededa & Gerlich, 2012; Green et al., 2012; Lacroix & Maddox, 2012; Pollard & O'Shaughnessy, 2019). Active RhoA (RhoA-GTP; guanosine triphosphate) promotes the assembly and ingression of the contractile ring by regulating effectors, including formins and ROCK (Rho-associated protein kinase), to form actin filaments and activate myosin, respectively (Fig. 1.3C; Piekny et al., 2005; Pollard & O'Shaughnessy, 2019). Ect2 (epithelial cell transforming 2) is the main GEF (guanine nucleotide exchange factor) that generates RhoA-GTP at the equatorial cortex (Gomez-Cavazos et al., 2020; Wolfe et al., 2009; Yuce et al., 2005). Active RhoA also recruits anillin, which is a scaffold protein that tethers the contractile ring to the plasma membrane (Green et al., 2012; Piekny et al., 2005; Piekny & Glotzer, 2008; Sun et al., 2015). Recent studies have shown that anillin positively feeds back to reinforce the division plane through the recruitment of phospholipid PI(4,5)P2 (phosphatidylinositol (4,5)-bisphosphate) and retention of active RhoA

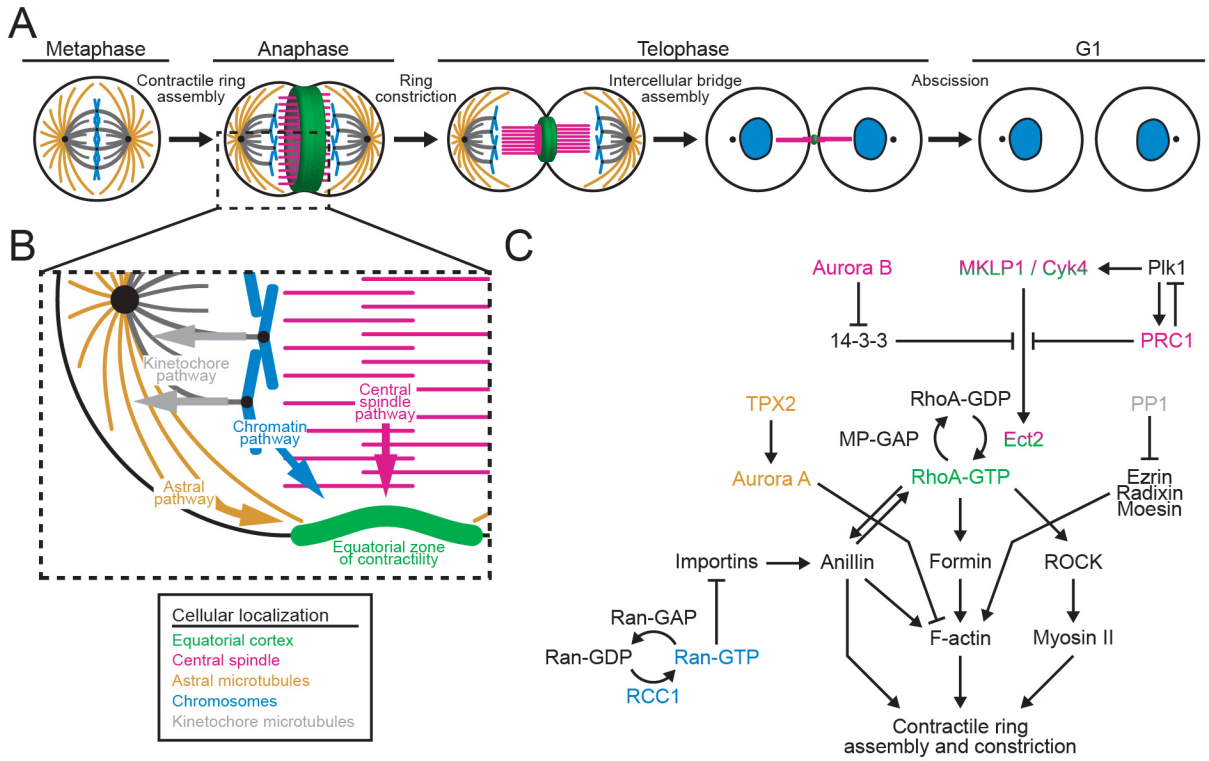

Figure 1.3. Overview of cytokinesis. A) A cartoon schematic shows a cell undergoing cytokinesis. During anaphase, cortical regulators accumulate at the equatorial cortex and assemble into a contractile ring. As cells progress through telophase, the ring constricts to pinch in the overlying plasma membrane, followed by formation of an intercellular bridge and midbody to promote abscission. **B)** A region of the cell is shown with a formed contractile ring to highlight the multiple pathways regulating contractile ring assembly. These include signals emanating from the central spindle (pink), astral microtubules (yellow), chromatin (blue) and kinetochores (grey). The protein shown in black have a broad localization, or their localization is affected by multiple pathways. **C)** The molecular components of the pathways regulating ring assembly are shown. These pathways regulate the generation and localization of active RhoA or regulate downstream components at the equatorial cortex (green). Active RhoA recruits and activates effectors (anillin, formin and Rho kinase) to generate actomyosin filaments and assemble the ring. A central spindle pathway (pink) promotes the recruitment and activation of Ect2 (RhoA-GEF) to the central spindle and equatorial cortex through Cyk4-binding. Astral microtubules (yellow) recruit TPX2, which activates Aurora A kinase to clear F-actin at the polar cortex. A chromatin pathway (blue) relies on a gradient of Ran-GTP that forms around chromatin and generates an inverse gradient of importins that control the localization and function of anillin at the equatorial cortex. A kinetochore-directed pathway (grey) induces relaxation of the polar cortex also by clearing F-actin, via PP1-mediated dephosphorylation of ERM proteins.

which preferentially binds to PI(4,5)P2 (Budnar et al., 2019). After ingression, the contractile ring and central spindle transition into a midbody, which is the site of abscission (Fig. 1.3A; El Amine

et al., 2013; Fededa & Gerlich, 2012; Green et al., 2012; Kechad et al., 2012; Mierzwa & Gerlich, 2014). The different stages of cytokinesis and their regulation have been described extensively in multiple reviews (Basant & Glotzer, 2018; D'Avino et al., 2015; Fededa & Gerlich, 2012; Glotzer, 2017; Green et al., 2012; Mierzwa & Gerlich, 2014; Ozugergin & Piekny, 2022; Piekny et al., 2005; Pollard & O'Shaughnessy, 2019 – among others).

1.6.2 Microtubule-dependent regulation of cytokinesis

The central dogma in cytokinesis is that the anaphase spindle provides cues to direct contractile ring assembly in the equatorial plane. Moving the spindle to a new location generates active RhoA and causes a new furrow to form in the location that bisects it (Bement et al., 2005; Rappaport, 1985). The centralspindlin complex is formed by MgcRacGAP (male germ cell Rac GTPase activating protein, referred to as Cyk4; Cytokinesis defect 4) and MKLP1 (mitotic kinesin-like protein 1, also known as KIF23). This complex regulates central spindle assembly and recruits Ect2 (Yuce et al., 2005). In human cells, Ect2 requires binding to Cyk4 to activate RhoA, and the contractile ring fails to form in cells depleted of Ect2 or Cyk4 (Kamijo et al., 2006; Nishimura & Yonemura, 2006; Yuce et al., 2005; Zhao & Fang, 2005). In metaphase, Cdk1 (cyclin-dependent kinase 1) phosphorylates sites in the S loop of Ect2, which inhibits its function. Autoinhibition occurs because this phosphorylated site binds to the N-terminal BRCT (BRCA1 C-terminus) domains, causing conformational changes that hinder the C-terminal DH domain (Dbl homology) required for GEF activity (Hara et al., 2006; Niiya et al., 2006). This mechanism restricts Ect2 activity to the time when it is required. When cells enter anaphase, Ect2 is dephosphorylated, and Cyk4-binding helps relieve autoinhibition. Cyk4 also requires phosphorylation by Plk1 (Polo-like kinase 1) to bind Ect2 (Burkard et al., 2009; Hara et al., 2006; Niiya et al., 2006; Petronczki et al.,

2007; Wolfe et al., 2009; Yuce et al., 2005). As the central spindle extends towards the cortex, Ect2 is enriched at the overlying membrane (Kotynkova et al., 2016; Lekomtsev et al., 2012; Su et al., 2011). Both Cyk4 and Ect2 have phospholipid-binding domains required for their function, and studies suggest that the role of the central spindle may be to position the Cyk4-Ect2 complex rather than to control its activity (Basant et al., 2015; Frenette et al., 2012; Lekomtsev et al., 2012). In multiple cell types, active RhoA localizes to a broader zone after the depletion of central spindle proteins such as PRC1 (protein regulator of cytokinesis 1) or MKLP1 (Adriaans et al., 2019; Mollinari et al., 2005; Yuce et al., 2005). Recent studies proposed that the central spindle positions Cyk4-MKLP1 complexes to activate Ect2 in proximity to the equatorial cortex (Adriaans et al., 2019; Mishima et al., 2002; Mishima et al., 2004). Plk1 is activated by PRC1 at the central spindle, where it could access Cyk4 for phosphorylation. Phospho-Cyk4 could then form a complex with Ect2 that is 'released' to the overlying cortex to generate active RhoA. Structural data also revealed that the PH (pleckstrin homology) domain of Ect2 could autoinhibit the DH domain, and binding to active RhoA and/or phospholipids relieves this inhibition (Chen et al., 2020). Thus, a model can be proposed where binding to phospho-Cyk4 and subsequence membrane recruitment both help relieve Ect2 autoinhibition. Importantly, these models do not provide an explanation for how active RhoA is spatially restricted to the equatorial cortex.

Several studies propose that astral microtubules, which extend from centrosomes to the cortex, could prevent cortical regulators from accumulating at the poles (van Oostende Triplet et al., 2014; Zanin et al., 2013). Astral microtubules may be acting to remove these cortical regulators in the absence of active RhoA outside the equatorial plane (Tse et al., 2011; van Oostende Triplet et al., 2014). In *Caenorhabditis elegans*, Astral TPXL-1/TPX2 (targeting protein for Xklp2) contributes to the polar clearance of ANI-1/anillin and F-actin by activating AIR-1/Aurora A

kinase (Aurora/Ipl1 related kinase 1), although the mechanism is not clear (Fig. 1.3C; Mangal et al., 2018). Astral microtubules also act in concert with MP-GAP (M phase GTPase activating protein), which is globally localized and directly inactivates RhoA by stimulating its GTPase activity (Zanin et al., 2013). Overall, central spindle and astral microtubules take on different roles by virtue of their position: being bundled by centralspindlin and PRC1 and controlling where Ect2 is active or removing components from the cortex (Foe & von Dassow, 2008; Inoue et al., 2004; Nishimura & Yonemura, 2006), respectively.

1.6.3 Microtubule-independent regulation of cytokinesis

Spindle-independent pathways also regulate the cortex during cytokinesis via chromatin, centrosomes and kinetochores (Beaudet et al., 2017; 2020; Cabernard et al., 2010; 2003; Canman et al., 2000; Kiyomitsu & Cheeseman, 2013; Ozugergin & Piekny, 2020; Rodrigues et al., 2015; von Dassow et al., 2009; Zanin et al., 2013). A kinetochore-derived pathway induces relaxation of the polar cortices in cultured mammalian and *Drosophila* cells (Rodrigues et al., 2015). This is accomplished by a kinetochore-tethered PP1 phosphatase-Sds22/PPP1R7 (protein phosphatase 1-suppressor of Dis2 mutant 2; protein phosphatase 1 regulatory subunit 7) complex that dephosphorylates the ERM (ezrin/radixin/moesin) proteins, which anchor the actin network to the plasma membrane. This reduces F-actin membrane anchorage and induces relaxation of the polar cortex (Rodrigues et al., 2015). Several studies also revealed a role for chromatin-associated active Ran (Ras-related nuclear protein) in coordinating the position of cortical regulators with segregating chromosomes (Beaudet et al., 2017; Kiyomitsu & Cheeseman, 2013; Rodrigues et al., 2015). Active Ran (Ran-GTP) is high around chromatin as its GEF, RCC1 (regulator of chromosome condensation 1) is bound to histones, whereas RanGAP (Ran GTPase activating

protein) is enriched in the cytosol. Active Ran displaces importins from NLS (nuclear localization signal)-containing proteins, which forms an inverse gradient where importins are free to bind to NLS-containing proteins at the cortex (Ozugergin & Piekny, 2020). Specifically, the NLS of anillin is required for importin-β-binding and for its cortical localization and function (Beaudet et al., 2017; 2020). Overall, these different pathways controlling the function of cortical regulators ensure robust cytokinesis, and their relative contribution could vary in different organisms and different cell types, depending on cell-intrinsic (*e.g.* cellular components, size and ploidy) and extrinsic (*e.g.* tissue organization and cell junctions) factors.

1.6.4 Regulation of cytokinesis across cell types

Most of our knowledge of the regulation of cytokinesis in human cells comes from studies of HeLa cells. However, several recent studies have revealed that cytokinesis is regulated differently in different cell types (Davies et al., 2018; Ozugergin et al., 2022a). In the 2-cell *C. elegans* embryo, the AB and P_1 cells have different speed and timing of ingression during cytokinesis, and their furrows ingress asymmetrically and symmetrically, respectively (Ozugergin et al., 2022a). Interestingly, these cells also inherit different levels of myosin from the previous cell division. In the 4-cell *C. elegans* embryo, inactivation of the formin CYK-1/mDia1 (Cytokinesis defect 1/Diaphanous-related formin 1) induces cytokinesis failure in the ABa and ABp cells, but not in the EMS and P_2 cells (Davies et al., 2018). This specific requirement for CYK-1 demonstrates the existence of different modes of cytokinesis regulation where the specific proteins and pathways at play vary from cell to cell and lead to different cytokinesis phenotypes. In humans, some cells are known to normally fail cytokinesis, including cardiomyocytes (Derks & Bergmann, 2020; Wang et al., 2017), while others, including neural progenitors, have a unique

requirement for specific cytokinesis regulators (Li et al., 2016; Tedeschi et al., 2020). However, the differences in how cytokinesis occurs and is regulated in different human cell types have not been characterized.

1.6.5 Endogenous tags as imaging tools to study cytokinesis

Few of the proteins involved in cytokinesis have been tagged endogenously in mammalian cells (Cai et al., 2018; Hoffman et al., 2019; Mahen et al., 2014; Mann & Wadsworth, 2018; Okumura et al., 2018; Peterman et al., 2020). Meanwhile, endogenous tags have been used to visualize several cytokinesis proteins in *C. elegans*, including UNC-59/Septin7 (uncoordinated 59; Chen et al., 2019), AIR-2/Aurora B kinase (Bai et al., 2020), PLST-1/Plastin-1 (Ding et al., 2017), CYK-1/mDia1 (Davies et al., 2018), LET-502/ROCK (lethal 502; Bell et al., 2020) and NMY-2/non-muscle myosin II (Dickinson et al., 2013). PLST-1/Plastin-1 is a component of the contractile ring that increases cortical connectivity by cross-linking actin (Ding et al., 2017). In another study, the endogenous tagging of CYK-1/mDia1 helped demonstrate a different requirement for CYK-1/mDia1 in EMS and P_2 cells compared to ABa and ABp cells in the 4-cell *C. elegans* embryo (Davies et al., 2018). Endogenous tagging of the RHO-1/RhoA effector LET-502/ROCK revealed that GCK-1/STK24, 25, 26 (germinal center kinase 1; serine/threonine-protein kinase 24, 25, 26) and CCM-3/PDCD10 (cerebral cavernous malformation 3; programmed cell death protein 10) dampen contractility by negatively regulating active RHO-1/RhoA (Bell et al., 2020). NMY-2/non-muscle myosin II was one of the first proteins to be tagged using CRISPR-Cas9 in *C. elegans* (Shown in Fig. 1.4A; Dickinson et al., 2013), paving the way for numerous studies of the mechanisms regulating cytokinesis and other contractile events during embryogenesis (Singh et al., 2019; Wernike et al., 2016). Broadly, endogenous tags can be used

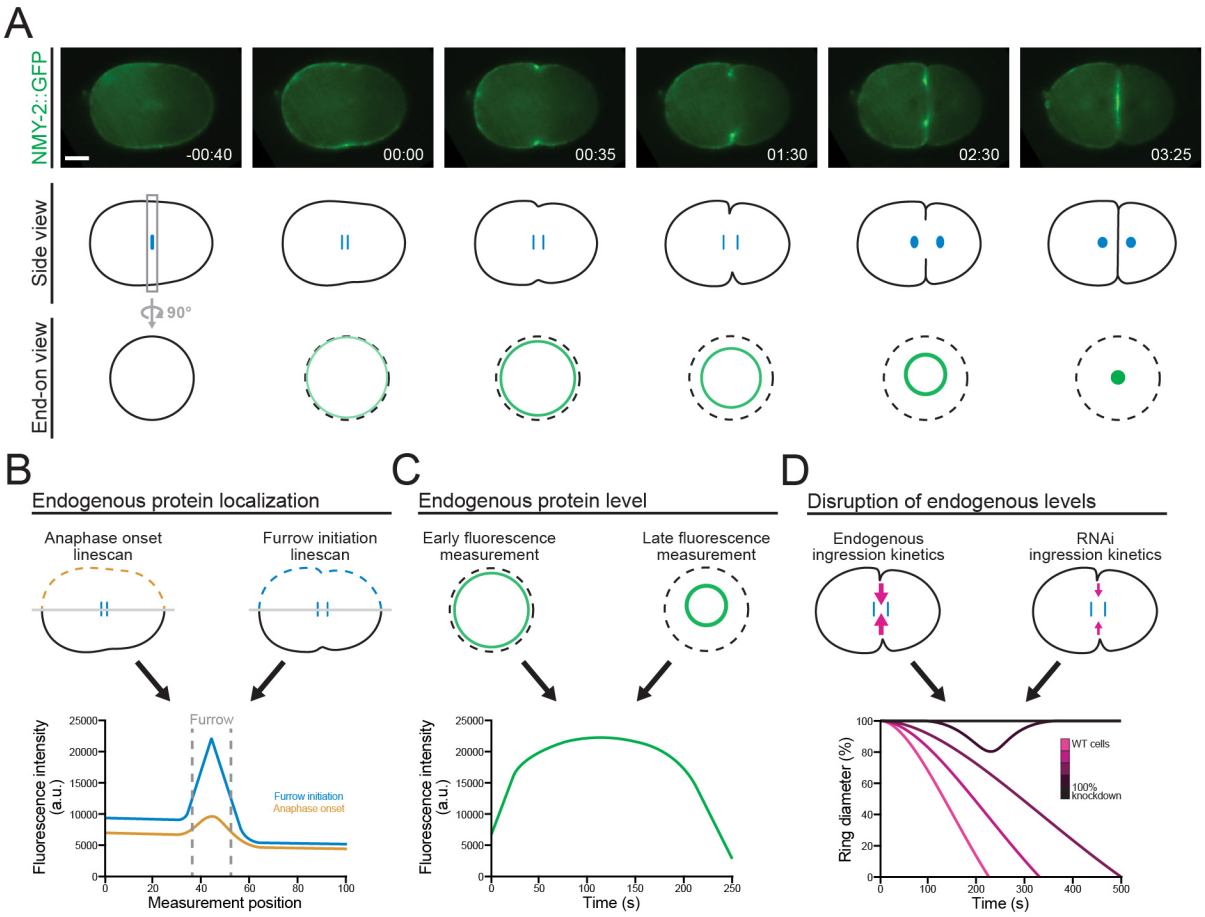

Figure 1.4. Uses of endogenous tags to study cytokinesis. A) Timelapse images show a one-cell *C. elegans* embryo expressing endogenously tagged NMY-2 during cytokinesis (times are in minutes, seconds). The scale bar is 10 µm, and the images are courtesy of Imge Özügergin. The cartoon images underneath show the progression of cytokinesis after anaphase onset from both a side (middle panel, DNA is shown in blue) and end-on view (bottom panel). **B)** The localization of cortical NMY-2 can be analyzed using a linescan to measure fluorescence intensity along the anterior-posterior axis at different time points. As shown in the mock graph, the linescan data can be used to show the change in fluorescence intensity in the furrow over time. **C)** Total levels of endogenous protein in the ring can be measured at different time points, and plotted to show how these levels correlate with different stages of ring ingression. **D)** Ring closure kinetics can be measured and precisely correlated with endogenous protein levels after RNAi or other perturbations to determine threshold requirements.

to visualize cellular processes in live cells (Fig. 1.4A), measure protein localization and protein levels over time (Fig. 1.4B and C), or to correlate phenotypes with precise protein levels after knockdown (Fig. 1.4D).

In addition to proteins directly involved in cytokinesis, probes are often used to visualize cellular markers, including the plasma membrane (*e.g.* PH domain of PLCγ, Phospholipase C gamma), microtubules (*e.g.* fluorescent-tagged tubulin or SiR-tubulin), F-actin (*e.g.* fluorescent-tagged LifeAct or SiR-actin) or chromatin (*e.g.* Hoechst or fluorescent-tagged histone). For example, a GFP-tagged NMY-2 *C. elegans* strain (Shown in Fig. 1.4A; Dickinson et al., 2013) has been an invaluable tool to study cytokinesis parameters such as equatorial cortical localization, ingression speed and ring closure symmetry (Carvalho et al., 2009; Khaliullin et al., 2018; Osório et al., 2019). Tools have been developed to tag common cellular markers endogenously in human cells. These tools include CRISPR constructs to generate mEGFP-TUBA1B (α-tubulin), mEGFP-ACTB (β-actin) or mEGFP-MYH10 (non-muscle myosin heavy chain IIB) in human cells (Roberts et al., 2017).

1.7 Human cell models

1.7.1 Transformed and cancerous cell lines

Most of our understanding of cellular processes in human cells comes from studies of cancerous or transformed cell lines. Specifically, HeLa cells (human cervical carcinoma) are the most studied model to understand human cell physiology, as they were the first stable human cell line and are easy to manipulate (Hyman & Simons, 2011; Masters, 2002). HEK293 cells (immortalized human embryonic kidney cells) provide a non-cancerous alternative as they were immortalized by transfecting sheared adenovirus 5 DNA (Lin et al., 2014b). HEK293 cells are particularly popular for biochemical experiments, virus production and gene editing, while HeLa cells are more popular for live imaging experiments. hTERT RPE-1 cells (retinal pigment epithelial), which are immortalized by the stable expression of the hTERT gene (human telomerase

reverse transcriptase) to prevent senescence, have become popular as a non-diseased cell line (Bodnar et al., 1998). Many other cancerous or transformed cell lines have been isolated from a range of healthy or diseased tissues. However, most differentiated cell lines are in a non-native transformed or diseased state, and often have genetic abnormalities, instability and heterogeneity (Ben-David et al., 2018; Cassio, 2013; Landry et al., 2013; Lin et al., 2014b; Liu et al., 2019). For example, HeLa cells carry a highly amplified and rearranged genome that varies between cells from the same population (Landry et al., 2013). Even though the genome of HEK293 cells carries less rearrangements, it is hypotriploid with 62-70 chromosomes and is also heterogeneous (Bylund et al., 2004). Moreover, since many cellular processes are expected to be differentially regulated in different cell types, we need to extend our understanding of the mechanisms controlling these cellular processes beyond a single transformed or diseased cell line.

1.7.2 Pluripotent stem cells

Pluripotent stem cells are healthy, self-renewing and undifferentiated cells that can be differentiated into any cell type. Human pluripotent stem cells can be embryonic stem cells (ESCs) derived from the inner cell mass of blastocyst-stage embryos (Lee & Lee, 2011), or induced pluripotent stem cells (iPSCs), which are derived from adult somatic cells that are reprogrammed to a pluripotent state (Takahashi et al., 2007). iPSCs closely resemble the characteristics of embryonic stem cells (ESCs), although some differences exist (Bilic & Izpisua Belmonte, 2012; Bock et al., 2011; Puri & Nagy, 2012; Shi et al., 2017; Takahashi et al., 2007; Yu et al., 2007). iPSCs can be generated from somatic cells from any individual and circumvent the need to isolate cells directly from human embryos. iPSCs are ideal models for biomedical research because they are healthy, carry a normal and stable genome, can grow *in vitro*, and can differentiate into any

cell type derived from the three germ layers (Shi et al., 2017). Efficient protocols have been developed to culture and differentiate iPSCs into various cell types (Shi et al., 2017; Williams et al., 2012). Differentiation involves using specific combinations of growth factors or molecules to activate or inhibit specific signaling pathways. For example, dual-SMAD inhibition using SB431542 and Noggin to block BMP and TGF-β signaling induces the direct differentiation of iPSCs into neural progenitor cells via the neuroectodermal lineage (Shi et al., 2012). Neural progenitor cells can be further differentiated into different types of neurons in the presence of different factors (Chambers et al., 2009; Shi et al., 2012). Differentiated cells are identified by the expression of lineage-specific markers. Although human stem cells are rarely used in studies of cellular processes compared to cancerous or transformed cell lines, they allow for comparative studies of different human cell types in an isogenic context (Balmas et al., 2023; Dambournet et al., 2014; Drubin & Hyman, 2017; Hyman & Simons, 2011).

1.8 Thesis overview

Advances in gene editing technologies have facilitated the genetic manipulation of human cells to study protein function by generating knockouts, point mutations and endogenous tags. Specifically, endogenous tags provide valuable tools to study protein localization in live cells. However, precise gene editing is inefficient, and generating edited cell lines is time-consuming. In this thesis, I present tools and protocols to tag proteins endogenously in multiple human cell lines, which enables the study of cytokinesis proteins in their native cellular context.

In chapter 2, I aimed to generate endogenous tags using CRISPR/Cas9 to study protein localization during cytokinesis in different human cell lines. For this, I tagged anillin, Ect2 and RhoA endogenously for the first time in human cells. I also developed a toolkit of plasmids to tag

several cellular markers (plasma membrane, H2B histones, β-actin and α-tubulin) with different fluorescent proteins, which can be used to study cytokinesis and other cellular processes. I also tagged anillin in five different transformed and cancerous mammalian cell lines, which presented distinct challenges for gene editing. I then used these cell lines to characterize cytokinesis parameters and quantify the localization of anillin during cytokinesis. I found that cytokinesis occurs differently in these cell lines, showing that the underlying mechanisms regulating cytokinesis differ with cell type.

The objective of chapter 3 was to facilitate endogenous tagging in human iPSCs to study protein localization in healthy human cells that can be differentiated into any cell type. I engineered a 'parent' iPS cell line that expresses the $mNG2_{1-10}$ fragment constitutively to facilitate high-throughput endogenous tagging with $mNG2_{11}$. I validated the parental cell line thoroughly to ensure that the cells behave normally after editing. I then showed that endogenous tagging with $mNG2_{11}$ is efficient across multiple genes. I also developed efficient protocols for clonal isolation, screening, and live imaging of edited iPSCs to facilitate future editing efforts and localization studies in live, healthy human cells.

This work provides new tools to study protein localization during cytokinesis and other cellular processes in human cells. It also provides plasmids to tag specific proteins in any human cell lines, and protocols for endogenous tagging in different cell lines. Finally, it paves the way towards a genome-scale view of protein localization across human cell types *in vitro* using endogenously tagged iPS cell lines.

CHAPTER 2

Cytokinetic diversity in mammalian cells is revealed by the characterization of endogenous anillin, Ect2 and RhoA

Manuscript published as: Husser, M. C., Ozugergin, I., Resta, T., Martin, V. J. J., & Piekny, A. J. (2022, Nov). Cytokinetic diversity in mammalian cells is revealed by the characterization of endogenous anillin, Ect2 and RhoA. *Open Biol, 12*(11), 220247.

2.1 Preamble

Endogenous tagging is a promising tool to study proteins in live cells. However, precise gene editing is inefficient and difficult to achieve in human cells. In this chapter, I aimed to use CRISPR/Cas9 to introduce fluorescent tags at endogenous gene loci to visualize several proteins at the endogenous level by fluorescence microscopy. Since cytokinesis has not been well-studied in the endogenous context and across human cell lines, I targeted several proteins involved in cytokinesis for endogenous tagging in multiple human and mammalian cell lines. With these cell lines, I characterized key cytokinesis parameters to compare how it occurs across different cell types. This work provides new imaging tools to study how cytokinesis is regulated across different human cell types.

2.2 Abstract

Cytokinesis is required to physically separate the daughter cells at the end of mitosis. This crucial process requires the assembly and ingression of an actomyosin ring, which must occur with high fidelity to avoid aneuploidy and cell fate changes. Most of our knowledge of mammalian

cytokinesis was generated using over-expressed transgenes in HeLa cells. Over-expression can introduce artefacts, while HeLa are cancerous human cells that have lost their epithelial identity, and the mechanisms controlling cytokinesis in these cells could be vastly different from other cell types. Here, we tagged endogenous anillin, Ect2 and RhoA with mNeonGreen and characterized their localization during cytokinesis for the first time in live human cells. Comparing anillin localization in multiple cell types revealed cytokinetic diversity with differences in the duration and symmetry of ring closure, and the timing of cortical recruitment. Our findings show that the breadth of anillin correlates with the rate of ring closure, and support models where cell size or ploidy affects the cortical organization, and intrinsic mechanisms control the symmetry of ring closure. This work highlights the need to study cytokinesis in more diverse cell types, which will be facilitated by the reagents generated for this study.

2.3 Introduction

Cytokinesis describes the physical separation of a cell into two daughters, which occurs at the end of mitosis. This process must be tightly spatio-temporally controlled as failure can cause changes in cell fate and disease (D'Avino et al., 2015; Lacroix & Maddox, 2012). Cytokinesis occurs via the assembly and ingression of a RhoA-dependent contractile ring that constricts to pull in the overlying plasma membrane. Multiple pathways regulate ring assembly in cultured cells and model organisms (Green et al., 2012; Husser et al., 2021; Ozugergin & Piekny, 2021; Pollard & O'Shaughnessy, 2019). These pathways ensure that active RhoA is enriched in the equatorial plane to assemble the ring. Ect2 is the guanine nucleotide exchange factor (GEF) that activates RhoA during cytokinesis and requires binding to phospholipids and the central spindle protein Cyk4 (MgcRacGAP) for its activity (Fig. 2.1A; Gomez-Cavazos et al., 2020; Wolfe et al., 2009; Yuce

et al., 2005). The depletion of Cyk4 or Ect2 in HeLa cells prevents the accumulation of active RhoA at the equatorial cortex and leads to cytokinesis failure (Kamijo et al., 2006; Kim et al., 2005; Nishimura & Yonemura, 2006; Yuce et al., 2005; Zhao & Fang, 2005). Active RhoA (RhoA-GTP) recruits and activates effectors, including formin and RhoA kinase (ROCK), to generate actomyosin filaments and assemble the ring (Fig. 2.1A; Piekny et al., 2005; Pollard & O'Shaughnessy, 2019). Anillin is also recruited by active RhoA and acts as a scaffold protein that tethers the ring to the plasma membrane (Green et al., 2012; Piekny & Glotzer, 2008; Piekny & Maddox, 2010; Sun et al., 2015). In support of its cross-linking function, the depletion of anillin in HeLa or S2 cells leads to ring oscillations and cytokinesis failure (Hickson & O'Farrell, 2008; Piekny & Glotzer, 2008; Piekny & Maddox, 2010). Anillin may also be involved in the retention of active RhoA at the equatorial cortex, as well as its removal during constriction (Budnar et al., 2019; Carim et al., 2020; El Amine et al., 2013). Multiple mechanisms control this core cytokinesis machinery in different model systems, yet their relative requirement remains unknown (Husser et al., 2021).

Multiple pathways regulate cytokinesis. The central spindle facilitates the recruitment and activation of Ect2 in proximity to the equatorial cortex where it generates active RhoA (Adriaans et al., 2019; Basant et al., 2015; Burkard et al., 2009; Frenette et al., 2012; Kotynkova et al., 2016; Lekomtsev et al., 2012; Mishima et al., 2002; Mishima et al., 2004; Petronczki et al., 2007; Su et al., 2011; Wolfe et al., 2009; Yuce et al., 2005). Astral microtubules also define the cleavage plane by removing cortical regulators from the poles (Chen et al., 2021; Lewellyn et al., 2010; Mangal et al., 2018; Tse et al., 2011; van Oostende Triplet et al., 2014; Zanin et al., 2013), while spindle-independent pathways polarize the cortex through signals associated with chromatin, centrosomes and kinetochores (Beaudet et al., 2017; Beaudet et al., 2020; Cabernard et al., 2010; Canman et

al., 2003; Canman et al., 2000; Kiyomitsu & Cheeseman, 2013; Ozugergin et al., 2022a; Ozugergin & Piekny, 2021; Rodrigues et al., 2015; von Dassow et al., 2009; Zanin et al., 2013). For example, studies showed that chromatin-associated active Ran (Ran-GTP; Ras-related nuclear protein) coordinates the position of the ring with segregating chromosomes (Beaudet et al., 2017; Beaudet et al., 2020; Kiyomitsu & Cheeseman, 2013; Ozugergin et al., 2022a; Ozugergin & Piekny, 2021). These pathways also act in concert with the negative regulator of RhoA, MP-GAP (M-phase GTPase-activating protein), which is globally localized (Zanin et al., 2013). Having multiple mechanisms to control the function of cortical regulators ensures robust cytokinesis, but their requirement is expected to differ with cell type.

Studies in different organisms and tissues have revealed differences in the regulators of cytokinesis (Cabernard et al., 2010; Davies et al., 2018; Fotopoulos et al., 2013; Lewellyn et al., 2010; Mangal et al., 2018; Ozugergin et al., 2022a; Paim & FitzHarris, 2022; Rodrigues et al., 2015; van Oostende Triplet et al., 2014). For example, anillin is essential for cytokinesis in cultured cells (HeLa and Drosophila S2 cells), but not in the early *Caenorhabditis elegans* zygote, and Dalmatian dogs carrying an anillin truncation mutant did not have obvious cell division defects (Hickson & O'Farrell, 2008; Holopainen et al., 2017; Maddox et al., 2005; Piekny & Glotzer, 2008). However, later in *C. elegans* development, neuronal precursor cells require anillin for cytokinesis (Fotopoulos et al., 2013; Wernike et al., 2016). Thus, the mechanisms regulating cytokinesis vary with cell fate, but also with other parameters including size, shape and ploidy. In the two-cell *C. elegans* embryo, the somatic AB and germline P_1 cells have different ring assembly and ingression kinetics with different levels of myosin in the ring (Ozugergin et al., 2022a). In the four-cell *C. elegans* embryo, the ABa and ABp cells have stronger requirements for formin-derived F-actin compared to EMS or P_2 cells, which are regulated by cell-extrinsic and intrinsic factors,

respectively (Davies et al., 2018). The observed cytokinetic diversity in different cell types highlights the importance of understanding how mechanisms regulating cytokinesis vary during development. However, most of our knowledge of human cell cytokinesis is derived from the over-expression of transgenes in HeLa cells, which are cancerous in origin and have lost their epithelial identity. Given the vast number of human cells with specialized functions, it is likely that the mechanisms regulating cytokinesis will vary with cell type. For example, liver hepatocytes abort cytokinesis to gain ploidy for their function (Lacroix & Maddox, 2012; Margall-Ducos et al., 2007; Wang et al., 2017), while the ring closes asymmetrically in epithelial cells, which could help them retain apicobasal polarity and be properly positioned after division (Herszterg et al., 2014; Morais-de-Sa & Sunkel, 2013; Sugioka, 2022; Thieleke-Matos et al., 2017). Understanding how these different modes of cytokinesis are controlled can help us understand and/or treat cytokinesis-related pathologies.

Gene editing tools provide an opportunity to study proteins in diverse cell types (Drubin & Hyman, 2017; Husser et al., 2021). In human cells, cytokinesis has mostly been studied using over-expressed transgenes fused to fluorescent tags for visualization and/or affinity tags for biochemical assays. In HeLa cells, the localization of endogenous anillin fixed and stained with antibodies is similar to anillin over-expression. However, Ect2 and RhoA show inconsistent localization patterns and/or cause cytokinesis phenotypes when over-expressed (Chalamalasetty et al., 2006; Piekny & Glotzer, 2008; Yuce et al., 2005). TCA-fixation-based immunofluorescence microscopy is still one of the most reliable methods to visualize the enrichment of RhoA at the equatorial cortex (Koh et al., 2021; Schneid et al., 2021; Yonemura et al., 2004; Yuce et al., 2005), and Ect2 over-expression can lead to cytokinesis failure (Chalamalasetty et al., 2006). In addition, measurements can be confounded by the variability in transgene expression between transfected

cells, whereas endogenous probes enable more quantitative measurements. There are also several examples where endogenously tagged proteins cause fewer phenotypes compared to proteins from over-expressed transgenes, which may not fold properly, fail to assemble into complexes and/or disrupt downstream processes (Doyon et al., 2011; Gibson et al., 2013; Husser et al., 2021; Mahen et al., 2014). Moreover, the same tools can be used to introduce genetic edits into different cell lines derived from the same organism.

The most widely used tool for gene editing is CRISPR/Cas9 (clustered regularly interspaced short palindromic repeats/CRISPR-associated protein 9) comprised of Cas9 nuclease and a sgRNA (single guide RNA), which contains a 20-nucleotide target sequence that corresponds to a genomic target site (Fig. 2.1B and C; Cong et al., 2013; Mali et al., 2013; Pickar-Oliver & Gersbach, 2019; Wang et al., 2016). Cas9 is targeted to this site by the sgRNA and cleaves the DNA to introduce a double-stranded break (DSB). Human cells typically repair DSBs by non-homologous end joining (NHEJ), but can also use the homology-directed repair (HDR) pathway, which makes use of a homologous repair template to fill in the gap where the DSB was introduced (Scully et al., 2019; Wright et al., 2018). To introduce a fluorescent marker at a precise location in the genome of human cells, CRISPR/Cas9 can be used along with a synthetic repair template designed to carry the fluorescent marker flanked with homology arms for HDR (Fig. 2.1C; Verma et al., 2017). When introduced in frame with a gene, the fluorescent marker will be expressed as a fusion with the protein of interest. Efforts to share validated tools for endogenous tagging (sgRNA sequence and repair template) have made these tags more readily accessible and easy to use (de Man et al., 2021; Pinder et al., 2015; Roberts et al., 2017; Sakuma et al., 2016; Savic et al., 2015; Sun et al., 2021; Allencell.org; Addgene.org). However, despite these shared resources and the

advantages to using endogenous tags, few cytokinesis proteins have been tagged endogenously in human cells (Mahen et al., 2014; Mann & Wadsworth, 2018; Peterman et al., 2020).

In this work, we generated reagents to endogenously tag anillin, Ect2 and RhoA with mNeonGreen using CRISPR/Cas9 gene editing, and re-purposed existing constructs to tag cellular markers with different fluorescent proteins. These reagents were used to characterize the spatio-temporal localization of endogenously tagged anillin, Ect2 and RhoA during cytokinesis in HeLa cells for the first time. We then tagged endogenous anillin with mNeonGreen in multiple mammalian cell lines, including HCT116, HepG2 and MDCK, which are difficult to genetically modify and have not been used for cytokinesis studies before. In-depth localization studies of anillin revealed cytokinetic diversity among the cell types. Specifically, we found differences in the breadth, enrichment and timing of the cortical localization of anillin. By making these tools available to the cell biology community, we hope to fuel new studies of the mechanisms regulating cytokinesis in diverse cell types.

2.4 Materials and methods

2.4.1 Cell culture

HEK293, HeLa and MDCK cells were cultured in Dulbecco's modified Eagle medium (DMEM; Wisent) media supplemented with 10% Cosmic calf serum (CCS; Cytoviva). HCT116 cells were cultured in McCoy's media (Wisent) supplemented with 10% CCS. HepG2 cells were cultured in Eagle's minimum essential medium (EMEM; Wisent) supplemented with 10% fetal bovine serum (FBS; Cytoviva). The cells were maintained in 10 cm dishes in incubators at 37°C with 5% CO_2 as per standard protocols (Beaudet et al., 2017; Beaudet et al., 2020). For long-term

storage, cells were washed and resuspended in freezing media (50% FBS, 40% DMEM or EMEM media and 10% DMSO) and stored in liquid nitrogen.

2.4.2 Cloning

To generate the pX459-HypaCas9-mRuby2 CRISPR construct (Addgene no. 183872), we digested the pX459V2.0-HypaCas9 plasmid (Obtained from Kato-Inui et al., 2018; Addgene no. 108294) with EcoRI (New England Biolabs) and used the GeneJET gel extraction kit (ThermoFisher Scientific) to extract the backbone as per manufacturer's protocols. To prevent re-ligation the backbone was dephosphorylated with Antarctic phosphatase (New England Biolabs) as per manufacturer's instructions. The mRuby2-T2A-Puro insert was generated by amplifying the mRuby2 and Puromycin resistance genes with shared overlap, and assembling them by SOEing (Splicing by Overlap Extension) PCR. This was done by first performing a Phusion PCR reaction (ThermoFisher Scientific) without primers for 15 cycles, then adding primers to the reaction for amplification during the remaining 25 cycles. The mRuby2-T2A-Puro PCR product was then purified and digested with EcoRI for ligation into the dephosphorylated backbone. Clones were screened by PCR and validated by sequencing the insert region (Eurofins Operon).

The sgRNA spacer sequences were selected using Benchling (Doench et al., 2016; Hsu et al., 2013) and CCTop (Stemmer et al., 2015) for the ANLN, ECT2, RHOA and MYH10 genes and the AAVS1 locus. Multiple spacers were selected for each target site. One of the AAVS1 spacer sequences was obtained from Oceguera-Yanez et al. (2016) and the spacer sequences for the H2BC11, ACTB, MYH10 and TUBA1B genes were obtained from the Allen Institute for Cell Science (Roberts et al., 2017; Allencell.org). All sgRNA spacers tested are listed in Table S2.1. The sgRNA spacers were cloned into the pX459V2.0-HypaCas9 and the pX459V2.0-HypaCas9-

mRuby2 plasmids using previously described methods (Ran et al., 2013b). Briefly, two complementary oligos containing the spacer sequence were designed as follows (where $(N)_{20}$ corresponds to the 20-nucleotide spacer sequence or its reverse complement):

Forward oligo: 5'-CACCG$(N)_{20}$-3'

Reverse oligo: 5'-AAAC$(N)_{20}$-3'

Oligos were annealed and ligated into the backbone (pX459V2.0-HypaCas9 or pX459V2.0-HypaCas9-mRuby2) pre-digested with BbsI (New England Biolabs). Two clones were selected for each sgRNA and sequenced to verify the spacer sequence.

To build the repair templates, the homology arms were first amplified from HEK293 genomic DNA extracted using the Qiagen DNeasy Blood and tissue kit or plasmid DNA by PCR. For genome sequences that were recalcitrant to PCR amplification, we used touchdown PCR conditions (Korbie & Mattick, 2008) with 1X GC buffer or 0.5X HF buffer instead of 1X HF buffer with Phusion polymerase (ThermoFisher Scientific). The fluorescent tags (mNeonGreen, mRuby2 and TagBFP) were amplified independently using primers that were designed to introduce overlap with the homology arms (15–51 bp of overlap). The primers used to clone the repair templates are listed in Table S2.2. The repair templates were assembled by SOEing PCR as described above, then blunt-end ligated into the pJET1.2 vector using the CloneJET PCR cloning kit (ThermoFisher Scientific). Multiple clones were screened by PCR and sequencing.

For transgene expression, the coding sequences for anillin, Ect2 and Ect2(C-term) were cloned into the Golden Gate entry vector pYTK001 (obtained from Lee et al., 2015; Addgene no. 65108). They were fused to mNeonGreen (Allele Biotech) or mScarlet-I (obtained from Mastop et al., 2017; Addgene no. 98839) and assembled into a custom Golden Gate expression vector (pGG). The Golden Gate assembly reaction was carried out using BsaI (New England Biolabs)

following standard protocols (Lee et al., 2015). Isolated colonies were picked and screened by PCR and sequencing.

2.4.3 Transfection, nucleofection and NHEJ inhibition

To improve editing efficiency, all cells were treated with NHEJ inhibitors NU7441 (2 μM; Tocris Bioscience) and SCR7 (1 μM; Xcess Biosciences) 4 h before transfection and for 48 h after transfection. HEK293, HeLa and HepG2 cells were seeded in 24-well dishes to reach 60% confluency on the day of transfection. Cells were transfected using Lipofectamine 3000 and P3000 reagent (ThermoFisher Scientific) according to manufacturer's instructions. Plasmids were introduced into HCT116 and MDCK cells using nucleofection with the 384-well HT Nucleofector and the SE cell line kit (Lonza) as per manufacturer's instructions. The cells were nucleofected using the EN-113 program for HCT116 cells, and the CA-152 program for MDCK cells, and the amount of repair template and plasmid were adjusted per cell type.

For transient transgene expression, vectors (pGG-mNG-Anillin, pGG-mNG-Ect2, pGG-mScar-Ect2(C-term) and GFP-RhoA) were transfected into HeLa cells plated on coverslips and grown to 60% confluency, using Lipofectamine 3000 and P3000 reagent (ThermoFisher Scientific) as per manufacturer's instructions.

2.4.4 Fluorescence-activated cell sorting

Tagged cells were isolated or enriched by FACS 7–14 days after transfection. The cells were resuspended thoroughly in FACS buffer comprised of 1 mM EDTA, 25 mM HEPES pH 7.0 and 1% FBS in PBS buffer, then passed through a 35 μm strainer to remove large cell clumps and transferred to 5 ml FACS tubes for sorting. Cells were sorted using a FACSMelody cell sorter (BD

Biosciences) with gates set to capture individual fluorescent cells. The fluorescent cells were sorted into individual wells of a 96-well plate containing recovery media (media supplemented with 20% FBS and 1X Penicillin-Streptomycin; 50 units ml^{-1} penicillin and 50 μg ml^{-1} streptomycin; Wisent). Alternatively, fluorescent cells were enriched by sorting 15 000 cells into a FACS tube with recovery media. The enriched population was then resuspended in fresh recovery media and seeded into one well of a 96-well plate. The cells were left to recover, and media was supplemented as needed. For flow cytometry, cells were prepared using the same protocol and measured on different days after transfection. Flow cytometry data was acquired using the FACSMelody cell sorter and analysed with the R package CytoExploreR (Hammill, 2021).

2.4.5 Genotyping

For genotyping, we first determined whether the tag was inserted into the target locus using PCR. Clones were expanded by splitting cells from individual colonies in 96-well plates into 48-well plates, and subsequently into 24-well plates. The target locus was amplified directly from the cells using the Phire Plant Direct PCR mastermix (ThermoFisher Scientific) in three junction PCR reactions as per manufacturer's protocols. The primers used for these reactions are listed in Table S2.3. The three PCR reactions were designed to amplify the wild-type (WT) locus as well as the left and right junctions of the integration sites. Touchdown PCR was used to improve the quality of the PCR products. Six to twelve positive clones were then expanded into 10 cm dishes for further genotyping. Genomic DNA was extracted using the Qiagen DNeasy Blood and tissue kit, then used to amplify the target locus with Phusion polymerase (ThermoFisher Scientific) by touchdown PCR. The genotype was verified by extracting PCR products and sequencing the

tagged and untagged alleles. When possible, homozygous clones carrying only tagged alleles were selected. Alternatively, heterozygous clones carrying a tagged allele and a wild-type allele were selected.

2.4.6 Microscopy

The endogenous tags and ectopic fluorescent protein expression were imaged using microscopy. Cells grown on 6-well plates were imaged 2 and 10 days after transfection on a Leica DMI6000B inverted epifluorescence microscope with filters for the appropriate wavelengths, using a 20x/0.35 NA objective, an Orca R2 CCD camera (Hamamatsu) and Volocity software (PerkinElmer). Single-cell-derived clones were initially screened for fluorescence and localization 7–10 days after FACS isolation using a Nikon Eclipse TS100 microscope equipped with a DS-Qi1Mc camera the 10x/0.25NA objective. Clones with uniform expression and expected cellular localization were selected for further screening.

To image cells during cytokinesis, tagged HeLa, HCT116, HepG2 and MDCK cell lines were seeded onto acid-etched round coverslips (25 mm, no. 1.5) in 6-well plates and grown to 70% confluency. The coverslips were transferred to a magnetic chamber (Quorum) with 1 ml media before imaging. Tagged HEK293 cells were seeded directly onto 4-well μ-slides (Ibidi) for imaging. To visualize chromatin, Hoechst 33342 (Invitrogen) was added to the cells at a final concentration of 0.4 μM for 30 min prior to imaging. Imaging was performed using an inverted Nikon Eclipse Ti microscope (Nikon) equipped with a Livescan Sweptfield scanner (Nikon), Piezo Z stage (Prior), IXON 879 EMCCD camera (Andor), and 405, 488 and 561 nm lasers (100 mW, Agilent) using the 100x/1.45 NA objective. The cells were kept at 37°C and 5% CO_2 during

imaging in an INU-TiZ-F1 chamber (MadCityLabs). Z-stacks of 1 μm thickness were acquired every 1–2 min using NIS Elements software (Nikon, v.4.0).

To collect images of the over-expressed transgenes, the coverslips were transferred to a magnetic chamber with 1 ml of media 1 day after transfection, and imaged on a Leica DMI6000B inverted epifluorescence microscope with filters for the appropriate wavelengths, a 10x/0.25 NA objective, an Orca R2 CCD camera (Hamamatsu) and Volocity software (PerkinElmer), or a Nikon Eclipse TiE inverted epifluorescence microscope using LEDs in the appropriate wavelength with an Evolve 512 EMCCD camera (Photometrics) and NIS Elements acquisition software (Nikon) using the 60x/1.4 NA objective.

2.4.7 Cell viability assay

To monitor the growth of the different cell lines, we used the WST-8 cell proliferation assay kit (Cayman Chemical), as per manufacturer's instructions. For each cell line, 10 000 cells were seeded per well in a 96-well plate and viability was assayed on days 0, 1, 2, 3 and 5, for a total of approximately 4 population doubling times. For the assay, the electron mediator solution and the WST-8 developer reagent were mixed in equal parts, then added to each well and incubated at 37°C for 2 h. After this, the absorbance at 450 nm was measured on a TECAN Infinite M200 plate reader. The assay was repeated in triplicate for each cell line.

2.4.8 Image analysis

Linescans were performed and measured for each tagged cell line using Fiji. All images acquired using NIS Elements (Nikon) were opened in Fiji (v.2.3, NIH) and analysed using a macro modified from Ozugergin et al. (2022a). Briefly, the macro was designed to isolate the green

channel from the movie file, subtract background signal and perform a bleach correction. The desired timepoint and Z slices were entered manually, and the macro generated a Z-stack average projection. A five-pixel-wide line was then traced along the cortex of the cell, from one pole to the other, along with a straight one-pixel-wide line intersecting the furrow. The macro then measured the fluorescence intensity of each pixel along the length of the linescan, and positioned the pixels in relation to the furrow. The average intensity projection of two central Z slices were used for cortical linescans, while six central slices were used to measure the central spindle in Ect2-tagged cells. All data was exported for use in Excel (Microsoft) and Prism (v.9.3, GraphPad) for further analysis. Pixel intensity values were normalized by subtracting the average baseline intensity (calculated as the average intensity of the first or last 50 pixels of the linescan) from the maximum intensity value. To obtain breadth measurements, the number of pixels above 50% or 75% of the peak value were counted and converted to microns. Intensities above 50% were used to compare the breadth of RhoA to Ect2 and anillin (Fig. 2.3 and S2.4A) to accommodate the relatively low peak intensity levels for RhoA, while intensities above 75% were used to compare anillin across cell lines (Fig. 2.4, S2.4B and S2.5). Pixels outside of the peak region that had intensities higher than the cutoff value were excluded from these calculations. Enrichment at the equatorial (furrow) versus polar cortex was calculated as a ratio between the average pixel intensity in the breadth and the poles (the first or last 50 pixels in the linescans). To measure the ratio of the cortical to cytosolic anillin in metaphase cells, the average intensity of the signal at the cortex was measured by a linescan drawn around the cortex using the macro described above, while the average intensity of the cytosol was measured by drawing a region of interest.

Ring closure was measured as described in Ozugergin et al. (2022a). In short, a 250 x 50-pixel area containing the ring was rotated using SciKit Image (v.0.16.2) to generate an end-on view

of the ring. The outline of the ring was drawn manually as an ellipse in FIJI and the coordinates were noted. Best-fit circles for each ellipse were plotted using Python 3 and the Jet colormap. The centre of the ring in the first timepoint was set to 0,0 and the radius was set to 1, and ellipse coordinates in the subsequent timepoints were normalized to the first timepoint. Symmetry values were obtained using the Pythagorean theorem to calculate the distance between the centre of the cell in the first timepoint and the centre of the ring in the last measured timepoint. Cells with values less than 0.2 (close to 0) were defined as having symmetric ring closure, while cells greater than 0.2 and greater than 0.6 were considered to have asymmetric and very asymmetric ring closure, respectively.

2.4.9 Statistical analysis

Box and whiskers plots were generated using Prism (v.9.3, GraphPad) to show median values (central line), quartiles (box edges) and minimum and maximum values (whiskers). Statistical significance was tested using a Brown–Forsythe and Welch's ANOVA, followed by multiple comparisons using Dunnett's T3 test, or by Welch *t*-test (GraphPad Prism v.9.3). Significance levels were defined as: $p > 0.5$ non-significant (ns), * $p \leq 0.05$; ** $p \leq 0.01$; *** $p \leq 0.001$; **** $p \leq 0.0001$.

2.5 Results

2.5.1 Endogenous tagging of cytokinesis proteins and cellular markers

To study cytokinesis regulators in their native cellular environment, we generated reagents to endogenously tag anillin (ANLN), Ect2 (ECT2) and RhoA (RHOA) with mNeonGreen in human cells using CRISPR/Cas9 (Fig. 2.1A-C). We designed sgRNAs to target the ANLN, ECT2

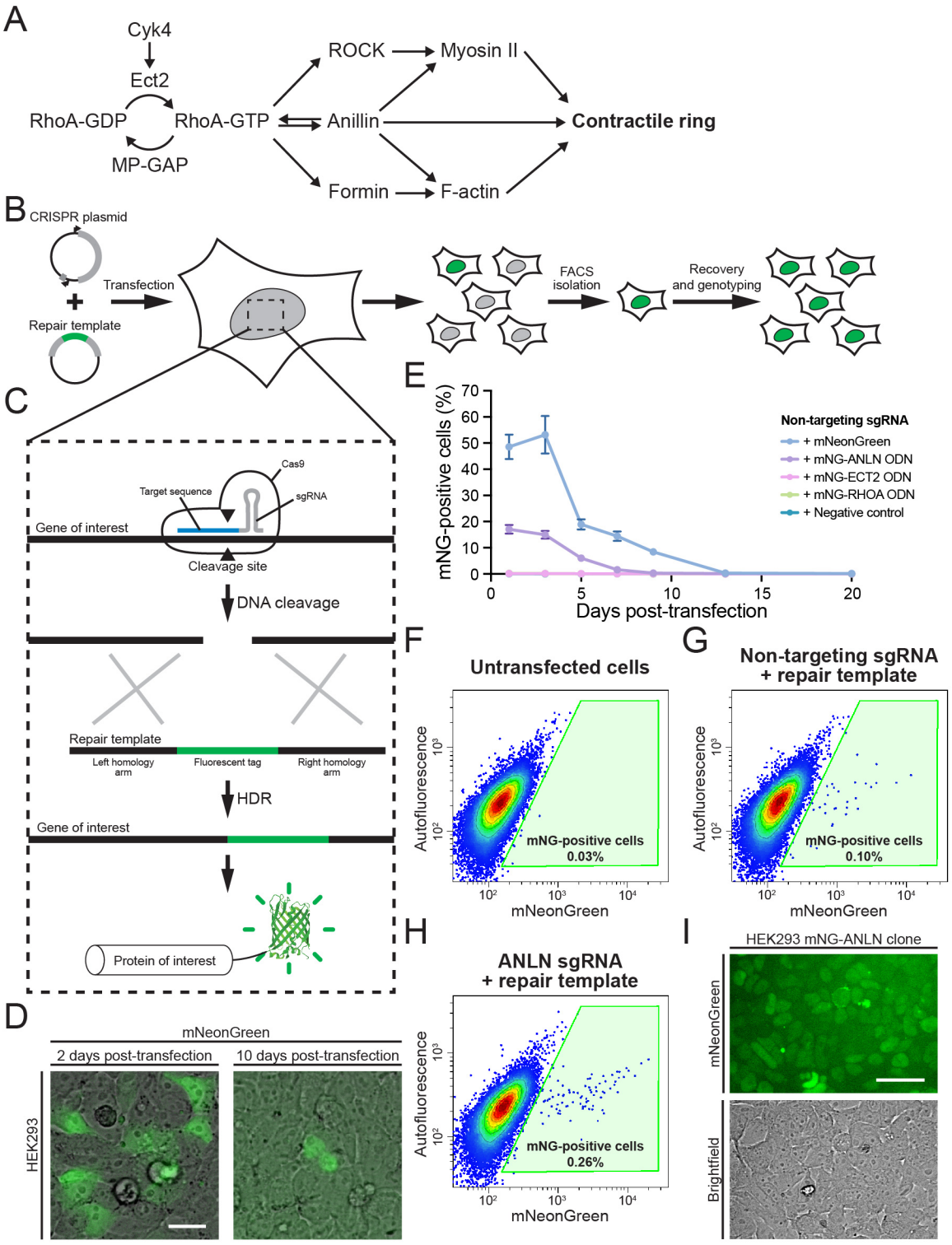

Figure 2.1. Endogenous tagging of cytokinesis proteins in human cells using CRISPR/Cas9. **A)** Diagram showing the core pathway regulating contractile ring assembly during cytokinesis. The generation of active RhoA (RhoA-GTP) by the GEF Ect2 at the equatorial cortex is required

for ring assembly. Active RhoA recruits and/or activates effectors (anillin, formin and ROCK proteins) to assemble actomyosin filaments into the contractile ring. **B)** The experimental workflow used for endogenous tagging is shown. Cultured cells were transfected with a CRISPR plasmid and a repair template to express the CRISPR/Cas9 components and integrate the coding sequence encoding a fluorescent protein. Some cells started to express the fluorescent protein after several days and were isolated by FACS. Clonal cell lines were then recovered and genotyped to verify the edits. **C)** The mechanism of endogenous tagging by CRISPR/Cas9 is shown. A gene-specific sgRNA directs DNA cleavage by Cas9 at the target site. The DSB generated by Cas9 can be repaired by HDR using the provided repair template and integrate the coding sequence for a fluorescent protein at the target site. This will result in the expression of the target protein fused to a fluorescent protein. **D)** Representative images show ectopic mNeonGreen expression 2 days after transfection (left) and nuclear mNeonGreen-anillin signal 10 days after transfection (right). The scale bar is 25 μm. **E)** The graph shows the percentage of mNeonGreen-positive cells over time after transfection with different mNeonGreen repair templates as indicated, assessed by flow cytometry. A constitutive mNeonGreen expression vector was used as a positive control compared with the mNeonGreen-anillin, mNeonGreen-Ect2 and mNeonGreen-RhoA repair templates, and an empty plasmid as a negative control. **F-H)** Representative flow cytometry plots show mNeonGreen fluorescence in HEK293 cells 13 days after transfection with constructs designed to tag anillin with mNeonGreen. Non-transfected cells (F) were used to remove non-fluorescent cells. A negative control lacking a sgRNA (G) shows residual ectopic expression of mNeonGreen from the transfection of a repair template alone, while (H) shows cells transfected with both the ANLN-targeting CRISPR plasmid and repair template. The gate shown in green was used to isolate tagged cells by FACS. **I)** A representative image shows a colony of mNeonGreen-anillin tagged HEK293 cells after single-cell isolation and recovery. The scale bar is 50 μm.

and RHOA genes, and corresponding repair templates to integrate the coding sequence of mNeonGreen in frame with their coding sequences. The repair templates were designed to have 1 kb homology arms flanking the mNeonGreen gene. Three sgRNAs were designed for each gene (Table S2.1) and cloned into a plasmid expressing the high-specificity HypaCas9 protein. We only targeted the N-terminus of RhoA because the C-terminus is post-translationally cleaved, but we targeted both ends of anillin and Ect2 for tagging. The sets of sgRNA-containing CRISPR plasmids and repair templates were validated by co-transfecting them into HEK293 cells (immortalized human female embryonic kidney cells with 64 modal chromosomes; hypotriploid) and monitoring the appearance of a mNeonGreen signal with the expected localization patterns.

When generating endogenously tagged cell lines, we observed non-specific ectopic expression of mNeonGreen directly following transfection (Fig. 2.1D). This ectopic signal has been reported previously (Fueller et al., 2020), and likely arises from ectopic expression from the repair template rather than genomic integration, as it progressively disappears over approximately 9 days following transfection (Fig. 2.1E). We observed the expected localization pattern for the tagged proteins starting approximately 4 days after transfection.

Using the workflow in Fig. 2.1B, we generated endogenous N-terminal mNeonGreen fusions of anillin, Ect2 and RhoA in HEK293 cells. Notably, we did not recover cells with C-terminal tags fused to anillin, while cells with C-terminal tags fused to Ect2 did not show the correct cellular localization (data not shown). The C-terminal tag likely disrupts the function of Ect2, but it is not clear why the tagging was unsuccessful for the C-terminal end of anillin. The successful repair templates and optimal sgRNAs used for each locus are listed in Table 2.1. After confirming each tag by visual inspection, single fluorescent cells were isolated by FACS (fluorescence-activated cell sorting; *e.g.* Fig. 2.1F-H). Single-cell clones were screened by fluorescence microscopy (*e.g.* Fig. 2.1I), PCR and sequencing (*e.g.* Fig. S2.1) to validate the cell lines. Finally, this workflow was repeated to generate HeLa (human female cervical carcinoma with 82 modal chromosomes; hypertriploid) cell lines expressing mNeonGreen-tagged anillin, Ect2 and RhoA. We were able to isolate HEK293 and HeLa cell lines where tagged anillin and Ect2 were homozygous. However, we were unable to isolate homozygous tagged RhoA cell lines despite screening 72 clones of RhoA-tagged HEK293 and 24 clones of RhoA-tagged HeLa. This may be due to the low tagging efficiency at this locus, or some impediment to RhoA function caused by the tag.

Table 2.1. A toolkit of repair templates to tag multiple proteins and cellular components. The repair templates generated and/or used in this study are listed. For each protein or cellular component, the terminus targeted for tagging, the protein linker sequence and the available fluorescent proteins are indicated. The best sgRNA sequence used for CRISPR targeting of each locus is also indicated. The cell lines that each repair template has been tested in and the Addgene ID for each repair template are also listed. Red asterisks indicate repair templates that were created and tested in WTC-11 iPSCs by the Allen Institute for Cell Science (Obtained from Addgene; Roberts et al., 2017; Allencell.org).

Protein/structure	Gene/locus	Fluorescent protein	Terminus	Protein linker	sgRNA sequence/PAM	Cell lines tested	Addgene ID (repair template)	Addgene ID (CRISPR plasmid)
Anillin	ANLN	mNeonGreen	N-	GGSGGS	GTCTCGTAGTCCGACGCCTG/GGG	HEK293, HeLa, HCT116, HepG2	183834	183874/183873
Ect2	ECT2	mNeonGreen	N-	GGSGGS	TATTAACATCCACTACTGGG/AGG	HEK293	183835	183876/183875
RhoA	RHOA	mNeonGreen	N-	GGSGGS	AATCACCAGTTTCTTCCGGA/TGG	HEK293	183836	183878/183877
Anillin	CfANLN	mNeonGreen	N-	GGSGGS	GGCGATGGACCCGTTTACCG/AGG	MDCK	183837	183880/183879
H2B histone	H2BC11	mEGFP	C-	DPPVAT	ACTCACTGTTTACTTAGCGC/TGG	WTC-11*, HEK293	109121*	183883/183881
		mRuby2				HEK293	183866	
		TagBFP				HEK293	183867	
Actin beta	ACTB	mEGFP	N-	AGSGT	GCCGTTGTCGACGACGAGCG/CGG	WTC-11*, HEK293	87425*	183885/183884
		mRuby2				HEK293	183868	
Myosin IIB	MYH10	mEGFP	N-	YSDLELKLRIP	GTTCTCTGCGCCATTGTAAA/TGG	WTC-11*	87428*	183887/183886
		mRuby2				-	183869	
Tubulin alpha	TUBA1B	TagRFP-T	N-	GGSGGS	GATGCACTCACGCTGCGGGA/AGG	WTC-11*, HEK293	101785*	183889/183888
Plasma membrane	AAVS1	mNeonGreen-CAAX	-	-	GGGGCCACTAGGGACAGGAT/TGG	HEK293	183870	183891/183890
		mRuby2-CAAX				HEK293	183871	

To expand on this toolset, we obtained repair templates and sgRNA sequences from the Allen Institute for Cell Science (Addgene) and replaced the mEGFP tag with either a red (mRuby2) or a blue (TagBFP) fluorophore. We also generated repair templates targeted to the AAVS1 locus (Adeno-Associated Virus Integration Site 1) to express membrane-specific tags by fusing mNeonGreen or mRuby2 with the CAAX domain of K-Ras (Zhou et al., 2012). The repair templates and sgRNAs that were generated and used in this study are listed in Table 2.1. Notably, we were unable to obtain MYH10-tagged cells after several attempts using four different sgRNAs in HEK293 and HeLa cells. Since this protein was tagged successfully in iPSCs (Roberts et al., 2017), there could be cell-specific differences in how this gene is expressed, or in the efficiency of repair at this locus. However, the other constructs were used to successfully generate multiple HEK293 cell lines expressing different combinations of endogenous tags (Fig. S2.2). We generated double-tagged H2B-TagBFP; mNeonGreen-anillin cells, which were then used to generate triple-tagged lines by also tagging the plasma membrane or β-actin with mRuby2 (Fig. S2.2A,B). We found no major differences in the growth and viability of the edited lines over 3–4 generation times (5 days) compared to non-edited HEK293 cells (Fig. S2.2C). We also found that the furrow peaks were well-aligned between double-tagged and single-tagged cells (Fig. S2.2D), showing that these cells can be used for localization studies when multiple components are tagged.

2.5.2 Endogenous tags are preferable for localization studies compared to transgenes

We then characterized the localization of endogenous mNeonGreen-tagged anillin, Ect2 and RhoA in live HeLa cells by fluorescence microscopy for the first time. To emphasize the drastic differences in expression between endogenous tags and transiently over-expressed

transgenes, we compared the levels of fluorescent proteins in multiple cells within fields of view. Indeed, there was a striking difference in the levels and variability across cell populations where fluorescent protein tags were transiently over-expressed compared to endogenous tags, which were weaker and more uniform (Fig. 2.2A,B). While there was some variability in anillin and Ect2 expression levels in the endogenously tagged cell lines, this was expected due to their cell cycle-dependent turnover, and was much lower compared to cells where they were over-expressed (Fig. 2.2A,B). The transfected cells also showed variable morphology with more rounded cells, likely due to apoptosis, and/or cell cycle phenotypes (Fig. 2.2B). We also observed binucleate cells indicative of cytokinesis failure with Ect2 and RhoA over-expression (Fig. 2.2B). These data show that the endogenous tagging of cytokinesis proteins provides more accurate readouts of protein expression compared to over-expressed transgenes, which can also cause cytokinesis phenotypes. This comparison reveals the importance of considering expression levels when generating stable cell lines from transgenes, as the lines chosen for further study could be extremely different compared to the endogenous proteins.

2.5.3 Core cytokinesis regulators have distinct spatio-temporal distributions

We then imaged cells during cytokinesis to follow the localization of endogenously tagged anillin, Ect2 and RhoA (Fig. 2.3A-C). As expected, anillin was enriched at the equatorial cortex shortly after anaphase onset and remained in the furrow throughout ingression, after which it localized to the midbody (Fig. 2.3A). We measured this enrichment using a linescan to plot the intensity of mNeonGreen-anillin along the cortex of cells at the start of furrowing (approx. 9–14 min after anaphase onset; Fig. 2.3D, E, left). To visualize localization over time, we repeated this analysis every 2 min, starting 2 min before anaphase onset and until furrowing appeared to be

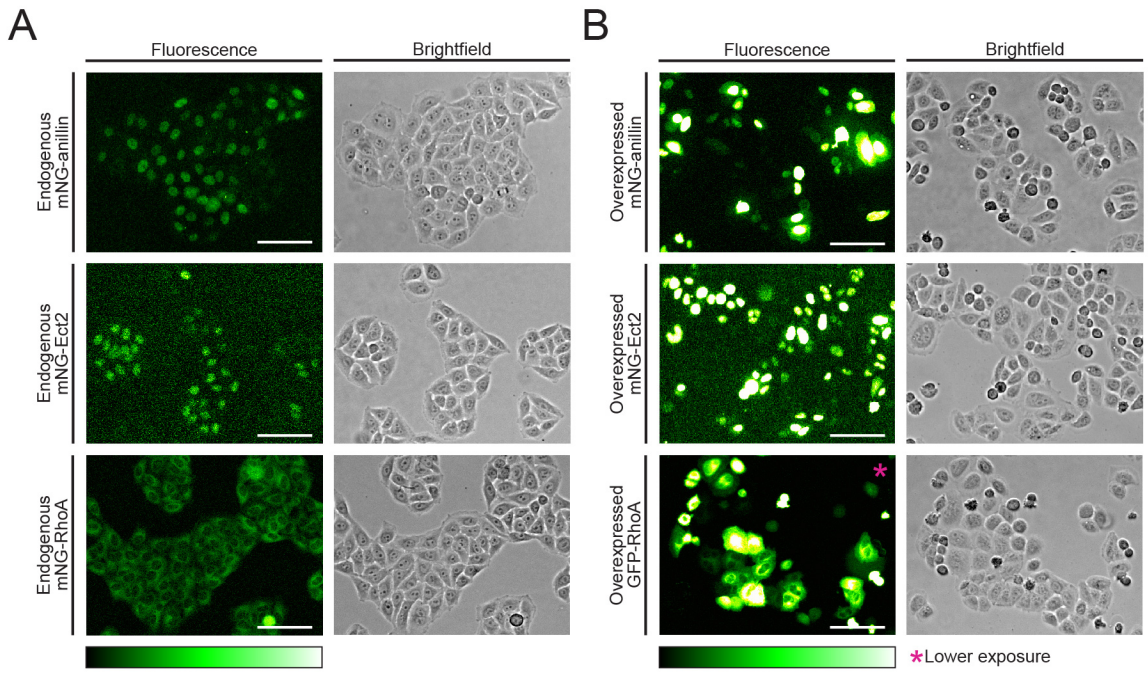

Figure 2.2. Endogenous tags are more reliable than transient over-expression. A) Fluorescent (left) and corresponding brightfield (right) images of HeLa cells show anillin (top), Ect2 (middle) and RhoA (bottom) endogenously tagged with mNeonGreen. **B)** Fluorescent (left) and corresponding brightfield (right) images of HeLa cells show exogenous expression of mNeonGreen-anillin (top), mNeonGreen-Ect2 (middle) and GFP-RhoA (bottom) 24 h after transfection. *Image taken with a lower exposure time. The scale bars are 100 µm. The relative intensity of mNeonGreen is shown in the corresponding scale.

completed (Fig. 2.3F, G, left). We observed an increase in the enrichment and a gradual decrease in the breadth of anillin at the equatorial cortex over time, with the enrichment being first visible 4–6 min after anaphase onset (Fig. 2.3G, left). Ect2 initially localized to the central spindle, then was also visible at the equatorial cortex and remained in both locations during ingression, followed by its localization to the midbody (Fig. 2.3B and S2.3A). We used linescans to measure the intensity of mNeonGreen-Ect2 along the cortex at furrow initiation (Fig. 2.3E, middle), and along the cortex and central spindle over time (Fig. 2.3G, middle, H, I). The localization of Ect2 to the central spindle preceded the equatorial cortex, which was first visible approximately 6 min after

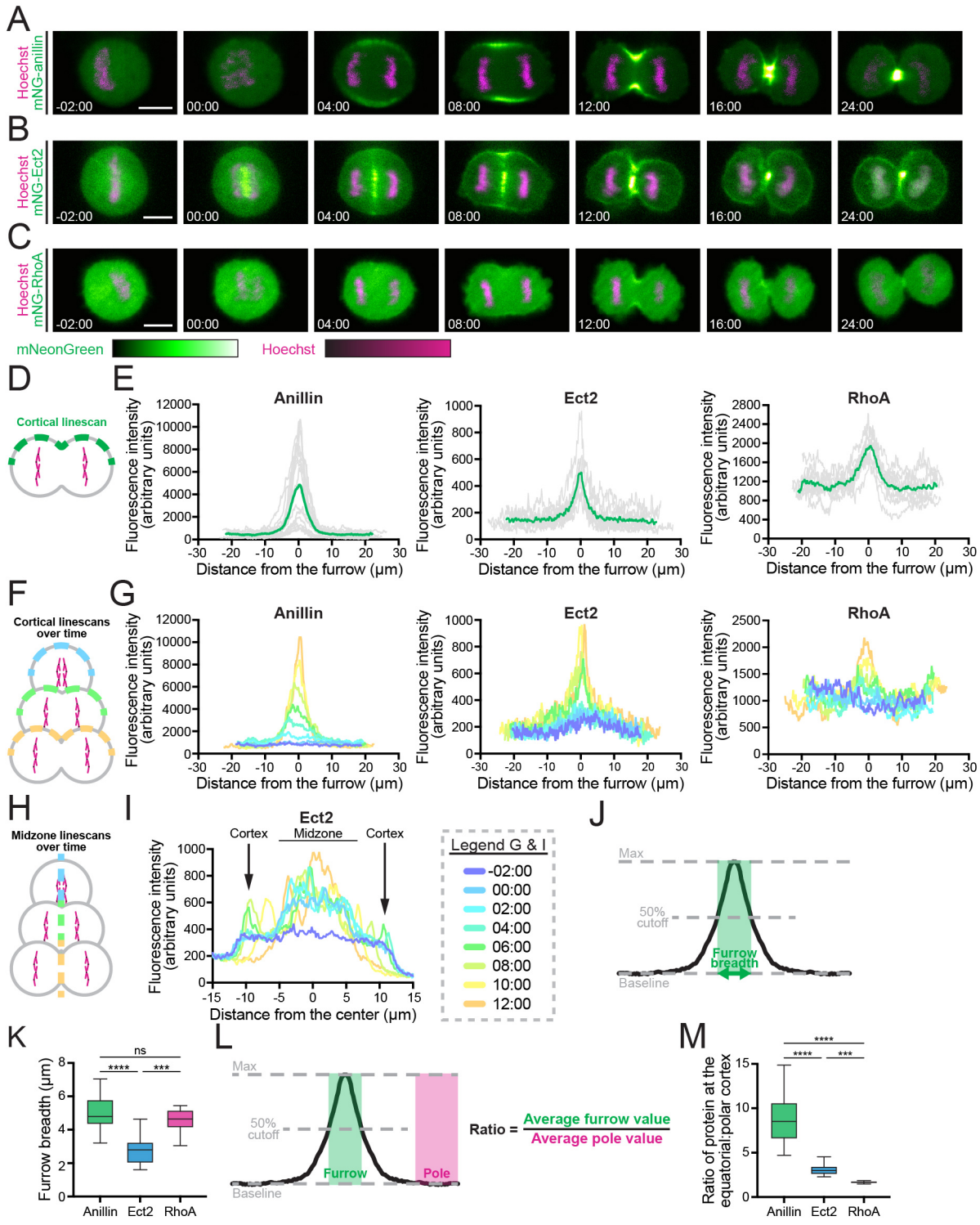

Figure 2.3. Endogenous anillin, Ect2 and RhoA show distinct localization patterns during cytokinesis in HeLa cells. A-C) Time-lapse images show cells expressing endogenous mNeonGreen-anillin (A), mNeonGreen-Ect2 (B) and mNeonGreen-RhoA (C) during cytokinesis. mNeonGreen is shown in green and DNA (stained with Hoechst) in magenta. Times are shown in

minutes and seconds relative to anaphase onset. The scale bar is 10 μm. The relative intensities of mNeonGreen and Hoechst are shown in the corresponding scales. **D-E)** A schematic (D) shows the location of the cortical linescan used to plot the intensity of fluorescence at the onset of furrowing (E, 8–12 min minutes after anaphase onset) in HeLa cells expressing endogenously tagged anillin (left, n = 16), Ect2 (middle, n = 10) and RhoA (right, n = 10). Individual replicates are shown in grey, and the average is shown in green. **F-G)** A schematic (F) shows the location and timing of the linescans used to plot the fluorescence intensity along the cortex in single HeLa cells (G) expressing endogenously tagged anillin (left), Ect2 (middle) and RhoA (right) at multiple timepoints starting 2 min before anaphase onset, and shown in different colours as indicated in the scale below. **H-I)** A schematic (H) shows the location and timing of the linescans used to plot the fluorescent intensity along the midzone of a single HeLa cell (I) expressing endogenously tagged Ect2 at multiple timepoints starting 2 min before anaphase onset, shown in the same colours as G. **J)** A schematic shows how the breadth at the equatorial cortex was calculated for K. **K)** Box plots show the breadth of anillin (n = 16), Ect2 (n = 10) and RhoA (n = 10) in HeLa cells. **L)** A schematic shows how the ratio of protein at the equatorial cortex (furrow) relative to the polar cortex was calculated for M. **M)** Box plots show the enrichment of anillin (n = 16), Ect2 (n = 10) and RhoA (n = 10) at the equatorial cortex in HeLa cells. Box plots in K and M show the median line, quartile box edges and minimum and maximum value whiskers. Statistical significance was determined by one-way ANOVA (ns, not significant; * $p \leq 0.05$; ** $p \leq 0.01$; *** $p \leq 0.001$; **** $p \leq 0.0001$).

anaphase onset and was narrow compared to anillin. Lastly, we found that RhoA was also enriched at the equatorial cortex at the onset of ingression (Fig. 2.3C, E, right). Linescans revealed that this enrichment was visible approximately 6–8 min after anaphase onset (Fig. 2.3C, G, right). This enrichment appeared weak compared to Ect2 and anillin, likely because of the large pool of cytoplasmic RhoA. To demonstrate that mNeonGreen-RhoA can be activated, we transiently over-expressed the C-terminus of Ect2 (Ect2 (C-term); amino acids 420-882), which contains the DH domain required for nucleotide exchange and activation of RhoA (Yuce et al., 2005). In interphase and metaphase cells expressing mScarlet-I-Ect2 (C-term), we observed an increase in the cortical localization of mNeonGreen-RhoA, which reflects an increase in activity since the active form is membrane-localized (Fig. S2.3B-C; Yuce et al., 2005).

Next, to compare the localization of anillin, Ect2 and RhoA during cytokinesis, we quantified their breadth and accumulation. To measure breadth, we used the linescans to determine the number of pixels above 50% of the normalized peak intensity (Fig. 2.3J) and found that while

the breadth of anillin and RhoA was similar (4.9 ± 1.1 and 4.5 ± 0.8 μm, respectively), Ect2 was narrower (2.8 ± 0.9 μm; Fig. 2.3K). Similar results were obtained when measuring breadth as a ratio of cortical length to control for variations in cell size (Fig. S2.4A). To measure accumulation, the ratio of the average pixel intensity of anillin, Ect2 and RhoA in the furrow relative to the polar cortex was determined (Fig. 2.3L). Our data revealed that anillin was most enriched, with 8.9 ± 2.9-fold (n = 16) more protein in the furrow than at the poles compared to Ect2 (3.1 ± 0.7-fold, n = 10) and RhoA (1.7 ± 0.1-fold, n = 10; Fig. 2.3M).

2.5.4 Endogenous tagging of anillin in different mammalian cell lines

Next, we tagged anillin with mNeonGreen in different cell lines to facilitate cytokinesis studies. In addition to the tagged HEK293 and HeLa cells described earlier, we tagged anillin with mNeonGreen in HCT116 (human male colon cancer with 45 modal chromosomes; near diploid), HepG2 (human male hepatoblastoma with 55 modal chromosomes, hyperdiploid) and MDCK (Madin–Darby canine female kidney with 78 or 87–90 modal chromosomes; diploid—hyperdiploid) cells. Since MDCK cells are not human, we created new sgRNAs and repair templates suited for the *Canis lupus familiaris* genome (Table 2.1). These cell lines are rarely used for gene editing and presented distinct challenges. HCT116 and MDCK cells have low transfection efficiency using liposome-based methods, requiring nucleofection to increase transfection efficiency and recover successfully tagged cells. We also used NHEJ inhibitors to increase the efficiency of integration by HDR. Another limitation was the rate of single-cell recovery after FACS. While HeLa and MDCK cells recovered well from single-cell isolation (greater than 90% recovery, data not shown), HepG2 cells showed very low recovery and we initially only recovered two non-fluorescent clones from 120 isolated HepG2 cells. To resolve this issue, we enriched

tagged cells by sorting 15 000 fluorescent cells together as a population and allowing them to recover for a few days. Then, we isolated clones by sorting 10–25 fluorescent cells per well of a 96-well plate and monitoring for the recovery of a single colony in each well. Altogether, these methods can greatly facilitate gene editing in cell lines that are difficult to edit. By incorporating these methods into our editing protocols, we successfully obtained multiple heterozygous and homozygous HeLa, HEK293, HCT116, HepG2 and MDCK cell lines where anillin was endogenously tagged with mNeonGreen.

2.5.5 Differences in anillin localization correlate with distinct ring closure kinetics

To reveal cytokinetic diversity, we compared differences in anillin localization between the newly generated mNeonGreen-anillin tagged cell lines. We observed differences in when anillin was first visible at the cortex, the breadth of anillin at the equatorial cortex and the duration of ingression after anaphase onset. For example, mNeonGreen-anillin localized to the cortex in HEK293, HCT116 and MDCK cells during metaphase, but not in HeLa and HepG2 cells, where it was strictly cytosolic (Fig. 2.3A, 2.4A-D; −02:00 time-point). All cell lines showed mNeonGreen-anillin enrichment in the equatorial cortex approximately 4–8 min after anaphase onset, where it remained in the furrow throughout ingression (Fig. 2.3A, 2.4A-D). However, linescans of mNeonGreen-anillin along the cortex at furrow initiation (Fig. 2.3E, left and 2.4E-H), and every 2 min from just before anaphase until the end of furrowing, revealed differences in the breadth of anillin between the cell lines (Fig. 2.3G, left and 2.4I-L). While anillin peaks were broad in HEK293, HCT116 and MDCK cells, anillin was narrow in HepG2 cells (Fig. 2.4). Also, furrowing appeared to take much longer in HepG2 and HEK293 cells compared to the other cell lines (Fig. 2.3A, G, 2.4A-D, I-L).

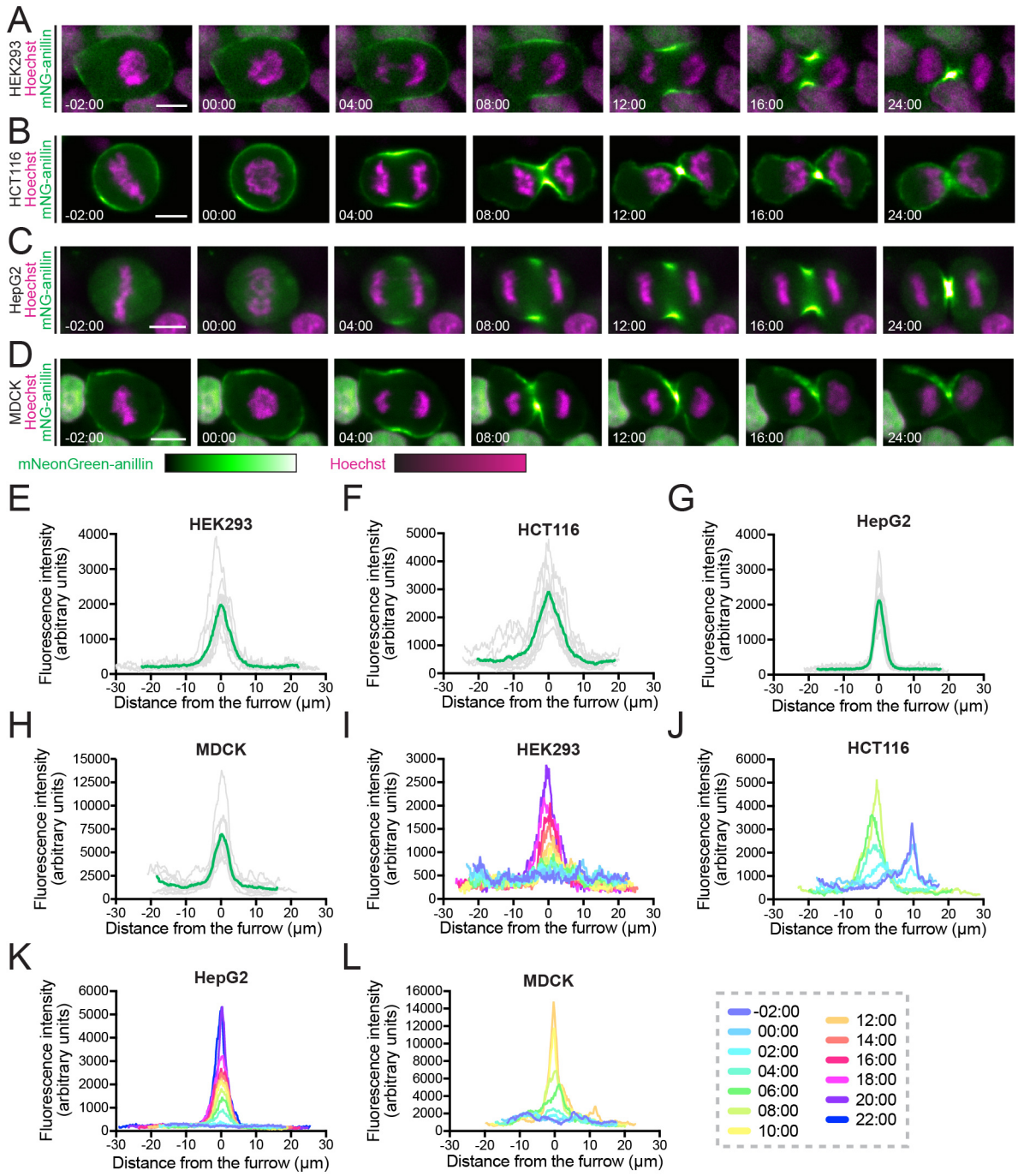

Figure 2.4. Endogenous tagging of anillin in different cell lines reveals differences in its localization during cytokinesis. A-D) Time-lapse images show endogenous mNeonGreen-anillin in HEK293 (A), HCT116 (B), HepG2 (C), and MDCK (D) cells during cytokinesis. mNeonGreen is shown in green and DNA (stained with Hoechst) is in magenta. Times are shown in minutes and seconds relative to anaphase onset. The scale bar is 10 µm. The relative intensities of mNeonGreen-anillin and Hoechst are shown in the corresponding scales. **E-H)** Graphs show fluorescence intensity of mNeonGreen-anillin along the cortex of HEK293 (E, n = 9), HCT116 (F,

n = 11), HepG2 (G, n = 13), and MDCK (H, n = 10) cells at furrow initiation. **I-L)** Graphs show fluorescence intensity of mNeonGreen-anillin along the cortex of a single HEK293 (I), HCT116 (J), HepG2 (K) and MDCK (L) cell at multiple timepoints starting 2 min before anaphase onset, shown in different colors as indicated by the scale.

Next, we quantified the differences in anillin localization and ring closure, using furrow ingression as a proxy, among the cell lines. First, we compared the duration of ring closure between the cell lines, starting from anaphase onset until the membrane appeared to be fully closed (Fig. 2.5A, B). While ingression took similar amounts of time on average in HeLa (20.4 ± 1.7 min, n = 11), HEK293 (22.3 ± 5.2 min, n = 7) and MDCK cells (17.7 ± 5.0 min, n = 6; Fig. 2.5B), HepG2 cells ingressed slower (31.0 ± 7.0 min, n = 11), and HCT116 cells ingressed faster (12.3 ± 1.4 min, n = 8). We also noted more variability in the duration of ingression in HEK293 and HepG2 cells compared to the other cell types.

Next, we quantified the cortical localization of anillin prior to anaphase between HCT116 and HepG2 cells, where the difference was most striking. To do this, we measured the ratio of cortical to cytosolic mNeonGreen-anillin during metaphase (Fig. 2.5C, D). Indeed, anillin was significantly enriched at the cortex during metaphase in HCT116 cells (1.6 ± 0.3-fold), but not in HepG2 cells (0.6 ± 0.1-fold; Fig. 2.5D). Then, we compared the breadth of anillin localization at the onset of furrowing in the different cell lines (Fig. 2.5E, F). Since anillin localized to the furrow as a well-defined peak across all cell lines, we measured breadth as the number of pixels above 75% of the normalized peak intensity (Fig. 2.5E, F). The mNeonGreen-anillin furrow was the broadest in HCT116 cells, narrowest in HepG2 cells, and was similar between HeLa, HEK293 and MDCK cells (Fig. 2.5F). Similar results were obtained when measuring breadth as a percentage of cortical length, showing that these differences were independent of cell size (Fig. S2.4B). mNeonGreen-anillin was similarly enriched in the equatorial cortex of HeLa, HEK293 and

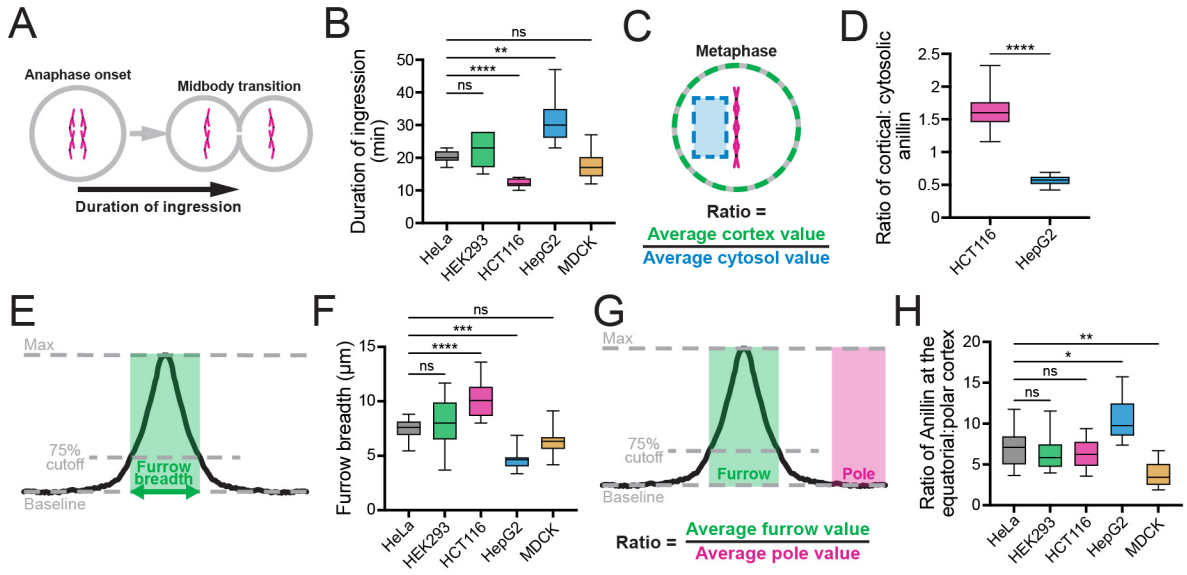

Figure 2.5. Breadth of anillin but not cumulative levels correlate with the efficiency of ring closure. A) A schematic shows how the duration of ingression was measured in B. **B)** A box plot shows the duration of ingression in HeLa (n = 11), HEK293 (n = 7), HCT116 (n = 8), HepG2 (n = 11) and MDCK (n = 6) cells. **C)** A schematic shows how the ratio of cortical to cytosolic mNeonGreen-anillin was measured for D. **D)** A box plot shows the enrichment of mNeonGreen-anillin at the cortex relative to the cytosol during metaphase in HCT116 (n = 8) and HepG2 (n = 12) cells. **E)** A schematic shows how the breadth at the equatorial cortex was calculated for F. **F)** A box plot shows the breadth of mNeonGreen-anillin localization along the equatorial cortex at furrow initiation in HeLa (n = 16), HEK293 (n = 9), HCT116 (n = 11), HepG2 (n = 13) and MDCK (n = 10) cells. **G)** A schematic shows how the ratio of protein in the furrow relative to the polar cortex was calculated for H. **H)** A box plot shows the ratio of anillin at the equatorial cortex compared to the polar cortex in HeLa (n = 16), HEK293 (n = 9), HCT116 (n = 11), HepG2 (n = 13) and MDCK (n = 10) cells. Box plots in B, D, F and H show the median line, quartile box edges and minimum and maximum value whiskers. Statistical significance was determined by one-way ANOVA in B, F and H, and Welch *t* test in D (ns, not significant; * $p \leq 0.05$; ** $p \leq 0.01$; *** $p \leq 0.001$; **** $p \leq 0.0001$).

HCT116 cells (7.1 ± 2.4, 6.3 ± 2.3 and 6.3 ± 1.9-fold enrichment, respectively), while HepG2 cells had a significantly stronger enrichment (10.4 ± 2.6-fold), and MDCK cells had a weaker enrichment (3.8 ± 1.5-fold; Fig. 2.5H). These data suggest that the breadth of anillin localization rather than accumulated levels correlate with the rate of ingression. This is further supported by measurements of two distinct populations of cells within the mNeonGreen-anillin HeLa cell line, which display higher or lower expression levels (Fig. S2.5). Since our genotyping revealed no

untagged alleles, we presume that this difference in anillin levels is due to aneuploidy causing heterogeneity and changes in gene expression. Comparing the same parameters in these two populations of cells revealed no difference in the duration of ingression and breadth of anillin (Fig. S2.5B-F), but the accumulated levels were higher in one population compared to the other (Fig. S2.5G, H).

2.5.6 Asymmetric ingression in MDCK cells is intrinsically controlled

We also observed that the furrow ingressed asymmetrically in MDCK cells, but not in the other cell lines (Fig. 2.4D and 2.6A). MDCK cells acquire apicobasal polarity when grown to confluency in culture, however to facilitate live imaging studies, our cells were not confluent (Balcarova-Stander et al., 1984). Since 2D side views of ingression can be misleading, we measured ring closure using end-on-views. To do this, we plotted the position of the ring over time starting before anaphase onset until the ring had closed (*e.g.* two cells are shown in Fig. 2.6B, C). We also calculated the distance between the centre of the cell at the first timepoint and the center of the ring at the last timepoint (Fig. 2.6D). We found that ring closure occurred asymmetrically in 61.9% of cells (symmetry value between 0.2 and 0.6; n = 13/21) and highly asymmetrically in 33.3% of cells (symmetry value greater than 0.6; n = 7/21). Meanwhile, only one cell (n = 1/21) closed symmetrically (symmetry value less than 0.2; Fig. 2.6D, E). We also measured the levels of anillin along the ingressing and non-ingressing cortex in an asymmetrically dividing MDCK cell. We found that anillin was cortical and more broadly distributed along the ingressing versus non-ingressing cortex until about 6 min after anaphase onset, when a peak of similar intensity formed on both sides (Fig. 2.6F, G). The peak on the ingressing cortex was also broader and continued to increase in intensity compared to the non-ingressing cortex (Fig. 2.6F, G). It is

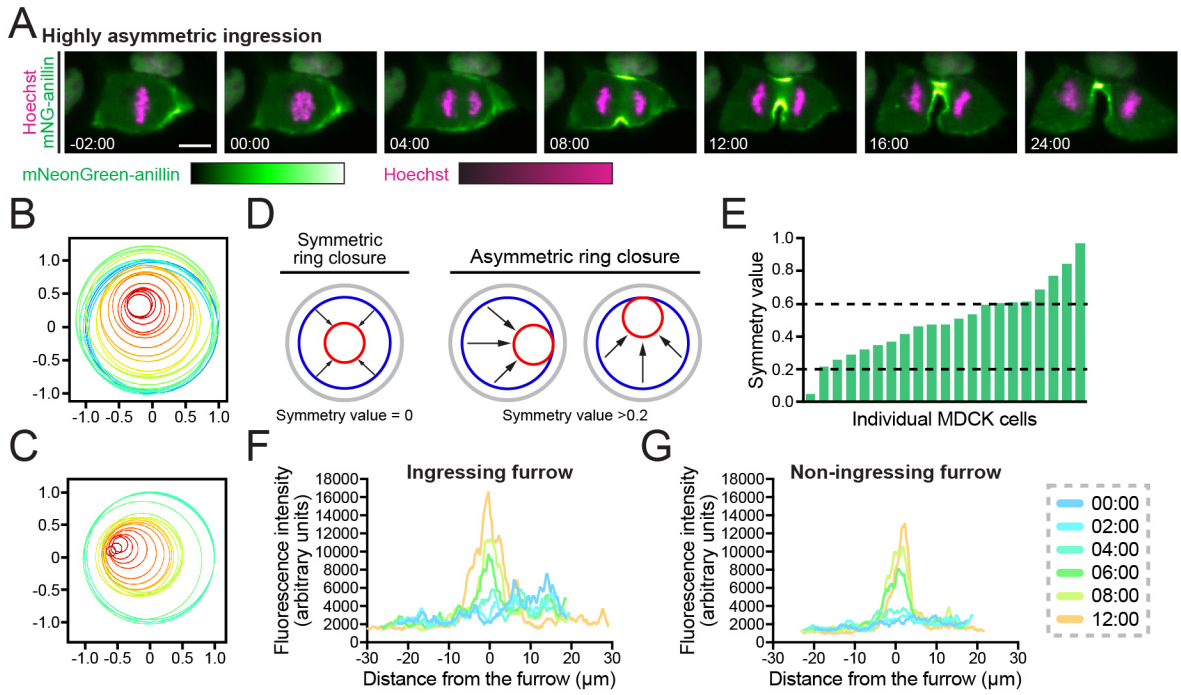

Figure 2.6. MDCK cells ingress asymmetrically. A) Time-lapse images show endogenous mNeonGreen-anillin localization in different MDCK cells during cytokinesis where ingression appeared to be highly asymmetric. mNeonGreen is shown in green and DNA (stained by Hoechst) is in magenta. The relative intensities of mNeonGreen and Hoechst are shown in the corresponding scales. Times are shown in minutes and seconds from anaphase onset. The scale bars are 10 µm. **B-C)** Graphs shows the position of the ring over time in cells that undergoes asymmetric (B) or highly asymmetric (C) ring closure. **D)** Schematics show the relative position of the ring as it closes symmetrically (left; values less than 0.2) or asymmetrically (right; values greater than 0.2). **E)** A graph shows the symmetry values for ring closure in 21 cells, ranging from symmetric (less than 0.2, n = 1) to asymmetric (between 0.2 and 0.6; n = 13/21) and highly asymmetric (greater than 0.6; n = 7/21). **F-G)** Graphs show fluorescence intensity of mNeonGreen-anillin along the ingressing (F) and the non-ingressing (G) sides of the cortex of an asymmetrically dividing MDCK cell starting 2 min before anaphase onset, with timepoints shown in different colours as indicated by the scale.

exciting to speculate that the asymmetric distribution of anillin could influence ring closure in these cells, and the lack of junctions to transmit forces between cells suggests that anillin distribution and asymmetric ingression are controlled intrinsically.

2.6 Discussion

In this study, we reveal cytokinetic diversity between different cell types by endogenously tagging cytokinesis proteins with fluorescent tags and visualizing them by live imaging. Specifically, we successfully tagged endogenous anillin, Ect2 and RhoA with mNeonGreen and visualized their localization for the first time in live human cells, enabling robust comparative studies of these key cytokinesis regulators. A limitation of gene editing tools is the risk of introducing undesired off-target mutations. To alleviate this issue, we used the high-specificity HypaCas9 variant, which has the advantage of preserving on-target editing while reducing off-target cutting (Chen et al., 2017; Kato-Inui et al., 2018). Several approaches have been devised to reduce the frequency of off-target cutting by Cas9 and the frequency of mutagenic repair, including the use of paired Cas9 nickases or Cas9-sgRNA ribonucleoprotein complexes (Cho et al., 2014; Kim et al., 2014). These improvements on CRISPR/Cas9 gene editing tools help generate high-quality engineered cell lines to ensure robust biological results without artefacts.

To date, most cytokinesis proteins have been studied using over-expressed transgenes in HeLa cells, which may influence the interpretation of their function. Additionally, probes to visualize RhoA or its GEF Ect2 have been notoriously difficult to use (Koh et al., 2021; Kotynkova et al., 2016; Piekny et al., 2005; Schneid et al., 2021; Yuce et al., 2005). Comparing the spatiotemporal localization of endogenous RhoA, Ect2 and anillin revealed that their enrichment at the equatorial cortex occurs at similar times and aligns with the timing of ring assembly and ingression. However, while anillin and RhoA broadly localize along the equatorial cortex, Ect2 localizes to a narrower region, suggesting differences in how the cortical localization of Ect2 is controlled compared to anillin and RhoA. Additionally, Ect2 is first visible at the central spindle, which supports prior findings that an Ect2–Cyk4 complex first forms at the central spindle during

mitotic exit and is then released or recruited to the overlying membrane. The localization of anillin and Ect2 is largely in agreement with previous studies done in HeLa cells using immunofluorescence with specific antibodies. Given that fixation can cause artefacts and that epitopes may not be consistently accessible, it was not known whether immunofluorescence provided an accurate picture of their localization pattern. Our findings clarify any variability in localization that may have been reported due to differences in chemical fixation and cell cycle stage (*e.g.* Piekny & Glotzer, 2008; Yonemura et al., 2004; Yuce et al., 2005). Crucially, this is the first study to our knowledge that reveals the localization of pools of endogenous RhoA during cytokinesis, which was predicted to be enriched at the equatorial membrane based on immunofluorescence after TCA fixation (Piekny et al., 2005; Yonemura et al., 2004; Yuce et al., 2005). Interestingly, RhoA was visibly enriched at the equatorial cortex after anillin. While the cytosolic pools of RhoA could obscure weaker cortical signals, this timing could also reflect the positive feedback between the two proteins, with anillin helping to cluster $PI_{4,5}P_2$ lipids that RhoA preferentially binds to, and by increasing the residence time of RhoA at the cortex (Budnar et al., 2019). There is also the caveat that N-terminally tagged RhoA may not be fully functional. However, its ability to respond to Ect2 over-expression and to accumulate at the equatorial cortex suggests that it is at least partially functional.

Our knowledge of mammalian cytokinesis is largely derived from studies of HeLa cells, but the mechanisms regulating cytokinesis are expected to vary with fate, size, ploidy and geometry. Here, we reveal cytokinetic diversity by comparing the spatio-temporal localization of endogenously tagged anillin between different cell lines. This includes HeLa cells as well as cell lines where cytokinesis has not been well-studied (HEK293, MDCK, HepG2, HCT116). We observed differences in 1) the duration of ingression, 2) the timing and breadth of the cortical

localization of anillin, 3) the amount of anillin in the furrow and 4) how symmetrically the ring closes.

The timing of anillin's cortical localization varies among the different cell types. Anillin is cortically localized before anaphase onset in HEK293, HCT116 and MDCK cells, but not in HeLa and HepG2 cells. Previous studies reported that anillin is cortically localized during metaphase in BHK-21 (baby hamster kidney) and *Drosophila* S2 cells, but this was not investigated further (El Amine et al., 2013; Field & Alberts, 1995; Oegema et al., 2000). Based on recent studies showing that importin-binding regulates the cortical localization of anillin, we propose that ploidy relative to cell size or chromatin position could determine whether importins reach sufficient levels to recruit anillin to the cortex in metaphase (Fig. 2.7A; Beaudet et al., 2017; Beaudet et al., 2020; Ozugergin et al., 2022a). Importins bind to nuclear localization signals (NLS) in proteins, which can be competed off by Ran-GTP (Clarke & Zhang, 2008; Xu & Massague, 2004). The RanGEF RCC1 is bound to histones and RanGAP is in the cytosol, causing Ran-GTP to be enriched around chromatin. The strength of this gradient and whether Ran-GTP levels are high enough to impact importin-binding to cortical NLS-proteins would determine if anillin is localized cortically or not (Fig. 2.7A; Clarke & Zhang, 2008; Xu & Massague, 2004). Thus, our model is that in cells that are small and/or have higher ploidy (*e.g.* HeLa, HepG2), importins cannot recruit anillin to the cortex during metaphase, but can recruit anillin to the equatorial cortex during anaphase as the chromosomes segregate (Fig. 2.7A, top). Thus, the Ran pathway could be a dominant mechanism that controls the breadth of anillin in these cells. In cells that are large and/or have lower ploidy (*e.g.* HCT116), Ran-free importins reach sufficient, uniform levels to recruit anillin to the cortex during metaphase (Fig. 2.7A, bottom), and other mechanisms determine the breadth of anillin during anaphase. Our model also has implications for cells where chromatin is asymmetrically

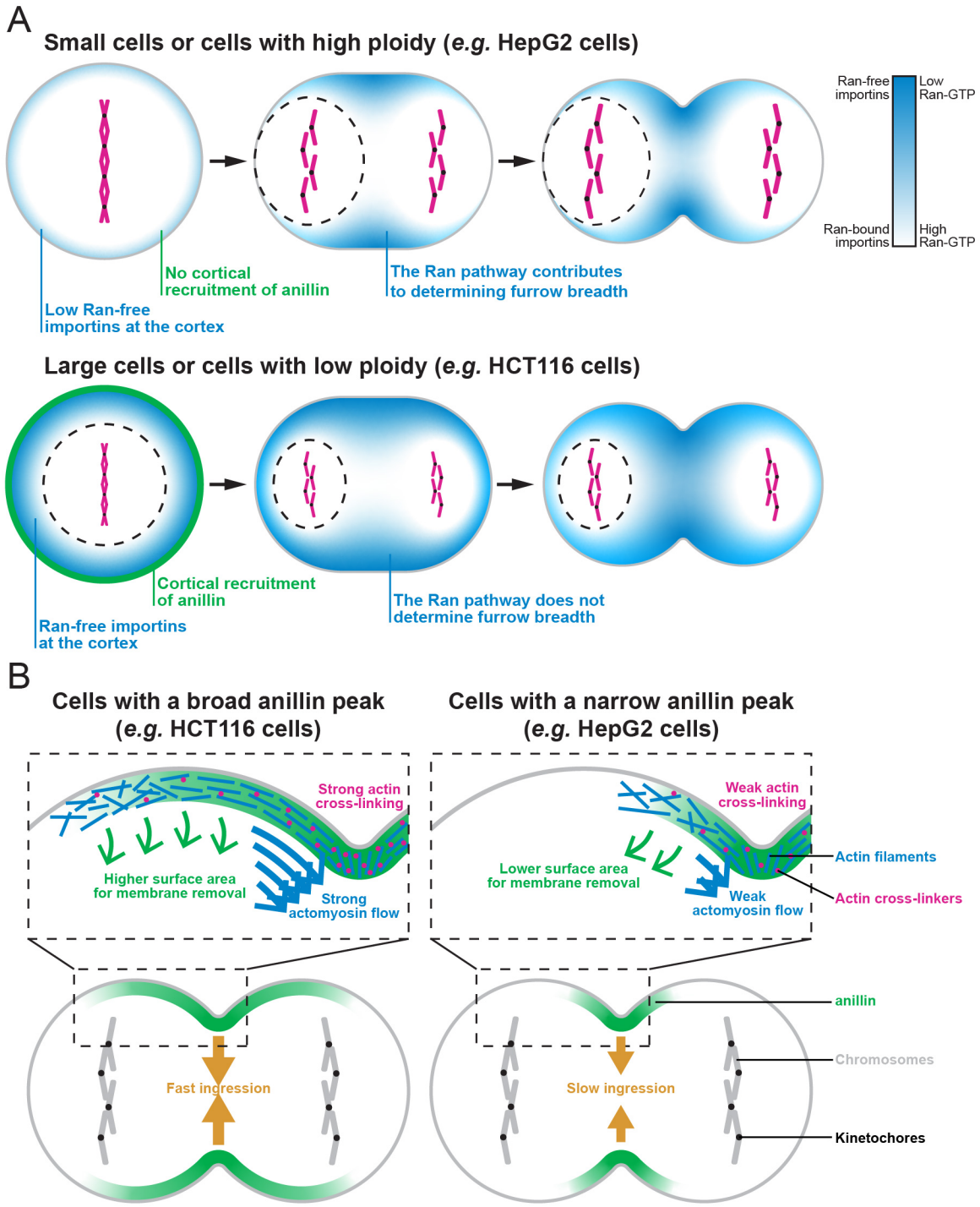

Figure 2.7. Mechanisms controlling ring assembly and constriction in human cells. A) Cartoon schematics show two different cell types in metaphase, anaphase and telophase, with the position and strength of Ran-GTP (white) and Ran-free importin (blue) levels. In small cells or cells with high ploidy (top), Ran-GTP levels reach the cortex, restricting where Ran-free importins can bind to anillin. In large cells or cells with low ploidy (bottom), Ran-GTP levels are too low to reach the cortex and Ran-free importins can globally bind to and recruit anillin, requiring other

pathways to control ring position. **B)** Cartoon schematics show how the breadth of anillin could influence ring closure. In cells where anillin is more broadly localized (left), there is more surface area for the removal of membrane microdomains by anillin–septin complexes, or there could be stronger actomyosin flows, and/or greater cross-linking of actin filaments to facilitate their alignment for faster ingression compared to cells where anillin is more narrow (right).

positioned, which could lead to the asymmetric localization of cortical anillin and influence filament organization for ingression (*e.g.* MDCK cells; Beaudet et al., 2017; Beaudet et al., 2020; Husser et al., 2021; Ozugergin & Piekny, 2021). Other mechanisms could also directly or indirectly control the localization of anillin in the different cell lines. Cells with higher ploidy would have more kinetochores and associated Sds22 that could increase PP1 phosphatase activity to downregulate ERM proteins (ezrin, moesin, radixin) and promote the removal of F-actin from the nearby cortex (Rodrigues et al., 2015). Astral-dependent machinery could also be expressed at different levels and impact the cortical localization of anillin (*e.g.* van Oostende Triplet et al., 2014; Mangal et al., 2018). These mechanisms could be tested using the reagents described here to study cytokinesis in combination with perturbations that selectively interrogate these pathways.

We also observed that the breadth of cortical anillin at furrow initiation varies among the different cell lines. Anillin is distributed broadly along the equatorial cortex in HCT116 cells, while it is narrow in HepG2 cells compared to the other cell lines. Interestingly, HCT116 cells also ingress faster and HepG2 cells take longer to ingress than other cell lines, suggesting a correlation between the breadth of anillin localization and the efficiency of ring closure. Importantly, this correlation does not reflect the *amount* of anillin in the furrow, rather how it is distributed. A recent hypothesis paper suggested that an anillin–septin complex controls the removal of membrane microdomains from the ring to relieve tension during closure (Carim et al., 2020). The model proposed by the Hickson laboratory would explain our findings as the broader distribution of anillin in HCT116 cells (Fig. 2.7B, left) could promote more efficient ring closure by providing a

greater surface area for this "outflow" and removal of microdomains compared to HepG2 cells (Fig. 2.7B, left; Carim et al., 2020). However, the breadth of anillin could also reflect differences in other mechanisms that have been experimentally shown to facilitate ingression by promoting the alignment of actin filaments. These mechanisms include cortical flows in the axial and equatorial axis, and the distribution of actin cross-linkers (Khaliullin et al., 2018; Leite et al., 2020; Osorio et al., 2019; Reymann et al., 2016; Sobral et al., 2021; Spira et al., 2017). Future studies are required to test these models and to reveal how anillin localization affects ring closure kinetics.

We also found that ring closure occurs asymmetrically in MDCK cells. Although these cells establish apicobasal polarity in culture when grown to confluency (Balcarova-Stander et al., 1984), we imaged these cells at lower confluency, revealing that intrinsic mechanisms control ring ingression. Few studies have explored the mechanisms controlling symmetry of ring closure, which is not well understood (Bourdages et al., 2014; Dorn et al., 2016; Maddox et al., 2007; Ozugergin et al., 2022a; Paim & FitzHarris, 2022). The ring may close at least partially asymmetrically in many cell types, and the extent of asymmetry could reflect differences in cell size and fate in addition to adhesion to neighbouring cells (Bourdages et al., 2014). For example, in the two-cell *C. elegans* embryo, ring closure occurs asymmetrically in the larger AB daughter cell fated to become somatic tissue, but not in the smaller P_1 cell fated to become the germline (Ozugergin et al., 2022a). Inducing changes in cell size or perturbing the Ran pathway affects the symmetry of ring closure in P_1 cells, suggesting that multiple factors control this process (Ozugergin et al., 2022a). The nature of the ring may lend itself to asymmetric closure. As the ring pulls in part of the membrane, curvature and flows are induced that promote actomyosin filament alignment and improve energy-efficiency for faster ingression in that location (Dorn et al., 2016). However, the asymmetric ingression we observed in MDCK cells was more extreme compared to

the other cell lines. A recent study showed that apical PAR proteins localize mutually exclusively to anillin in cells within developing mouse embryos suggesting they could compete for the same filamentous networks (Paim & FitzHarris, 2022). These proteins could be asymmetrically distributed prior to establishing full apicobasal polarity, which could cause anillin to be more broadly distributed along the asymmetrically ingressing cortex (*e.g.* Fig. 2.6A). However, the mechanisms controlling their distribution in cells prior to establishing polarity are not clear, nor is the biological significance of asymmetric closure.

In addition to generating new tools and fundamental knowledge of cytokinesis, our work provides methodologies for more consistent analysis of cytokinesis. Studies of cytokinesis tend to differ in how parameters are measured and reported. Previous studies in *C. elegans* provide a strong foundation for methodologies that could be universally applied to other cell types (*e.g.* Carvalho et al., 2009; Chan et al., 2019; Maddox et al., 2007; Ozugergin et al., 2022a), including the macros used in this study, which are publicly available. We also expanded on the CRISPR/Cas9 reagents generated by the Allen Institute for Cell Science by tagging multiple cellular components with different fluorescent proteins, which will be useful for studies of cytokinesis and other biological processes in human cells. All the reagents used to generate the endogenously tagged cell lines in this study are available to the community through Addgene. Combining the use of endogenous tags with quantitative measurements will help capture cytokinetic diversity across a broader range of mammalian cell types and generate new knowledge of the mechanistic differences regulating cytokinesis.

2.7 Supplementary figures and tables

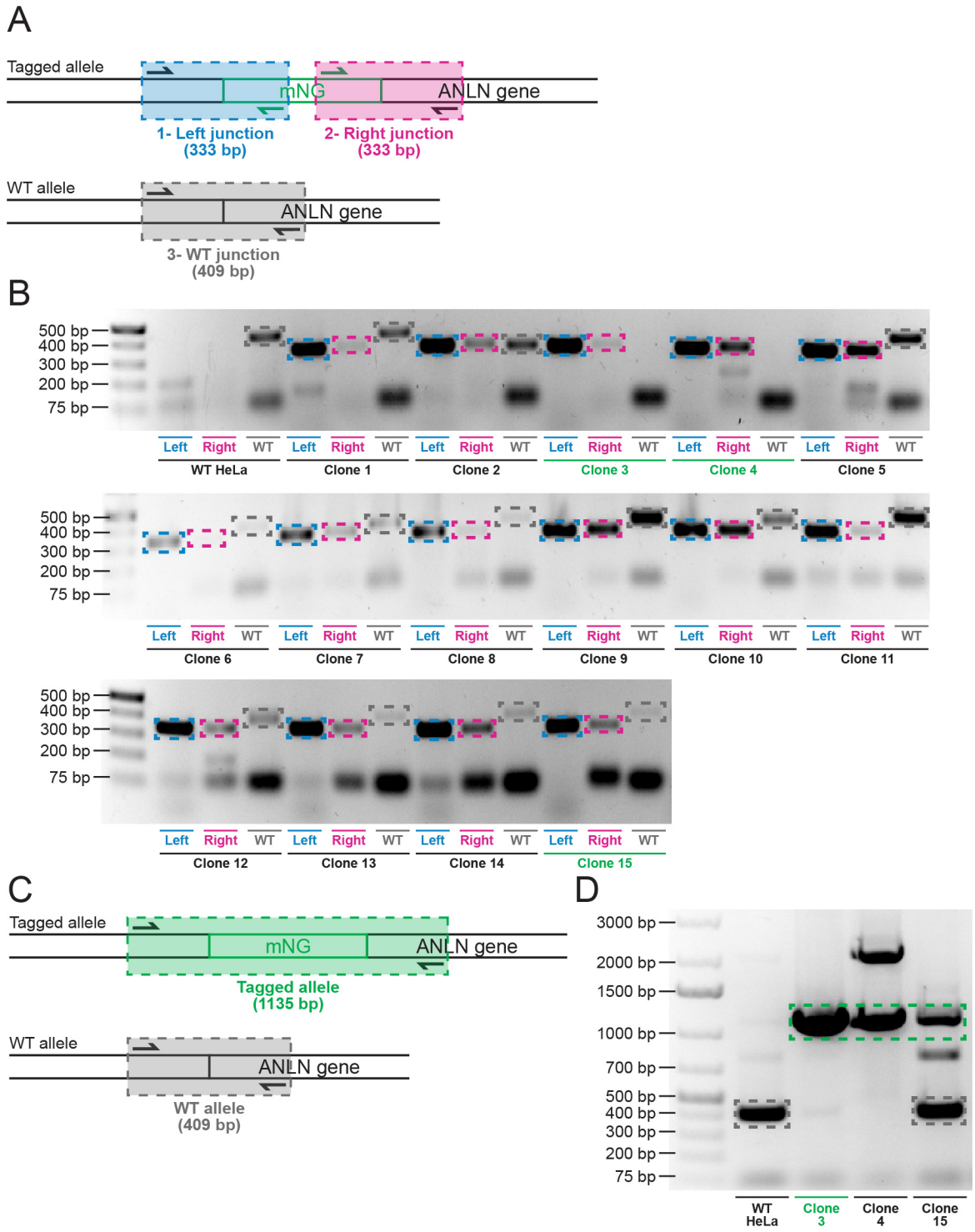

Figure S2.1. Screening and genotyping of mNeonGreen-anillin in HeLa cells. A) The schematic shows how a junction PCR strategy was used to screen the mNeonGreen-anillin clones. Three PCR reactions (left junction, right junction and unedited, WT junction) were used to amplify

the tagged and untagged alleles. **B)** Gel images show junction PCR reactions for 15 mNeonGreen-anillin clones. The presence of each band is highlighted by colored boxes (blue for the left junction, pink for the right junction, and grey for the WT junction). The clones selected for further screening are indicated in green. **C)** Schematics show the PCR genotyping strategy that was used to validate the mNeonGreen-anillin HeLa cell line, with the tagged allele highlighted in green compared to the untagged allele in grey. **D)** Gel images show the PCR products used to genotype the mNeonGreen-anillin HeLa cell lines. Green boxes indicate bands corresponding to tagged alleles, while grey boxes indicate untagged alleles. The final clone selected for sequencing and phenotyping (clone 3) is homozygous for the mNeonGreen insert.

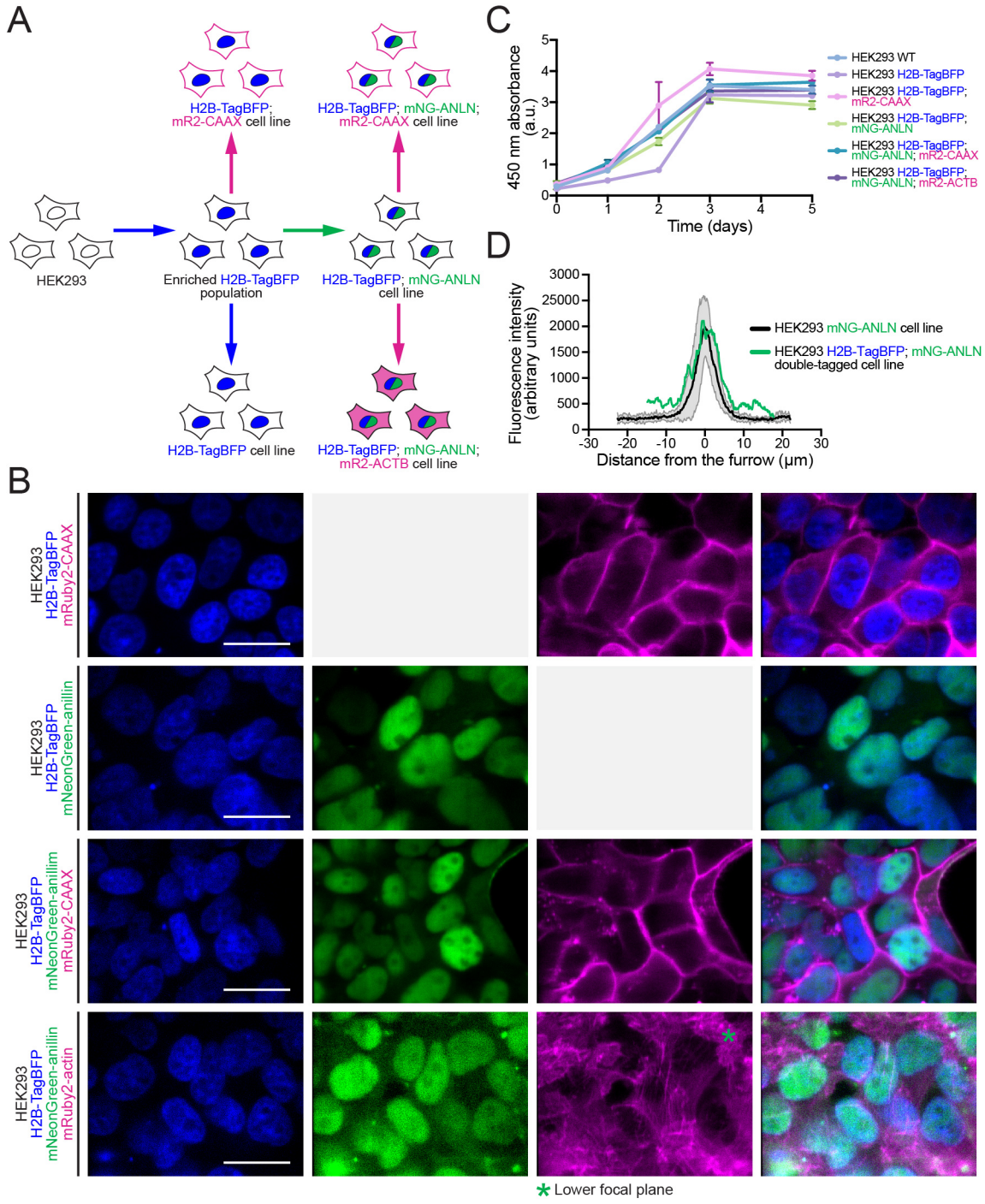

Figure S2.2. Generation of cell lines expressing multiple endogenous tags for multi-color imaging. A) A schematic shows the workflow used to generate multi-tagged HEK293 cell lines. H2B histones were first tagged with TagBFP and FACS was used to obtain an 'enriched' population. In this enriched population, anillin or the plasma membrane were tagged with mNeonGreen and mRuby2, respectively. Clonal lines were isolated to obtain single and double-tagged cell lines. Finally, triple-tagged cell lines were generated by tagging β-actin or the plasma

membrane with mRuby2 in the H2B-TagBFP; mNeonGreen-anillin double-tagged cell line. **B)** Images show cells from the multi-tagged HEK293 cell lines generated in A, with H2B-TagBFP in blue, mNeonGreen-anillin in green and mRuby2-CAAX or mRuby2-actin in magenta. The scale bars are 25 μm. *This image was taken at a lower focal plane to show the actin filaments. **C)** A graph shows the growth of the single-, double- and triple-tagged HEK293 cell lines measured by absorbance compared to unedited cells (WT) over 5 days (~3-4 population doubling times). **D)** A graph shows linescans comparing the fluorescence intensity of mNeonGreen-anillin in single-tagged HEK293 cells (shown in black with standard deviation in grey) with a double-tagged H2B-TagBFP; mNeonGreen-anillin HEK293 cell (shown in green).

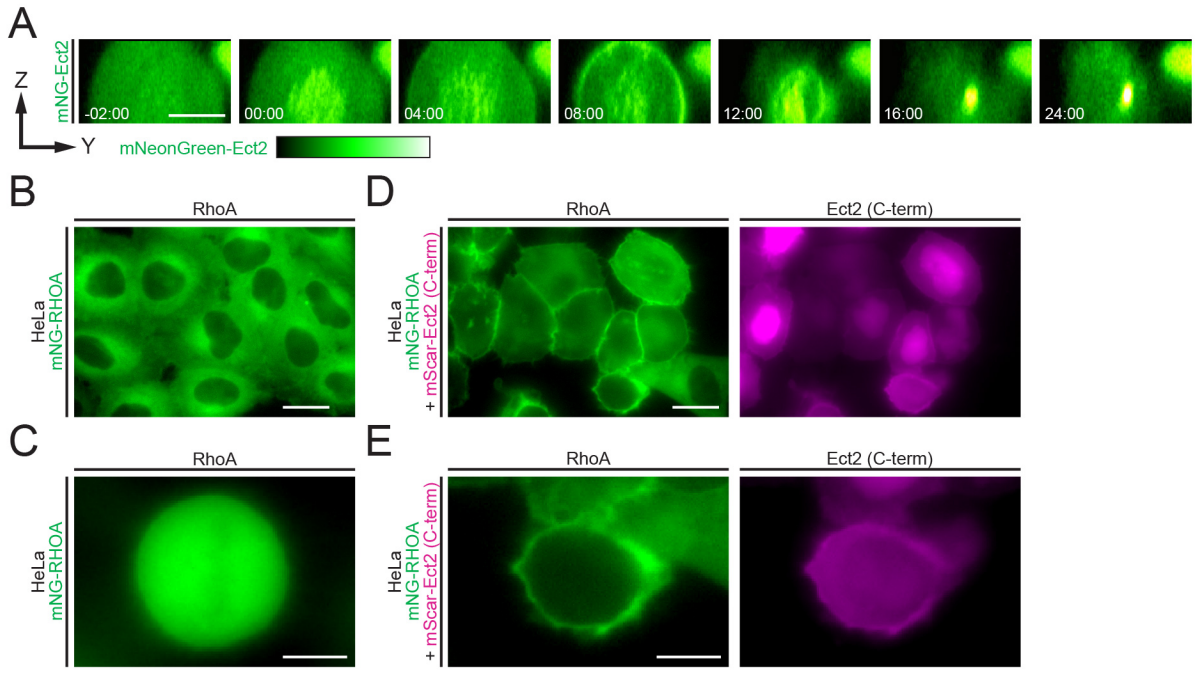

Figure S2.3. Ect2 cortical localization correlates with the cortical recruitment of RhoA in HeLa cells. A) Timelapse images show an end-on ring view of mNeonGreen-Ect2 (green) during cytokinesis. Times are shown in minutes and seconds relative to anaphase onset, and the scale bar is 10 μm. The relative intensity of mNeonGreen is shown in the corresponding scale. **B-C)** A representative image shows endogenous mNeonGreen-RhoA localization in interphase cells (B) and in a metaphase cell (C). **D-E)** Images show endogenous mNeonGreen-RhoA (green; left) localization in interphase cells (D) and a mitotic cell (E) transiently expressing the C-terminus of Ect2 tagged with mScarlet-I 24 hours after transfection (magenta; right). The scale bars for the field-of view images are 20 μm, and 10 μm for the metaphase cells.

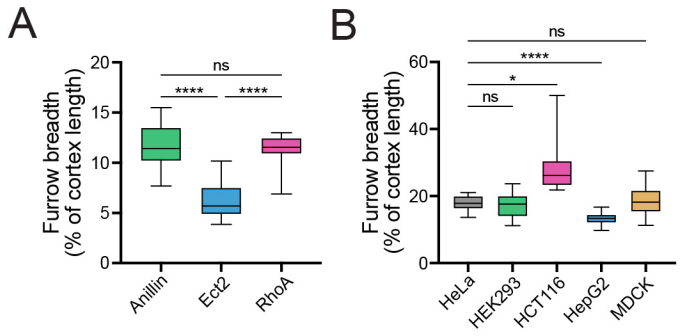

Figure S2.4. The breadth of anillin, Ect2 and RhoA is independent of cell size. A) A box plot shows the breadth of mNeonGreen-anillin (n=16), -Ect2 (n=10) and -RhoA (n=10) in HeLa cells as a proportion of cortical length. **B)** A box plot shows the breadth of mNeonGreen-anillin in HeLa (n=16), HEK293 (n=9), HCT116 (n=11), HepG2 (n=13) and MDCK (n=10) cells as a proportion of cortical length. Box plots show the median line, quartile box edges and minimum and maximum whiskers. Statistical significance was determined by one-way ANOVA (ns, not significant; * $p \leq 0.05$; ** $p \leq 0.01$; *** $p \leq 0.001$; **** $p \leq 0.0001$).

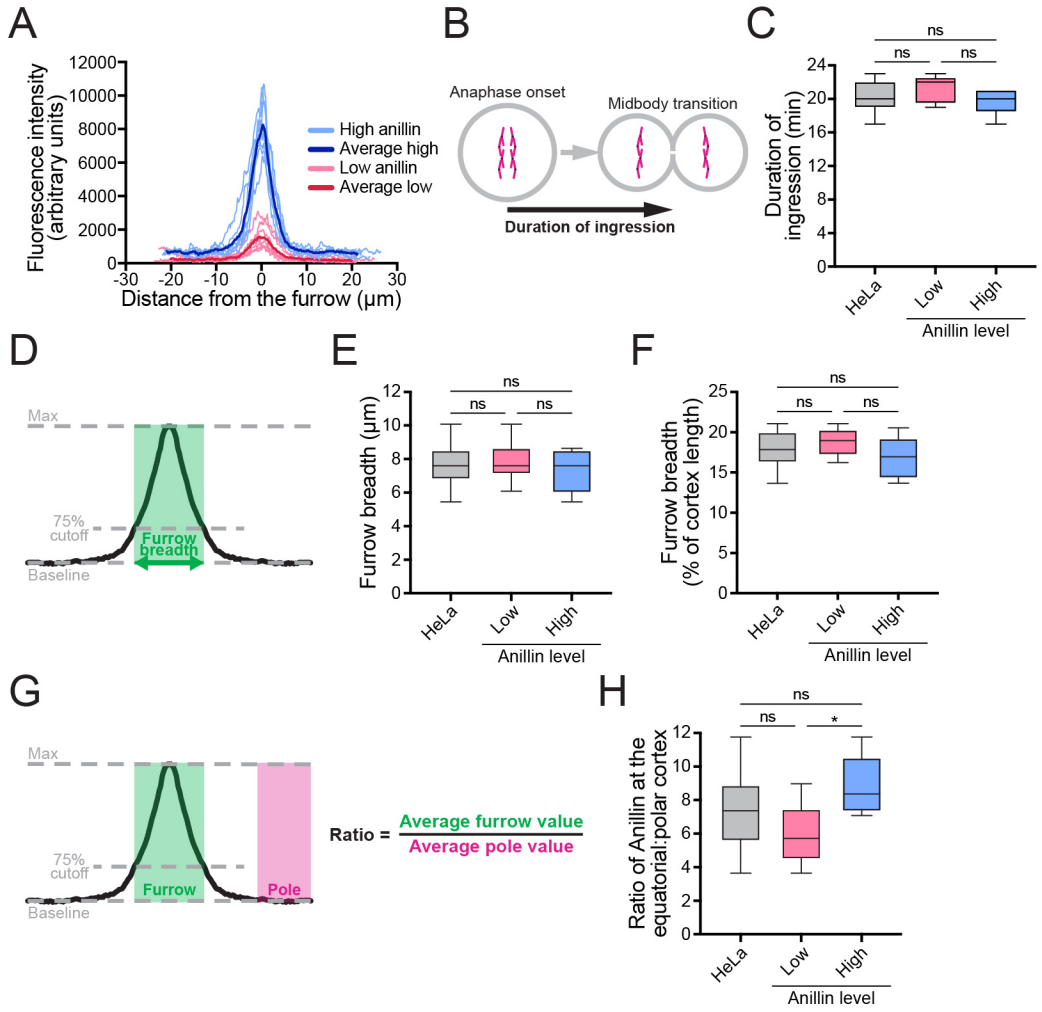

Figures S2.5. The breadth of anillin localization correlates with the duration of ring closure in HeLa cells. A) A graph shows the fluorescence intensity from linescans of mNeonGreen-anillin along the cortex of 'high' (blue, n=8) and 'low' (red, n=8) expressing HeLa cells. Individual cells are shown in light colors and the average for each population is shown in dark colors. **B)** A schematic shows how the duration of ingression was measured for C. **C)** A box plot shows the duration of ingression in high- (n=6) and low- (n=5) expressing mNeonGreen-anillin HeLa cells compared to combined populations. **D)** A schematic shows how the breadth at the equatorial cortex was calculated for E and F. **E)** A box plot shows the breadth of mNeonGreen-anillin in high- (n=8) and low- (n=8) expressing HeLa cells compared to combined populations. **F)** A box plot shows the breadth of mNeonGreen-anillin as a proportion of cortical length in high- (n=8) and low- (n=8) expressing HeLa cells compared to combined populations. **G)** A schematic shows how the ratio of protein in the furrow relative to the polar cortex was calculated for H. **H)** A box plot shows the ratio of mNeonGreen-anillin in the furrow relative to the polar cortex in high- (n=8) and low- (n=8) expressing HeLa cells compared to combined populations. Box plots in C, E, F and H show the median line, quartile box edges and minimum and maximum whiskers. Statistical significance was determined by one-way ANOVA (ns, not significant; * $p \leq 0.05$; ** $p \leq 0.01$; *** $p \leq 0.001$; **** $p \leq 0.0001$).

Table S2.1. List of sgRNAs used in this study. The sequence of the sgRNAs tested for each target locus are listed, as well as their position relative to the site of integration. The oligos used to clone each sgRNA into the CRISPR plasmid (pX459V2.0-HypaCas9) are also shown. The preferred sgRNA for each site is highlighted in green.

Gene/locus	sgRNA	Location	sgRNA sequence / PAM	Forward oligo	Reverse oligo	Orientation relative to gene	Distance relative to target site (bp)	Source
ANLN	1	N-terminus	TGGGGCGATGGATCCGTTTA/CGG	CACCGTGGGGCGATGGATCCGTTTA	AAACTAAACGGATCCATCGCCCCAC	Forward	+7	This study
ANLN	2	N-terminus	GTCTCGTAGTCCGACGCCTG/GGG	CACCGGTCTCGTAGTCCGACGCCTG	AAACCAGGCGTCGGACTACGAGACC	Forward	-11	This study
ANLN	3	N-terminus	GGACTACGAGACGATGGAAA/CGG	CACCGGGACTACGAGACGATGGAAA	AAACTTTCCATCGTCTCGTAGTCCC	Reverse	-33	This study
ANLN	4	C-terminus	CATGGAAATTTCCCGGTTTA/AGG	CACCGCATGGAAATTTCCCGGTTTA	AAACTAAACCGGGAAATTTCCATGC	Reverse	+3	This study
ANLN	5	C-terminus	TCAAAAACCTCTAGATAGCA/TGG	CACCGTCAAAAACCTCTAGATAGCA	AAACTGCTATCTAGAGGTTTTTGAC	Reverse	+21	This study
ANLN	6	C-terminus	GATGCTTGCTACAAACCTAT/TGG	CACCGGATGCTTGCTACAAACCTAT	AAACATAGGTTTGTAGCAAGCATCC	Forward	-13	This study
cfANLN	1	N-terminus	GGCGATGGACCCGTTTACCG/AGG	CACCGGGCGATGGACCCGTTTACCG	AAACCGGTAAACGGGTCCATCGCCC	Forward	+10	This study
cfANLN	2	N-terminus	GGTAAACGGGTCCATCGCCC/CGG	CACCGGGTAAACGGGTCCATCGCCC	AAACGGGCGATGGACCCGTTTACCC	Reverse	+8	This study
cfANLN	3	N-terminus	GCTTTCTCACCTCGGTAAAC/GGG	CACCGGCTTTCTCACCTCGGTAAAC	AAACGTTTACCGAGGTGAGAAAGCC	Reverse	-5	This study
cfANLN	4	C-terminus	TATTGGGAAGCCTTAAACTG/TGG	CACCGTATTGGGAAGCCTTAAACTG	AAACCAGTTTAAGGCTTCCCAATAC	Forward	+4	This study
cfANLN	5	C-terminus	CTTAAACTGTGGAAGTTTCC/AGG	CACCGCTTAAACTGTGGAAGTTTCC	AAACGGAAACTTCCACAGTTTAAGC	Forward	+15	This study
cfANLN	6	C-terminus	GATGCTTGCTACAAACCTAT/TGG	CACCGGATGCTTGCTACAAACCTAT	AAACATAGGTTTGTAGCAAGCATCC	Forward	-13	This study
cfANLN	7	C-terminus	ACAGTTTAAGGCTTCCCAAT/AGG	CACCGACAGTTTAAGGCTTCCCAAT	AAACATTGGGAAGCCTTAAACTGTC	Reverse	-9	This study
ECT2	1	N-terminus	AGTGTATTAACATCCACTAC/TGG	CACCGAGTGTATTAACATCCACTAC	AAACGTAGTGGATGTTAATACACTC	Forward	+26	This study
ECT2	2	N-terminus	CAAGCTAGTCCTCCCAGTAG/TGG	CACCGCAAGCTAGTCCTCCCAGTAG	AAACCTACTGGGAGGACTAGCTTGC	Reverse	+28	This study
ECT2	3	N-terminus	TATTAACATCCACTACTGGG/AGG	CACCGTATTAACATCCACTACTGGG	AAACCCCAGTAGTGGATGTTAATAC	Forward	+30	This study
ECT2	4	C-terminus	GCCTTCCTTCCTTCTTTGAA/AGG	CACCGGCCTTCCTTCCTTCTTTGAA	AAACTTCAAAGAAGGAAGGAAGGCC	Forward	-45	This study
ECT2	5	C-terminus	CAGTTTCTTATTTGAGTATG/AGG	CACCGCAGTTTCTTATTTGAGTATG	AAACCATACTCAAATAAGAAACTGC	Reverse	+48	This study
ECT2	6	C-terminus	CTTCTCCTTTCAAAGAAGGA/AGG	CACCGCTTCTCCTTTCAAAGAAGGA	AAACTCCTTCTTTGAAAGGAGAAGC	Reverse	-51	This study
ECT2	7	C-terminus	ATTTCTATAATTTAAGATTT/TGG	CACCGATTTCTATAATTTAAGATTT	AAACAAATCTTAAATTATAGAAATC	Reverse	-64	This study
ECT2	8	C-terminus	AGAAGGAAGGAAGGCTGACA/AGG	CACCGAGAAGGAAGGAAGGCTGACA	AAACTGTCAGCCTTCCTTCCTTCTC	Reverse	+16	This study
RHOA	1	N-terminus	AATCACCAGTTTCTTCCGGA/TGG	CACCGAATCACCAGTTTCTTCCGGA	AAACTCCGGAAGAAACTGGTGATTC	Reverse	+10	This study
RHOA	2	N-terminus	GGCTGCCATCCGGAAGAAAC/TGG	CACCGGGCTGCCATCCGGAAGAAAC	AAACGTTTCTTCCGGATGGCAGCCC	Forward	+16	This study
RHOA	3	N-terminus	TTTCAGCAATGGCTGCCATC/CGG	CACCGTTTCAGCAATGGCTGCCATC	AAACGATGGCAGCCATTGCTGAAAC	Forward	+6	This study
H2BC11	1	C-terminus	ACTCACTGTTTACTTAGCGC/TGG	CACCGACTCACTGTTTACTTAGCGC	AAACGCGCTAAGTAAACAGTGAGTC	Reverse	-5	Allen Institute for Cell Science
ACTB	1	N-terminus	GCCGTTGTCGACGACGAGCG/CGG	CACCGGCCGTTGTCGACGACGAGCG	AAACCGCTCGTCGTCGACAACGGCC	Reverse	+19	Allen Institute for Cell Science
MYH10	1	N-terminus	GTTCTCTGCGCCATTGTAAA/TGG	CACCGGTTCTCTGCGCCATTGTAAA	AAACTTTACAATGGCGCAGAGAACC	Reverse	-6	Allen Institute for Cell Science
MYH10	2	N-terminus	TTTACAATGGCGCAGAGAAC/TGG	CACCGTTTACAATGGCGCAGAGAAC	AAACGTTCTCTGCGCCATTGTAAAC	Forward	+8	Roberts et al., 2017
MYH10	3	N-terminus	TTGGATCGTTCCATTTACAA/TGG	CACCGTTGGATCGTTCCATTTACAA	AAACTTGTAAATGGAACGATCCAAC	Forward	-5	This study
MYH10	4	N-terminus	GGCGCAGAGAACTGGACTCG/AGG	CACCGGGCGCAGAGAACTGGACTCG	AAACCGAGTCCAGTTCTCTGCGCCC	Forward	+16	Roberts et al., 2017
TUBA1B	1	N-terminus	GATGCACTCACGCTGCGGGA/AGG	CACCGGATGCACTCACGCTGCGGGA	AAACTCCCGCAGCGTGAGTGCATCC	Reverse	-8	Allen Institute for Cell Science
AAVS1	1	-	GGGGCCACTAGGGACAGGAT/TGG	CACCGGGGGCCACTAGGGACAGGAT	AAACATCCTGTCCCTAGTGGCCCCC	Forward	+11	Oceguera-Yanez et al., 2016
AAVS1	2	-	CTAGTGGCCCCACTGTGGGG/TGG	CACCGCTAGTGGCCCCACTGTGGGG	AAACCCCCACAGTGGGGCCACTAGC	Reverse	-12	This study
AAVS1	3	-	TGTCCCTAGTGGCCCCACTG/TGG	CACCGTGTCCCTAGTGGCCCCACTG	AAACCAGTGGGGCCACTAGGGACAC	Reverse	-7	This study

Table S2.2. List of primers used for repair template cloning. The primers used to amplify the homology arms and the fluorescent markers to clone each repair template are shown. The different parts of the primer sequences are shown in different colors (annealing region in green, tail in red, protein linker in dark blue and point mutations to abolish Cas9 cutting in light blue).

Construct	Terminus	Part	Orientation	Sequence (annealing region / tail / protein linker / point mutations)
pODN-mNG-ANLN	N-	Left HA	Forward	ACAAAGCTACTGAAGGCCAACG
pODN-mNG-ANLN	N-	Left HA	Reverse	CGCCCCTGCCGTCGGACTACGAGACGATGCAATCGGTGGTTCAAATTCAGGAAGAGA
pODN-mNG-ANLN	N-	mNeonGreen	Forward	CCGACGGCAGGGGCGATGGTGAGCAAGGGCGAG
pODN-mNG-ANLN	N-	mNeonGreen	Reverse	ACTCACCTCCGTAAACGGATCCATGGAGCCTCCTGAACCTCCCTTGTACAGCTCGTCCATGCC
pODN-mNG-ANLN	N-	Right HA	Forward	ATGGATCCGTTTACGGAGGTGA
pODN-mNG-ANLN	N-	Right HA	Reverse	ACATCTCCCCGAAAGAATTACCAC
pODN-ANLN-mNG	C-	Left HA	Forward	AGCACAGTTTCCAGTACATGGAATG
pODN-ANLN-mNG	C-	Left HA	Reverse	AGGCTTTCCAATTGGCTTGTAGCAAGCATCAGGTTGCC
pODN-ANLN-mNG	C-	mNeonGreen	Forward	TTGCTACAAGCCAATTGGAAAGCCTGGAGGTTCAGGAGGCAGCATGGTGAGCAAGGGCGAG
pODN-ANLN-mNG	C-	mNeonGreen	Reverse	CCTCTAGATAGCCTTGAAATTTCCCAGCTTACTTGTACAGCTCGTCCATGC
pODN-ANLN-mNG	C-	Right HA	Forward	TAAGCTGGGAAATTTCAAGGCTATCTAGAGGTTTTTGATGTCATCTTAAGA
pODN-ANLN-mNG	C-	Right HA	Reverse	GGCGTTTAAAGGTGATAGGTGACTT
pODN-mNG-ECT2	N-	Left HA	Forward	TCTAGCTTTTAAACTCTTCTTAAGTCCTGG
pODN-mNG-ECT2	N-	Left HA	Reverse	CATGATTTGTATTCTTCTAAATCAGCTGAAAAAATAAA
pODN-mNG-ECT2	N-	mNeonGreen	Forward	TTTTTATTCAAATTTATTTTTTCAGCTGATTTAGAAGAATACAAATCATGGTGAGCAAGGGCGAG
pODN-mNG-ECT2	N-	mNeonGreen	Reverse	TCGTAGAAGTTAGTACTGAATTCTCTGCCATGGAGCCTCCTGAACCTCCCTTGTACAGCTCGTCCATGCC
pODN-mNG-ECT2	N-	Right HA	Forward	CCATGGCAGAGAATTCAGTACTAACTTCTACGACGGGAAGGACTAGCTTGGCAGACTCTT
pODN-mNG-ECT2	N-	Right HA	Reverse	AGGACAACTTTCTTTTATCTTTATAACAGGGAC
pODN-ECT2-mNG	C-	Left HA	Forward	TAAATGCTTCATTTTACAACCTTGTTGATGAG
pODN-mNG-ECT2	C-	Left HA	Reverse	AATCAAGTGAGTAGTAGACCGACTAAGCGTGTGACTCCGCCTCTCGAAAAAGCTAGGAAGGCTGACAAGGGAGG
pODN-mNG-ECT2	C-	mNeonGreen	Forward	ACGCTTAGTCGGTCTACTACTCACTTGATTGGAGGTTCAGGAGGCAGCATGGTGAGCAAGGGCGAG
pODN-mNG-ECT2	C-	mNeonGreen	Reverse	GACGTGTGTATATATTTGTATAGTTTGAGATATTAGTACCGATTCACTTGTACAGCTCGTCCATGCC
pODN-mNG-ECT2	C-	Right HA	Forward	TGAATCGGTACTAATATCTCAAACTATACAAATATATACACACGTCTTACTCAAATAAGAAACTGACTTAAATGGTACTTG
pODN-mNG-ECT2	C-	Right HA	Reverse	CTGACTATAAAAAGGCTATTGTGAAAGATATCACA
pODN-mNG-RHOA	N-	Left HA	Forward	TACCCTGCTTGACAAATTGTTTCCT
pODN-mNG-RHOA	N-	Left HA	Reverse	TGCTGAAACACAAAACACAGATATTACC
pODN-mNG-RHOA	N-	mNeonGreen	Forward	GCAGGTAATATCTGTGTTTTGTGTTTCAGCAATGGTGAGCAAGGGCGAG
pODN-mNG-RHOA	N-	mNeonGreen	Reverse	ACCAGTTTTTTGCGAATAGCTGCCATGGAGCCTCCTGAACCTCCCTTGTACAGCTCGTCCATGCC
pODN-mNG-RHOA	N-	Right HA	Forward	ATGGCAGCTATTCGCAAAAAACTGGTGATTGTTGGTGATGGA
pODN-mNG-RHOA	N-	Right HA	Reverse	GCCTGTAATCCCAGCTACTCTACT
pODN-mNG-cfANLN	N-	Left HA	Forward	TTTCAGCCCAACACGTCCAC
pODN-mNG-cfANLN	N-	Left HA	Reverse	CTCGACTGCGCGACGAC
pODN-mNG-cfANLN	N-	mNeonGreen	Forward	CGTCGTCGCGCAGTCGAGCCGCGGAGTCCGGGGCGATGGTGAGCAAGGGCGAG
pODN-mNG-cfANLN	N-	mNeonGreen	Reverse	GCTTTCTCACCTCGGTAAATGGATCCATGCTGCCTCCTGAACCTCCCTTGTACAGCTCGTCCATGCC
pODN-mNG-cfANLN	N-	Right HA	Forward	ATGGATCCATTTACCGAGGTGAGAAAGCCTG
pODN-mNG-cfANLN	N-	Right HA	Reverse	GTATGTTCTCAACAAGACTGGCCA
pODN-H2BC11-FP	C-	Left HA	Forward	CTTTGCCCAGCAGCTTGTTG
pODN-H2BC11-FP	C-	Left HA	Reverse	GGTGGCCACAGGAGGGT
pODN-H2BC11-FP	C-	Right HA	Forward	TAAACAGTGAGTTGGTTGCAAACTCT
pODN-H2BC11-FP	C-	Right HA	Reverse	CCTTTGCTTATATAGATATACCATAAAGGGAAAATAGT
pODN-H2BC11-mR2	C-	mRuby2	Forward	GGACCCTCCTGTGGCCACCATGGTGTCTAAGGGCGAAGAG
pODN-H2BC11-mR2	C-	mRuby2	Reverse	GATTGAGAGTTTGCAACCAACTCACTGTTTACTTGTACAGCTCGTCCATCCC
pODN-H2BC11-TagBFP	C-	TagBFP	Forward	GGACCCTCCTGTGGCCACCATGAGCGAACTGATCAAAGAGAACAT
pODN-H2BC11-TagBFP	C-	TagBFP	Reverse	GATTGAGAGTTTGCAACCAACTCACTGTTTAATTCAGTTTATGACCCAGCTTGCT
pODN-mR2-ACTB	N-	Left HA	Forward	GCTCGAGCGGCCGC
pODN-mR2-ACTB	N-	Left HA	Reverse	CATGGTGAGCTGCGAGAATAGCCGGGC
pODN-mR2-ACTB	N-	mRuby2	Forward	GGCTATTCTCGCAGCTCACCATGGTGTCTAAGGGCGAAGAG
pODN-mR2-ACTB	N-	mRuby2	Reverse	CATGGTACCGGAGCCGGCCTTGTACAGCTCGTCCATCCC
pODN-mR2-ACTB	N-	Right HA	Forward	GCCGGCTCCGGTACCATGGATGACGACATTGCAGCGCTCGTCGTCGACA
pODN-mR2-ACTB	N-	Right HA	Reverse	TACAGGGATAGCACAGCCTGG
pODN-mR2-MYH10	N-	Left HA	Forward	AAGTGATGGAGCTTCCTCTGCT
pODN-mR2-MYH10	N-	Left HA	Reverse	CATTGTAAATGGAACGATCCAAAAGCA
pODN-mR2-MYH10	N-	mRuby2	Forward	GCAATTGCTTTTGGATCGTTCCATTTACAATGGTGTCTAAGGGCGAAGAG
pODN-mR2-MYH10	N-	mRuby2	Reverse	CATAGGGATCCGCAGCTTCAGCTCCAGATCGCTGTACTTGTACAGCTCGTCCATCCC
pODN-mR2-MYH10	N-	Right HA	Forward	AGCTGAAGCTGCGGATCCCTATGGCACAAAGGACAGGGCTGG
pODN-mR2-MYH10	N-	Right HA	Reverse	TTAGTATCTGGCTTACATTTTTCCTCTCTACA
pODN-AAVS1-EGFP	-	Left HA	Forward	CTCAGTCTGGTCTATCTGCCTGG
pODN-AAVS1-EGFP	-	Left HA	Reverse	GGCCCCACTGTGTGGTCGAGGGGACAGATAAAAGTACCCAGA
pODN-AAVS1-EGFP	-	CMV-EGFP	Forward	CTCGACCACACAGTGGGGCCTAGTAATCAATTACGGGGTCATTAGTTCATAG
pODN-AAVS1-EGFP	-	CMV-EGFP	Reverse	GCTTTCTGTCACTAAGCCTGTCCCTAGTAAAATTTAACGCGAATTTTAACAAAATATTAACGC
pODN-AAVS1-EGFP	-	Right HA	Forward	ACTAGGGACAGGCTTAGTGACAGAAAAGCCCCATCCT
pODN-AAVS1-EGFP	-	Right HA	Reverse	CCCCACAGTTGGAGGAGAATC
pODN-AAVS1-mNG	-	mNeonGreen	Forward	TGACTGACACCGGTCGCCACCATGGTGAGCAAGGGCGAG
pODN-AAVS1-mNG	-	mNeonGreen	Reverse	GCATGCATCGTACGTTACTTGTACAGCTCGTCCATGC
pODN-AAVS1-mNG-CAAX	-	mNeonGreen-CAAX	Forward	CGAATTCAAAGATGAGCAAAGATGGTAAAAAGAAGAAAAAGAAGTCAAAGACAAAGTGTGTAATTATGTAAAGCGGCCGCGACTC
pODN-AAVS1-mNG-CAAX	-	mNeonGreen-CAAX	Reverse	TCTTCTTTTTACCATCTTTGCTCATCTTTGAATTCGAAGCTTGAGCTCGAGATCTGAGTCCGGACTTGTACAGCTCGTCCATGCC
pODN-AAVS1-mR2	-	mRuby2	Forward	TGACTGACACCGGTCGCCACCATGGTGTCTAAGGGCGAAGAG
pODN-AAVS1-mR2	-	mRuby2	Reverse	GCATGCATCGTACGTTACTTGTACAGCTCGTCCATCCC
pODN-AAVS1-mR2-CAAX	-	mRuby2-CAAX	Forward	CGAATTCAAAGATGAGCAAAGATGGTAAAAAGAAGAAAAAGAAGTCAAAGACAAAGTGTGTAATTATGTAAAGCGGCCGCGACTC
pODN-AAVS1-mR2-CAAX	-	mRuby2-CAAX	Reverse	TCTTCTTTTTACCATCTTTGCTCATCTTTGAATTCGAAGCTTGAGCTCGAGATCTGAGTCCGGACTTGTACAGCTCGTCCATCCC

Table S2.3. List of primers used for genotyping. The primers used to amplify each target locus for genotyping by PCR are shown.

Gene/locus	Orientation	Sequence
ANLN	Forward	GCCGAGTCCGTCACTGG
ANLN	Reverse	TTCCTCCCTGAGTTTTATCTGTAGGAC
CfANLN	Forward	GGAGCAGTTTGGGAGCGTC
CfANLN	Reverse	ACACCCGCTGCGCAC
ECT2	Forward	GAAATTGGTTGAGGGCAAAGGTG
ECT2	Reverse	GCCTCCCTTTTCAAAGCTGC
RHOA	Forward	ATTCTTGTCTTGTTCCTGATCTTAGGG
RHOA	Reverse	ATTCTAACATGGAAAATGGCATCAGTTG
H2BC11	Forward	TGGGCATCATGAATTCGTTTGTGA
H2BC11	Reverse	TACTTCAGACCAAAAAACACAGTAGCA
ACTB	Forward	TAATAACGCGGCCGGCC
ACTB	Reverse	GAAGGAAAGGACAAGAAGCCCTG
MYH10	Forward	TGAGGGCAAACCCATCAGAC
MYH10	Reverse	TTTGATACTAGCTGCCTCAAAACCAT
TUBA1B	Forward	TGCAGTGAGCCTAGATGGCA
TUBA1B	Reverse	GAAGGTGTTGAAGGAGTCATCTCC
AAVS1	Forward	GTCCACTTCAGGACAGCATGTT
AAVS1	Reverse	CATCGTAAGCAAACCTTAGAGGTTCT
mNeonGreen	Forward	CCAAGACCGAGCTCAACTTCA
mNeonGreen	Reverse	GTCACCCTTGGTGGACTTCAG
mRuby2	Forward	TCGTAGTACAACGCGAACACG
mRuby2	Reverse	ATGGTTTGAGTTCCCATGTACGG
mTagBFP	Forward	GACAACCACCACTTTAAGTGCAC
mTagBFP	Reverse	CTCATTATTCGCTTCTTTAATGCGTTCC

Table S2.4. List of cell lines generated in this study. The characteristics of the different engineered cell lines generated and used in this study are shown.

Parental cell line	Modified locus	Fluorescent tag	Zygosity
HEK293	ANLN	mNeonGreen	Homozygous
HEK293	ECT2	mNeonGreen	Homozygous
HEK293	RHOA	mNeonGreen	Heterozygous
HeLa	ANLN	mNeonGreen	Homozygous
HeLa	ECT2	mNeonGreen	Homozygous
HeLa	RHOA	mNeonGreen	Heterozygous
HCT116	ANLN	mNeonGreen	Heterozygous
HepG2	ANLN	mNeonGreen	Heterozygous
MDCK	ANLN	mNeonGreen	Homozygous
HEK293	H2BC11	TagBFP	Homozygous
HEK293	H2BC11 ANLN	TagBFP mNeonGreen	Heterozygous Homozygous
HEK293	H2BC11 AAVS1	TagBFP mRuby2-CAAX	Heterozygous Heterozygous
HEK293	H2BC11 ANLN AAVS1	TagBFP mNeonGreen mRuby2-CAAX	Heterozygous Homozygous Heterozygous
HEK293	H2BC11 ANLN ACTB	TagBFP mNeonGreen mRuby2	Heterozygous Homozygous Heterozygous

CHAPTER 3

Endogenous tagging using split mNeonGreen in human iPSCs for live imaging studies

Preprint manuscript (submitted for publication): Husser, M. C., Pham, N. P., Law, C., Araujo, F. R. B., Martin, V. J. J., & Piekny, A. (2023). Endogenous tagging using split mNeonGreen in human iPSCs for live imaging studies. *bioRxiv*, 2023-06.

3.1 Preamble

Endogenous tagging is a powerful tool that facilitates the study of protein in live cells. However, the generation of cell lines that carry endogenous tags is slow and time-consuming. Moreover, most studies still use cancerous or transformed cell lines, as stem cells are more difficult to culture and to edit. In this chapter, I aimed to facilitate endogenous tagging in human iPSCs to enable more studies of cellular processes in these cells. For this, I engineered an iPS cell line that expresses the large $mNG2_{1-10}$ fragment of the split mNeonGreen protein, which allows for endogenous tagging with the short $mNG2_{11}$ fragment. This work provides a basis for the generation of a genome-scale endogenous tag library in human stem cells, which will be useful to study a large variety of cellular processes.

3.2 Abstract

Endogenous tags have become invaluable tools to visualize and study native proteins in live cells. However, generating human cell lines carrying endogenous tags is difficult due to the low efficiency of homology-directed repair. Recently, an engineered split mNeonGreen protein

was used to generate a large-scale endogenous tag library in HEK293 cells. Using split mNeonGreen for large-scale endogenous tagging in human iPSCs would open the door to studying protein function in healthy cells and across differentiated cell types. We engineered an iPS cell line to express the large fragment of the split mNeonGreen protein ($mNG2_{1-10}$) and showed that it enables fast and efficient endogenous tagging of proteins with the short fragment ($mNG2_{11}$). We also demonstrate that neural network-based image restoration enables live imaging studies of highly dynamic cellular processes such as cytokinesis in iPSCs. This work represents the first step towards a genome-wide endogenous tag library in human stem cells.

3.3 Introduction

Since GFP was first described as a fluorescent reporter (Chalfie et al., 1994), the use of fluorescent proteins has become a standard method to study the localization and function of proteins inside living cells. Generally, reporter protein fusions are transiently or stably expressed from exogenous plasmids carrying their own promoter. However, expression levels can be quite high and variable from these strong, non-specific promoters (Husser et al., 2022). Further, over-expression can induce artifacts of localization and protein-protein interactions, making data challenging to interpret (Gibson et al., 2013; Mahen et al., 2014). With the advent of gene editing tools such as CRISPR/Cas9, the genes encoding fluorescent proteins can now be inserted directly into the genome at a desired locus (Bukhari & Muller, 2019; Husser et al., 2021). CRISPR/Cas9 is used to introduce a double-stranded break at the target site, which can be repaired by homology directed repair (HDR) using a repair template carrying the fluorescent marker (Verma et al., 2017). With this approach, the protein of interest is still expressed from its endogenous promoter, fused with the fluorescent protein. This enables the study of proteins at endogenous expression levels

and provides more reliable measurements of protein behavior (Dambournet et al., 2018; Doyon et al., 2011; Husser et al., 2022; Mahen et al., 2014). Endogenous tagging is commonly done in model organisms such as *Saccharomyces cerevisiae*, for which whole-genome libraries of endogenous tags have been generated (Huh et al., 2003). However, gene editing in human cells is less widely used due to limitations in efficiency caused by transfection and HDR, among other issues. Because of these bottlenecks, the majority of human proteins have not been tagged and studied at the endogenous level. Although several efforts have been made to tag multiple proteins endogenously in various human cell lines (*e.g.* Husser et al., 2022; Roberts et al., 2017), the generation of a genome-wide library of tagged proteins in human cells requires higher throughput.

The recently developed self-complementing split fluorescent proteins can be used as tools for large-scale endogenous tagging (Feng et al., 2017; Feng et al., 2019; Kamiyama et al., 2016; Tamura et al., 2021; Zhou et al., 2020). In the split mNeonGreen system, the mNeonGreen protein is expressed as two separate fragments: a large fragment composed of the first ten beta-strands of mNeonGreen ($mNG2_{1-10}$) and a short fragment corresponding to the eleventh beta strand (mNG211; Feng et al., 2017). The two fragments have been engineered to interact and form a functional fluorescent protein when co-expressed (Feng et al., 2017). This system allows for easy and efficient endogenous tagging with $mNG2_{11}$ in cells where $mNG2_{1-10}$ is constitutively expressed (Cho et al., 2022; Leonetti et al., 2016; Mahdessian et al., 2021). The $mNG2_{11}$ fragment is only 16 amino acids long, so it can be inserted into the genome by HDR using a repair template with short homology arms (generally 40-80 bp), which can be purchased commercially as a single-stranded oligo-deoxynucleotide (ssODN). This enables large-scale tagging using commercially synthesized ssODNs and sgRNAs to target multiple proteins in parallel (Cho et al., 2022; Leonetti et al., 2016). However, this approach requires the generation of a parental cell line that

constitutively expresses the mNG2$_{1-10}$ fragment. This has been done by random lentiviral integration followed by antibiotic selection, which is fast but generates a heterogeneous population where the expression of the large fragment is inconsistent across the cell population and is subject to epigenetic silencing (Cabrera et al., 2022). Large-scale endogenous tagging in HEK293 cells was recently achieved by the OpenCell project, with 1,310 proteins tagged to date (Cho et al., 2022). However, while this library will be a valuable resource for the community, there is a need to study protein function in other cell types, where the mechanisms regulating biological processes could vary drastically.

Since their discovery in 2007, human induced pluripotent stem cells (iPSCs) have become a popular tool to study human cells in developmental contexts and to identify disease-causing mutations, amongst other valuable applications (Shi et al., 2017; Takahashi et al., 2007). iPSCs are derived from somatic cells that are reprogrammed to be self-renewing and pluripotent. These cells can be cultured and differentiated into any desired cell type *in vitro* using specific protocols (*e.g.* Grancharova et al., 2021; Hong & Do, 2019; Oceguera-Yanez et al., 2022). Despite this incredible resource, few studies have investigated cellular processes in human stem cells and differentiated cell types with high spatiotemporal resolution (Dambournet et al., 2018; Viana et al., 2023). For example, several studies describe the regulation of mitosis and cytokinesis in mouse embryos and embryonic stem cells (Chaigne et al., 2020; Chaigne et al., 2021; Paim & FitzHarris, 2022), but not in human stem cells. Since most of our knowledge of human cell cytokinesis is derived from diseased and/or transformed cell lines, the field will benefit greatly from studying iPSCs before and after differentiation in an isogenic context, particularly since they represent 'healthy' human cells (Dambournet et al., 2018; Drubin & Hyman, 2017).

Here, we used the split mNeonGreen system for endogenous tagging in human iPSCs (Fig. 3.1A). First, we engineered a human iPS cell line that constitutively expresses the $mNG2_{1-10}$ fragment. We validated this cell line extensively, and named it "smNG2-P" (split mNeonGreen2 parental cell line). As a proof-of-concept, we efficiently targeted multiple genes for endogenous tagging with $mNG2_{11}$, and clonally isolated several tagged iPS cell lines. To facilitate this process, we developed protocols for efficient single-cell isolation by FACS and screening of edited clones by Nanopore sequencing. Finally, we show how the endogenously tagged iPS cell lines can be used for live imaging studies of cytokinesis, which is a highly dynamic cellular process. Timelapse imaging of endogenous tags in iPSCs required the use of an image restoration algorithm to alleviate cell toxicity and obtain high quality images with high temporal resolution. This work provides the foundation for a genome-wide endogenous tag library in human stem cells and provides protocols to efficiently generate and study endogenous tags in human iPSCs.

3.4 Materials and Methods

3.4.1 Cell culture

201B7 iPSCs were obtained from ATCC. Cells were cultured in 6-well plates coated with iMatrix-511 Silk (Nippi) as per manufacturer's protocol, in mTeSR Plus media (STEMCELL Technologies). The cells were kept at 37°C and 5% CO_2. The cells were passaged every 3-4 days by dissociating them using Accutase (STEMCELL Technologies) according to manufacturer's protocol. After dissociation, the cells were resuspended and 50,000-100,000 cells were transferred into fresh matrix-coated plates with mTeSR Plus media containing 10 μM Y-27632 (ROCK inhibitor, STEMCELL Technologies). Fresh media without ROCK inhibitor was fed the next, and the media was replaced daily until the next passage.

3.4.2 Constructs

All plasmids were maintained and cloned in *Escherichia coli* DH5α unless specified otherwise. Point mutations were introduced into pNCS-mNeonGreen (Allele Biotechnology) by PCR-based site-directed mutagenesis to convert it to mNeonGreen2 (Feng et al., 2017). The $mNG2_{1-10}$ fragment was then amplified by PCR. The left and right homology arms for the AAVS1 locus and the puromycin gene were amplified individually from the pAAVS1-P-CAG-GFP plasmid (Addgene #80491; Oceguera-Yanez et al., 2016). These fragments were cloned into the pYTK089 backbone by Golden Gate using a standard protocol (Lee et al., 2015). Since the CAG promoter was recalcitrant to amplification by PCR, it was digested directly from pAAVS1-P-CAG-GFP using BclI and EcoRI, gel extracted, and ligated into the pre-digested promoter-less plasmid to generate the pAAVS1-P-CAG-$mNG2_{1-10}$ repair template. For BclI digestion, the plasmids were extracted from methylase-deficient *E. coli* ER2925. pH2B-$mNG2_{11}$ was generated by amplifying the H2B gene from an H2B-mRuby plasmid (Beaudet et al., 2017) with primers designed to add $mNG2_{11}$ on the end of H2B. This gene was then cloned into pEGFP-N1 digested with BamHI and NotI to replace EGFP with H2B-$mNG2_{11}$.

3.4.3 Transfection

Cells were edited using transfection. Cells were treated with the NHEJ inhibitors NU7441 (2 μM; Tocris Bioscience) and SCR7 (1 μM; Xcess Biosciences) for 4 hours before and 48 hours after nucleofection, while 10 μM ROCK inhibitor was added to the media 2 hours before nucleofection to increase recovery. For AAVS1 targeting, the pAAVS1-P-CAG-$mNG2_{1-10}$ repair template was purified prior to nucleofection using the GeneJET plasmid maxiprep kit (Thermo Fisher Scientific). Synthetic sgRNAs were purchased from MilliporeSigma and Synthego (listed

in Table S3.3) and ArciTect Cas9-eGFP and SpCas9-2NLS were purchased from STEMCELL Technologies and Synthego, respectively. sgRNA spacer sequences were obtained from previous studies (listed in Table S3.3) or designed using Benchling (Doench et al., 2016; Hsu et al., 2013). Cas9/sgRNA complexes were pre-mixed at room temperature for 15 minutes before nucleofection. ssODN repair templates were purchased from BioCorp and ThermoFisher Scientific (listed in Table S3.4). For AAVS1 targeting, 201B7 cells were transfected with 1 μg of repair template and 7.5 pmoles sgRNA pre-complexed with 7.5 pmoles Cas9. For endogenous tagging with $mNG2_{11}$, cells were transfected with 82 pmoles ssODN and 91.5 pmoles sgRNA pre-complexed with 30.5 pmoles Cas9. For transient H2B-$mNG2_{11}$ expression, cells were transfected with 750 ng of plasmid purified using the GeneJET plasmid miniprep kit (Thermo Fisher Scientific). Briefly, $5x10^5$ cells were resuspended in 20 μL P3 nucleofection buffer, mixed with the transfection reagents, and nucleofected using the DN100 program on a 4D-Nucleofector (Lonza). After nucleofection, the cells were gently resuspended in media and transferred into 6-well plates in mTeSR Plus media containing CloneR2 reagent (STEMCELL Technologies) for AAVS1 targeting, or 24-well plates containing mTeSR Plus media with 10 μM ROCK inhibitor for $mNG2_{11}$ tagging or transient protein expression.

3.4.4 Antibiotic selection

For AAVS1 integration, antibiotic selection was carried out as described in Oceguera-Yanez et al. (2016). Briefly, cells were left to recover for 3 days following transfection. On day 3, the media was changed to media with 0.5 μg/mL puromycin, which was changed every day for 10 days. Following antibiotic selection, colonies were passaged and allowed to become confluent. Edited populations were frozen and subjected to clonal isolation by FACS.

3.4.5 Fluorescence-activated cell sorting, single-cell recovery and flow cytometry

FACS was used to enrich populations of edited cells or for clonal isolation. Cells were sorted using a FACSMelody cell sorter (BD Biosciences) after recovery from antibiotic selection or 8 days after nucleofection for endogenous tagging. Briefly, cells were dissociated using Accutase, resuspended in PBS (Wisent) and then passed through a 35 μm strainer to remove large cell clumps. Cells were sorted using gates set to capture individual fluorescent cells. Individual cells or enriched populations of 500 tagged cells were sorted into individual wells of a 96-well plate containing recovery media [mTeSR Plus media with CloneR2 reagent and Pen-Strep (50 units/mL Penicillin and 50 μg/mL Streptomycin; Wisent)]. To recover clones, cells were kept in recovery media for 6 days with media changes on days 2 and 4. The media was then changed daily with mTeSR Plus until day 11. On day 11, the cells were passaged into fresh 96-well plates and grown to confluency before freezing and screening.

For flow cytometry, cells were prepared and analyzed using the same protocol, and data was analyzed using the R package CytoExploreR (Hammill, 2021).

3.4.6 Screening clones in 96-well plates

96-well plates containing single-cell clones were imaged on a Cytation 5 microscope (Agilent) 10 days after sorting. Briefly, 3 x 4 images were acquired for each well using a 4X phase contrast objective and stitched into one image per well. Laser autofocus was used to find the focal plane where colonies were expected to be found. Images were exported and analyzed using a custom ImageJ macro designed to identify wells with colonies. Briefly, the colony segmentation macro first crops out the well edge from the images, and identifies colonies by subtracting background signal, performing a Gaussian blur and thresholding high-contrast regions. Finally, it

outlines objects and overlays them with the original well image for quality control. Finally, the macro determines object number to exclude wells with debris and/or multiple colonies and provides a list of positive and negative wells.

3.4.7 Cell lysis for PCR

Cell lysates were generated for all PCR-based assays. Edited clones grown in 96-well plates were dissociated with Accutase and split into two 96-well plates for freezing and cell lysis. The cells were washed once with PBS and resuspended thoroughly in 50 µL of QuickExtract reagent (Lucigen) per well. The resuspended cells were then transferred to PCR-compatible 96-well plates and placed at 65°C for 15 minutes followed by brief vortexing, then 98°C for 15 minutes, followed by 4°C. Lysates were stored at -20°C and thawed as needed for experiments.

3.4.8 qPCR-based screening

qPCR was performed on the ViiA7 Real-Time PCR system (Applied Biosystems). The VIC-labelled RNaseP assay was purchased from ThermoFisher Scientific and used as an internal PCR control. The AmpR-specific primers and hydrolysis probe were taken from Roberts et al. (2017), and the $mNG2_{1-10}$-specific primers and hydrolysis probe were designed as follows:

Forward primer: 5'-TACCGCTACACCTACGAGGG-3'

Reverse primer: 5'- GTCATCACAGGACCGTCAGC-3'

Probe: 5'-6-FAM/AT CAA AGG A/ZEN/G AGG CCC AGG TGA TG/IABkFQ-3'

The primers and hydrolysis probes were purchased from ThermoFisher Scientific and IDT, respectively. The AmpR and $mNG2_{1-10}$ assays were prepared by mixing 18 µM of each primer with 5 µM of the hydrolysis probe. qPCR reactions consisted of 1 µL cell lysate, 0.5 µL RNaseP

assay (ThermoFisher Scientific), 0.5 µL mNG2$_{1-10}$ or AmpR assay, 5 µL QuantStudio 3D Digital PCR Master Mix V2 (ThermoFisher Scientific) and 3 µL water for a final volume of 10 µL. The qPCR thermocycling conditions were carried out as per manufacturer's instructions for the QuantStudio 3D Digital PCR Master Mix V2. The data was analyzed using the ViiA7 software and clones that were positive for mNG2$_{1-10}$ and negative for AmpR were selected for further screening by PCR as described below.

3.4.9 PCR screening and sequencing

Integration of the mNG2$_{1-10}$ cassette at the AAVS1 locus was verified by amplifying the left and right junctions of the integration, as well as the WT AAVS1 locus. Briefly, 50 µL PCR reactions were prepared as follows: 10 µL GC buffer (ThermoFisher Scientific), 1 µL 10 mM dNTP mix (ThermoFisher Scientific), 1 µL DMSO (ThermoFisher Scientific), 0.25 µL of each primer at 100 µM, 5 µL cell lysate, 0.5 µL Phusion polymerase (ThermoFisher Scientific) and 32 µL water. The primers used for each PCR reaction are listed in Table S3.5. The following touchdown cycles were then performed: 98°C for 3 minutes, followed by 40 cycles of: 98°C for 10 seconds, initial annealing at 72°C and decreasing by 1°C every cycle until down to 55°C, and 72°C for 30 seconds per kb; followed by a final extension at 72°C for 10 minutes and hold at 12°C. The PCR products were run on a 0.8% agarose gel stained with ethidium bromide and analyzed manually. The bands corresponding to the expected amplicons were gel extracted using the GeneJET gel extraction kit (Thermo Fisher Scientific) and sequenced by Sanger sequencing (Eurofins).

3.4.10 Digital PCR

Digital PCR reactions were prepared as follow: 1.5 µL cell lysate, 8.7 µL QuantStudio 3D Digital PCR Master Mix V2 (Thermo Fisher Scientific), 0.87 µL RNaseP reference assay (Thermo Fisher Scientific), 0.87 µL $mNG2_{1-10}$ or AmpR assay (prepared as described above), and 5.46 µL water. The amount of lysate was calculated based on the number of cells used and the dynamic range of the QuantStudio 3D system (400-4000 copies/µL), and input lysate volumes were adjusted as needed to obtain data within this dynamic range. 14.5 µL of the reaction mix was loaded onto dPCR chips using the QuantStudio 3D Digital PCR 20K Chip Kit V2 (Thermo Fisher Scientific), taken through PCR thermocycling and analyzed on the QuantStudio 3D system (Thermo Fisher Scientific) according to manufacturer's instructions. Data was analyzed using the QuantStudio 3D AnalysisSuite Cloud Software (Thermo Fisher Scientific).

3.4.11 Karyotyping

G-banding karyotyping was carried out and analyzed by the Banque de cellules leucémiques du Québec. 22 cells in metaphase were analyzed at a resolution of 400 bands per haploid karyotype and showed normal karyotypes (46, XX).

3.4.12 Pluripotency marker staining

Cells were fixed and stained for common pluripotency markers to verify the absence of differentiation. smNG2-P cells were dissociated with Accutase, washed once with PBS and fixed in 4% paraformaldehyde (PFA) in PBS for 30 minutes at room temperature. To stain OCT3/4 and NANOG, the cells were washed once with PBS and treated with a permeabilization/blocking solution containing 0.1% Triton X-100 (Sigma) and 5% Normal Donkey Serum (NDS; Jackson

ImmunoResearch) in PBS for 30 minutes at room temperature. To stain TRA-1-60, which is a cell surface marker, the cells were washed once and treated with a blocking solution containing 5% NDS in PBS for 30 minutes at room temperature. The following antibody dilutions were prepared in permeabilization/blocking solution or blocking solution: 1:25 anti-NANOG antibody (1 µg/mL final concentration, PCRP-NANOGP1-2D8, DSHB), 1:20 anti-OCT3/4 antibody (10 µg/mL final concentration; Santa Cruz Biotechnology), or 1:20 Alexa488-conjugated anti-TRA-1-60 antibody (7.5 µg/mL final concentration; STEMCELL Technologies). The cells were stained in 100 µL of diluted antibody per 10^6 cells overnight at 4°C. For unconjugated primary antibodies, the cells were washed with permeabilization/blocking solution and stained with a 1:400 dilution of Alexa488-conjugated anti-mouse antibody (Invitrogen) for 1h at 4°C. The cells were then washed with permeabilization/blocking solution or blocking solution and resuspended in 1 mL PBS before flow cytometry. Cells stained with only the secondary antibody were used as a negative control.

3.4.13 Trilineage differentiation and differentiation marker staining

Cells were differentiated into the three germ layers to ensure they retained pluripotent potential after editing. Directed differentiation was performed using the STEMdiff Trilineage Differentiation Kit (STEMCELL Technologies) as per manufacturer's instructions. The following modifications were made: ectoderm differentiation was carried out on 24-well plates coated with iMatrix-511 Silk by seeding the recommended number of cells (400,000) on day 0, mesoderm differentiation was carried out on 24-well plates coated with iMatrix-511 Silk by seeding 50,000 cells per well on day 0, and endoderm differentiation was carried out on 24-well plates coated with Matrigel (Corning) by seeding 20,000 cells per well on day 0. After differentiation, the cells were harvested by dissociation with Accutase, washed with PBS, fixed with PFA and stained as

described above for PAX6 (ectoderm lineage), FOXA2 (endoderm lineage) or the cell surface marker NCAM (mesoderm lineage). The following antibody dilutions were prepared in permeabilization/blocking solution or blocking solution: 1:45 anti-PAX6 antibody for ectoderm cells (1 μg/mL final concentration, PAX6, DSHB), 1:240 anti-NCAM antibody for mesoderm cells (0.25 μg/mL final concentration, 5.1H11, DSHB), 1:50 PE-conjugated anti-FOXA2 antibody (1 μg/mL final concentration; BD Biosciences) and 1:400 dilution of Alexa488-conjugated anti-mouse antibody (Invitrogen). The cells were stained in 100 μL of diluted antibody per 10^6 cells for 1 hour at 4°C. Stained undifferentiated cells and unstained cells were used as negative controls.

3.4.14 Off-target sequencing

Potential off-target sites for the AAVS1 sgRNA were selected from Wang et al. (2014), Benchling (Hsu et al., 2013) and CRISPOR (Concordet & Haeussler, 2018) based on previous studies of Cas9 or predicted off-target sites with high scores. Each off-target site was amplified as described above by touchdown Phusion PCR from 201B7 and smNG2-P cell lysates, and sequenced by Sanger sequencing (Eurofins). The primers used to amplify the 12 off-target sites were designed using Primer-BLAST (Ye et al., 2012) and are listed in Table S3.5. No mutations were found at the predicted off-target cut sites, and all 12 sites sequenced in the edited cell line matched the sequence from the WT cells.

3.4.15 Mycoplasma test

PCR-based mycoplasma detection was performed using the Mycoplasma PCR detection kit (Applied Biological Materials) according to the manufacturer's protocol. For each test, a

positive and negative control was included. The PCR products were run on a 0.8% agarose gel stained with ethidium bromide and analyzed manually.

3.4.16 Nanopore sequencing and data analysis

For Nanopore sequencing of mixed edited populations, PCR reactions were carried out as described above with a stable annealing temperature of 65°C for 30 cycles to minimize non-specific amplification and PCR bias. The samples were then gel extracted and pooled in equimolar amounts before library preparation for Nanopore sequencing.

For multiplexed clone sequencing, the edited loci from each clone were amplified individually and barcoded by PCR prior to Nanopore sequencing. For this, individual clones were subjected to a first round of PCR to amplify the target loci and add universal adapters with the primers listed in Table S3.5. The locus-specific primers were designed using Primer-BLAST (Ye et al., 2012) and the sequence of the universal adapters were taken from Karst et al. (2021). The first round of PCR was carried out as described above with annealing at 65°C and for 15 cycles. The PCR products were diluted 1/100 into the second PCR reactions, which contained a unique pair of barcoding primers for each clone for a specific target locus. The second PCR was carried out as described above with annealing at 65°C and for 15 cycles. The PCR products for a specific edited locus were pooled, run on a 0.8% agarose gel and gel extracted. The concentration of pooled products was then measured and the PCR products for clones edited at different target loci were then pooled in equal molar ratios before Nanopore library preparation.

Library preparation for Nanopore sequencing was carried out using the NEBNext Companion Module for Oxford Nanopore Technologies Ligation Sequencing (New England Biolabs), the Ligation Sequencing Kit V14 and the Flongle Sequencing Expansion (Oxford

Nanopore Technologies), as per manufacturer's protocols. The final library concentration was measured using a Qubit fluorometer (Invitrogen) using the Qubit dsDNA HS assay kit (Invitrogen), and 5 fmoles of the library were loaded onto a Flongle flow cell and sequenced overnight.

Basecalling of the Nanopore FAST5 files was performed with Guppy (R10.4.1 flow cell, 400 bps, super accuracy configuration) using the Compute Canada server, and low-quality reads with Q scores below 10 were excluded. Reads were demultiplexed using a custom Bowtie-based pipeline (https://github.com/frba/nanopore_demultiplex). When sequencing amplicons from mixed edited populations, reads were demultiplexed based on the presence of either of two gene-specific barcodes (listed in Table S3.6). The FASTQ files were analyzed using CRISPResso2 (Clement et al., 2019) to obtain the frequency of WT, HDR and indel alleles in the population. All HDR alleles were included in the same category because of the high sequencing error rate. For clone sequencing, reads were demultiplexed based on the presence of two gene-specific and two clone-specific barcodes (listed in Table S3.6). The FASTQ reads were aligned to the expected WT and edited sequences using Minimap2 (Li, 2018), and the alignments were visualized using IGV (Thorvaldsdottir et al., 2013). The genotypes of edited clones were inferred manually by looking at the alignments of sequencing reads with the WT and edited alleles for each clone.

3.4.17 Fluorescence microscopy

The fluorescence from $mNG2_{1-10}$/$mNG2_{11}$ complementation was visualized the day after transfection with the pH2B-$mNG2_{11}$ plasmid using a Cytation 5 microscope (Agilent) equipped with a 20x/0.45 NA phase contrast objective, a 465 nm LED cube and green filter cube (excitation 469/35 nm, emission 525/39 nm and dichroic mirror 497 nm).

Cells with $mNG2_{11}$ integrated at endogenous loci were imaged at least 8 days after nucleofection on a Leica DMI6000B inverted epifluorescence microscope equipped with a EL6000 mercury lamp and a GFP3035B filter cube (excitation 472/30 nm, emission 520/35 and dichroic mirror 495 nm) using a 20x/0.35 NA objective, an Orca R2 CCD camera (Hamamatsu) and Volocity software (PerkinElmer).

Because of its weak fluorescent signal, the CDH1-$mNG2_{11}$ edited cells were seeded a 35 mm polymer coverslip dish (Cellvis) coated with iMatrix-511 Silk, and imaged on an inverted Nikon Eclipse Ti microscope (Nikon) equipped with a Livescan Sweptfield scanner (Nikon), Piezo Z stage (Prior), IXON 879 EMCCD camera (Andor), and a 488 nm laser (50 mW, Agilent) using the 100x/1.45 NA objective.

For live imaging, cells were adapted to culture on Matrigel (Corning) for at least 2 passages. Cells were passaged as described above, and seeded onto 35 mm polymer coverslip dishes (Cellvis) freshly coated with Matrigel. The cells were then allowed to grow into colonies for 4 to 5 days before imaging. Fresh mTeSR Plus media was added to the cells at least 30 minutes before imaging. To visualize chromatin, Hoechst 33342 (Invitrogen) was added to the cells at a final concentration of 1.78 μM (1 μg/mL) for 30 minutes prior to imaging. Imaging was performed using the inverted Nikon Eclipse Ti microscope with the Livescan Sweptfield scanner described above, equipped with 405 and 488 nm lasers (50 mW, Agilent). The cells were kept at 37°C and 5% CO_2 during imaging in an INU-TiZ-F1 chamber (MadCityLabs). Z-stacks of 9 slices at 1 μm intervals were acquired every minute using NIS Elements software (Nikon, version 4.0). For CARE training, images were collected using low- and high-exposure setting with a 16-slice Z-stack of 0.75 μm intervals. The imaging parameters (laser power and exposure time) used for each cell line in low- and high-exposure conditions are listed in Table S3.7.

3.4.18 Image restoration by CARE

For image restoration, we used the CSBDeep neural network developed by Weigert et al. (2018). Briefly, a training dataset composed of >100 matched 2-channel fluorescent images (green for mNG and blue for Hoechst) with low- and high-exposure settings was acquired for each tagged cell line. The training datasets were designed to include cells in interphase and at different stages of mitosis. We used the Python implementation of CSBDeep to train the standard model of the neural network for each cell line individually. We then applied this model to restore timelapse Z-stack 2-channel images of the corresponding cell lines.

3.4.19 Image analysis

All images acquired using NIS Elements (Nikon) were opened in Fiji (Version 2.3, NIH) for analysis. For signal-to-noise ratio measurements, two regions of interest were drawn over an area of homogeneous signal inside a cell, and over a region of background signal (in a region with no cells). The mean pixel intensity and standard deviation (SD) were measured for both regions of interest, and the signal-to-noise ratio was calculated as follows: SNR = (mean signal - mean background) / signal SD. The measurement was repeated using the same regions of interest for matched low- and high-exposure images.

Linescans were performed and measured for tagged cell lines using a macro in Fiji modified from Ozugergin et al. (2022a). The macro was designed to isolate the 488 nm channel from the image file, subtract background signal and perform a bleach correction. The desired timepoint and two central Z slices were picked manually, and the macro generated a Z-stack average projection. A five pixel-wide line was then traced along the cortex of the cell, from one

pole to the other, along with a straight one pixel-wide line to define the midplane. The macro then measured the fluorescence intensity of each pixel along the length of the linescan and positioned the pixels in relation to the midplane. For the measurement of tubulin at the central spindle, the same macro was used to draw a five pixel-wide line across the cell equator. All data was exported for use in Excel (Microsoft) and Prism (Version 9.3, GraphPad) for further analysis.

For breadth measurements, the number of pixels above 50% of the normalized peak intensities were counted for each linescan and converted to microns. Pixels with intensities higher than the cutoff value outside of the peak region were excluded from these calculations. For measurements of the ratio of cortical to cytosolic protein in metaphase cells, the average intensity of pixels at the cortex was measured by a linescan as described above, and the average intensity of pixels in the cytosol was measured by drawing a region of interest over the cytosol.

3.4.20 Statistical analysis

Box and whiskers plots were generated using Prism (Version 9.3, GraphPad) to show median values (central line), quartiles (box edges) and minimum and maximum values (whiskers). Statistical significance was tested using a Brown-Forsythe and Welch's ANOVA, followed by multiple comparisons using Dunnett's T3 test, or by Welch's t test (Graphpad Prism version 9.3). Significance levels were defined as: $p>0.5$ non-significant (ns), * $p\leq0.05$; ** $p\leq0.01$; *** $p\leq0.001$; **** $p\leq0.0001$.

3.5 Results

3.5.1 Generation of a split mNeonGreen iPS cell line for efficient endogenous tagging

Our first goal was to generate a human iPS cell line where $mNG2_{1-10}$ is constitutively expressed. To do this, we generated a repair template that contains a $mNG2_{1-10}$ expression cassette for integration into the AAVS1 locus, based on a previously published design (Fig. 3.1B; Oceguera-Yanez et al., 2016). This cassette contains the CAG promoter to drive high levels of $mNG2_{1-10}$ expression, and resist silencing at the AAVS1 locus over time and during differentiation (Luo et al., 2014; Oceguera-Yanez et al., 2016). The cassette also includes the gene for Puromycin resistance, which is expressed upon integration at the AAVS1 locus via a splicing acceptor and self-cleaving T2A peptide (Fig. 3.1B). We introduced this $mNG2_{1-10}$ expression cassette into the 201B7 cell line, which was generated by retroviral transduction of reprogramming factors into dermal fibroblasts and is well-characterized (Takahashi et al., 2007). After transfecting 201B7 human iPSCs with the AAVS1-$mNG2_{1-10}$ repair template and an AAVS1-targeting Cas9/sgRNA RNP (ribonucleoprotein) complex, the cells were selected for Puromycin resistance and single-cell clones were isolated by FACS for screening. Clones were first screened by qPCR for the presence of the $mNG2_{1-10}$ gene and the absence of the Ampicillin resistance (AmpR) gene, which was part of the backbone of the repair template (Fig. S3.1A-D). Clones that were positive for $mNG2_{1-10}$ and negative for the AmpR gene were then screened for integration at the AAVS1 locus by junction PCR (Fig. S3.1E-H). We found 6 clones that were heterozygous for AAVS1-$mNG2_{1-10}$ integration, and one clone was selected for full validation (clone 28).

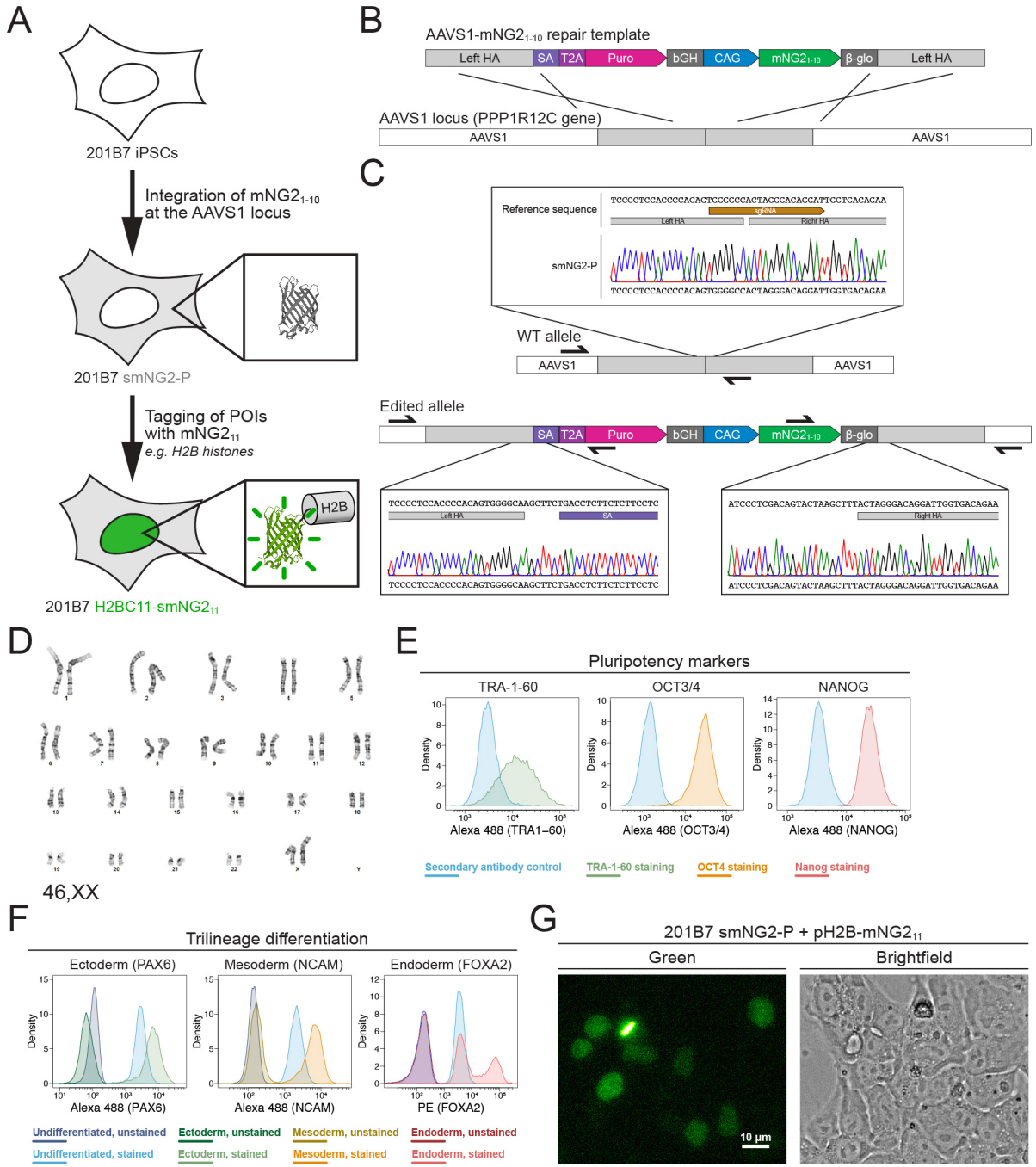

Figure 3.1. Generation of a split mNeonGreen human iPS cell line. A) A schematic representation of the split tagging strategy used in this study. An expression cassette carrying the mNG2$_{1-10}$ fragment was integrated at the AAVS1 locus in 201B7 iPSCs to generate the parental split mNeonGreen2 cell line (smNG2-P). Proteins of interest were tagged endogenously with the mNG2$_{11}$ fragment to visualize their expression and localization. The structure of mNeonGreen was generated from PDB (Protein Data Bank, structure identifier 5LTP; Clavel et al., 2016). **B)** A schematic of the mNG2$_{1-10}$ expression cassette is shown with the CAG promoter (blue) and

sequences for stable expression (dark grey), Puromycin resistance marker (pink), and homology arms (light grey) for integration at the AAVS1 locus. Abbreviations: SA = splicing acceptor, T2A = Thosea asigna virus 2A peptide, bGH = bovine growth hormone poly-adenylation signal, β-glo = rabbit β-globin poly-adenylation signal. **C)** Sequencing chromatograms show the edited AAVS1 allele junctions in the smNG2-P cell line (bottom) compared to the WT allele (top). **D)** Representative G-banding karyotype of the smNG2-P cell line shows that the edited cells have a normal karyotype (46, XX). **E)** Flow cytometry plots show smNG2-P cells stained for pluripotency markers TRA-1-60 (left, green), OCT3/4 (center, yellow) and NANOG (right, red) or a secondary antibody control (blue). **F)** Flow cytometry plots show differentiated smNG2-P cells stained for PAX6 (ectoderm; left, green), NCAM (mesoderm; center, yellow) and FOXA2 (endoderm; right, red) compared to undifferentiated cells (blue) and unstained controls (dark colors). **G)** Fluorescent and brightfield images show fluorescence complementation after transfecting smNG2-P cells with a plasmid expressing H2B fused to $mNG2_{11}$. The scale bar is 10 microns.

3.5.2 Validation of the smNG2-P iPS cell line

We further validated clone 28 to ensure that the cells are still healthy and carry only the desired AAVS1-$mNG2_{1-10}$ integration. Sequencing of the AAVS1 locus revealed that one allele contains the $mNG2_{1-10}$ expression cassette, while the other allele is unedited (Fig. 3.1C). To ensure that only one copy of the cassette was integrated properly, we measured the genomic copy number for $mNG2_{1-10}$ and for the AmpR gene by digital PCR (dPCR). Our data confirmed the presence of a single copy of $mNG2_{1-10}$ with no ectopic integration (Fig. S3.2A). Next, 12 sites predicted to be susceptible to off-target editing based on previous studies and prediction software were selected for sequencing (Concordet & Haeussler, 2018; Hsu et al., 2013; Wang et al., 2014). We found no differences in the sequence of the 12 off-target sites between the WT 201B7 cell line and our edited cells (Fig. S3.2B-M). To ensure that the clone 28 cells have a normal genome, we performed G-banding karyotyping and found no chromosomal abnormalities (46, XX karyotype; Fig. 3.1D). To verify that clone 28 cells are undifferentiated, we used immunofluorescence staining and flow cytometry with antibodies specific for TRA-1-60, OCT3/4 and NANOG (Fig. 3.1E). We found that all three pluripotency markers were expressed. We also found that clone 28 cells retain pluripotency by successfully differentiating them into ectoderm, mesoderm and endoderm, as

determined by immunofluorescence staining and flow cytometry with antibodies specific for PAX6 (ectoderm), NCAM (mesoderm) and FOXA2 (endoderm) (Fig. 3.1F). Clone 28 cells also have normal iPSC morphology and tested negative for mycoplasma contamination (Fig. S3.2N-O). Finally, we verified that mNeonGreen fluorescence could be reconstituted in the presence of the mNG_{11} fragment. Transfection of clone 28 cells with a plasmid expressing H2B (histone) fused to the mNG_{11} fragment resulted in the expression of a fluorescent signal localized to chromatin as expected for the functional complementation of the $mNG2_{1-10}$ and $mNG2_{11}$ fragments (Fig. 3.1G). After these validation and quality control steps, we chose clone 28 as the AAVS1-$mNG2_{1-10}$ cell line, which we hereafter refer to as "smNG2-P" (split mNeonGreen2 parental cell line).

3.5.3 Efficient endogenous tagging with $mNG2_{11}$ in smNG2-P cells

Since fluorescence could be reconstituted by expressing the mNG_{11} fragment in the smNG2-P cell line, we aimed to integrate $mNG2_{11}$ into different endogenous loci. We selected 17 genes for tagging, some of which had been previously endogenously tagged with the split mNG system (*e.g.* ACTB, TUBA1B, KRT18; Cho et al., 2022) or with full-length fluorescent proteins (*e.g.* H2BC11, ACTB, ANLN, RHOA; Husser et al., 2022; Roberts et al., 2017), while other genes had not been tagged previously (*e.g.* RACGAP1, KRT5, TUBB3, FOXA2). We expected some of these genes to be expressed at varying levels in iPSCs (*e.g.* H2BC11, ANLN, SOX2; Iwasaki et al., 2022), while others were expected to be silent until differentiation into specific lineages (*e.g.* KRT5, KRT14, PAX6, FOXA2). Altogether, these genes cover a range of expression levels, localization patterns and involvement in different cellular processes. After transfecting smNG2-P cells with Cas9/sgRNA RNP complexes and ssODNs designed to integrate $mNG2_{11}$ at these loci, we quantified the proportion of WT, indel and tagged alleles in the edited cell populations by

Nanopore sequencing (Fig. 3.2A-B). We found that Cas9 targeting was efficient for all loci, as shown by the high proportion of indels in the edited cell populations. However, the proportion of tagged alleles was variable, with 37.5% of CDH1 alleles tagged, while only 0.69% of TUBA1B alleles were tagged (Fig. 3.2B). This data shows that while endogenous tagging with $mNG2_{11}$ can be highly efficient, it varies considerably for each locus.

Next, we monitored the reconstitution of mNeonGreen fluorescence in edited populations by flow cytometry and fluorescence microscopy. As expected for genes that are expressed in iPSCs, we observed a fluorescent signal in H2BC11, ACTB, TUBA1B, ANLN, RHOA, KRT18, SOX2, NES and TUBB3-tagged populations (Fig. S3.3A-S). Tagged cell populations were enriched by FACS, and we used microscopy to determine if their localization was consistent with prior studies (Fig. 3.2C). Indeed, the fluorescent signal from H2B histone was nuclear, β-actin was cortical and filamentous, α-tubulin was cytosolic and enriched in mitotic spindles, anillin was nuclear and enriched at the furrow of dividing cells, RhoA was cytosolic and cortical, keratin 18 was filamentous but distinct from actin, SOX2 was nuclear, Nestin also formed filaments distinct from actin and keratin, and β-3-tubulin was weakly expressed and cytosolic. Despite the high tagging efficiency observed for CDH1, we did not observe any fluorescent signal by flow cytometry (Fig. S3.3J). However, microscopy revealed that E-cadherin-$mNG2_{11}$ was enriched at cell junctions (Fig. S3.3T). This suggests that weakly expressed proteins may require different methods to verify expression following endogenous tagging. We also did not observe any fluorescent signal from tagged Cyk4 (RACGAP1 gene) by flow cytometry or microscopy (Fig. S3.3F). The lack of signal could be due to the low tagging efficiency (Fig. 3.2B), and/or the weak expression of Cyk4 in stem cells (Iwasaki et al., 2022). Of the other genes that were tagged, there was no fluorescent signal in the KRT5, KRT14, PAX6, TBXT, NCAM1 and FOXA2-edited

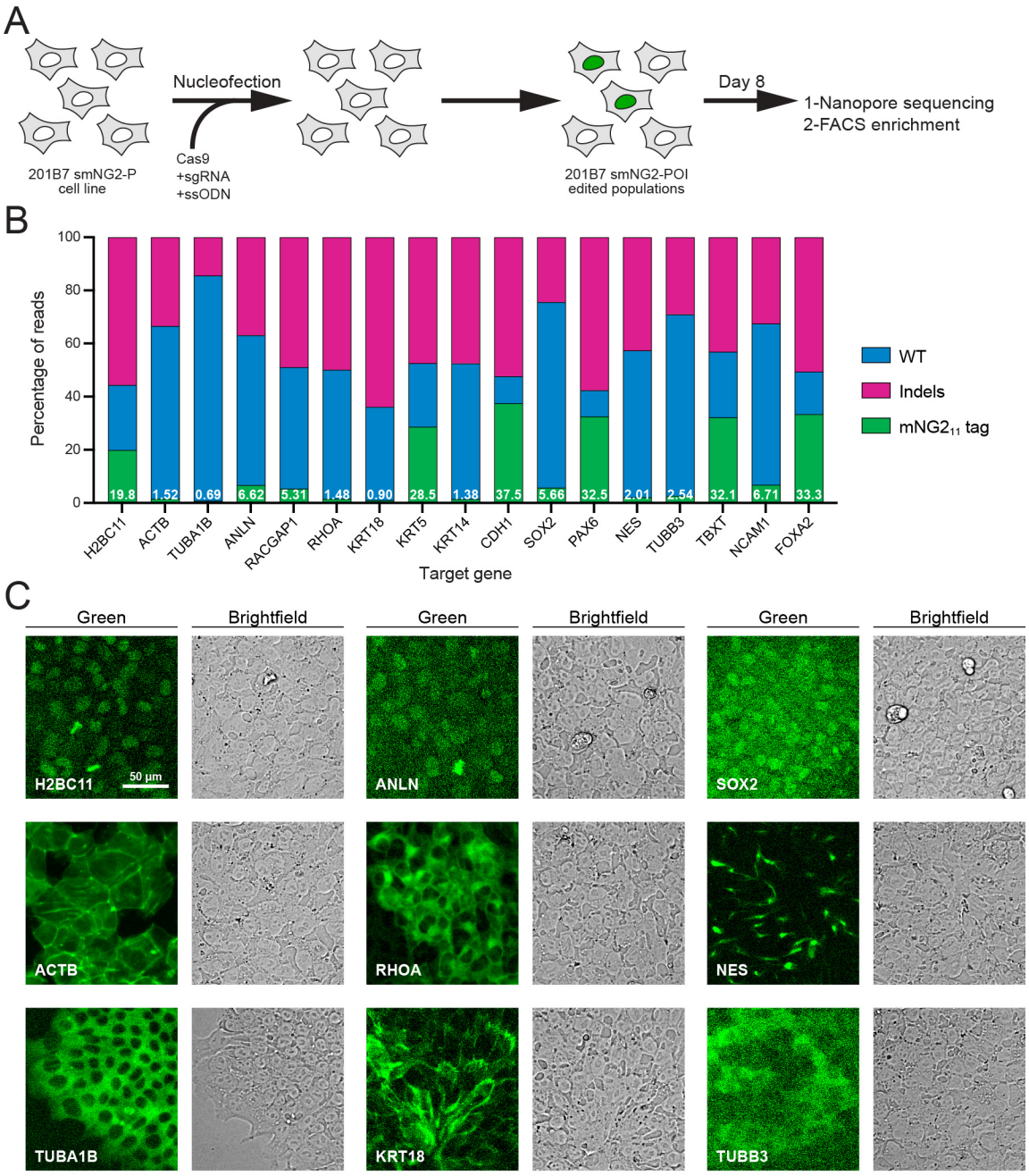

Figure 3.2. Efficient endogenous tagging with mNG2$_{11}$ in smNG2-P cells. A) A schematic shows the workflow used to tag proteins of interest with the mNG2$_{11}$ fragment. smNG2-P cells were transfected with Cas9/sgRNA RNPs and a ssODN repair template to integrate mNG2$_{11}$ at a target locus. After recovery, the edited populations were frozen, then assessed by Nanopore sequencing and flow cytometry. **B)** A bar graph shows the distribution of alleles (WT, indels or mNG2$_{11}$ tagged) in edited populations. The percentage of mNG2$_{11}$ alleles is indicated in white for each gene. **C)** Fluorescent and brightfield images show populations of tagged cells after enrichment by FACS as indicated. The scale bar is 50 microns.

populations as expected for differentiation markers, despite their high tagging efficiency (Fig. 3.2B, data not shown). We observed nuclear fluorescence by microscopy in FOXA2-tagged cells after induction into endoderm (Fig. S3.3U-V), but we did not investigate the expression of the others as this goes beyond the scope of our study.

3.5.4 Efficient clonal isolation and screening of tagged iPS cell lines

Next, we isolated 5 clonal cell lines expressing H2B histones, β-actin, α-tubulin, anillin and RhoA tagged with $mNG2_{11}$, as these proteins could easily be detected and have distinct localization patterns during cell division (Beaudet et al., 2017; Husser et al., 2022; Rodrigues et al., 2015; van Oostende Triplet et al., 2014). We optimized a protocol to efficiently recover single-cell clones after FACS (shown in Fig. 3.3A), resulting in an average recovery of 61.4% in 96-well plates across the 5 genes (Fig. S3.4A). To facilitate screening of clonal recovery in 96-well plates, we developed an ImageJ macro that automatically identifies positive and negative wells from 96-well plate images (Fig. S3.4B-G). Isolated clones were then screened based on their genotype by multiplexed Nanopore sequencing. We found that clones had diverse genotypes with alleles containing $mNG2_{11}$, mutated $mNG2_{11}$, indel mutations and WT sequences (Fig. 3.3B). The diversity of genotypes amongst tagged cells suggests that clonal isolation is important to obtain a high-quality homogeneous population of cells for further study. For each tagged protein, a single clone was selected based on its genotype for further study (Fig. 3.3C-G). These cell lines were also tested for mycoplasma contamination (Fig. S3.4H). Fluorescent images of the final $mNG2_{11}$-tagged cell lines acquired using confocal sweptfield microscopy are shown in Figure 3.3H. Consistent with the expected localization for these proteins, H2B was nuclear during interphase and localized to condensed chromatin during mitosis, actin was cortical in both interphase and

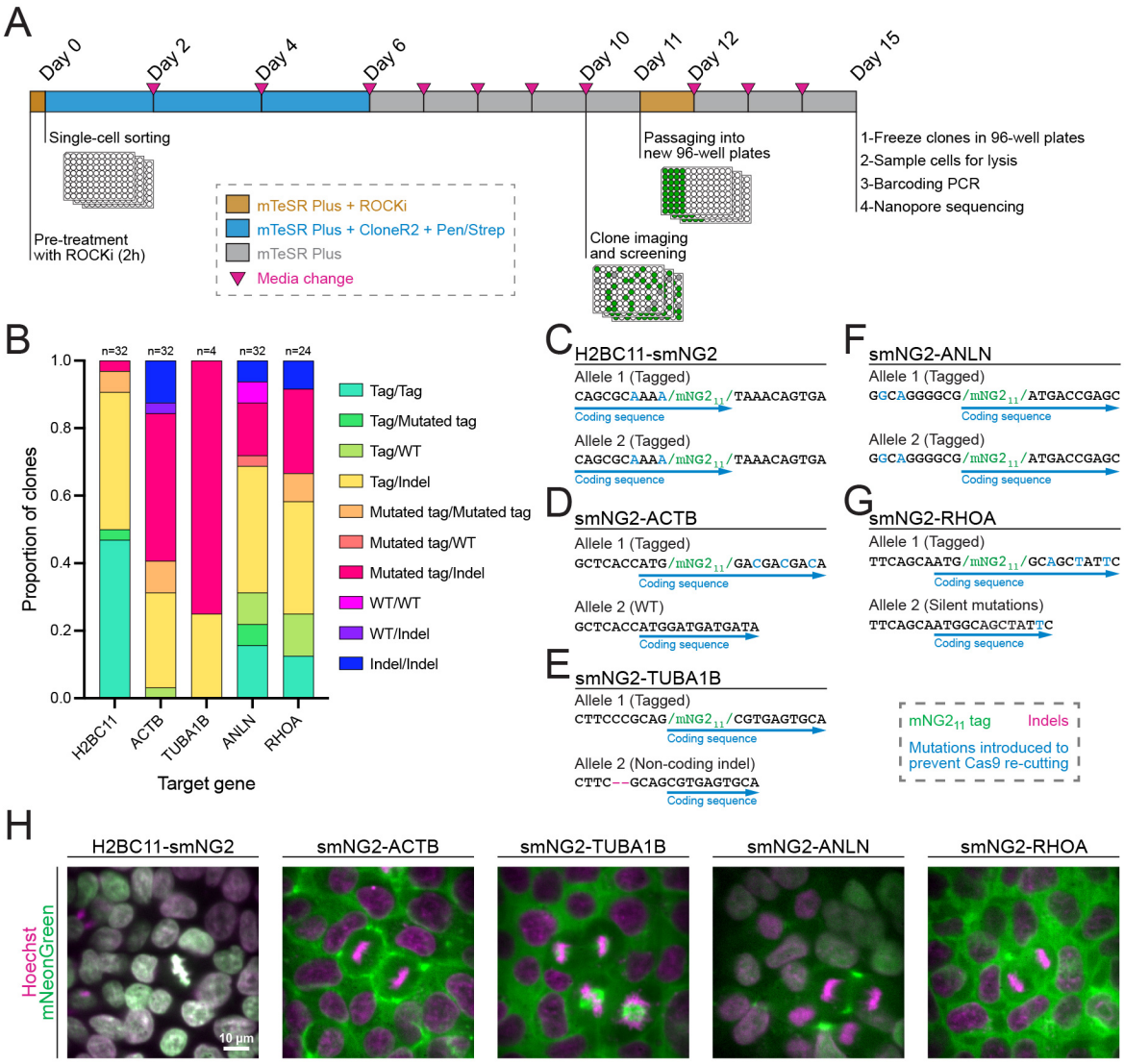

Figure 3.3. Efficient clonal isolation and screening of tagged iPS cell lines. A) The protocol used for single-cell isolation and the recovery of tagged iPSC clones is shown. Tagged cell populations were pre-treated with ROCK inhibitor Y-27632 for 2 hours before sorting individual cells into 96-well plates by FACS. Cells were kept in recovery media for 6 days, then colonies were screened on day 10 to select those for further passaging into 96-well plates on day 11. Fully-grown clones were frozen on day 15, and cells were genotyped by barcoding PCR followed by Nanopore sequencing. **B)** A stacked bar graph shows the distribution of genotypes inferred from multiplexed Nanopore sequencing for isolated clones of tagged H2BC11, ACTB, TUBA1B, ANLN and RHOA (sample size is indicated above each bar). **C-G)** The genotypes of the final tagged cell lines are shown: H2BC11-smNG2 (C), smNG2-ACTB (D), smNG2-TUBA1B (E), smNG2-ANLN (F) and smNG2-RHOA (G). The target gene coding sequence is in blue, indel mutations are in red and mNG$_{11}$ tag in green. **H)** Fluorescent images show the localization of smNG2 (green) and DNA (stained with Hoechst; magenta) in the final tagged cell lines. The scale bar is 10 microns.

mitotic cells, tubulin was cytosolic during interphase and localized to mitotic spindles, anillin was nuclear during interphase and enriched in the cleavage furrow during cytokinesis, and RhoA was cytosolic during interphase and cortically enriched during mitosis.

3.5.5 Image reconstitution for live imaging of cellular processes in iPSCs

The endogenously tagged iPS cell lines can be used to study the mechanisms controlling different cellular processes in healthy cells and how they vary with cell type. Our knowledge of human cytokinesis is derived from transformed and/or cancerous, differentiated cell lines and has not been studied in human pluripotent stem cells. In metazoans, cytokinesis initiates by the assembly of a contractile ring in anaphase which ingresses during telophase to pinch in the membrane, and then transitions to a stable midbody for abscission (Ozugergin & Piekny, 2022; Pollard & O'Shaughnessy, 2019). To characterize cytokinesis in human stem cells, we imaged the $mNG2_{11}$-tagged cell lines from metaphase onwards. Cytokinesis is dynamic and requires imaging over long periods of time (tens to hundreds of minutes) at frequent intervals. We found that iPSCs are more sensitive to toxicity compared to transformed cell lines, and cells stopped dividing and detached after a few minutes of imaging using standard optical settings. To overcome this issue, we optimized the settings to reduce exposure time and laser power, decrease z-stack depth and increase imaging intervals so that cells could be imaged for more than 80 minutes. However, endogenous tags that are weakly expressed are barely detectable using these imaging conditions. Indeed, the signal-to-noise ratio was very low for H2B, α-tubulin, anillin and RhoA in images acquired with low-exposure settings that supported cell survival, compared to images acquired using high-exposure settings that did not support cell viability (Fig. 3.4A). Only β-actin, which is more highly expressed in iPSCs, had a reasonable signal-to-noise ratio under these conditions,

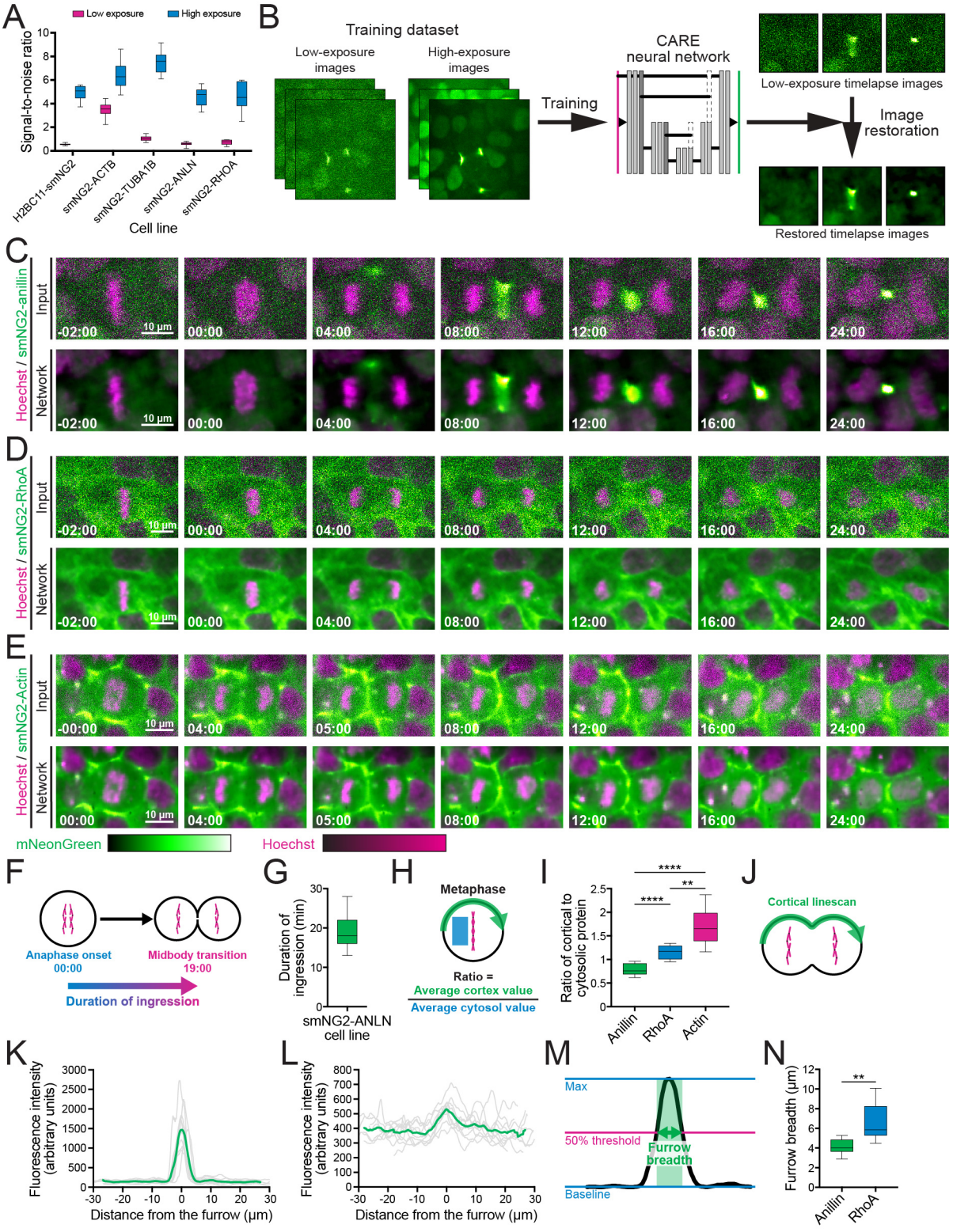
A
Low exposure
High exposure
Signal-to-noise ratio
H2BC11-smNG2
smNG2-ACTB
smNG2-TUBA1B
smNG2-ANLN
smNG2-RHOA
Cell line
B
Training dataset
Low-exposure images
High-exposure images
Training
CARE neural network
Low-exposure timelapse images
Image restoration
Restored timelapse images
C
Hoechst / smNG2-anillin
Input
Network
D
Hoechst / smNG2-RhoA
E
Hoechst / smNG2-Actin
mNeonGreen
Hoechst
F
Anaphase onset 00:00
Midbody transition 19:00
Duration of ingression
G
Duration of ingression (min)
smNG2-ANLN cell line
H
Metaphase
Ratio =
Average cortex value
Average cytosol value
I
Ratio of cortical to cytosolic protein
Anillin
RhoA
Actin
J
Cortical linescan
K
Fluorescence intensity (arbitrary units)
Distance from the furrow (μm)
L
Fluorescence intensity (arbitrary units)
Distance from the furrow (μm)
M
Max
50% threshold
Furrow breadth
Baseline
N
Furrow breadth (μm)
Anillin
RhoA

Figure 3.4. Image reconstitution for live imaging and quantitative measurements in iPSCs. **A)** A graph shows the signal-to-noise ratio measured from low- (pink) and high-exposure (blue) images of the tagged iPS cell lines as indicated. **B)** A schematic shows the training and application of the CARE neural network for image restoration. The neural network developed by Weigert et al. (2018) was trained on sets of low- and high-exposure images for each tagged cell line and used to restore timelapse movies. **C-E)** Comparisons of raw (Input; top panel) and restored timelapse images (Network; bottom panel) by the CARE neural network are shown for iPSCs expressing smNG2-anillin (C), smNG2-RhoA (D) and smNG2-actin (E) undergoing cytokinesis (smNG2 in green; DNA stained with Hoechst in magenta). The scale bars are 10 microns, and time is relative to anaphase onset (00:00). **F)** A schematic shows how the duration of ingression was measured in G. **G)** A graph shows the duration of furrow ingression (in minutes) in anillin-tagged iPSCs (n = 39). **H)** A schematic shows how the ratio of cortical to cytosolic protein was measured for I. **I)** A graph shows the ratio of smNG2-anillin, smNG2-RhoA and smNG2-actin at the cortex relative to the cytosol in metaphase cells (n = 10 for each line). **J)** A schematic shows the location of the linescans used to plot the intensity of fluorescence along the cortex at the onset of furrowing. **K-L)** Graphs show the fluorescence intensity of smNG2-anillin (K) and smNG2-RhoA (L) along the cortex of tagged cells at furrow initiation (n = 10 for each). **M)** A schematic shows how the breadth of protein at the equatorial cortex was calculated for N. **N)** A graph shows the breadth of enriched smNG2-anillin and smNG2-RhoA localization at furrow initiation (n = 10 for each). Box plots in G, I and N show the median line, quartile box edges and minimum and maximum value whiskers. Statistical significance was determined by Brown-Forsythe and Welch's ANOVA for I and Welch's t test for N (ns, not significant; * $p \leq 0.05$; ** $p \leq 0.01$; *** $p \leq 0.001$; **** $p \leq 0.0001$).

which was still improved when using higher imaging settings (Fig. 3.4A). To overcome this issue, we used deep learning-based image restoration to obtain high resolution images from those with low signal-to-noise ratios caused by low-exposure settings. We trained a CARE (Content-Aware image REstoration) neural network on sets of matched high- and low-exposure images for each cell line (Fig. 3.4B; Weigert et al., 2018), and used the trained model to restore timelapse movies acquired with low-exposure settings (Fig. 3.4C-E and S3.5A-B). The signal-to-noise ratio was drastically improved for timelapse images of H2B, α-tubulin, anillin and RhoA (Fig. 3.4C-E and S3.5A-B). Most importantly, this approach allowed us to image live iPSCs with high temporal resolution.

We then used the restored images to measure several parameters of cytokinesis in human iPSCs for the first time. We first measured the duration of contractile ring ingression in anillin-

tagged iPSCs from anaphase onset, and found that it occurs in 18.6 ± 4.0 minutes (Fig. 3.4F-G). We then measured the localization of anillin, RhoA and actin before and during cytokinesis. In metaphase cells, we found that anillin is cytosolic, while RhoA is weakly enriched at the cortex and actin is strongly enriched at the cortex (Fig. 3.4H-I). During mitotic exit, anillin accumulates in the equatorial cortex ~4 minutes after anaphase onset, while RhoA accumulates by ~6 minutes, and actin remains strongly cortical with some equatorial enrichment by ~4-5 minutes (Fig. 3.4C-E and S3.5C-E). We also found that actin is enriched at cell junctions, which remodel between adjacent cells during cytokinesis (Fig. S3.5F). In an extreme example, junctions disappeared, and foci appeared adjacent to the site of ingression, likely resulting from the mechanical response to the forces generated by the furrow (Fig. S3.5F). We then measured the breadth of cortically enriched anillin and RhoA at the onset of ingression and found that anillin forms a narrow peak (4.1 ± 0.7 μm), while RhoA localizes more broadly (6.6 ± 2.2 μm; Fig 3.4J-N). The same result was obtained when measuring furrow breadth as a percentage of cortex length, showing that the difference between RhoA and anillin localization is independent of cell size (Fig. S3.5G). Finally, we measured the enrichment of tubulin at the midzone during mitotic exit to verify the presence of a central spindle in human iPSCs. We found that tubulin is weakly enriched in the midzone ~2 minutes after anaphase onset (Fig. S3.5H-I). This data demonstrates the utility of endogenous tags to study cellular processes in human iPSCs and differentiated cell types with isogenic backgrounds by live imaging.

3.6 Discussion

Recent advances in genetic engineering have accelerated the development of tools for fundamental research. Endogenous tags are particularly valuable as they enable the visualization

of protein behavior in live cells at endogenous expression levels. Self-complementing split fluorescent proteins have been used for efficient endogenous tagging, and this approach was recently used for the construction of the first library of endogenous tags in HEK293 cells, with 1,310 proteins tagged in mixed populations enriched by FACS (Cho et al., 2022). While this library is a powerful resource for the community, researchers will need to generate single clones of individual tagged proteins before they can be studied. Further, the knowledge generated by this library is restricted to this single cell type. Given the predicted diversity in mechanisms controlling cellular processes across cell types, there is a need to also generate endogenous tags in stem cells that can be differentiated into multiple cell types. In this study, we generated a fully validated human iPS cell line expressing $mNG2_{1-10}$ for efficient endogenous tagging with $mNG2_{11}$ in human stem cells capable of differentiating into any cell type. The 201B7 smNG2-P cell line is heterozygous for the $mNG2_{1-10}$ expression cassette which was integrated at the AAVS1 safe-harbor locus. Compared to lentiviral delivery, this design minimizes the risk of $mNG2_{1-10}$ silencing and provides high and consistent expression of $mNG2_{1-10}$ across all cells in the population, even over time and during differentiation (Oceguera-Yanez et al., 2016). We tagged multiple genes with $mNG2_{11}$, with efficiencies ranging from 0.69% to 37.5% measured by Nanopore sequencing (Fig. 3.2B). Tagging efficiency with $mNG2_{11}$ in iPSCs was lower than in mouse embryos (40 to 100% of injected embryos; O'Hagan et al., 2021), and lower than tagging with GFP_{11} in HEK293 cells (<1% to 56% tagged alleles; Cho et al., 2022). However, endogenous tagging with $mNG2_{11}$ was overall more efficient than endogenous tagging with full-length mEGFP in iPSCs (mostly <0.1 to 4%, and up to 24% GFP-positive cells; Roberts et al., 2017). Although different protocols can cause differences in editing efficiency, our results are consistent with iPSCs being more challenging to edit compared to other cell types, and $mNG2_{11}$ integrating at higher frequency than

larger tags. We also found that low endogenous expression levels can limit the detection of tagged proteins by flow cytometry, similar to previous studies (Cho et al., 2022; Leonetti et al., 2016; O'Hagan et al., 2021), requiring microscopy with highly sensitive cameras or detectors. Alternative methods such as fixation and antibody staining can also be used for more sensitive detection of weakly expressed endogenous tags (O'Hagan et al., 2021). Regardless, the detection of a broader range of endogenous protein expression in live cells will require further improvements in the brightness of fluorescent proteins or in the sensitivity of detectors.

We also found that edited cells had diverse genotypes caused by gene editing, including alleles carrying mutated $mNG2_{11}$ tags and indel mutations, warranting clonal isolation. Such mutations have been reported previously but are not fully understood (Burgio & Teboul, 2020; Skryabin et al., 2020). Single-nucleotide mutations may come from mutations introduced during ssODN synthesis. Meanwhile, ssODN re-arrangements could be caused by microhomologies, repair by NHEJ instead of HDR, or a combination of NHEJ and HDR repair (Skryabin et al., 2020). We recommend isolating and screening clonal cell lines to perform quantitative studies of desired cellular processes, as they provide a more reliable readout of protein expression, where variations in signal between cells within a population represent true cell-to-cell variability. Clonal isolation is notoriously inefficient in iPSCs, which are programmed to undergo dissociation-induced apoptosis upon loss of attachment or cell-cell contact (Bhargava et al., 2022; Chen & Pruett-Miller, 2018; Singh, 2019; Tristan et al., 2023; Watanabe et al., 2007). We optimized a protocol for efficient single-cell recovery of 201B7 iPSCs after FACS, with up to 80% of wells in a 96-well plate showing clonal growth after 10 days (Fig. 3.3A and S3.4A). We also created a macro for image-based colony screening in 96-well plates (Fig. S3.4B-G), and used multiplexed Nanopore sequencing for high-throughput screening of selected colonies, as many amplicons can be

sequenced simultaneously (Whitford et al., 2022). Automated instrumentation could be used to further increase the scale of clonal cell isolation, and to isolate cell lines where transcriptionally silent genes are tagged endogenously (Roberts et al., 2019). After clonal isolation, we found that the cells in each edited line had consistent, stable fluorescence. Further, we observed fluorescence across a range of intensities in the tagged cell lines, as expected for endogenous protein levels, showing that $mNG2_{1-10}$/$mNG2_{11}$ complementation is comparable to full-length fluorescent proteins.

The goal of endogenous tagging in iPSCs is to enable live imaging studies of diverse cellular processes for comparative studies among different human cell types. We found that iPSCs are particularly sensitive to phototoxicity, making it difficult to image weakly expressed endogenous tags over longer periods of time or with short time intervals. This sensitivity has not been previously reported in human or in mouse stem cells, likely because imaging conditions are rarely reported and vary with different setups. In addition, timelapse imaging often involves the use of overexpressing transgenes or dyes, which generate higher fluorescent signal intensity and enable the use of optical settings with lower laser power and exposure time (Chaigne et al., 2021; Roberts et al., 2017). Since many labs have access to spinning disk confocal or epifluorescence widefield microscopes, image restoration methods provide a way to obtain high-quality images of iPSCs without compromising on temporal resolution. We used CARE, a content-aware image restoration neural network developed by Weigert et al. (2018), where training datasets are created with matched images obtained using low- and high-exposures (Fig. 3.4B-E). With this network, cells can be imaged over extended periods of time with high temporal resolution using low exposure settings, and image files can be restored to generate high-quality movies. This approach allowed us to measure the timing and localization of proteins known to be involved in cytokinesis

for the first time in live human iPSCs (Fig. 3.4F-J). We found that anillin is recruited to a narrow band at the equatorial cortex ~4 minutes after anaphase onset, while RhoA is also enriched but only after ~6 minutes and is more broadly distributed (Fig. 3.4I-J and S3.5C). We previously showed that anillin and RhoA have similar breadths in HeLa cells (Husser et al., 2022). Active RhoA is generated at the equatorial cortex by the GEF Ect2 which is activated by Cyk4 at the central spindle (Koh et al., 2022; Mahlandt et al., 2021; Yuce et al., 2005). The formation of a weak central spindle in iPSCs may explain the broad localization of RhoA (Fig. S3.5G). Indeed, perturbations that weaken the central spindle result in more diffuse Ect2-Cyk4 complexes and a broader band of RhoA activation (Adriaans et al., 2019; Kotynkova et al., 2016; Su et al., 2011; Yuce et al., 2005). Active RhoA is also required for the cortical recruitment of anillin, yet the localization of anillin in iPSCs is more narrow compared to 6 mammalian cell lines that we previously characterized (Fig. S3.5G; Husser et al., 2022; Piekny & Glotzer, 2008). Interactions with other proteins or phospholipids could control the localization of anillin in different cell types (Ozugergin & Piekny, 2022). In addition, anillin-tagged iPSCs completed ingression in 18.6 ± 4.0 minutes; faster than HepG2, HEK293 and HeLa cells, and slower than HCT116 and MDCK cells (Fig. 3.4G; Husser et al., 2022). Previously, we speculated that the breadth of anillin localization inversely correlates with the speed of ingression. The iPSCs seem to differ from this model, suggesting that other factors should also be considered, such as the distribution of other actin crosslinkers or cortical flows (Khaliullin et al., 2018; Leite et al., 2020; Osorio et al., 2019; Reymann et al., 2016; Sobral et al., 2021; Spira et al., 2017). Further studies are needed to reveal the mechanisms regulating cytokinesis in human iPSCs and differentiated cells.

Our work combines approaches to alleviate some of the challenges of gene editing in human stem cells. High transfection and editing efficiencies can be achieved in iPSCs by using

electroporation and delivering Cas9/sgRNA RNP complexes instead of plasmids (Kim et al., 2014; Liang et al., 2015). Using a short tag that can be carried on single-stranded repair templates (ssODNs) bypasses the requirement for cloning dsODNs with large homology arms. Tagging efficiency is further increased by using NHEJ inhibitors (Chu et al., 2015; Maruyama et al., 2015; Maurissen & Woltjen, 2020; Schimmel et al., 2023). Cells with mutated $mNG2_{11}$ tags can be eliminated by screening single-cell clones based on genotype, using single cell isolation and image-based colony screening in 96-well plates, combined with multiplexed genotyping of clones by Nanopore sequencing. Finally, we showed how iPSCs could be imaged with high temporal resolution using CARE for studies of cytokinesis, an essential dynamic cellular process. Altogether, this work provides the basis for a high-quality endogenous tag library in human iPSCs, which will be used to study protein function in human stem cells and across human cell types *in vitro*.

3.7 Supplementary figures and tables

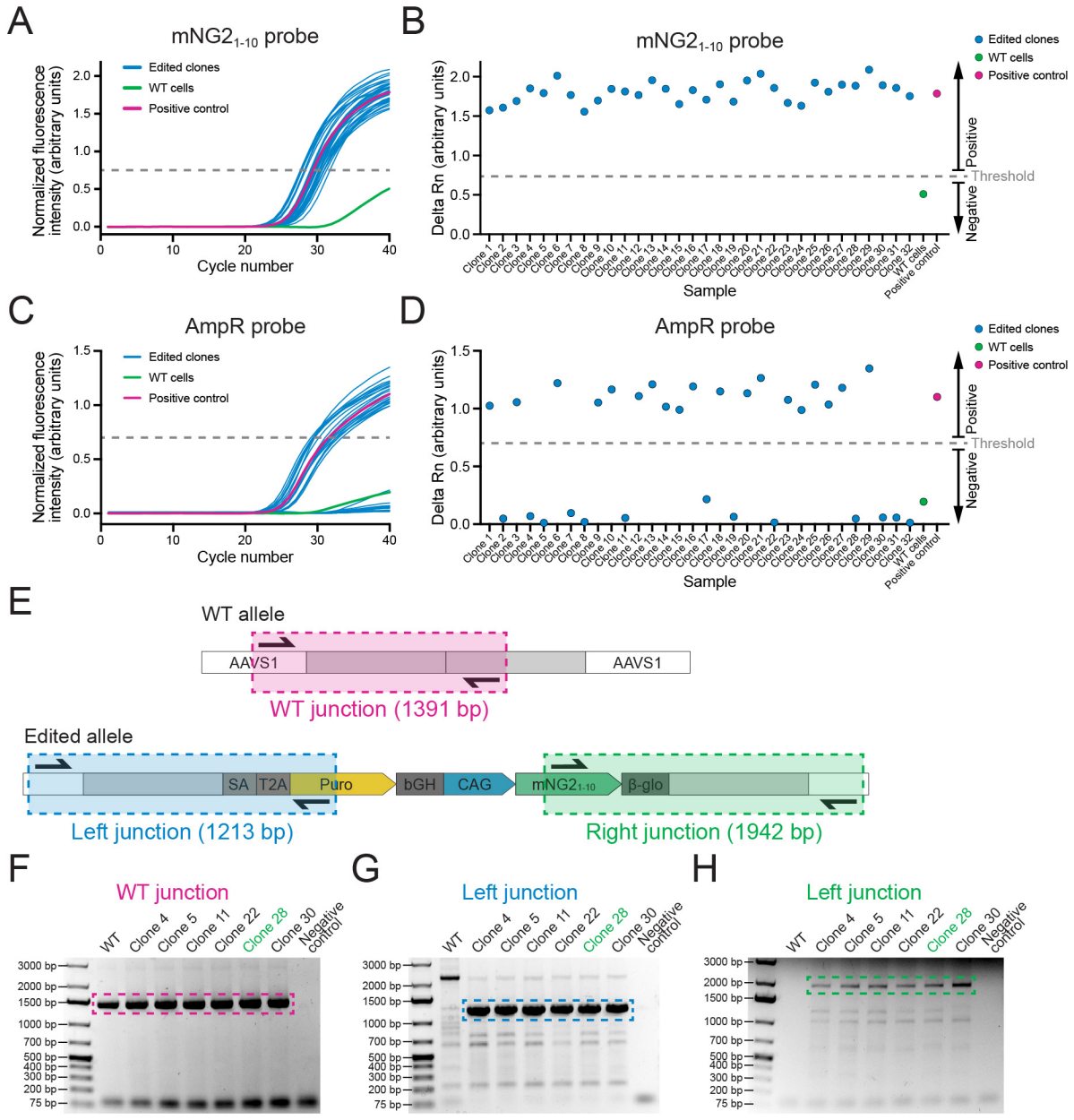

Figure S3.1. Screening of AAVS1-mNG2$_{1-10}$ clones. A) A graph shows qPCR amplification curves for the mNG2$_{1-10}$ probe across 32 edited clones (blue), WT cells (green) and a positive control (pink). **B)** A graph shows the delta Rn values (increase in fluorescence over the 40 qPCR cycles) to show the presence or absence of the mNG2$_{1-10}$ gene in 32 clones edited clones (blue), WT cells (green) and a positive control (pink). Clones with delta Rn values above the threshold were considered positive for mNG2$_{1-10}$. **C)** A graph shows qPCR amplification curves for the AmpR probe in 32 edited clones (blue), WT cells (green) and a positive control (pink). **D)** A graph shows the delta Rn values (increase in fluorescence over the 40 qPCR cycles) to show the presence or absence of the AmpR gene in 32 edited clones (blue), WT cells (green) and a positive control

(pink). Clones with delta Rn values below threshold were considered negative for AmpR. **E)** A schematic shows the strategy for junction PCR screening. Three sets of primers were used to amplify the WT AAVS1 allele (top, pink), and the left (bottom left, blue) and right (bottom right, green) integration junctions to verify the $mNG2_{1-10}$ insertion. **F-H)** Gel images show the results of the junction PCR screening for WT (F), left junction (G) and right junction (H) with WT cells and 6 edited clones. The hatched boxes indicate the relevant DNA band. Clone 28 (green) was selected for further validation.

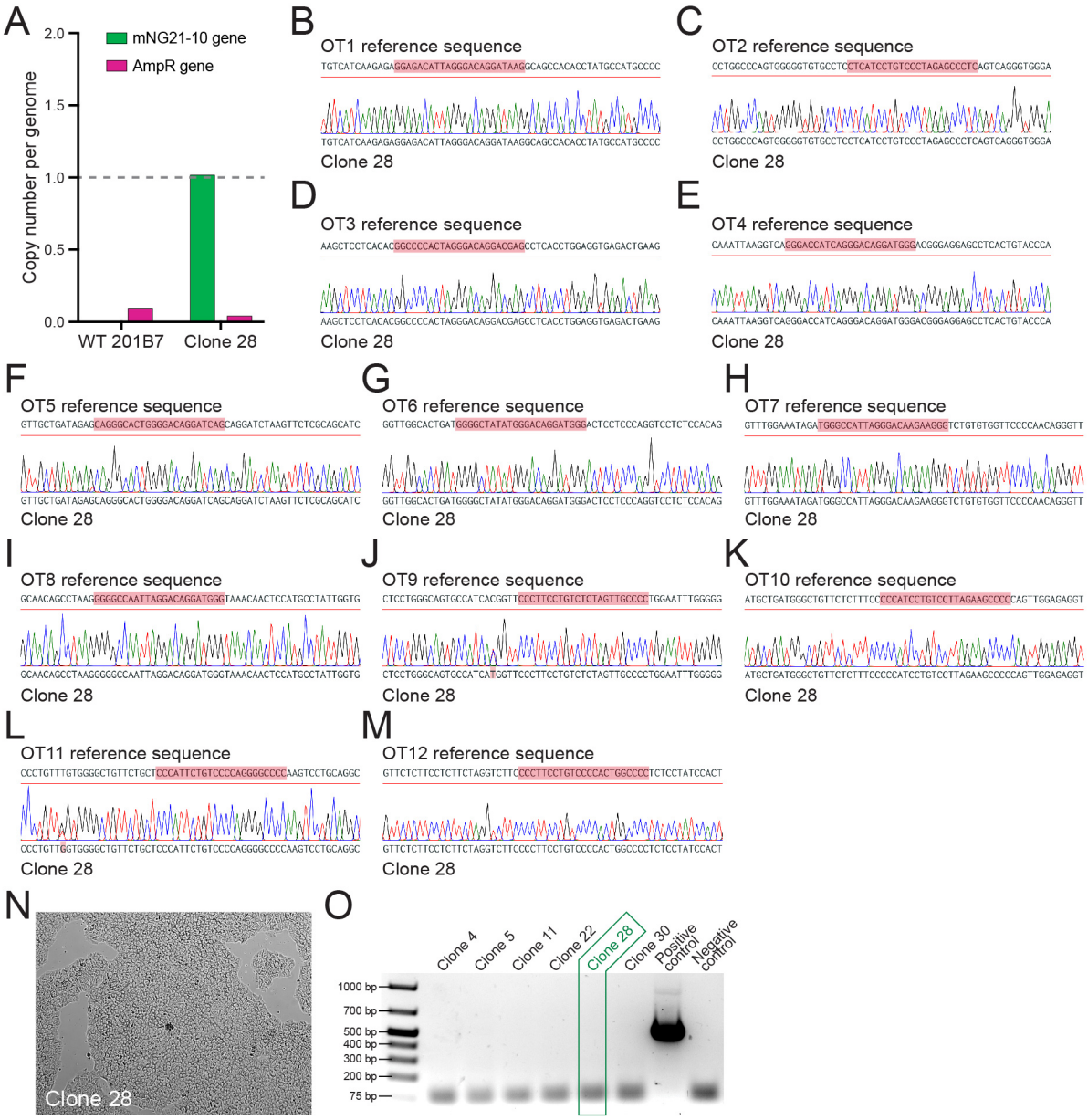

Figure S3.2. Validation of the smNG2-P cell line. A) A bar graph shows the copy number of the mNG2$_{1-10}$ (green) and AmpR (pink) genes in clone 28 and WT cells determined by digital PCR. **B-M)** Sequence chromatograms for 12 AAVS1 off-target sites in AAVS1-mNG2$_{1-10}$ clone 28 cells are shown below the reference sequence from the human genome. The mismatched sgRNA target and PAM sites are highlighted in red. **N)** A brightfield image shows AAVS1-mNG2$_{1-10}$ clone 28 cells growing on an iMatrix-511 Silk-coated plate. **O)** A gel image shows the mycoplasma PCR test with cells from several AAVS1-mNG2$_{1-10}$ clones, along with positive and negative controls. Clone 28 is highlighted in green.

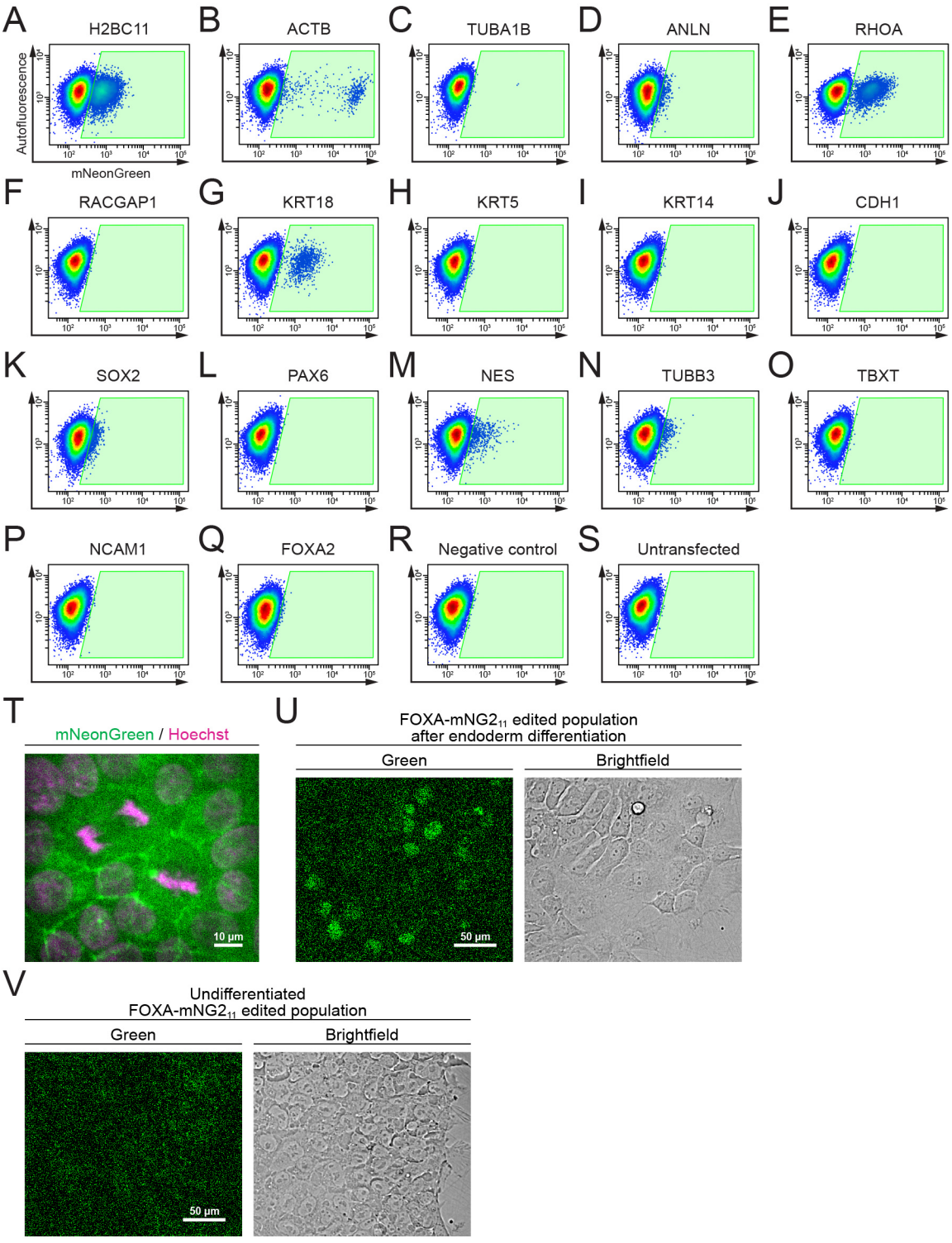

Figure S3.3. Fluorescent signal from endogenous mNG2$_{11}$ tags. A-S) Flow cytometry plots show 17 different cell populations with smNG2 fluorescence after being edited with the mNG2$_{11}$ tag. A negative control transfected with pooled ssODNs and scrambled sgRNAs (R), and an untransfected control (S) were used to set a gate to identify fluorescent cells (gate shown in green).

T) Fluorescent images show the localization of smNG2-tagged E-cadherin (green) and DNA (stained with Hoechst, magenta). The scale bar is 10 microns. **U-V)** Fluorescent and brightfield images show the expression of smNG2-tagged FOXA2 in the edited cell population after differentiation into endoderm (U) but not in the undifferentiated cell population (V). The scale bar is 50 microns.

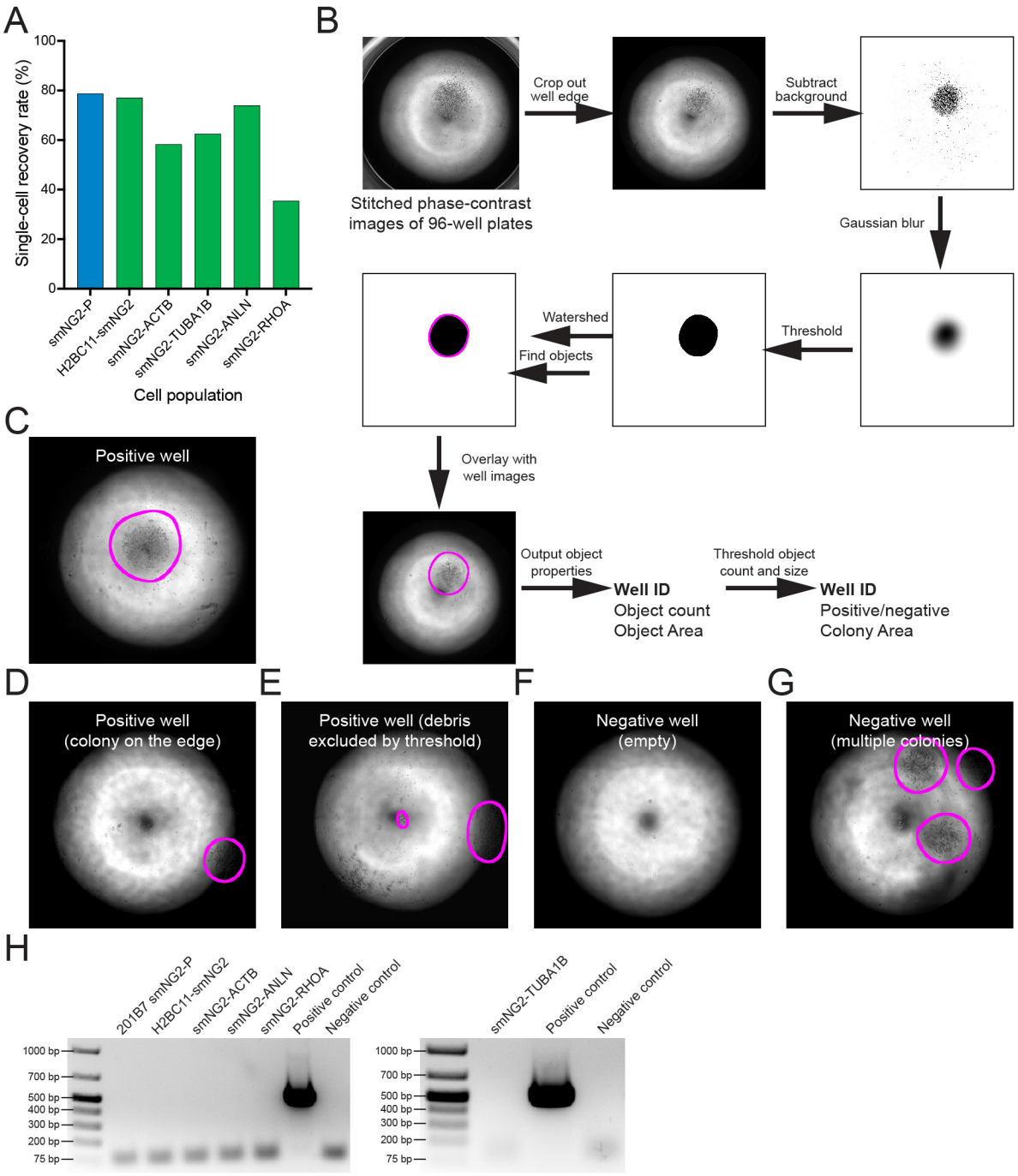

Figure S3.4. Clonal isolation and screening of tagged clones. A) A bar graph shows the recovery rate of different edited and WT cell populations after single-cell isolation by FACS. **B)** The steps used by the macro to process images for colony screening in 96-well plates are shown. **C-G)** Representative images of results from colony screening using the macro in B). **H)** Gel images show the results of the mycoplasma PCR test for the final mNG2$_{11}$-tagged cell lines compared to positive and negative controls.

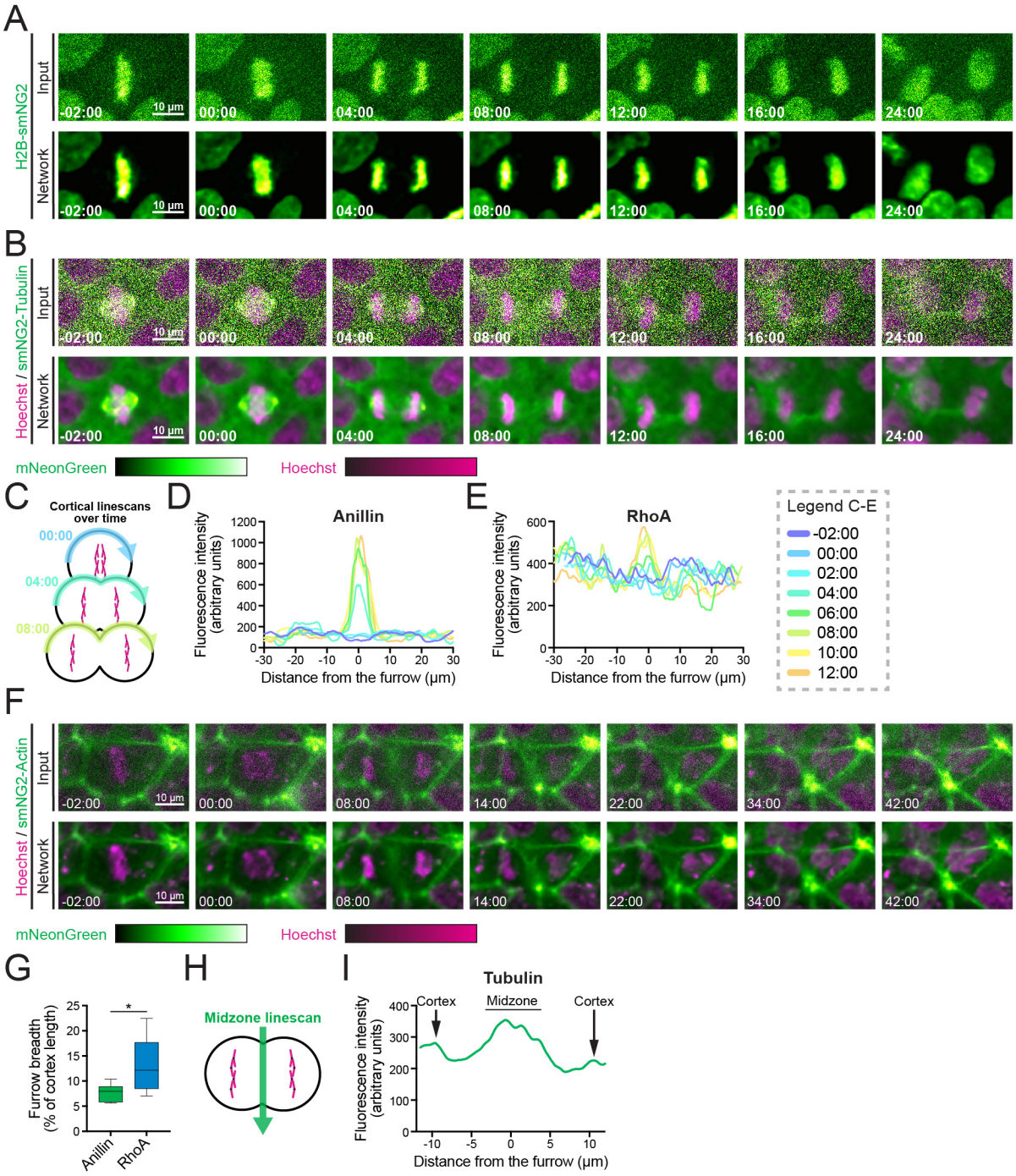

Figure S3.5. Protein localization in iPSCs during cytokinesis. A-B) Timelapse images show cells expressing H2B-smNG2 (A) and smNG2-tubulin (B) during cytokinesis. The input images are shown above the same images after restoration by the CARE neural network. The mNG2 signal is shown in green, and in B), the DNA is stained with Hoechst (magenta). **C)** A schematic shows the location and timing of the linescans used to plot the fluorescence intensity along the cortex in single iPSCs for D and E. **D-E)** Graphs show the fluorescence intensity of smNG2-anillin (D) and smNG2-RhoA (E) along the cortex of single cells at multiple timepoints starting two minutes

before anaphase onset, shown in different colors as indicated in the scale. **F)** Timelapse images show a cell expressing smNG2-actin during cytokinesis. The input images are shown above the same images after restoration by the CARE neural network. The mNG2 signal is shown in green and the DNA is stained with Hoechst (magenta). **G)** A graph shows the breadth of smNG2-anillin and smNG2-RhoA localization at the furrow as a percentage of cortex length (n = 10 for each). **H)** A schematic shows the location of the linescan used to plot the fluorescence intensity along the midzone of a cell in I. **I)** A graph shows the fluorescence intensity of smNG2-tubulin along the cell equator 2 minutes after anaphase onset. For all timelapse images, the scale bars are 10 microns and times are shown relative to anaphase onset (00:00). The box plot in G shows the median line, quartile box edges and minimum and maximum value whiskers. Statistical significance was determined by Welch's t test (ns, not significant; * $p \leq 0.05$; ** $p \leq 0.01$; *** $p \leq 0.001$; **** $p \leq 0.0001$).

Table S3.1. Characterization and validation of the smNG2-P cell line. The results from the validation and quality control steps carried out on the smNG2-P cell line are listed.

Characterization	Test	Result	Data
Genotype of the desired edit	PCR	Positive	Fig. S1E-H
	Sequencing		Fig. 1C
Allelic status	PCR	Heterozygous	Fig. S1E-H
	Sequencing		Fig. 1C
	Digital PCR		Fig. S2A-E
Karyotype	G-banding karyotype	Normal (46, XX)	Fig. 1D
Pluripotency status	Flow cytometry (TRA1-60, OCT3/4, NANOG)	Positive	Fig. 1E
Differentiation potential	Directed differentiation and flow cytometry (ectoderm: PAX6, mesoderm: NCAM, endoderm: FOXA2)	Positive	Fig. 1F
Absence of random integrations	Digital PCR	Negative	Fig. S2A-E
Off-target mutation analysis	Sequencing of the top 12 predicted off-target sites	Negative	Fig. S2F and Tab. S2
Colony morphology	Microscopy	Normal	Fig. S2G
Contamination status	Mycoplasma PCR test	Negative	Fig. S2H

Table S3.2. AAVS1 off-target sites sequencing in 201B7 smNG2-P cells. The top off-target sites for the AAVS1 sgRNA are listed, along with the results of sequencing these sites in the smNG2-P cell line compared to WT cells.

Name	Sequence	PAM	Mismatches	Sequence in smNG2-P cell line	Chromosome	Strand	Position	Location	Source
OT1	GGAGACATTAGGGACAGGAT	AAG	GG*G*CA*TAGGGACA*GAT/T*G	WT	10	+	119439186	Intron (GRK5)	Benchling
OT2	GAGGGCTCTAGGGACAGGAT	GAG	G*GG*C*CTAGGGACAGGAT/T*G	WT	9	-	90086414	Intergenic	Benchling
OT3	GGCCCCACTAGGGACAGGAC	GAG	GG**CCACTAGGGACAGGA*/TGG	WT	7	+	122844142	Intron (CADPS2)	Benchling
OT4	GGGACCATCAGGGACAGGAT	GGG	GGG*CCA**AGGGACAGGAT/TGG	WT	6	+	36797704	Intron (CPNE5)	Benchling, CRISPOR
OT5	CAGGGCACTGGGGACAGGAT	CAG	**GG*CACT*GGGACAGGAT/T*G	WT	14	+	92970608	Intron (ITPK1)	Benchling
OT6	GGGGCTATATGGGACAGGAT	GGG	GGGGC*A***GGGACAGGAT/TGG	WT	1	+	21602005	Intron (RAP1GAP)	CRISPOR
OT7	TGGGCCATTAGGGACAAGAA	GGG	*GGGCCA*TAGGGACA*GA*/TGG	WT	15	+	63926606	Intron (DAPK2)	CRISPOR
OT8	GGGGCCAATTAGGACAGGAT	GGG	GGGGCCA*T**GGACAGGAT/TGG	WT	13	+	105960580	Intron (ENSG00000287923)	CRISPOR
OT9	GGGGCAACTAGAGACAGGAA	GGG	GGGGC*ACTAG*GACAGGA*/TGG	WT	8	-	22778074	Intron (PEBP4)	CRISPOR, Wang 2013
OT10	GGGGCTTCTAAGGACAGGAT	GGG	GGGGC**CTA*GGACAGGAT/TGG	WT	19	-	16064183	Intergenic	Wang 2013
OT11	GGGGCCCCTGGGGACAGAAT	GGG	GGGGCC*CT*GGGACAG*AT/TGG	WT	21	-	41521021	Intron (TMPRSS2)	Wang 2013
OT12	GGGGCCAGTGGGGACAGGAA	GGG	GGGGCCA*T*GGGACAGGA*/TGG	WT	2	-	231959836	Intergenic	Wang 2013

Table S3.3. List of sgRNAs used in this study. The sequences of all sgRNAs used in this study are listed.

Target gene/locus	Spacer sequence	Location	Spacer orientation	Distance to edit	Format	Chemical modifications	Source	Reference
AAVS1	GGGGCCACTAGGGACAGGAT	-	Forward	+11	crRNA+tracrRNA	No	Sigma	Oceguera-Yanez et al., 2016
H2BC11	ACTCACTGTTTACTTAGCGC	C-terminus	Reverse	-5	sgRNA	Yes	Synthego	Allencell.org
ACTB	GCCGTTGTCGACGACGAGCG	N-terminus	Reverse	+19	sgRNA	Yes	Synthego	Roberts et al., 2017
TUBA1B	GATGCACTCACGCTGCGGGA	N-terminus	Reverse	-5	sgRNA	Yes	Synthego	Roberts et al., 2017
ANLN	GTCTCGTAGTCCGACGCCTG	N-terminus	Forward	-8	sgRNA	Yes	Synthego	Husser et al., 2022
RHOA	AATCACCAGTTTCTTCCGGA	N-terminus	Reverse	+10	sgRNA	Yes	Synthego	Husser et al., 2022
RACGAP1	AGTCAATGCTGGGAAGTAAC	C-terminus	Reverse	+20	sgRNA	Yes	Synthego	This study
KRT18	TGCTGTCCGGGGAGAGAGAA	N-terminus	Reverse	-16	sgRNA	Yes	Synthego	Cho et al., 2022
KRT5	CACACTTGACTGGCGAGACA	N-terminus	Reverse	+1	sgRNA	Yes	Synthego	This study
KRT14	TGCAGGTGGTCATGGTGCAG	N-terminus	Reverse	-4	sgRNA	Yes	Synthego	This study
CDH1	GAGGCGGCGAGGACGACTAG	C-terminus	Forward	0	sgRNA	Yes	Synthego	Artegiani et al., 2020
SOX2	TGCCCCTCTCACACATGTGA	C-terminus	Forward	0	sgRNA	Yes	Synthego	Allencell.org
PAX6	GCACTTACTGTTCTGCATGC	N-terminus	Reverse	+1	sgRNA	Yes	Synthego	This study
NES	CTTTTCCTAGTCCTCCCCTG	C-terminus	Reverse	-8	sgRNA	Yes	Synthego	This study
TUBB3	CGCCAGACGCGCCCAGTATG	N-terminus	Forward	0	sgRNA	Yes	Synthego	This study
TBXT	GCCTTGCTGCTTCACATGGA	C-terminus	Reverse	-3	sgRNA	Yes	Synthego	This study
NCAM1	AGAACGAGAGCAAAGCATGA	C-terminus	Forward	0	sgRNA	Yes	Synthego	This study
FOXA2	AACTCCTCTTAAGAAGACGA	C-terminus	Forward	+8	sgRNA	Yes	Synthego	This study

Table S3.4. List of ssODNs used for endogenous tagging with mNG2$_{11}$. The sequences of the single-stranded oligonucleotides used as repair templates to integrate mNG2$_{11}$ at various loci are shown.

Target gene/locus	Strand	Sequence	Source
H2BC11	+	GGGAGTTGGCCAAGCACGCCGTGTCCGAGGGTACTAAGGCCGTCACCAAGTACACCAGCGCAAAAGGAGGTGGCACCGAGCTCAACTTCAAGGAGTGGCAAAAG GCCTTTACCGATATGATGTAAACAGTGAGTTGGTTGCAAACTCTCAACCCTAACGGCTCTTTTAAGAGCCACCCATGT	BioCorp
ACTB	+	GGCCAGGGCGGGGGCGACCTCGGCTCACAGCGCGCCCGGCTATTCTCGCAGCTCACCATGACCGAGCTCAACTTCAAGGAGTGGCAAAAGGCCTTTACCGATAT GATGGGAGGTGGCATGGACGACGACATTGCTGCACTCGTCGTCGACAACGGCTCCGGCATGTGCAAGGCCGGCTTCGCGGGCGACGATGCCCCCC	BioCorp
TUBA1B	+	ATCTTTTTTCCTTCCCGCAGACCGAGCTCAACTTCAAGGAGTGGCAAAAGGCCTTTACCGATATGATGGGAGGTGGCATGCGTGAGTGCATCTCCATCCA	ThermoFisher Scientific
ANLN	-	GAGCGGTGGGTCATGGCTGGCTGCACCCGCAAACTCACTCACCTCCGTAAACGGATCCATGCCACCTCCCATCATATCGGTAAAGGCCTTTTGCCACTCCTTGAA GTTGAGCTCGGTCATCGCCCCTGCCGTCGGACTACGAGACGATGGAAACGGTGGTTCAAATTCAGGAAGAGAAAAGTGAGTCTC	BioCorp
RHOA	+	AAGCTACCTATGACTTCTTGTGCATTGCAGGTAATATCTGTGTTTTGTGTTTCAGCAATGACCGAGCTCAACTTCAAGGAGTGGCAAAAGGCCTTTACCGATATGAT GGGAGGTGGCATGGCAGCTATTCGGAAGAAACTGGTGATTGTTGGTGATGGAGCCTGTGGAAAGACATGCTTGCTCATAGTCT	BioCorp
RACGAP1	+	AGCAAGTCTGCCACTAACCTAGGACGACAAGGCAACTTTTTTGCTTCTCCAATGCTCAAGGGAGGTGGCACCGAGCTCAACTTCAAGGAGTGGCAAAAGGCCTTT ACCGATATGATGTAGAGACATATGTCCGTCTCACTTCCCAGCATTGACTGACTATAAGAAAGGACACATCTGTACTCTGCTCTGCAGCCTCC	BioCorp
KRT18	+	TCGGGTCGCGCGGCTCGCGCAGGCCGCCACCGTCGTCCGCAAAGCCTGAGTCCTGTCCTTCCTCTCCTCTCCAGACAGCATGACCGAGCTCAACTTCAAGGAGTG GCAAAAGGCCTTTACCGATATGATGGGAGGTGGCATGAGCTTCACCACTCGCTCCACCTTCTCCACCAACTACCGGTCCCTGGG	BioCorp
KRT5	+	CAGCACCTCCCAACCCACTAGTGCCTGGTTCTCTTGCTCCACCAGGAACAAGCCACCATGACCGAGCTCAACTTCAAGGAGTGGCAAAAGGCCTTTACCGATATG ATGGGAGGTGGCATGTCTCGCCAGTCAAGTGTGTCCTTCCGGAGCGGGGGCAGTCGTAGCTTCAGCACCGCCTCTG	BioCorp
KRT14	+	TCCAATTTACCCGAGCACCTTCTCTTCACTCAGCCAACTGCTCGCTCGCTCACCTCCCTCTTCTCGCACCATGACCGAGCTCAACTTCAAGGAGTGGCAAAAGGCC TTTACCGATATGATGGGAGGTGGCATGACCACCTGCAGCCGCCAGTTCACCTCCTCCAGCTCCATGAAGGGCTCCTGCGGCATC	BioCorp
CDH1	-	AACGTGATTTCTGCATTTCCCAGCACATGGGTCTGGGGCCCGCCTCTCTCGAGTCCCCTACATCATATCGGTAAAGGCCTTTTGCCACTCCTTGAAGTTGAGCTCGG TGCCACCTCCGTCGTCCTCGCCGCCTCCGTACATGTCAGCCAGCTTCTTGAAGCGATTGCCCCATTCGTT	BioCorp
SOX2	-	CCATTTCCCTCGTTTTTCTTTGAAAATTTCTCCCCCCTCCAGTTCGCTGTCCGGCCCTCACATCATATCGGTAAAGGCCTTTTGCCACTCCTTGAAGTTGAGCTCGGT GCCACCTCCCATGTGTGAGAGGGGCAGTGTGCCGTTAATGGCCGTGCCGGGCACCGGGCCGCTCTGGTA	BioCorp
PAX6	+	GCTAACAGAGCCCCATATTCGAGCCCCGTGGAATCCCGCGGCCCCCAGCCAGAGCCAGCATGACCGAGCTCAACTTCAAGGAGTGGCAAAAGGCCTTTACCGAT ATGATGGGCGGTGGAATGCAGAACAGTAAGTGCCTCTGGTCTTTCTGGGACTTCGGGCTCGGGGTGCGCGGACCCG	BioCorp
NES	+	GGGCCAGGGTCAGTTCCTGAAGTTCACTCAGAGGGAAGGAGATAGAGAGTCCTGGTCCTCTGGAGAAGATGGAGGTGGCACCGAGCTCAACTTCAAGGAGTGGCA AAAGGCCTTTACCGATATGATGTAGGAAAAGACCATCTGCCCGGCACTGGGGACTTAGGGGTGCGGGGAGGGGAAGGACGCC	BioCorp
TUBB3	-	CACCTTGGCCCCGATCTGGTTGCCGCACTGGCCGGCCTGGATGTGCACGATCTCCCTCATGCCACCTCCCATCATATCGGTAAAGGCCTTTTGCCACTCCTTGAAG TTGAGCTCGGTCATACTGGGCGCGTCTGGCGGGCGGCTGCGGACGGGCGCGGGCGGGCCGGGCTGGCTGCTGAG	BioCorp
TBXT	+	TACGACGCCGCAGCCCAAGGCCGCCTCATAGCCTCATGGACACCTGTGTCGCCACCTTCCATGGGAGGTGGCACCGAGCTCAACTTCAAGGAGTGGCAAAAGGC CTTTACCGATATGATGTGAAGCAGCAAGGCCCAGGTCCCGAAAGATGCAGTGACTTTTTGTCGTGGCAGCCAG	BioCorp
NCAM1	-	CTGGTGAAGCTGCTGTGTCACTTTTTATTTTGATCTTTGCTCGGTTCTCTTCACCCATCACATCATATCGGTAAAGGCCTTTTGCCACTCCTTGAAGTTGAGCTCGGT GCCACCTCCTGCTTTGCTCTCGTTCTCCTTTGTCTGTGTGGCGTCATTGGGGACCGTCTTGACTTC	BioCorp
FOXA2	-	ACTTGCTCTCTCACTTGTCCTCGATCCGGGGTGCCAGAGTTAGCCGGGCCTGAAGCCGTCTTCGTCCTACATCATATCGGTAAAGGCCTTTTGCCACTCCTTGAAGT TGAGCTCGGTGCCACCTCCAGAGGAGTTCATAATGGGCCGGGAGTACACCCCCTGGTAGTAGGAGGTATCTGCGGCCAG	BioCorp

Table S3.5. List of genotyping primers. The primers used to amplify and sequence each edited locus are listed.

Locus	Orientation	Sequence
AAVS1	Forward	TCGACTTCCCCTCTTCCGATG
AAVS1	Reverse	CTCAGGTTCTGGGAGAGGGTAG
AAVS1-mNG21-10 left junction	Forward	TCGACTTCCCCTCTTCCGATG
AAVS1-mNG21-10 left junction	Reverse	GAGCCTAGGGCCGGGATTCTC
AAVS1-mNG21-10 right junction	Forward	TTCCATCAGTACCTGCCCTACC
AAVS1-mNG21-10 right junction	Reverse	TGGGGTCCAGGCCAAGTAG
AAVS1_OT1	Forward	GGATTTGGGTACATTAACCACTCCG
AAVS1_OT1	Reverse	TGGAGGGTGACTGGGAAAGTTAG
AAVS1_OT2	Forward	CTTGTCAAAGTGTGGGTTTGGTATC
AAVS1_OT2	Reverse	TCTGACAACCTCCTAGAACTGACTC
AAVS1_OT3	Forward	AAAGAGGGCCATGGGTCTAGC
AAVS1_OT3	Reverse	GAGTATCTCATTTGGAGTCAAGGGC
AAVS1_OT4	Forward	AATAGGGACAAGAGAGGTCACCC
AAVS1_OT4	Reverse	AGTGGTAGGCCAACTTCCCG
AAVS1_OT5	Forward	CAGTGGTTACTGGTCCACATCC
AAVS1_OT5	Reverse	GACCCATGTTGGAGGATAAGCAG
AAVS1_OT6	Forward	GGAAGGACGGTTCACCACTC
AAVS1_OT6	Reverse	CCCCGGACATCAGAGGCTA
AAVS1_OT7	Forward	GCCTGTTCAGCTAAGTCCAATTC
AAVS1_OT7	Reverse	GTGACTCCTGTGCTTCTAGCTC
AAVS1_OT8	Forward	AATTTCAGAGTGGTGCTCCACAAG
AAVS1_OT8	Reverse	CACCTTCCCATCCTCTAATGAGAATC
AAVS1_OT9	Forward	TGAGGAGGAGGAGAGAATCCG
AAVS1_OT9	Reverse	GGACTAAGTGGGGCATCTTCC
AAVS1_OT10	Forward	TTGCAGTTATTGGTTGTCTTGCC
AAVS1_OT10	Reverse	CAGGTGGTGTGGCTAATTCCAG
AAVS1_OT11	Forward	CTTTGCCAGTCACCACACTCG
AAVS1_OT11	Reverse	CCACCTTTTTCACGGGGGAAG
AAVS1_OT12	Forward	GGCTTCACCTCCTATTTCTAGTCC
AAVS1_OT12	Reverse	ACACACACAGGCCTCAATCG
H2BC11	Forward	CAAGCAGAAGACGGCATACGAGATNNNYRNNNYRNNNYRNNNCTATGCCAGAGCCAGCGAAG
H2BC11	Reverse	AATGATACGGCGACCACCGAGATCNNNYRNNNYRNNNYRNNNAGGAGGAATACAAGCACCAGC
ACTB	Forward	CAAGCAGAAGACGGCATACGAGATNNNYRNNNYRNNNYRNNNCTGTTTGAACCGGGCGGAG
ACTB	Reverse	AATGATACGGCGACCACCGAGATCNNNYRNNNYRNNNYRNNNCGTGCTCGATGGGGTACTTC
TUBA1B	Forward	CAAGCAGAAGACGGCATACGAGATNNNYRNNNYRNNNYRNNNTTGCATGAGTATTTTGTTCCACTTGAC
TUBA1B	Reverse	AATGATACGGCGACCACCGAGATCNNNYRNNNYRNNNYRNNNTTCCTTGCCTGTGATGAGCTG
ANLN	Forward	CAAGCAGAAGACGGCATACGAGATNNNYRNNNYRNNNYRNNNGCTGGTTGTGGGAGAGTTCC
ANLN	Reverse	AATGATACGGCGACCACCGAGATCNNNYRNNNYRNNNYRNNNCATTAGCATCTCCCCTGCGG
RHOA	Forward	CAAGCAGAAGACGGCATACGAGATNNNYRNNNYRNNNYRNNNAGGTGGATCGGCGTACTAGAAG
RHOA	Reverse	AATGATACGGCGACCACCGAGATCNNNYRNNNYRNNNYRNNNCTTGGACTAAGATGGCAGGATGAG
RACGAP1	Forward	CAAGCAGAAGACGGCATACGAGATNNNYRNNNYRNNNYRNNNACACTCCTAGGTATGCAGAATTGG
RACGAP1	Reverse	AATGATACGGCGACCACCGAGATCNNNYRNNNYRNNNYRNNNTCCATACTAACCCTTCTACCCCTG
KRT18	Forward	CAAGCAGAAGACGGCATACGAGATNNNYRNNNYRNNNYRNNNTGCGATATAACTCGGGTCGC
KRT18	Reverse	AATGATACGGCGACCACCGAGATCNNNYRNNNYRNNNYRNNNGGTCCCTCCTACCCCTTACC
KRT5	Forward	CAAGCAGAAGACGGCATACGAGATNNNYRNNNYRNNNYRNNNAAAGGGGGCATCACCGTTC
KRT5	Reverse	AATGATACGGCGACCACCGAGATCNNNYRNNNYRNNNYRNNNAACCAAATCCACTACCGGCAC
KRT14	Forward	CAAGCAGAAGACGGCATACGAGATNNNYRNNNYRNNNYRNNNCAGCAGCAGGCTTCCTCTAC
KRT14	Reverse	AATGATACGGCGACCACCGAGATCNNNYRNNNYRNNNYRNNNAGGAGAAGCGGGAGGATGAG
CDH1	Forward	CAAGCAGAAGACGGCATACGAGATNNNYRNNNYRNNNYRNNNCGTTGTTGGTGTTCACTGCTC
CDH1	Reverse	AATGATACGGCGACCACCGAGATCNNNYRNNNYRNNNYRNNNCCAGAAACTCATCTCAAGGGAAGG
SOX2	Forward	CAAGCAGAAGACGGCATACGAGATNNNYRNNNYRNNNYRNNNGTTCGGTGGTCAAGTCCGAG
SOX2	Reverse	AATGATACGGCGACCACCGAGATCNNNYRNNNYRNNNYRNNNTACCAACGGTGTCAACCTGC
PAX6	Forward	CAAGCAGAAGACGGCATACGAGATNNNYRNNNYRNNNYRNNNTGTTTCAAGCCCCAAAGGGTAG
PAX6	Reverse	AATGATACGGCGACCACCGAGATCNNNYRNNNYRNNNYRNNNAAGAGCCAAGCAAACGCCC
NES	Forward	CAAGCAGAAGACGGCATACGAGATNNNYRNNNYRNNNYRNNNGAGTGATGAACGGGCTGGAG
NES	Reverse	AATGATACGGCGACCACCGAGATCNNNYRNNNYRNNNYRNNNGGAGCAGGCAAGAGATTCCC
TUBB3	Forward	CAAGCAGAAGACGGCATACGAGATNNNYRNNNYRNNNYRNNNCATCAGCCGATGCGAAGGG
TUBB3	Reverse	AATGATACGGCGACCACCGAGATCNNNYRNNNYRNNNYRNNNGTCTCACTCAAGGCTATGCCG
TBXT	Forward	CAAGCAGAAGACGGCATACGAGATNNNYRNNNYRNNNYRNNNTGGTCTGTGAGCAACGGC
TBXT	Reverse	AATGATACGGCGACCACCGAGATCNNNYRNNNYRNNNYRNNNTTCATCTGTAAGCCACCTGGG
NCAM1	Forward	CAAGCAGAAGACGGCATACGAGATNNNYRNNNYRNNNYRNNNCCTCTGGCATCAACTTAGGGC
NCAM1	Reverse	AATGATACGGCGACCACCGAGATCNNNYRNNNYRNNNYRNNNCAAGTGAGTGTGCAACAAAGGG
FOXA2	Forward	CAAGCAGAAGACGGCATACGAGATNNNYRNNNYRNNNYRNNNCTCAAGGCCTACGAACAGGTG
FOXA2	Reverse	AATGATACGGCGACCACCGAGATCNNNYRNNNYRNNNYRNNNGCAACAACAGCAATGGAGGAG

Table S3.6. List of barcoding primers. The primers used to add unique barcodes onto locus-specific amplicons for pooled Nanopore sequencing are shown.

Primer name	Orientation	Barcode sequence	Primer sequence
H2BC11_Fwd	Forward	TCTGCTCCCGCCCCGAAAAAGGGC	Gene-specific primers are listed in Table S5
H2BC11_Rev	Reverse	TCTTTCTTTGAGAACATGGGTGGC	Gene-specific primers are listed in Table S5
ACTB_Fwd	Forward	GCGGGGCTGGCGCCCGGTTGGGAG	Gene-specific primers are listed in Table S5
ACTB_Rev	Reverse	AGGGTGAGGATGCCTCTCTTGCTC	Gene-specific primers are listed in Table S5
TUBA1B_Fwd	Forward	AGTCATCAATAGATTGGTTTAAAT	Gene-specific primers are listed in Table S5
TUBA1B_Rev	Reverse	CTCAGGGTGGAAGAGCTGGCGGTA	Gene-specific primers are listed in Table S5
ANLN_Fwd	Forward	CCCGCCTCAGACTCCTGGTTTTTT	Gene-specific primers are listed in Table S5
ANLN_Rev	Reverse	GCTGCGTGAACTCCGCAAATCACA	Gene-specific primers are listed in Table S5
RHOA_Fwd	Forward	TTTGAATTTGAGTATGCTAATAGA	Gene-specific primers are listed in Table S5
RHOA_Rev	Reverse	AATGGATTCTTCTTTCCAACATTT	Gene-specific primers are listed in Table S5
RACGAP1_Fwd	Forward	CCTTCCTAGGAAATAAAAAACAAC	Gene-specific primers are listed in Table S5
RACGAP1_Rev	Reverse	GAAAGATGTCTCATCTAAAAGCTC	Gene-specific primers are listed in Table S5
KRT18_Fwd	Forward	GCGGCTCGCGCAGGCCGCCACCGT	Gene-specific primers are listed in Table S5
KRT18_Rev	Reverse	TGAGCCCTCAGGTCCTCGATGATC	Gene-specific primers are listed in Table S5
KRT5_Fwd	Forward	CTGGGTAACAGAGCCACCTTCTGC	Gene-specific primers are listed in Table S5
KRT5_Rev	Reverse	CACCTCCAAAGCCATAGCCGCCTC	Gene-specific primers are listed in Table S5
KRT14_Fwd	Forward	GTGGATGTTAAAGGCCCATTCAGT	Gene-specific primers are listed in Table S5
KRT14_Rev	Reverse	ACAGACAGGCCGCCCCCGTAGGTG	Gene-specific primers are listed in Table S5
CDH1_Fwd	Forward	CGTGGTGTGCCACAAGTCTGGGTG	Gene-specific primers are listed in Table S5
CDH1_Rev	Reverse	GAGCTGAAAAACCACCAGCAACGT	Gene-specific primers are listed in Table S5
SOX2_Fwd	Forward	GCCAGCTCCAGCCCCCCTGTGGTT	Gene-specific primers are listed in Table S5
SOX2_Rev	Reverse	ATGGCCATTTTTGCTTTTAACAGT	Gene-specific primers are listed in Table S5
PAX6_Fwd	Forward	ATTTTGTATGCACTGCAGGGCAGA	Gene-specific primers are listed in Table S5
PAX6_Rev	Reverse	TCCCCTCCCGGGCTGCCGGGCGCG	Gene-specific primers are listed in Table S5
NES_Fwd	Forward	CAGTCTGAGGAAGTGGGGCAAGGA	Gene-specific primers are listed in Table S5
NES_Rev	Reverse	TTTGCAGGGTGGGAGGTTATATTC	Gene-specific primers are listed in Table S5
TUBB3_Fwd	Forward	CGGGGCCGCGGCTATAAGAGCGCG	Gene-specific primers are listed in Table S5
TUBB3_Rev	Reverse	CGGCCCCAAAAAAGAGGGCCACGC	Gene-specific primers are listed in Table S5
TBXT_Fwd	Forward	GCCGTCACCCCGGGCTCCCAGGCA	Gene-specific primers are listed in Table S5
TBXT_Rev	Reverse	ACAGCACCGCTACTGCAGGTGTGA	Gene-specific primers are listed in Table S5
NCAM1_Fwd	Forward	TGGAAGAGGAAAGGACTCGTTCTT	Gene-specific primers are listed in Table S5
NCAM1_Rev	Reverse	ACCCTTTCTATAAACCTACAAAAA	Gene-specific primers are listed in Table S5
FOXA2_Fwd	Forward	ATGCACTACCCCGGCTACGGTTCC	Gene-specific primers are listed in Table S5
FOXA2_Rev	Reverse	AACAACAACAACAAAAAAATCAGA	Gene-specific primers are listed in Table S5
BC1_Fwd	Forward	CACAAAGACACCGACAACTTTCTT	CACAAAGACACCGACAACTTTCTTCAAGCAGAAGACGGCATACGAGAT
BC2_Fwd	Forward	ACAGACGACTACAAACGGAATCGA	ACAGACGACTACAAACGGAATCGACAAGCAGAAGACGGCATACGAGAT
BC3_Fwd	Forward	CCTGGTAACTGGGACACAAGACTC	CCTGGTAACTGGGACACAAGACTCCAAGCAGAAGACGGCATACGAGAT
BC4_Fwd	Forward	TAGGGAAACACGATAGAATCCGAA	TAGGGAAACACGATAGAATCCGAACAAGCAGAAGACGGCATACGAGAT
BC5_Fwd	Forward	AAGGTTACACAAACCCTGGACAAG	AAGGTTACACAAACCCTGGACAAGCAAGCAGAAGACGGCATACGAGAT
BC6_Fwd	Forward	GACTACTTTCTGCCTTTGCGAGAA	GACTACTTTCTGCCTTTGCGAGAACAAGCAGAAGACGGCATACGAGAT
BC7_Fwd	Forward	AAGGATTCATTCCCACGGTAACAC	AAGGATTCATTCCCACGGTAACACCAAGCAGAAGACGGCATACGAGAT
BC8_Fwd	Forward	ACGTAACTTGGTTTGTTCCCTGAA	ACGTAACTTGGTTTGTTCCCTGAACAAGCAGAAGACGGCATACGAGAT
BC9_Rev	Reverse	AACCAAGACTCGCTGTGCCTAGTT	AACCAAGACTCGCTGTGCCTAGTTAATGATACGGCGACCACCGAGATC
BC10_Rev	Reverse	GAGAGGACAAAGGTTTCAACGCTT	GAGAGGACAAAGGTTTCAACGCTTAATGATACGGCGACCACCGAGATC
BC11_Rev	Reverse	TCCATTCCCTCCGATAGATGAAAC	TCCATTCCCTCCGATAGATGAAACAATGATACGGCGACCACCGAGATC
BC12_Rev	Reverse	TCCGATTCTGCTTCTTTCTACCTG	TCCGATTCTGCTTCTTTCTACCTGAATGATACGGCGACCACCGAGATC
BC13_Rev	Reverse	AGAACGACTTCCATACTCGTGTGA	AGAACGACTTCCATACTCGTGTGAAATGATACGGCGACCACCGAGATC
BC14_Rev	Reverse	AACGAGTCTCTTGGGACCCATAGA	AACGAGTCTCTTGGGACCCATAGAAATGATACGGCGACCACCGAGATC
BC15_Rev	Reverse	AGGTCTACCTCGCTAACACCACTG	AGGTCTACCTCGCTAACACCACTGAATGATACGGCGACCACCGAGATC
BC16_Rev	Reverse	CGTCAACTGACAGTGGTTCGTACT	CGTCAACTGACAGTGGTTCGTACTAATGATACGGCGACCACCGAGATC
BC17_Rev	Reverse	ACCCTCCAGGAAAGTACCTCTGAT	ACCCTCCAGGAAAGTACCTCTGATAATGATACGGCGACCACCGAGATC
BC18_Rev	Reverse	CCAAACCCAACAACCTAGATAGGC	CCAAACCCAACAACCTAGATAGGCAATGATACGGCGACCACCGAGATC
BC19_Rev	Reverse	GTTCCTCGTGCAGTGTCAAGAGAT	GTTCCTCGTGCAGTGTCAAGAGATAATGATACGGCGACCACCGAGATC
BC20_Rev	Reverse	TTGCGTCCTGTTACGAGAACTCAT	TTGCGTCCTGTTACGAGAACTCATAATGATACGGCGACCACCGAGATC

Table S3.7. List of live imaging parameters. For each cell lines imaged, the laser power and exposure time used to acquire low- and high-exposure images are listed. These parameters were used to acquire the neural network training dataset, and the low-exposure settings were used to acquire timelapse images for restoration.

Cell line	Imaging condition	405 nm laser, 50 mW		488 nm laser, 50 mW	
		Laser power (%)	Exposure time (ms)	Laser power (%)	Exposure time (ms)
H2BC11-smNG2	Low exposure	3	200	8	200
	High exposure	30	800	90	800
smNG2-ACTB	Low exposure	6	200	12	200
	High exposure	50	200	25	200
smNG2-TUBA1B	Low exposure	3	200	6	200
	High exposure	50	200	60	200
smNG2-ANLN	Low exposure	4	200	16	200
	High exposure	30	800	90	800
smNG2-RHOA	Low exposure	4	200	20	200
	High exposure	30	800	90	800

CHAPTER 4

Discussion

4.1 Preamble

Endogenous tagging is the most reliable way to study protein behavior in live cells. This approach circumvents the need to over-express proteins using strong promoters, which can generate artefacts and provide misleading results. In this thesis, I generated multiple precisely-engineered cell lines (Table 4.1) where tagged proteins can be visualized at endogenous levels in their native cellular context. The constructs used to generate these cell lines are available through Addgene. Moreover, I developed cell line-specific protocols for gene editing, clone isolation and screening, as well as imaging protocols to characterize how cytokinesis occurs in different cell lines. One of these engineered cell lines is an iPS cell line that expresses the large fragment of a split mNeonGreen protein capable of complementing with the corresponding small fragment to reconstitute fluorescence. This cell line enables endogenous tagging by inserting the small fragment of mNeonGreen into any gene of interest and can be used to build a library of tagged iPSCs to study any protein or cellular process. In this chapter, I summarize the implications and future directions of this work. The fundamental questions addressed in Chapter 2 revealed cytokinetic diversity in mammalian cells, highlighting the need to study cytokinesis in more cell types and in developmentally relevant contexts. Meanwhile, the tools and methodologies developed in Chapters 2 and 3 are critical to expand our understanding of cytokinesis and will also benefit fundamental research in cell biology across different fields.

Table 4.1. Summary of the cell lines generated in this thesis. For each cell line, the target locus, desired knock-in and zygosity are listed.

Parental cell line	Modified locus	Knock-in	Zygosity
HEK293	ANLN	mNeonGreen	Homozygous
HEK293	ECT2	mNeonGreen	Homozygous
HEK293	RHOA	mNeonGreen	Heterozygous
HeLa	ANLN	mNeonGreen	Homozygous
HeLa	ECT2	mNeonGreen	Homozygous
HeLa	RHOA	mNeonGreen	Heterozygous
HCT116	ANLN	mNeonGreen	Heterozygous
HepG2	ANLN	mNeonGreen	Heterozygous
MDCK	ANLN	mNeonGreen	Homozygous
HEK293	H2BC11	TagBFP	Homozygous
HEK293	H2BC11 ANLN	TagBFP mNeonGreen	Heterozygous Homozygous
HEK293	H2BC11 AAVS1	TagBFP CMV-mRuby2-CAAX	Heterozygous Heterozygous
HEK293	H2BC11 ANLN AAVS1	TagBFP mNeonGreen CMV-mRuby2-CAAX	Heterozygous Homozygous Heterozygous
HEK293	H2BC11 ANLN ACTB	TagBFP mNeonGreen mRuby2	Heterozygous Homozygous Heterozygous
201B7	AAVS1	CAG-mNG2$_{1-10}$	Heterozygous
201B7	AAVS1 H2BC11	CAG-mNG2$_{1-10}$ mNG2$_{11}$	Heterozygous Homozygous
201B7	AAVS1 ACTB	CAG-mNG2$_{1-10}$ mNG2$_{11}$	Heterozygous Heterozygous
201B7	AAVS1 TUBA1B	CAG-mNG2$_{1-10}$ mNG2$_{11}$	Heterozygous Heterozygous
201B7	AAVS1 ANLN	CAG-mNG2$_{1-10}$ mNG2$_{11}$	Heterozygous Homozygous
201B7	AAVS1 RHOA	CAG-mNG2$_{1-10}$ mNG2$_{11}$	Heterozygous Heterozygous

4.2 Cytokinesis

4.2.1 Cytokinetic diversity

Since Rappaport (Rappaport, 1985) showed the dependence of ring positioning on the mitotic spindle in sea urchin embryos, cytokinesis has been explored in diverse contexts: frog embryos and epithelial tissue, Drosophila embryos and cultured S2 cells, *C. elegans* embryos, germline and epithelial tissue, mouse embryos and mammalian cell lines (*e.g.* HeLa, HEK293, MDCK, among a few others). These studies have uncovered several pathways that control the assembly and positioning of the contractile ring, with the assumption that most pathways exist in most organisms, but that their requirement varies between organisms. Recent studies done in *C. elegans* provided insights into the mechanisms regulating cytokinesis in cells with different fates in the early embryo, which differ in more extreme ways than previously thought (Davies et al., 2018; Ozugergin et al., 2022b; Ozugergin & Piekny, 2022). While most of our understanding of cytokinesis in mammalian cells comes from studies of HeLa cells or other cancerous or transformed cells lines in culture, there is evidence of cytokinetic diversity among mouse or human cell types. For example, hepatocytes (the major cell type of the liver) become polyploid by undergoing controlled cytokinesis failure as part of their normal function (Donne et al., 2020; Margall-Ducos et al., 2007; Tormos et al., 2015). Interestingly, anillin and other cytokinesis regulators are often over-expressed in liver cancer cells, which must rely on cytokinesis to proliferate, unlike normal hepatocytes (Lin et al., 2021; Zhang et al., 2018a). In mice, *in vivo* knockdown of ANLN does not affect liver size or function, but significantly reduces tumor progression in different liver cancer models (Zhang et al., 2018a; Zhang et al., 2018b). This finding highlights the need to understand the mechanisms regulating cytokinesis across different cell types and in diseases (Bourdages et al., 2014; Lazaro-Dieguez & Musch, 2017; Paim & FitzHarris,

2022). In Chapter 2, endogenous tagging of anillin in four human cell lines and one canine cell line revealed differences in cytokinesis, supporting the hypothesis that distinct mechanisms control these differences depending on genetic background, cell fate and tissue of origin. These findings also raised the question of whether cytokinesis is regulated differently simply because of different transcriptional programs, or also as a mechanism to regulate an organism's developmental program. More work is required to describe the diversity of cytokinetic programs across healthy and diseases cell types, and how it interplays with embryo and tissue development.

Cytokinesis occurs via the ingression of a contractile ring. In Chapter 2, I found that the speed of ingression correlated with the breadth of anillin localization in five cell lines, where cells with broader anillin had faster ingression. Ingression is driven by actomyosin flows directed towards the equatorial cortex, which facilitate actomyosin filament alignment and constriction of the actomyosin ring (Illukkumbura et al., 2020; Khaliullin et al., 2018; Ozugergin et al., 2022b; Reymann et al., 2016; Silva et al., 2016; Singh & Pohl, 2014). Anillin could control ingression by positive feedback of RhoA activation at the equatorial cortex to increase actomyosin flow or to crosslink actin filaments and facilitate their alignment. However, constriction also generates tension that resists ingression, and the distribution of actomyosin filaments over a broader area could help spread the resistive forces to reduce their impact on ingression. Ring components also need to be removed as the ring constricts, and having a broader area for removal may make ingression more efficient (Carim et al., 2020). Anillin forms a complex with septins, and previous studies showed that this complex is shed during ingression (Carim & Hickson, 2023; El Amine et al., 2013; El-Amine et al., 2019; Jananji et al., 2017). A model has been proposed where this shedding removes membrane microdomains to reduce tension and allow for further constriction (Carim et al., 2020). To test these models, the breadth of anillin localization could be increased or

decreased in different cell lines. For example, CRISPRi (CRISPR interference) and CRISPRa (CRISPR activation) can be used to decrease or increase anillin expression, respectively, to obtain a narrower or a broader localization of anillin at the equatorial cortex (Husser et al., 2021; Pickar-Oliver & Gersbach, 2019). The breadth of anillin localization can then be measured, along with the strength of actomyosin flows, filament alignment and the speed of ingression. Finally, the outflow of anillin from the ring during ingression could be measured by particle image velocimetry in cells with different furrow breadths to quantify the removal of ring components during ingression (Singh et al., 2019). Interestingly, I found that iPSCs undergo ingression relatively quickly, yet anillin is localized narrowly while RhoA is localized more broadly at the equatorial cortex. More studies are needed to reveal how contractile components and cytokinesis regulators localize in iPSCs, and to determine the function of anillin in these cells. For example, the affinity of anillin for different complexes (actomyosin, RhoA or septins) may be different compared to other cell types. Actomyosin flows into the equatorial region and anillin outflow and shedding could also vary between cell types.

Cytokinesis occurs differently when cells are part of a tissue, where forces from neighbouring cells impact ingression kinetics, and cells need to maintain polarity and remodel cell-cell junctions as they divide (Herszterg et al., 2014; Morais-de-Sa & Sunkel, 2013; Sugioka, 2022; Thieleke-Matos et al., 2017). For example, we found that actin was enriched at cell junctions in iPSCs, which were remodeled during and after cytokinesis. Cell polarity influences cytokinesis by the asymmetric recruitment of cortical regulators, while neighbouring cells provide mechanical resistance (Herszterg et al., 2014; Sugioka, 2022; Thieleke-Matos et al., 2017). Ingression may also occur asymmetrically in polarized cells as the cytokinesis machinery competes with actin filament systems present at cell junctions. MDCK cells are used as a model to study epithelial cell

physiology as they become polarized at high confluency, form junctions, and can be induced to form cysts with a lumen (Balcarova-Stander et al., 1984; Gudipaty et al., 2017; Hart et al., 2017; Yamamoto et al., 2021). Cytokinesis has not been well-studied in mammalian and human epithelial tissue. The regulation of cytokinesis in epithelial tissue could be studied by disrupting polarity proteins (*e.g.* PAR-6 beta) or cell junctions (*e.g.* ZO-1 or E-cadherin) in the endogenously-tagged MDCK cell line generated in Chapter 2 (Bruckner & Janshoff, 2018; Paim & FitzHarris, 2022).

The current dogma is that multiple redundant pathways regulate the localization of cortical regulators for ring assembly and ingression, and their relative contribution varies between cell types (Husser et al., 2021; Ozugergin & Piekny, 2022). In Chapter 2, we found that the timing and breadth of anillin localization varied extensively between the different cell lines and correlated (at least partially) with ploidy, suggesting that the chromatin sensing pathway plays a stronger role in regulating cytokinesis in cells with high aneuploidy. To show this, the relative contribution of different pathways could be elucidated by precisely disrupting or activating specific pathways and measuring the effect on anillin localization. For example, astral microtubules can be stabilized by knocking down the microtubule depolymerizer MCAK (also known as KIF2C) or via treatment with microtubule stabilizing compound Taxol (van Oostende Triplet et al., 2014; Zanin et al., 2013). We previously found that stabilizing microtubules causes a decrease in the breadth and cortical accumulation of anillin during early anaphase in HeLa cells (van Oostende Triplet et al., 2014; Zanin et al., 2013). The central spindle can be prevented from forming by knocking down MKLP1, which forms a complex with Cyk4 required for bundling central spindle microtubules. In HeLa cells, MKLP1 knockdown causes an increase in the breadth of anillin and active RhoA localization during early telophase (van Oostende Triplet et al., 2014; Yuce et al., 2005). Meanwhile, the Ran gradient can be manipulated by changing cell ploidy, by the depletion or over-

expression of Ran regulators (*e.g.* RCC1, RanGAP, importin-beta), expressing membrane-tethered constitutively-active Ran (RanQ69L), or by the optogenetic recruitment or disruption of pathway components (Beaudet et al., 2017; Ozugergin et al., 2022b; Wang et al., 2020). In HeLa cells, anillin requires importin binding for cortical recruitment during anaphase, with the astral pathway restricting this localization to the equatorial cortex. A similar situation could explain why the breadth of anillin localization is narrower than the breadth of RhoA localization in iPSCs (Chapter 3). Perturbations similar to those performed in HeLa cells can be done in our endogenously tagged cell lines to reveal how the timing and contribution of the different pathways controlling cytokinesis changes with cell type.

4.2.2 Using iPSCs to study protein localization

iPSCs are a promising system to study cellular processes in healthy human cells. Unlike most cell lines cultured *in vitro*, iPSCs are not cancerous or transformed, carry a normal genome, and have the potential to differentiate into any cell type derived from the three embryonic germ layers. These characteristics enable comparative studies of cytokinesis and other cellular processes across differentiated cell types in an isogenic system (Drubin & Hyman, 2017). iPSCs can also be used to form organoids, which recapitulate the development and structure of human organs (Kim et al., 2020). In the future, the derivation of embryo-like structures from human iPSCs will also allow for the study of early embryonic development (Handford et al., 2023). However, differentiated cells and organoids are difficult to transfect, and immunofluorescence staining precludes the study of live cells. Endogenous tags generated in iPSCs prior to differentiation or organoid formation can provide quantitative readouts of protein expression and localization in live systems. In Chapter 3, I generated human iPSCs with endogenously tagged proteins that can be

used for localization studies in live cells. The parental line used to generate these lines will accelerate endogenous tagging in human iPSCs, which will benefit studies of cellular processes, cell differentiation, embryonic development, and tissue and organ development.

4.2.3 Applications of endogenous tags beyond localization

In this thesis, I used timelapse imaging to study the localization of endogenously tagged proteins. However, other methods could also be used with these tags to obtain additional important information. For example, fluorescence correlation spectroscopy can be used to measure absolute protein concentration in cells (Yu et al., 2021), while super-resolution microscopy can be used to reveal finer structural details (Ratz et al., 2015). Endogenous tags can also be used to screen and identify protein-targeting compounds for therapy (Khachatryan et al., 2023). Finally, biochemical assays can be performed on endogenously tagged proteins. For example, Cho et al. (2022) performed pull-downs of proteins endogenously tagged with $mNG2_{11}$ to identify protein-protein interactions and protein complexes. For biochemical studies, endogenous tagging with epitope tags or enzymes provides more accurate readouts of endogenous protein complexes than over-expression (Dolgalev & Poverennaya, 2021; O'Hagan et al., 2021; Vandemoortele et al., 2019). However, cell lines tagged endogenously with biochemical tags are harder to generate without a fluorescent marker for isolation and screening.

4.3 Re-purposing tools for endogenous tagging

In Chapters 2 and 3, I generated multiple tools and resources that are available to the community, including the constructs used for endogenous tagging, as well as the tagged cell lines. Successful endogenous tagging requires a sgRNA that can efficiently target a gene at a specific

site (usually at the start or end of the coding sequence), and a repair template to introduce the fluorescent tag at the correct site. In Chapter 2, I re-purposed pre-existing designs to endogenously tag H2B histones, actin, and tubulin with different fluorescent proteins (Allencell.org; Roberts et al., 2017). This enabled the co-visualization of proteins tagged with fluorescent proteins with different emission wavelengths. I also showed that endogenous tagging constructs designed to target the human genome can be used to tag the same protein in any human cell line, although each cell line presented unique challenges. Other groups have generated and shared similar tools with the community (de Man et al., 2021; Pinder et al., 2015; Roberts et al., 2017; Sakuma et al., 2016; Savic et al., 2015; Sun et al., 2021; Allencell.org; Addgene.org). The tools generated in Chapter 2 focused on specific proteins: anillin, Ect2, RhoA, H2B, actin and tubulin. Several of these proteins are involved in cytokinesis, but also in other cellular processes. For example, RhoA is a small GTPase that controls actin polymerization and myosin activation in the context of cell migration, polarity, and adhesion, amongst other cellular processes (Kim et al., 2018a). Furthermore, H2B histones, actin and tubulin are commonly used to visualize DNA and cytoskeletal structures, which can be useful for more generally following cell division, cell shape, and other processes (Aoki et al., 2017; Kiyonari et al., 2019; Melak et al., 2017). Therefore, the utility of these tools extends well beyond the field of cytokinesis to studies of different cellular processes in human cells.

4.4 Large-scale endogenous tagging in human iPSCs

4.4.1 Mapping genome-wide protein localization

Mapping the localization of all proteins encoded in the human genome has been the subject of multiple large-scale projects (Cho et al., 2022; Simpson et al., 2000; Thul & Lindskog, 2018). The Human Protein Atlas aimed to generate and use protein-specific antibodies to reveal protein

localization in fixed cells and tissues (Thul & Lindskog, 2018). Another approach involves the generation of whole-genome ORF libraries to express tagged ORFs in human cells to visualize protein localization (Simpson et al., 2000). However, over-expression can cause localization artefacts (as shown in Chapter 2; Mahen et al., 2014; Rizzo et al., 2009). Finally, the OpenCell project aimed to endogenously tag proteins with split mNeonGreen in HEK293 cells, enabling large-scale endogenous tagging for the first time in human cells (Cho et al., 2022). However, large-scale endogenous tagging has only been done in HEK293 cells, limiting studies of the tagged proteins to this cell line. By enabling large-scale endogenous tagging in iPSCs, my work provides the basis for the visualization of all proteins encoded by the entire genome at the endogenous level and across a broader range of differentiated cells. This project could be extended to studying protein localization in tissues and organoids cultured *in vitro*, as well as during different cell cycle stages in different cell types. Further editing can be done to model diseases and uncover how protein localization changes in diseases. Creating such an atlas of human protein localization will enable comparative studies of protein function across cell types and in pathologies.

4.4.2 High-throughput gene editing

As described in Chapter 3, my work provides tools for large-scale endogenous tagging in human iPSCs. However, high-throughput gene editing in human cells will require automation to handle hundreds to thousands of samples at once. Towards this objective, I designed a workflow for the automation of endogenous tagging in human iPSCs (Fig. 4.1). Using equipment available in the Concordia Genome Foundry, this workflow automates as many steps as possible, from nucleofection to the screening of edited clones, using an automated liquid-handling platform connected to an incubator, microscope and nucleofector. Specifically, the following steps can be

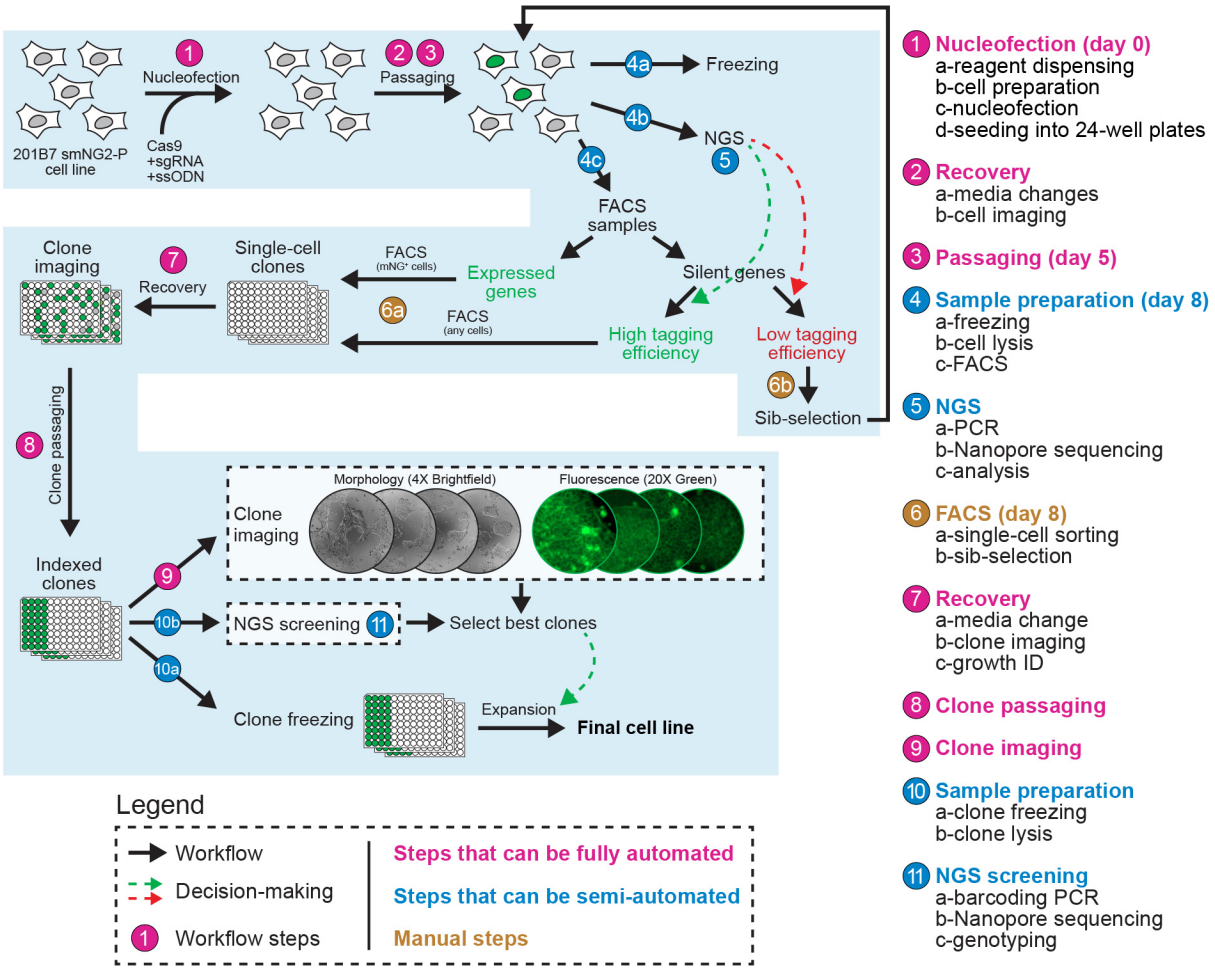

Figure 4.1. Automation of the endogenous tagging workflow in iPSCs. A theoretical workflow to automate the generation of endogenously-tagged iPSC cell lines is shown. Starting with the smNG2-P cell line (top left), the steps required for endogenous tagging, maintenance, clone isolation and screening are indicated by colored circles. The steps are listed in more detail on the right. Steps that can be readily automated are shown in pink, steps that can be semi-automated are shown in blue, and manual steps are shown in brown. Different workflows are shown for the tagging of silent genes, and workflow decisions are indicated in dashed arrows when required.

fully automated: nucleofection, media changes, monitoring of cell growth and cell passaging; and the following steps can be semi-automated: sample freezing, cell preparation for lysis and FACS, and PCR genotyping. iPSC culture has been automated before using different robotic systems,

often for the purpose of iPSC generation or differentiation (Bando et al., 2022; Boussaad et al., 2021; Elanzew et al., 2020; Paull et al., 2015; Tristan et al., 2021; Truong et al., 2021). The decision-making steps required during culturing can also be automated using image-based measurements of confluency and colony morphology to automatically assess whether the cells are ready to be passaged daily (Ker et al., 2011). Similarly, as shown in Chapter 3, 96-well plates can be screened for clonal recovery after FACS using an image-based pipeline, and the positive wells can be automatically selected for further passaging and analysis. Finally, the analysis of flow cytometry and sequencing data can also be automated to make decisions that can be verified by the user.

4.4.3 Challenges of high-throughput endogenous tagging in iPSCs

The isolation of tagged clones by FACS relies on the expression of the tagged protein to produce a fluorescent signal. However, some genes are not expressed in iPSCs but only in differentiated cells. Such genes can be tagged endogenously for the purpose of studying protein expression and function in differentiated cells. For these silent genes, isolating tagged cells can be challenging as the fluorescent tag is not expressed in undifferentiated cells. In cases where tagging is very efficient (*e.g.* PAX6, TBXT and FOXA2 in Chapter 3), many clones can be isolated and screened at the genetic level until a tagged clone is found. However, when tagging efficiency is lower (*e.g.* KRT14 in Chapter 3), hundreds to thousands of clones may need to be screened. Alternatively, an approach called sub-selection can be used, where an edited population is split into sub-populations of 100-10,000 cells, which are then screened for the presence of the edited allele (Fig. 4.1; Deneault et al., 2018; Miyaoka et al., 2014; Sumer et al., 2020). The sub-population with the highest frequency of edited alleles is then selected for more rounds of splitting and

screening, until a nearly clonal population is obtained. Other strategies can be used where the tag is introduced with an antibiotic resistance or fluorescence marker, which can be removed later (Kim et al., 2018b; Li et al., 2016; Perez-Leal et al., 2021; Roberts et al., 2019). However, larger knock-ins require larger repair templates that will integrate with lower efficiency compared to smaller knock-ins.

The automation of endogenous tagging will generate many cell lines that need to be validated. First, the observed localization of each protein should be verified against existing knowledge to avoid false positives. For this, localization to different subcellular locations can be quantified and compared to existing datasets like the Human Protein Atlas (Cho et al., 2022; Thul & Lindskog, 2018). Proteins that form higher-level complexes often have similar localization patterns (Cho et al., 2022). Moreover, edited iPS cell lines require extensive quality control, as shown in Chapter 3 for the smNG2-P cell line. Quality control steps should be simplified and automated to validate a large number of edited cell lines in parallel. For example, high-throughput karyotyping can be carried out by selecting a few genomic sites for copy number quantification by qPCR (D'Hulst et al., 2013). Similarly, the evaluation of pluripotency and differentiation marker expression can be carried out using RT-qPCR (reverse transcriptase quantitative PCR), which is more amenable to automation (Kuang et al., 2019; Mittal et al., 2022).

4.5 Conclusion

Despite challenges, precision gene editing is a valuable tool to study how human cells function. Specifically, CRISPR/Cas9 can be used to generate cell lines that carry endogenous tags, in which a protein of interest can be visualized in its native cellular environment. In this thesis, I demonstrated the utility of endogenous tags compared to over-expressed transgenes for studies of

protein localization by tagging and characterizing several proteins involved in cytokinesis. Future work should focus on using iPSCs as a model to study cellular processes in a broad range of healthy human cell types. The tools developed in this work for genome-scale endogenous tagging can support this effort to study healthy human cells, as well as tissue and organ development *in vitro*.

BIBLIOGRAPHY

Abe, T., Kiyonari, H., Shioi, G., Inoue, K., Nakao, K., Aizawa, S., & Fujimori, T. (2011, Jul). Establishment of conditional reporter mouse lines at ROSA26 locus for live cell imaging. *Genesis, 49*(7), 579-590. https://doi.org/10.1002/dvg.20753

Ackerson, S. M., Romney, C., Schuck, P. L., & Stewart, J. A. (2021). To Join or Not to Join: Decision Points Along the Pathway to Double-Strand Break Repair vs. Chromosome End Protection. *Front Cell Dev Biol, 9*, 708763. https://doi.org/10.3389/fcell.2021.708763

Adli, M. (2018, May 15). The CRISPR tool kit for genome editing and beyond. *Nat Commun, 9*(1), 1911. https://doi.org/10.1038/s41467-018-04252-2

Adriaans, I. E., Basant, A., Ponsioen, B., Glotzer, M., & Lens, S. M. A. (2019, Apr 1). PLK1 plays dual roles in centralspindlin regulation during cytokinesis. *J Cell Biol, 218*(4), 1250-1264. https://doi.org/10.1083/jcb.201805036

Aird, E. J., Lovendahl, K. N., St Martin, A., Harris, R. S., & Gordon, W. R. (2018). Increasing Cas9-mediated homology-directed repair efficiency through covalent tethering of DNA repair template. *Commun Biol, 1*, 54. https://doi.org/10.1038/s42003-018-0054-2

Allen, D., Rosenberg, M., & Hendel, A. (2020). Using Synthetically Engineered Guide RNAs to Enhance CRISPR Genome Editing Systems in Mammalian Cells. *Front Genome Ed, 2*, 617910. https://doi.org/10.3389/fgeed.2020.617910

Anzalone, A. V., Koblan, L. W., & Liu, D. R. (2020, Jul). Genome editing with CRISPR-Cas nucleases, base editors, transposases and prime editors. *Nat Biotechnol, 38*(7), 824-844. https://doi.org/10.1038/s41587-020-0561-9

Anzalone, A. V., Randolph, P. B., Davis, J. R., Sousa, A. A., Koblan, L. W., Levy, J. M., Chen, P. J., Wilson, C., Newby, G. A., Raguram, A., & Liu, D. R. (2019, Dec). Search-and-replace genome editing without double-strand breaks or donor DNA. *Nature, 576*(7785), 149-157. https://doi.org/10.1038/s41586-019-1711-4

Aoki, K., Kondo, Y., Naoki, H., Hiratsuka, T., Itoh, R. E., & Matsuda, M. (2017, Nov 6). Propagating Wave of ERK Activation Orients Collective Cell Migration. *Dev Cell, 43*(3), 305-317 e305. https://doi.org/10.1016/j.devcel.2017.10.016

Arias-Fuenzalida, J., Jarazo, J., Qing, X., Walter, J., Gomez-Giro, G., Nickels, S. L., Zaehres, H., Scholer, H. R., & Schwamborn, J. C. (2017, Nov 14). FACS-Assisted CRISPR-Cas9 Genome Editing Facilitates Parkinson's Disease Modeling. *Stem Cell Reports, 9*(5), 1423-1431. https://doi.org/10.1016/j.stemcr.2017.08.026

Artegiani, B., Hendriks, D., Beumer, J., Kok, R., Zheng, X., Joore, I., Chuva de Sousa Lopes, S., van Zon, J., Tans, S., & Clevers, H. (2020, Mar). Fast and efficient generation of knock-in human

organoids using homology-independent CRISPR-Cas9 precision genome editing. *Nat Cell Biol, 22*(3), 321-331. https://doi.org/10.1038/s41556-020-0472-5

Asmamaw Mengstie, M. (2022). Viral Vectors for the in Vivo Delivery of CRISPR Components: Advances and Challenges. *Front Bioeng Biotechnol, 10*, 895713. https://doi.org/10.3389/fbioe.2022.895713

Aznauryan, E., Yermanos, A., Kinzina, E., Devaux, A., Kapetanovic, E., Milanova, D., Church, G. M., & Reddy, S. T. (2022, Jan 24). Discovery and validation of human genomic safe harbor sites for gene and cell therapies. *Cell Rep Methods, 2*(1), 100154. https://doi.org/10.1016/j.crmeth.2021.100154

Bai, X., Melesse, M., Sorensen Turpin, C. G., Sloan, D. E., Chen, C. Y., Wang, W. C., Lee, P. Y., Simmons, J. R., Nebenfuehr, B., Mitchell, D., Klebanow, L. R., Mattson, N., Betzig, E., Chen, B. C., Cheerambathur, D., & Bembenek, J. N. (2020, Jan 8). Aurora B functions at the apical surface after specialized cytokinesis during morphogenesis in C. elegans. *Development, 147*(1). https://doi.org/10.1242/dev.181099

Balcarova-Stander, J., Pfeiffer, S. E., Fuller, S. D., & Simons, K. (1984, Nov). Development of cell surface polarity in the epithelial Madin-Darby canine kidney (MDCK) cell line. *EMBO J, 3*(11), 2687-2694. https://doi.org/10.1002/j.1460-2075.1984.tb02194.x

Balmas, E., Sozza, F., Bottini, S., Ratto, M. L., Savore, G., Becca, S., Snijders, K. E., & Bertero, A. (2023, Jul 30). Manipulating and studying gene function in human pluripotent stem cell models. *FEBS Lett*. https://doi.org/10.1002/1873-3468.14709

Bando, K., Yamashita, H., Tsumori, M., Minoura, H., Okumura, K., & Hattori, F. (2022). Compact automated culture machine for human induced pluripotent stem cell maintenance and differentiation. *Front Bioeng Biotechnol, 10*, 1074990. https://doi.org/10.3389/fbioe.2022.1074990

Basant, A., & Glotzer, M. (2018, May 7). Spatiotemporal Regulation of RhoA during Cytokinesis. *Curr Biol, 28*(9), R570-R580. https://doi.org/10.1016/j.cub.2018.03.045

Basant, A., Lekomtsev, S., Tse, Y. C., Zhang, D., Longhini, K. M., Petronczki, M., & Glotzer, M. (2015, Apr 20). Aurora B kinase promotes cytokinesis by inducing centralspindlin oligomers that associate with the plasma membrane. *Dev Cell, 33*(2), 204-215. https://doi.org/10.1016/j.devcel.2015.03.015

Beaudet, D., Akhshi, T., Phillipp, J., Law, C., & Piekny, A. (2017, Nov 15). Active Ran regulates anillin function during cytokinesis. *Mol Biol Cell, 28*(24), 3517-3531. https://doi.org/10.1091/mbc.E17-04-0253

Beaudet, D., Pham, N., Skaik, N., & Piekny, A. (2020, May 15). Importin binding mediates the intramolecular regulation of anillin during cytokinesis. *Mol Biol Cell, 31*(11), 1124-1139. https://doi.org/10.1091/mbc.E20-01-0006

Bell, K. R., Werner, M. E., Doshi, A., Cortes, D. B., Sattler, A., Vuong-Brender, T., Labouesse, M., & Maddox, A. S. (2020, Jul 15). Novel cytokinetic ring components drive negative feedback in cortical contractility. *Mol Biol Cell, 31*(15), 1623-1636. https://doi.org/10.1091/mbc.E20-05-0304

Bement, W. M., Benink, H. A., & von Dassow, G. (2005, Jul 4). A microtubule-dependent zone of active RhoA during cleavage plane specification. *J Cell Biol, 170*(1), 91-101. https://doi.org/10.1083/jcb.200501131

Ben-David, U., Siranosian, B., Ha, G., Tang, H., Oren, Y., Hinohara, K., Strathdee, C. A., Dempster, J., Lyons, N. J., Burns, R., Nag, A., Kugener, G., Cimini, B., Tsvetkov, P., Maruvka, Y. E., O'Rourke, R., Garrity, A., Tubelli, A. A., Bandopadhayay, P., Tsherniak, A., Vazquez, F., Wong, B., Birger, C., Ghandi, M., Thorner, A. R., Bittker, J. A., Meyerson, M., Getz, G., Beroukhim, R., & Golub, T. R. (2018, Aug). Genetic and transcriptional evolution alters cancer cell line drug response. *Nature, 560*(7718), 325-330. https://doi.org/10.1038/s41586-018-0409-3

Bhargava, N., Thakur, P., Muruganandam, T. P., Jaitly, S., Gupta, P., Lohani, N., Goswami, S. G., Saravanakumar, V., Bhattacharya, S. K., Jain, S., & Ramalingam, S. (2022, Aug). Development of an efficient single-cell cloning and expansion strategy for genome edited induced pluripotent stem cells. *Mol Biol Rep, 49*(8), 7887-7898. https://doi.org/10.1007/s11033-022-07621-9

Bharucha, N., Ataam, J. A., Gavidia, A. A., & Karakikes, I. (2021, Nov 24). Generation of AAVS1 integrated doxycycline-inducible CRISPR-Prime Editor human induced pluripotent stem cell line. *Stem Cell Res, 57*, 102610. https://doi.org/10.1016/j.scr.2021.102610

Bilic, J., & Izpisua Belmonte, J. C. (2012, Jan). Concise review: Induced pluripotent stem cells versus embryonic stem cells: close enough or yet too far apart? *Stem Cells, 30*(1), 33-41. https://doi.org/10.1002/stem.700

Birling, M. C., Schaeffer, L., Andre, P., Lindner, L., Marechal, D., Ayadi, A., Sorg, T., Pavlovic, G., & Herault, Y. (2017, Mar 7). Efficient and rapid generation of large genomic variants in rats and mice using CRISMERE. *Sci Rep, 7*, 43331. https://doi.org/10.1038/srep43331

Bock, C., Kiskinis, E., Verstappen, G., Gu, H., Boulting, G., Smith, Z. D., Ziller, M., Croft, G. F., Amoroso, M. W., Oakley, D. H., Gnirke, A., Eggan, K., & Meissner, A. (2011, Feb 4). Reference Maps of human ES and iPS cell variation enable high-throughput characterization of pluripotent cell lines. *Cell, 144*(3), 439-452. https://doi.org/10.1016/j.cell.2010.12.032

Bodnar, A. G., Ouellette, M., Frolkis, M., Holt, S. E., Chiu, C. P., Morin, G. B., Harley, C. B., Shay, J. W., Lichtsteiner, S., & Wright, W. E. (1998, Jan 16). Extension of life-span by introduction of telomerase into normal human cells. *Science, 279*(5349), 349-352. https://doi.org/10.1126/science.279.5349.349

Boroviak, K., Fu, B., Yang, F., Doe, B., & Bradley, A. (2017, Oct 9). Revealing hidden complexities of genomic rearrangements generated with Cas9. *Sci Rep, 7*(1), 12867. https://doi.org/10.1038/s41598-017-12740-6

Bourdages, K. G., Lacroix, B., Dorn, J. F., Descovich, C. P., & Maddox, A. S. (2014). Quantitative analysis of cytokinesis in situ during C. elegans postembryonic development. *PLoS One, 9*(10), e110689. https://doi.org/10.1371/journal.pone.0110689

Boussaad, I., Cruciani, G., Bolognin, S., Antony, P., Dording, C. M., Kwon, Y. J., Heutink, P., Fava, E., Schwamborn, J. C., & Kruger, R. (2021, Jan 14). Integrated, automated maintenance, expansion and differentiation of 2D and 3D patient-derived cellular models for high throughput drug screening. *Sci Rep, 11*(1), 1439. https://doi.org/10.1038/s41598-021-81129-3

Bruckner, B. R., & Janshoff, A. (2018, Sep 20). Importance of integrity of cell-cell junctions for the mechanics of confluent MDCK II cells. *Sci Rep, 8*(1), 14117. https://doi.org/10.1038/s41598-018-32421-2

Budnar, S., Husain, K. B., Gomez, G. A., Naghibosadat, M., Varma, A., Verma, S., Hamilton, N. A., Morris, R. G., & Yap, A. S. (2019, Jun 17). Anillin Promotes Cell Contractility by Cyclic Resetting of RhoA Residence Kinetics. *Dev Cell, 49*(6), 894-906 e812. https://doi.org/10.1016/j.devcel.2019.04.031

Bukhari, H., & Muller, T. (2019, Nov). Endogenous Fluorescence Tagging by CRISPR. *Trends Cell Biol, 29*(11), 912-928. https://doi.org/10.1016/j.tcb.2019.08.004

Burgio, G., & Teboul, L. (2020, Dec). Anticipating and Identifying Collateral Damage in Genome Editing. *Trends Genet, 36*(12), 905-914. https://doi.org/10.1016/j.tig.2020.09.011

Burkard, M. E., Maciejowski, J., Rodriguez-Bravo, V., Repka, M., Lowery, D. M., Clauser, K. R., Zhang, C., Shokat, K. M., Carr, S. A., Yaffe, M. B., & Jallepalli, P. V. (2009, May 5). Plk1 self-organization and priming phosphorylation of HsCYK-4 at the spindle midzone regulate the onset of division in human cells. *PLoS Biol, 7*(5), e1000111. https://doi.org/10.1371/journal.pbio.1000111

Bylund, L., Kytola, S., Lui, W. O., Larsson, C., & Weber, G. (2004). Analysis of the cytogenetic stability of the human embryonal kidney cell line 293 by cytogenetic and STR profiling approaches. *Cytogenet Genome Res, 106*(1), 28-32. https://doi.org/10.1159/000078556

Cabernard, C., Prehoda, K. E., & Doe, C. Q. (2010, Sep 2). A spindle-independent cleavage furrow positioning pathway. *Nature, 467*(7311), 91-94. https://doi.org/10.1038/nature09334

Cabrera, A., Edelstein, H. I., Glykofrydis, F., Love, K. S., Palacios, S., Tycko, J., Zhang, M., Lensch, S., Shields, C. E., Livingston, M., Weiss, R., Zhao, H., Haynes, K. A., Morsut, L., Chen, Y. Y., Khalil, A. S., Wong, W. W., Collins, J. J., Rosser, S. J., Polizzi, K., Elowitz, M. B., Fussenegger, M., Hilton, I. B., Leonard, J. N., Bintu, L., Galloway, K. E., & Deans, T. L. (2022,

Dec 21). The sound of silence: Transgene silencing in mammalian cell engineering. *Cell Syst, 13*(12), 950-973. https://doi.org/10.1016/j.cels.2022.11.005

Cai, Y., Hossain, M. J., Heriche, J. K., Politi, A. Z., Walther, N., Koch, B., Wachsmuth, M., Nijmeijer, B., Kueblbeck, M., Martinic-Kavur, M., Ladurner, R., Alexander, S., Peters, J. M., & Ellenberg, J. (2018, Sep). Experimental and computational framework for a dynamic protein atlas of human cell division. *Nature, 561*(7723), 411-415. https://doi.org/10.1038/s41586-018-0518-z

Campa, C. C., Weisbach, N. R., Santinha, A. J., Incarnato, D., & Platt, R. J. (2019, Sep). Multiplexed genome engineering by Cas12a and CRISPR arrays encoded on single transcripts. *Nat Methods, 16*(9), 887-893. https://doi.org/10.1038/s41592-019-0508-6

Canman, J. C., Cameron, L. A., Maddox, P. S., Straight, A., Tirnauer, J. S., Mitchison, T. J., Fang, G., Kapoor, T. M., & Salmon, E. D. (2003, Aug 28). Determining the position of the cell division plane. *Nature, 424*(6952), 1074-1078. https://doi.org/10.1038/nature01860

Canman, J. C., Hoffman, D. B., & Salmon, E. D. (2000, May 18). The role of pre- and post-anaphase microtubules in the cytokinesis phase of the cell cycle. *Curr Biol, 10*(10), 611-614. https://doi.org/10.1016/s0960-9822(00)00490-5

Canny, M. D., Moatti, N., Wan, L. C. K., Fradet-Turcotte, A., Krasner, D., Mateos-Gomez, P. A., Zimmermann, M., Orthwein, A., Juang, Y. C., Zhang, W., Noordermeer, S. M., Seclen, E., Wilson, M. D., Vorobyov, A., Munro, M., Ernst, A., Ng, T. F., Cho, T., Cannon, P. M., Sidhu, S. S., Sicheri, F., & Durocher, D. (2018, Jan). Inhibition of 53BP1 favors homology-dependent DNA repair and increases CRISPR-Cas9 genome-editing efficiency. *Nat Biotechnol, 36*(1), 95-102. https://doi.org/10.1038/nbt.4021

Carim, S. C., & Hickson, G. R. X. (2023, Jun 16). The Rho1 GTPase controls anillo-septin assembly to facilitate contractile ring closure during cytokinesis. *iScience, 26*(6), 106903. https://doi.org/10.1016/j.isci.2023.106903

Carim, S. C., Kechad, A., & Hickson, G. R. X. (2020). Animal Cell Cytokinesis: The Rho-Dependent Actomyosin-Anilloseptin Contractile Ring as a Membrane Microdomain Gathering, Compressing, and Sorting Machine. *Front Cell Dev Biol, 8*, 575226. https://doi.org/10.3389/fcell.2020.575226

Carvalho, A., Desai, A., & Oegema, K. (2009, May 29). Structural memory in the contractile ring makes the duration of cytokinesis independent of cell size. *Cell, 137*(5), 926-937. https://doi.org/10.1016/j.cell.2009.03.021

Cassio, D. (2013, Apr 24). Long term culture of MDCK strains alters chromosome content. *BMC Res Notes, 6*, 162. https://doi.org/10.1186/1756-0500-6-162

Cerbini, T., Funahashi, R., Luo, Y., Liu, C., Park, K., Rao, M., Malik, N., & Zou, J. (2015a). Transcription activator-like effector nuclease (TALEN)-mediated CLYBL targeting enables enhanced transgene expression and one-step generation of dual reporter human induced pluripotent

stem cell (iPSC) and neural stem cell (NSC) lines. *PLoS One, 10*(1), e0116032. https://doi.org/10.1371/journal.pone.0116032

Cerbini, T., Luo, Y., Rao, M. S., & Zou, J. (2015b, Feb 1). Transfection, selection, and colony-picking of human induced pluripotent stem cells TALEN-targeted with a GFP gene into the AAVS1 safe harbor. *J Vis Exp*(96). https://doi.org/10.3791/52504

Chaigne, A., Labouesse, C., White, I. J., Agnew, M., Hannezo, E., Chalut, K. J., & Paluch, E. K. (2020, Oct 26). Abscission Couples Cell Division to Embryonic Stem Cell Fate. *Dev Cell, 55*(2), 195-208 e195. https://doi.org/10.1016/j.devcel.2020.09.001

Chaigne, A., Smith, M. B., Lopez Cavestany, R., Hannezo, E., Chalut, K. J., & Paluch, E. K. (2021, Jul 15). Three-dimensional geometry controls division symmetry in stem cell colonies. *J Cell Sci, 134*(14). https://doi.org/10.1242/jcs.255018

Chalamalasetty, R. B., Hummer, S., Nigg, E. A., & Sillje, H. H. (2006, Jul 15). Influence of human Ect2 depletion and overexpression on cleavage furrow formation and abscission. *J Cell Sci, 119*(Pt 14), 3008-3019. https://doi.org/10.1242/jcs.03032

Chalfie, M., Tu, Y., Euskirchen, G., Ward, W. W., & Prasher, D. C. (1994, Feb 11). Green fluorescent protein as a marker for gene expression. *Science, 263*(5148), 802-805. https://doi.org/10.1126/science.8303295

Chambers, S. M., Fasano, C. A., Papapetrou, E. P., Tomishima, M., Sadelain, M., & Studer, L. (2009, Mar). Highly efficient neural conversion of human ES and iPS cells by dual inhibition of SMAD signaling. *Nat Biotechnol, 27*(3), 275-280. https://doi.org/10.1038/nbt.1529

Chan, F. Y., Silva, A. M., Saramago, J., Pereira-Sousa, J., Brighton, H. E., Pereira, M., Oegema, K., Gassmann, R., & Carvalho, A. X. (2019, Jan 1). The ARP2/3 complex prevents excessive formin activity during cytokinesis. *Mol Biol Cell, 30*(1), 96-107. https://doi.org/10.1091/mbc.E18-07-0471

Chen, A., Ulloa Severino, L., Panagiotou, T. C., Moraes, T. F., Yuen, D. A., Lavoie, B. D., & Wilde, A. (2021, Apr 23). Inhibition of polar actin assembly by astral microtubules is required for cytokinesis. *Nat Commun, 12*(1), 2409. https://doi.org/10.1038/s41467-021-22677-0

Chen, D., Hastie, E., & Sherwood, D. (2019, Dec 20). Endogenous expression of UNC-59/Septin in C. elegans. *MicroPubl Biol, 2019*. https://doi.org/10.17912/micropub.biology.000200

Chen, J. S., Dagdas, Y. S., Kleinstiver, B. P., Welch, M. M., Sousa, A. A., Harrington, L. B., Sternberg, S. H., Joung, J. K., Yildiz, A., & Doudna, J. A. (2017, Oct 19). Enhanced proofreading governs CRISPR-Cas9 targeting accuracy. *Nature, 550*(7676), 407-410. https://doi.org/10.1038/nature24268

Chen, M., Pan, H., Sun, L., Shi, P., Zhang, Y., Li, L., Huang, Y., Chen, J., Jiang, P., Fang, X., Wu, C., & Chen, Z. (2020, Jan 14). Structure and regulation of human epithelial cell transforming 2 protein. *Proc Natl Acad Sci U S A, 117*(2), 1027-1035. https://doi.org/10.1073/pnas.1913054117

Chen, S., Chen, D., Liu, B., & Haisma, H. J. (2022, Apr). Modulating CRISPR/Cas9 genome-editing activity by small molecules. *Drug Discov Today, 27*(4), 951-966. https://doi.org/10.1016/j.drudis.2021.11.018

Chen, X., Zaro, J. L., & Shen, W. C. (2013, Oct). Fusion protein linkers: property, design and functionality. *Adv Drug Deliv Rev, 65*(10), 1357-1369. https://doi.org/10.1016/j.addr.2012.09.039

Chen, Y. H., & Pruett-Miller, S. M. (2018, Aug). Improving single-cell cloning workflow for gene editing in human pluripotent stem cells. *Stem Cell Res, 31*, 186-192. https://doi.org/10.1016/j.scr.2018.08.003

Cho, N. H., Cheveralls, K. C., Brunner, A. D., Kim, K., Michaelis, A. C., Raghavan, P., Kobayashi, H., Savy, L., Li, J. Y., Canaj, H., Kim, J. Y. S., Stewart, E. M., Gnann, C., McCarthy, F., Cabrera, J. P., Brunetti, R. M., Chhun, B. B., Dingle, G., Hein, M. Y., Huang, B., Mehta, S. B., Weissman, J. S., Gomez-Sjoberg, R., Itzhak, D. N., Royer, L. A., Mann, M., & Leonetti, M. D. (2022, Mar 11). OpenCell: Endogenous tagging for the cartography of human cellular organization. *Science, 375*(6585), eabi6983. https://doi.org/10.1126/science.abi6983

Cho, S. W., Kim, S., Kim, Y., Kweon, J., Kim, H. S., Bae, S., & Kim, J. S. (2014, Jan). Analysis of off-target effects of CRISPR/Cas-derived RNA-guided endonucleases and nickases. *Genome Res, 24*(1), 132-141. https://doi.org/10.1101/gr.162339.113

Chu, V. T., Weber, T., Wefers, B., Wurst, W., Sander, S., Rajewsky, K., & Kuhn, R. (2015, May). Increasing the efficiency of homology-directed repair for CRISPR-Cas9-induced precise gene editing in mammalian cells. *Nat Biotechnol, 33*(5), 543-548. https://doi.org/10.1038/nbt.3198

Clarke, P. R., & Zhang, C. (2008, Jun). Spatial and temporal coordination of mitosis by Ran GTPase. *Nat Rev Mol Cell Biol, 9*(6), 464-477. https://doi.org/10.1038/nrm2410

Clavel, D., Gotthard, G., von Stetten, D., De Sanctis, D., Pasquier, H., Lambert, G. G., Shaner, N. C., & Royant, A. (2016, Dec 1). Structural analysis of the bright monomeric yellow-green fluorescent protein mNeonGreen obtained by directed evolution. *Acta Crystallogr D Struct Biol, 72*(Pt 12), 1298-1307. https://doi.org/10.1107/S2059798316018623

Clement, K., Rees, H., Canver, M. C., Gehrke, J. M., Farouni, R., Hsu, J. Y., Cole, M. A., Liu, D. R., Joung, J. K., Bauer, D. E., & Pinello, L. (2019, Mar). CRISPResso2 provides accurate and rapid genome editing sequence analysis. *Nat Biotechnol, 37*(3), 224-226. https://doi.org/10.1038/s41587-019-0032-3

Concordet, J. P., & Haeussler, M. (2018, Jul 2). CRISPOR: intuitive guide selection for CRISPR/Cas9 genome editing experiments and screens. *Nucleic Acids Res, 46*(W1), W242-W245. https://doi.org/10.1093/nar/gky354

Cong, L., Ran, F. A., Cox, D., Lin, S., Barretto, R., Habib, N., Hsu, P. D., Wu, X., Jiang, W., Marraffini, L. A., & Zhang, F. (2013, Feb 15). Multiplex genome engineering using CRISPR/Cas systems. *Science, 339*(6121), 819-823. https://doi.org/10.1126/science.1231143

Cui, Y., Xu, J., Cheng, M., Liao, X., & Peng, S. (2018, Jun). Review of CRISPR/Cas9 sgRNA Design Tools. *Interdiscip Sci, 10*(2), 455-465. https://doi.org/10.1007/s12539-018-0298-z

Cullot, G., Boutin, J., Toutain, J., Prat, F., Pennamen, P., Rooryck, C., Teichmann, M., Rousseau, E., Lamrissi-Garcia, I., Guyonnet-Duperat, V., Bibeyran, A., Lalanne, M., Prouzet-Mauleon, V., Turcq, B., Ged, C., Blouin, J. M., Richard, E., Dabernat, S., Moreau-Gaudry, F., & Bedel, A. (2019, Mar 8). CRISPR-Cas9 genome editing induces megabase-scale chromosomal truncations. *Nat Commun, 10*(1), 1136. https://doi.org/10.1038/s41467-019-09006-2

D'Avino, P. P., Giansanti, M. G., & Petronczki, M. (2015, Feb 13). Cytokinesis in animal cells. *Cold Spring Harb Perspect Biol, 7*(4), a015834. https://doi.org/10.1101/cshperspect.a015834

D'Hulst, C., Parvanova, I., Tomoiaga, D., Sapar, M. L., & Feinstein, P. (2013). Fast quantitative real-time PCR-based screening for common chromosomal aneuploidies in mouse embryonic stem cells. *Stem Cell Reports, 1*(4), 350-359. https://doi.org/10.1016/j.stemcr.2013.08.003

Dambournet, D., Hong, S. H., Grassart, A., & Drubin, D. G. (2014). Tagging endogenous loci for live-cell fluorescence imaging and molecule counting using ZFNs, TALENs, and Cas9. *Methods Enzymol, 546*, 139-160. https://doi.org/10.1016/B978-0-12-801185-0.00007-6

Dambournet, D., Sochacki, K. A., Cheng, A. T., Akamatsu, M., Taraska, J. W., Hockemeyer, D., & Drubin, D. G. (2018, Sep 3). Genome-edited human stem cells expressing fluorescently labeled endocytic markers allow quantitative analysis of clathrin-mediated endocytosis during differentiation. *J Cell Biol, 217*(9), 3301-3311. https://doi.org/10.1083/jcb.201710084

Davies, T., Kim, H. X., Romano Spica, N., Lesea-Pringle, B. J., Dumont, J., Shirasu-Hiza, M., & Canman, J. C. (2018, Jul 20). Cell-intrinsic and -extrinsic mechanisms promote cell-type-specific cytokinetic diversity. *Elife, 7*. https://doi.org/10.7554/eLife.36204

Dawes, J. C., Webster, P., Iadarola, B., Garcia-Diaz, C., Dore, M., Bolt, B. J., Dewchand, H., Dharmalingam, G., McLatchie, A. P., Kaczor, J., Caceres, J. J., Paccanaro, A., Game, L., Parrinello, S., & Uren, A. G. (2020). LUMI-PCR: an Illumina platform ligation-mediated PCR protocol for integration site cloning, provides molecular quantitation of integration sites. *Mob DNA, 11*, 7. https://doi.org/10.1186/s13100-020-0201-4

de Man, S. M., Zwanenburg, G., van der Wal, T., Hink, M. A., & van Amerongen, R. (2021, Jun 30). Quantitative live-cell imaging and computational modeling shed new light on endogenous WNT/CTNNB1 signaling dynamics. *Elife, 10*. https://doi.org/10.7554/eLife.66440

Deneault, E., White, S. H., Rodrigues, D. C., Ross, P. J., Faheem, M., Zaslavsky, K., Wang, Z., Alexandrova, R., Pellecchia, G., Wei, W., Piekna, A., Kaur, G., Howe, J. L., Kwan, V.,

Thiruvahindrapuram, B., Walker, S., Lionel, A. C., Pasceri, P., Merico, D., Yuen, R. K. C., Singh, K. K., Ellis, J., & Scherer, S. W. (2018, Nov 13). Complete Disruption of Autism-Susceptibility Genes by Gene Editing Predominantly Reduces Functional Connectivity of Isogenic Human Neurons. *Stem Cell Reports, 11*(5), 1211-1225. https://doi.org/10.1016/j.stemcr.2018.10.003

Derks, W., & Bergmann, O. (2020, Feb 14). Polyploidy in Cardiomyocytes: Roadblock to Heart Regeneration? *Circ Res, 126*(4), 552-565. https://doi.org/10.1161/CIRCRESAHA.119.315408

Dickinson, D. J., Ward, J. D., Reiner, D. J., & Goldstein, B. (2013, Oct). Engineering the Caenorhabditis elegans genome using Cas9-triggered homologous recombination. *Nat Methods, 10*(10), 1028-1034. https://doi.org/10.1038/nmeth.2641

Ding, W. Y., Ong, H. T., Hara, Y., Wongsantichon, J., Toyama, Y., Robinson, R. C., Nedelec, F., & Zaidel-Bar, R. (2017, May 1). Plastin increases cortical connectivity to facilitate robust polarization and timely cytokinesis. *J Cell Biol, 216*(5), 1371-1386. https://doi.org/10.1083/jcb.201603070

Doench, J. G., Fusi, N., Sullender, M., Hegde, M., Vaimberg, E. W., Donovan, K. F., Smith, I., Tothova, Z., Wilen, C., Orchard, R., Virgin, H. W., Listgarten, J., & Root, D. E. (2016, Feb). Optimized sgRNA design to maximize activity and minimize off-target effects of CRISPR-Cas9. *Nat Biotechnol, 34*(2), 184-191. https://doi.org/10.1038/nbt.3437

Dolgalev, G., & Poverennaya, E. (2021, Nov 12). Applications of CRISPR-Cas Technologies to Proteomics. *Genes (Basel), 12*(11). https://doi.org/10.3390/genes12111790

Donaldson, J. G. (2015, Dec 1). Immunofluorescence Staining. *Curr Protoc Cell Biol, 69*, 4 3 1-4 3 7. https://doi.org/10.1002/0471143030.cb0403s69

Donne, R., Saroul-Ainama, M., Cordier, P., Celton-Morizur, S., & Desdouets, C. (2020, Jul). Polyploidy in liver development, homeostasis and disease. *Nat Rev Gastroenterol Hepatol, 17*(7), 391-405. https://doi.org/10.1038/s41575-020-0284-x

Dorn, J. F., Zhang, L., Phi, T. T., Lacroix, B., Maddox, P. S., Liu, J., & Maddox, A. S. (2016, Apr 15). A theoretical model of cytokinesis implicates feedback between membrane curvature and cytoskeletal organization in asymmetric cytokinetic furrowing. *Mol Biol Cell, 27*(8), 1286-1299. https://doi.org/10.1091/mbc.E15-06-0374

Doyon, J. B., Zeitler, B., Cheng, J., Cheng, A. T., Cherone, J. M., Santiago, Y., Lee, A. H., Vo, T. D., Doyon, Y., Miller, J. C., Paschon, D. E., Zhang, L., Rebar, E. J., Gregory, P. D., Urnov, F. D., & Drubin, D. G. (2011, Mar). Rapid and efficient clathrin-mediated endocytosis revealed in genome-edited mammalian cells. *Nat Cell Biol, 13*(3), 331-337. https://doi.org/10.1038/ncb2175

Drubin, D. G., & Hyman, A. A. (2017, Jun 1). Stem cells: the new "model organism". *Mol Biol Cell, 28*(11), 1409-1411. https://doi.org/10.1091/mbc.E17-03-0183

El Amine, N., Kechad, A., Jananji, S., & Hickson, G. R. (2013, Nov 11). Opposing actions of septins and Sticky on Anillin promote the transition from contractile to midbody ring. *J Cell Biol, 203*(3), 487-504. https://doi.org/10.1083/jcb.201305053

El-Amine, N., Carim, S. C., Wernike, D., & Hickson, G. R. X. (2019, Aug 1). Rho-dependent control of the Citron kinase, Sticky, drives midbody ring maturation. *Mol Biol Cell, 30*(17), 2185-2204. https://doi.org/10.1091/mbc.E19-04-0194

Elanzew, A., Niessing, B., Langendoerfer, D., Rippel, O., Piotrowski, T., Schenk, F., Kulik, M., Peitz, M., Breitkreuz, Y., Jung, S., Wanek, P., Stappert, L., Schmitt, R. H., Haupt, S., Zenke, M., Konig, N., & Brustle, O. (2020). The StemCellFactory: A Modular System Integration for Automated Generation and Expansion of Human Induced Pluripotent Stem Cells. *Front Bioeng Biotechnol, 8*, 580352. https://doi.org/10.3389/fbioe.2020.580352

Erbs, V., Lorentz, R., Eisenman, B., Schaeffer, L., Luppi, L., Lindner, L., Herault, Y., Pavlovic, G., Wattenhofer-Donze, M., & Birling, M. C. (2023, Feb 3). Increased On-Target Rate and Risk of Concatemerization after CRISPR-Enhanced Targeting in ES Cells. *Genes (Basel), 14*(2). https://doi.org/10.3390/genes14020401

Eroglu, M., Yu, B., & Derry, B. (2023, May 31). Efficient CRISPR/Cas9 mediated large insertions using long single-stranded oligonucleotide donors in C. elegans. *FEBS J.* https://doi.org/10.1111/febs.16876

Fededa, J. P., & Gerlich, D. W. (2012, May 2). Molecular control of animal cell cytokinesis. *Nat Cell Biol, 14*(5), 440-447. https://doi.org/10.1038/ncb2482

Feng, S., Sekine, S., Pessino, V., Li, H., Leonetti, M. D., & Huang, B. (2017, Aug 29). Improved split fluorescent proteins for endogenous protein labeling. *Nat Commun, 8*(1), 370. https://doi.org/10.1038/s41467-017-00494-8

Feng, S., Varshney, A., Coto Villa, D., Modavi, C., Kohler, J., Farah, F., Zhou, S., Ali, N., Muller, J. D., Van Hoven, M. K., & Huang, B. (2019). Bright split red fluorescent proteins for the visualization of endogenous proteins and synapses. *Commun Biol, 2*, 344. https://doi.org/10.1038/s42003-019-0589-x

Ferreira da Silva, J., Oliveira, G. P., Arasa-Verge, E. A., Kagiou, C., Moretton, A., Timelthaler, G., Jiricny, J., & Loizou, J. I. (2022, Feb 9). Prime editing efficiency and fidelity are enhanced in the absence of mismatch repair. *Nat Commun, 13*(1), 760. https://doi.org/10.1038/s41467-022-28442-1

Field, C. M., & Alberts, B. M. (1995, Oct). Anillin, a contractile ring protein that cycles from the nucleus to the cell cortex. *J Cell Biol, 131*(1), 165-178. https://doi.org/10.1083/jcb.131.1.165

Foe, V. E., & von Dassow, G. (2008, Nov 3). Stable and dynamic microtubules coordinately shape the myosin activation zone during cytokinetic furrow formation. *J Cell Biol, 183*(3), 457-470. https://doi.org/10.1083/jcb.200807128

Fotopoulos, N., Wernike, D., Chen, Y., Makil, N., Marte, A., & Piekny, A. (2013, Nov 1). Caenorhabditis elegans anillin (ani-1) regulates neuroblast cytokinesis and epidermal morphogenesis during embryonic development. *Dev Biol, 383*(1), 61-74. https://doi.org/10.1016/j.ydbio.2013.08.024

Frenette, P., Haines, E., Loloyan, M., Kinal, M., Pakarian, P., & Piekny, A. (2012). An anillin-Ect2 complex stabilizes central spindle microtubules at the cortex during cytokinesis. *PLoS One, 7*(4), e34888. https://doi.org/10.1371/journal.pone.0034888

Friedland, A. E., Baral, R., Singhal, P., Loveluck, K., Shen, S., Sanchez, M., Marco, E., Gotta, G. M., Maeder, M. L., Kennedy, E. M., Kornepati, A. V., Sousa, A., Collins, M. A., Jayaram, H., Cullen, B. R., & Bumcrot, D. (2015, Nov 24). Characterization of Staphylococcus aureus Cas9: a smaller Cas9 for all-in-one adeno-associated virus delivery and paired nickase applications. *Genome Biol, 16*, 257. https://doi.org/10.1186/s13059-015-0817-8

Fu, Y. W., Dai, X. Y., Wang, W. T., Yang, Z. X., Zhao, J. J., Zhang, J. P., Wen, W., Zhang, F., Oberg, K. C., Zhang, L., Cheng, T., & Zhang, X. B. (2021, Jan 25). Dynamics and competition of CRISPR-Cas9 ribonucleoproteins and AAV donor-mediated NHEJ, MMEJ and HDR editing. *Nucleic Acids Res, 49*(2), 969-985. https://doi.org/10.1093/nar/gkaa1251

Fueller, J., Herbst, K., Meurer, M., Gubicza, K., Kurtulmus, B., Knopf, J. D., Kirrmaier, D., Buchmuller, B. C., Pereira, G., Lemberg, M. K., & Knop, M. (2020, Jun 1). CRISPR-Cas12a-assisted PCR tagging of mammalian genes. *J Cell Biol, 219*(6). https://doi.org/10.1083/jcb.201910210

Fus-Kujawa, A., Prus, P., Bajdak-Rusinek, K., Teper, P., Gawron, K., Kowalczuk, A., & Sieron, A. L. (2021). An Overview of Methods and Tools for Transfection of Eukaryotic Cells in vitro. *Front Bioeng Biotechnol, 9*, 701031. https://doi.org/10.3389/fbioe.2021.701031

Gaj, T., Staahl, B. T., Rodrigues, G. M. C., Limsirichai, P., Ekman, F. K., Doudna, J. A., & Schaffer, D. V. (2017, Jun 20). Targeted gene knock-in by homology-directed genome editing using Cas9 ribonucleoprotein and AAV donor delivery. *Nucleic Acids Res, 45*(11), e98. https://doi.org/10.1093/nar/gkx154

Ghanta, K. S., & Mello, C. C. (2020, Nov). Melting dsDNA Donor Molecules Greatly Improves Precision Genome Editing in Caenorhabditis elegans. *Genetics, 216*(3), 643-650. https://doi.org/10.1534/genetics.120.303564

Ghasemi, H. I., Bacal, J., Yoon, A. C., Tavasoli, K. U., Cruz, C., Vu, J. T., Gardner, B. M., & Richardson, C. D. (2023, Feb 27). Interstrand crosslinking of homologous repair template DNA enhances gene editing in human cells. *Nat Biotechnol*. https://doi.org/10.1038/s41587-022-01654-y

Ghetti, S., Burigotto, M., Mattivi, A., Magnani, G., Casini, A., Bianchi, A., Cereseto, A., & Fava, L. L. (2021, Jun 18). CRISPR/Cas9 ribonucleoprotein-mediated knockin generation in hTERT-RPE1 cells. *STAR Protoc, 2*(2), 100407. https://doi.org/10.1016/j.xpro.2021.100407

Gibson, T. J., Seiler, M., & Veitia, R. A. (2013, Aug). The transience of transient overexpression. *Nat Methods, 10*(8), 715-721. https://doi.org/10.1038/nmeth.2534

Giuliano, C. J., Lin, A., Girish, V., & Sheltzer, J. M. (2019, Sep). Generating Single Cell-Derived Knockout Clones in Mammalian Cells with CRISPR/Cas9. *Curr Protoc Mol Biol, 128*(1), e100. https://doi.org/10.1002/cpmb.100

Glaser, A., McColl, B., & Vadolas, J. (2016, Jul 12). GFP to BFP Conversion: A Versatile Assay for the Quantification of CRISPR/Cas9-mediated Genome Editing. *Mol Ther Nucleic Acids, 5*(7), e334. https://doi.org/10.1038/mtna.2016.48

Glotzer, M. (2017, Oct 3). Cytokinesis in Metazoa and Fungi. *Cold Spring Harb Perspect Biol, 9*(10). https://doi.org/10.1101/cshperspect.a022343

Gomez-Cavazos, J. S., Lee, K. Y., Lara-Gonzalez, P., Li, Y., Desai, A., Shiau, A. K., & Oegema, K. (2020, Aug 17). A Non-canonical BRCT-Phosphopeptide Recognition Mechanism Underlies RhoA Activation in Cytokinesis. *Curr Biol, 30*(16), 3101-3115 e3111. https://doi.org/10.1016/j.cub.2020.05.090

Grancharova, T., Gerbin, K. A., Rosenberg, A. B., Roco, C. M., Arakaki, J. E., DeLizo, C. M., Dinh, S. Q., Donovan-Maiye, R. M., Hirano, M., Nelson, A. M., Tang, J., Theriot, J. A., Yan, C., Menon, V., Palecek, S. P., Seelig, G., & Gunawardane, R. N. (2021, Aug 4). A comprehensive analysis of gene expression changes in a high replicate and open-source dataset of differentiating hiPSC-derived cardiomyocytes. *Sci Rep, 11*(1), 15845. https://doi.org/10.1038/s41598-021-94732-1

Grassart, A., Cheng, A. T., Hong, S. H., Zhang, F., Zenzer, N., Feng, Y., Briner, D. M., Davis, G. D., Malkov, D., & Drubin, D. G. (2014, Jun 9). Actin and dynamin2 dynamics and interplay during clathrin-mediated endocytosis. *J Cell Biol, 205*(5), 721-735. https://doi.org/10.1083/jcb.201403041

Green, R. A., Paluch, E., & Oegema, K. (2012). Cytokinesis in animal cells. *Annu Rev Cell Dev Biol, 28*, 29-58. https://doi.org/10.1146/annurev-cellbio-101011-155718

Gudipaty, S. A., Lindblom, J., Loftus, P. D., Redd, M. J., Edes, K., Davey, C. F., Krishnegowda, V., & Rosenblatt, J. (2017, Mar 2). Mechanical stretch triggers rapid epithelial cell division through Piezo1. *Nature, 543*(7643), 118-121. https://doi.org/10.1038/nature21407

Gupta, R. M., & Musunuru, K. (2014, Oct). Expanding the genetic editing tool kit: ZFNs, TALENs, and CRISPR-Cas9. *J Clin Invest, 124*(10), 4154-4161. https://doi.org/10.1172/JCI72992

Gutschner, T., Haemmerle, M., Genovese, G., Draetta, G. F., & Chin, L. (2016, Feb 16). Post-translational Regulation of Cas9 during G1 Enhances Homology-Directed Repair. *Cell Rep, 14*(6), 1555-1566. https://doi.org/10.1016/j.celrep.2016.01.019

Hackley, C. R. (2021, Apr). A Novel Set of Cas9 Fusion Proteins to Stimulate Homologous Recombination: Cas9-HRs. *CRISPR J, 4*(2), 253-263. https://doi.org/10.1089/crispr.2020.0034

Hammill, D. (2021). CytoExploreR: Interactive Analysis of Cytometry Data. R package version 1.1.0. *Github*. https://github.com/DillonHammill/CytoExploreR

Handford, C. E., Panda, P., Mohammad Choudhury, I. B., Amadei, G., & Zernicka-Goetz, M. (2023, Jun 8). Generation of Stem Cell-Based Mouse Embryo-Like Structures. *Methods Mol Biol*. https://doi.org/10.1007/7651_2023_493

Hanss, Z., Boussaad, I., Jarazo, J., Schwamborn, J. C., & Kruger, R. (2019). Quality Control Strategy for CRISPR-Cas9-Based Gene Editing Complicated by a Pseudogene. *Front Genet, 10*, 1297. https://doi.org/10.3389/fgene.2019.01297

Hara, T., Abe, M., Inoue, H., Yu, L. R., Veenstra, T. D., Kang, Y. H., Lee, K. S., & Miki, T. (2006, Jan 26). Cytokinesis regulator ECT2 changes its conformation through phosphorylation at Thr-341 in G2/M phase. *Oncogene, 25*(4), 566-578. https://doi.org/10.1038/sj.onc.1209078

Hart, K. C., Tan, J., Siemers, K. A., Sim, J. Y., Pruitt, B. L., Nelson, W. J., & Gloerich, M. (2017, Jul 18). E-cadherin and LGN align epithelial cell divisions with tissue tension independently of cell shape. *Proc Natl Acad Sci U S A, 114*(29), E5845-E5853. https://doi.org/10.1073/pnas.1701703114

Haupt, A., Grancharova, T., Arakaki, J., Fuqua, M. A., Roberts, B., & Gunawardane, R. N. (2018, Aug 25). Endogenous Protein Tagging in Human Induced Pluripotent Stem Cells Using CRISPR/Cas9. *J Vis Exp*(138). https://doi.org/10.3791/58130

He, X., Tan, C., Wang, F., Wang, Y., Zhou, R., Cui, D., You, W., Zhao, H., Ren, J., & Feng, B. (2016, May 19). Knock-in of large reporter genes in human cells via CRISPR/Cas9-induced homology-dependent and independent DNA repair. *Nucleic Acids Res, 44*(9), e85. https://doi.org/10.1093/nar/gkw064

Hendel, A., Bak, R. O., Clark, J. T., Kennedy, A. B., Ryan, D. E., Roy, S., Steinfeld, I., Lunstad, B. D., Kaiser, R. J., Wilkens, A. B., Bacchetta, R., Tsalenko, A., Dellinger, D., Bruhn, L., & Porteus, M. H. (2015, Sep). Chemically modified guide RNAs enhance CRISPR-Cas genome editing in human primary cells. *Nat Biotechnol, 33*(9), 985-989. https://doi.org/10.1038/nbt.3290

Herszterg, S., Pinheiro, D., & Bellaiche, Y. (2014, May). A multicellular view of cytokinesis in epithelial tissue. *Trends Cell Biol, 24*(5), 285-293. https://doi.org/10.1016/j.tcb.2013.11.009

Hickson, G. R., & O'Farrell, P. H. (2008, Jan 28). Rho-dependent control of anillin behavior during cytokinesis. *J Cell Biol, 180*(2), 285-294. https://doi.org/10.1083/jcb.200709005

Hoffman, H. K., Fernandez, M. V., Groves, N. S., Freed, E. O., & van Engelenburg, S. B. (2019, Nov 1). Genomic tagging of endogenous human ESCRT-I complex preserves ESCRT-mediated membrane-remodeling functions. *J Biol Chem, 294*(44), 16266-16281. https://doi.org/10.1074/jbc.RA119.009372

Holopainen, S., Hytonen, M. K., Syrja, P., Arumilli, M., Jarvinen, A. K., Rajamaki, M., & Lohi, H. (2017, Feb). ANLN truncation causes a familial fatal acute respiratory distress syndrome in Dalmatian dogs. *PLoS Genet, 13*(2), e1006625. https://doi.org/10.1371/journal.pgen.1006625

Hong, Y. J., & Do, J. T. (2019). Neural Lineage Differentiation From Pluripotent Stem Cells to Mimic Human Brain Tissues. *Front Bioeng Biotechnol, 7*, 400. https://doi.org/10.3389/fbioe.2019.00400

Horlbeck, M. A., Witkowsky, L. B., Guglielmi, B., Replogle, J. M., Gilbert, L. A., Villalta, J. E., Torigoe, S. E., Tjian, R., & Weissman, J. S. (2016, Mar 17). Nucleosomes impede Cas9 access to DNA in vivo and in vitro. *Elife, 5*. https://doi.org/10.7554/eLife.12677

Hsu, P. D., Scott, D. A., Weinstein, J. A., Ran, F. A., Konermann, S., Agarwala, V., Li, Y., Fine, E. J., Wu, X., Shalem, O., Cradick, T. J., Marraffini, L. A., Bao, G., & Zhang, F. (2013, Sep). DNA targeting specificity of RNA-guided Cas9 nucleases. *Nat Biotechnol, 31*(9), 827-832. https://doi.org/10.1038/nbt.2647

Huebinger, J., Spindler, J., Holl, K. J., & Koos, B. (2018, Dec 10). Quantification of protein mobility and associated reshuffling of cytoplasm during chemical fixation. *Sci Rep, 8*(1), 17756. https://doi.org/10.1038/s41598-018-36112-w

Huh, W. K., Falvo, J. V., Gerke, L. C., Carroll, A. S., Howson, R. W., Weissman, J. S., & O'Shea, E. K. (2003, Oct 16). Global analysis of protein localization in budding yeast. *Nature, 425*(6959), 686-691. https://doi.org/10.1038/nature02026

Husser, M. C., Ozugergin, I., Resta, T., Martin, V. J. J., & Piekny, A. J. (2022, Nov). Cytokinetic diversity in mammalian cells is revealed by the characterization of endogenous anillin, Ect2 and RhoA. *Open Biol, 12*(11), 220247. https://doi.org/10.1098/rsob.220247

Husser, M. C., Skaik, N., Martin, V. J. J., & Piekny, A. (2021, Apr 15). CRISPR-Cas tools to study gene function in cytokinesis. *J Cell Sci, 134*(8). https://doi.org/10.1242/jcs.254409

Hyman, A. H., & Simons, K. (2011, Nov 30). The new cell biology: Beyond HeLa cells. *Nature, 480*(7375), 34. https://doi.org/10.1038/480034a

Illukkumbura, R., Bland, T., & Goehring, N. W. (2020, Feb). Patterning and polarization of cells by intracellular flows. *Curr Opin Cell Biol, 62*, 123-134. https://doi.org/10.1016/j.ceb.2019.10.005

Inoue, Y. H., Savoian, M. S., Suzuki, T., Mathe, E., Yamamoto, M. T., & Glover, D. M. (2004, Jul 5). Mutations in orbit/mast reveal that the central spindle is comprised of two microtubule

populations, those that initiate cleavage and those that propagate furrow ingression. *J Cell Biol, 166*(1), 49-60. https://doi.org/10.1083/jcb.200402052

Inoue, Y. U., Morimoto, Y., Yamada, M., Kaneko, R., Shimaoka, K., Oki, S., Hotta, M., Asami, J., Koike, E., Hori, K., Hoshino, M., Imayoshi, I., & Inoue, T. (2021, Apr 30). An Optimized Preparation Method for Long ssDNA Donors to Facilitate Quick Knock-In Mouse Generation. *Cells, 10*(5). https://doi.org/10.3390/cells10051076

Irgen-Gioro, S., Yoshida, S., Walling, V., & Chong, S. (2022, Nov 29). Fixation can change the appearance of phase separation in living cells. *Elife, 11*. https://doi.org/10.7554/eLife.79903

Iwasaki, M., Kawahara, Y., Okubo, C., Yamakawa, T., Nakamura, M., Tabata, T., Nishi, Y., Narita, M., Ohta, A., Saito, H., Yamamoto, T., Nakagawa, M., Yamanaka, S., & Takahashi, K. (2022, May 20). Multi-omics approach reveals posttranscriptionally regulated genes are essential for human pluripotent stem cells. *iScience, 25*(5), 104289. https://doi.org/10.1016/j.isci.2022.104289

Jacobsen, L., Calvin, S., & Lobenhofer, E. (2009, Jul). Transcriptional effects of transfection: the potential for misinterpretation of gene expression data generated from transiently transfected cells. *Biotechniques, 47*(1), 617-624. https://doi.org/10.2144/000113132

Jananji, S., Risi, C., Lindamulage, I. K. S., Picard, L. P., Van Sciver, R., Laflamme, G., Albaghjati, A., Hickson, G. R. X., Kwok, B. H., & Galkin, V. E. (2017, Mar 10). Multimodal and Polymorphic Interactions between Anillin and Actin: Their Implications for Cytokinesis. *J Mol Biol, 429*(5), 715-731. https://doi.org/10.1016/j.jmb.2017.01.020

Jinek, M., Chylinski, K., Fonfara, I., Hauer, M., Doudna, J. A., & Charpentier, E. (2012, Aug 17). A programmable dual-RNA-guided DNA endonuclease in adaptive bacterial immunity. *Science, 337*(6096), 816-821. https://doi.org/10.1126/science.1225829

Kagita, A., Lung, M. S. Y., Xu, H., Kita, Y., Sasakawa, N., Iguchi, T., Ono, M., Wang, X. H., Gee, P., & Hotta, A. (2021, Apr 13). Efficient ssODN-Mediated Targeting by Avoiding Cellular Inhibitory RNAs through Precomplexed CRISPR-Cas9/sgRNA Ribonucleoprotein. *Stem Cell Reports, 16*(4), 985-996. https://doi.org/10.1016/j.stemcr.2021.02.013

Kamijo, K., Ohara, N., Abe, M., Uchimura, T., Hosoya, H., Lee, J. S., & Miki, T. (2006, Jan). Dissecting the role of Rho-mediated signaling in contractile ring formation. *Mol Biol Cell, 17*(1), 43-55. https://doi.org/10.1091/mbc.e05-06-0569

Kamiyama, D., Sekine, S., Barsi-Rhyne, B., Hu, J., Chen, B., Gilbert, L. A., Ishikawa, H., Leonetti, M. D., Marshall, W. F., Weissman, J. S., & Huang, B. (2016, Mar 18). Versatile protein tagging in cells with split fluorescent protein. *Nat Commun, 7*, 11046. https://doi.org/10.1038/ncomms11046

Karst, S. M., Ziels, R. M., Kirkegaard, R. H., Sorensen, E. A., McDonald, D., Zhu, Q., Knight, R., & Albertsen, M. (2021, Feb). High-accuracy long-read amplicon sequences using unique

molecular identifiers with Nanopore or PacBio sequencing. *Nat Methods, 18*(2), 165-169. https://doi.org/10.1038/s41592-020-01041-y

Kato-Inui, T., Takahashi, G., Hsu, S., & Miyaoka, Y. (2018, May 18). Clustered regularly interspaced short palindromic repeats (CRISPR)/CRISPR-associated protein 9 with improved proof-reading enhances homology-directed repair. *Nucleic Acids Res, 46*(9), 4677-4688. https://doi.org/10.1093/nar/gky264

Kechad, A., & Hickson, G. R. (2017). Imaging cytokinesis of Drosophila S2 cells. *Methods Cell Biol, 137*, 47-72. https://doi.org/10.1016/bs.mcb.2016.03.034

Kechad, A., Jananji, S., Ruella, Y., & Hickson, G. R. (2012, Feb 7). Anillin acts as a bifunctional linker coordinating midbody ring biogenesis during cytokinesis. *Curr Biol, 22*(3), 197-203. https://doi.org/10.1016/j.cub.2011.11.062

Keller, L., Bery, N., Tardy, C., Ligat, L., Favre, G., Rabbitts, T. H., & Olichon, A. (2019, Jan 9). Selection and Characterization of a Nanobody Biosensor of GTP-Bound RHO Activities. *Antibodies (Basel), 8*(1). https://doi.org/10.3390/antib8010008

Ker, D. F., Weiss, L. E., Junkers, S. N., Chen, M., Yin, Z., Sandbothe, M. F., Huh, S. I., Eom, S., Bise, R., Osuna-Highley, E., Kanade, T., & Campbell, P. G. (2011). An engineered approach to stem cell culture: automating the decision process for real-time adaptive subculture of stem cells. *PLoS One, 6*(11), e27672. https://doi.org/10.1371/journal.pone.0027672

Khachatryan, H., Olszowy, B., Barrero, C. A., Gordon, J., & Perez-Leal, O. (2023, Jan 29). Identification of Inhibitors of Tubulin Polymerization Using a CRISPR-Edited Cell Line with Endogenous Fluorescent Tagging of beta-Tubulin and Histone H1. *Biomolecules, 13*(2). https://doi.org/10.3390/biom13020249

Khaliullin, R. N., Green, R. A., Shi, L. Z., Gomez-Cavazos, J. S., Berns, M. W., Desai, A., & Oegema, K. (2018, Jul 2). A positive-feedback-based mechanism for constriction rate acceleration during cytokinesis in Caenorhabditis elegans. *Elife, 7*. https://doi.org/10.7554/eLife.36073

Kim, J., Koo, B. K., & Knoblich, J. A. (2020, Oct). Human organoids: model systems for human biology and medicine. *Nat Rev Mol Cell Biol, 21*(10), 571-584. https://doi.org/10.1038/s41580-020-0259-3

Kim, J. E., Billadeau, D. D., & Chen, J. (2005, Feb 18). The tandem BRCT domains of Ect2 are required for both negative and positive regulation of Ect2 in cytokinesis. *J Biol Chem, 280*(7), 5733-5739. https://doi.org/10.1074/jbc.M409298200

Kim, J. G., Islam, R., Cho, J. Y., Jeong, H., Cap, K. C., Park, Y., Hossain, A. J., & Park, J. B. (2018a, Sep). Regulation of RhoA GTPase and various transcription factors in the RhoA pathway. *J Cell Physiol, 233*(9), 6381-6392. https://doi.org/10.1002/jcp.26487

Kim, S., Kim, D., Cho, S. W., Kim, J., & Kim, J. S. (2014, Jun). Highly efficient RNA-guided genome editing in human cells via delivery of purified Cas9 ribonucleoproteins. *Genome Res, 24*(6), 1012-1019. https://doi.org/10.1101/gr.171322.113

Kim, S. I., Matsumoto, T., Kagawa, H., Nakamura, M., Hirohata, R., Ueno, A., Ohishi, M., Sakuma, T., Soga, T., Yamamoto, T., & Woltjen, K. (2018b, Mar 5). Microhomology-assisted scarless genome editing in human iPSCs. *Nat Commun, 9*(1), 939. https://doi.org/10.1038/s41467-018-03044-y

Kim, T. K., & Eberwine, J. H. (2010, Aug). Mammalian cell transfection: the present and the future. *Anal Bioanal Chem, 397*(8), 3173-3178. https://doi.org/10.1007/s00216-010-3821-6

Kim, Y. H., Kim, N., Okafor, I., Choi, S., Min, S., Lee, J., Bae, S. M., Choi, K., Choi, J., Harihar, V., Kim, Y., Kim, J. S., Kleinstiver, B. P., Lee, J. K., Ha, T., & Kim, H. H. (2023, Mar 9). Sniper2L is a high-fidelity Cas9 variant with high activity. *Nat Chem Biol*. https://doi.org/10.1038/s41589-023-01279-5

Kime, C., Mandegar, M. A., Srivastava, D., Yamanaka, S., Conklin, B. R., & Rand, T. A. (2016, Jan 1). Efficient CRISPR/Cas9-Based Genome Engineering in Human Pluripotent Stem Cells. *Curr Protoc Hum Genet, 88*, 21 24 21-21 24 23. https://doi.org/10.1002/0471142905.hg2104s88

Kiyomitsu, T., & Cheeseman, I. M. (2013, Jul 18). Cortical dynein and asymmetric membrane elongation coordinately position the spindle in anaphase. *Cell, 154*(2), 391-402. https://doi.org/10.1016/j.cell.2013.06.010

Kiyonari, H., Kaneko, M., Abe, T., Shioi, G., Aizawa, S., Furuta, Y., & Fujimori, T. (2019, Feb). Dynamic organelle localization and cytoskeletal reorganization during preimplantation mouse embryo development revealed by live imaging of genetically encoded fluorescent fusion proteins. *Genesis, 57*(2), e23277. https://doi.org/10.1002/dvg.23277

Koeppel, J., Weller, J., Peets, E. M., Pallaseni, A., Kuzmin, I., Raudvere, U., Peterson, H., Liberante, F. G., & Parts, L. (2023, Feb 16). Prediction of prime editing insertion efficiencies using sequence features and DNA repair determinants. *Nat Biotechnol*. https://doi.org/10.1038/s41587-023-01678-y

Koh, S. P., Pham, N. P., & Piekny, A. (2021, Aug 18). Seeing is believing: tools to study the role of Rho GTPases during cytokinesis. *Small GTPases*, 1-14. https://doi.org/10.1080/21541248.2021.1957384

Koh, S. P., Pham, N. P., & Piekny, A. (2022, Jan). Seeing is believing: tools to study the role of Rho GTPases during cytokinesis. *Small GTPases, 13*(1), 211-224. https://doi.org/10.1080/21541248.2021.1957384

Korbie, D. J., & Mattick, J. S. (2008). Touchdown PCR for increased specificity and sensitivity in PCR amplification. *Nat Protoc, 3*(9), 1452-1456. https://doi.org/10.1038/nprot.2008.133

Kosicki, M., Tomberg, K., & Bradley, A. (2018, Sep). Repair of double-strand breaks induced by CRISPR-Cas9 leads to large deletions and complex rearrangements. *Nat Biotechnol, 36*(8), 765-771. https://doi.org/10.1038/nbt.4192

Kotin, R. M., Siniscalco, M., Samulski, R. J., Zhu, X. D., Hunter, L., Laughlin, C. A., McLaughlin, S., Muzyczka, N., Rocchi, M., & Berns, K. I. (1990, Mar). Site-specific integration by adeno-associated virus. *Proc Natl Acad Sci U S A, 87*(6), 2211-2215. https://doi.org/10.1073/pnas.87.6.2211

Kotynkova, K., Su, K. C., West, S. C., & Petronczki, M. (2016, Dec 6). Plasma Membrane Association but Not Midzone Recruitment of RhoGEF ECT2 Is Essential for Cytokinesis. *Cell Rep, 17*(10), 2672-2686. https://doi.org/10.1016/j.celrep.2016.11.029

Kuang, Y. L., Munoz, A., Nalula, G., Santostefano, K. E., Sanghez, V., Sanchez, G., Terada, N., Mattis, A. N., Iacovino, M., Iribarren, C., Krauss, R. M., & Medina, M. W. (2019, May). Evaluation of commonly used ectoderm markers in iPSC trilineage differentiation. *Stem Cell Res, 37*, 101434. https://doi.org/10.1016/j.scr.2019.101434

Kuscu, C., Arslan, S., Singh, R., Thorpe, J., & Adli, M. (2014, Jul). Genome-wide analysis reveals characteristics of off-target sites bound by the Cas9 endonuclease. *Nat Biotechnol, 32*(7), 677-683. https://doi.org/10.1038/nbt.2916

Lacroix, B., & Maddox, A. S. (2012, Jan). Cytokinesis, ploidy and aneuploidy. *J Pathol, 226*(2), 338-351. https://doi.org/10.1002/path.3013

Landry, J. J., Pyl, P. T., Rausch, T., Zichner, T., Tekkedil, M. M., Stutz, A. M., Jauch, A., Aiyar, R. S., Pau, G., Delhomme, N., Gagneur, J., Korbel, J. O., Huber, W., & Steinmetz, L. M. (2013, Aug 7). The genomic and transcriptomic landscape of a HeLa cell line. *G3 (Bethesda), 3*(8), 1213-1224. https://doi.org/10.1534/g3.113.005777

Lazaro-Dieguez, F., & Musch, A. (2017, Nov 6). Cell-cell adhesion accounts for the different orientation of columnar and hepatocytic cell divisions. *J Cell Biol, 216*(11), 3847-3859. https://doi.org/10.1083/jcb.201608065

Lee, J. E., & Lee, D. R. (2011, Jun). Human embryonic stem cells: derivation, maintenance and cryopreservation. *Int J Stem Cells, 4*(1), 9-17. https://doi.org/10.15283/ijsc.2011.4.1.9

Lee, M. E., DeLoache, W. C., Cervantes, B., & Dueber, J. E. (2015, Sep 18). A Highly Characterized Yeast Toolkit for Modular, Multipart Assembly. *ACS Synth Biol, 4*(9), 975-986. https://doi.org/10.1021/sb500366v

Leibowitz, M. L., Papathanasiou, S., Doerfler, P. A., Blaine, L. J., Sun, L., Yao, Y., Zhang, C. Z., Weiss, M. J., & Pellman, D. (2021, Jun). Chromothripsis as an on-target consequence of CRISPR-Cas9 genome editing. *Nat Genet, 53*(6), 895-905. https://doi.org/10.1038/s41588-021-00838-7

Leite, J., Chan, F. Y., Osorio, D. S., Saramago, J., Sobral, A. F., Silva, A. M., Gassmann, R., & Carvalho, A. X. (2020). Equatorial Non-muscle Myosin II and Plastin Cooperate to Align and Compact F-actin Bundles in the Cytokinetic Ring. *Front Cell Dev Biol, 8*, 573393. https://doi.org/10.3389/fcell.2020.573393

Lekomtsev, S., Su, K. C., Pye, V. E., Blight, K., Sundaramoorthy, S., Takaki, T., Collinson, L. M., Cherepanov, P., Divecha, N., & Petronczki, M. (2012, Dec 13). Centralspindlin links the mitotic spindle to the plasma membrane during cytokinesis. *Nature, 492*(7428), 276-279. https://doi.org/10.1038/nature11773

Leonetti, M. D., Sekine, S., Kamiyama, D., Weissman, J. S., & Huang, B. (2016, Jun 21). A scalable strategy for high-throughput GFP tagging of endogenous human proteins. *Proc Natl Acad Sci U S A, 113*(25), E3501-3508. https://doi.org/10.1073/pnas.1606731113

Lewellyn, L., Dumont, J., Desai, A., & Oegema, K. (2010, Jan 1). Analyzing the effects of delaying aster separation on furrow formation during cytokinesis in the Caenorhabditis elegans embryo. *Mol Biol Cell, 21*(1), 50-62. https://doi.org/10.1091/mbc.E09-01-0089

Li, H. (2018, Sep 15). Minimap2: pairwise alignment for nucleotide sequences. *Bioinformatics, 34*(18), 3094-3100. https://doi.org/10.1093/bioinformatics/bty191

Li, H., Bielas, S. L., Zaki, M. S., Ismail, S., Farfara, D., Um, K., Rosti, R. O., Scott, E. C., Tu, S., Chi, N. C., Gabriel, S., Erson-Omay, E. Z., Ercan-Sencicek, A. G., Yasuno, K., Caglayan, A. O., Kaymakcalan, H., Ekici, B., Bilguvar, K., Gunel, M., & Gleeson, J. G. (2016, Aug 4). Biallelic Mutations in Citron Kinase Link Mitotic Cytokinesis to Human Primary Microcephaly. *Am J Hum Genet, 99*(2), 501-510. https://doi.org/10.1016/j.ajhg.2016.07.004

Liang, X., Potter, J., Kumar, S., Zou, Y., Quintanilla, R., Sridharan, M., Carte, J., Chen, W., Roark, N., Ranganathan, S., Ravinder, N., & Chesnut, J. D. (2015, Aug 20). Rapid and highly efficient mammalian cell engineering via Cas9 protein transfection. *J Biotechnol, 208*, 44-53. https://doi.org/10.1016/j.jbiotec.2015.04.024

Lim, S., Yocum, R. R., Silver, P. A., & Way, J. C. (2023, Apr 26). High spontaneous integration rates of end-modified linear DNAs upon mammalian cell transfection. *Sci Rep, 13*(1), 6835. https://doi.org/10.1038/s41598-023-33862-0

Lin, H., Huang, Y. S., Fustin, J. M., Doi, M., Chen, H., Lai, H. H., Lin, S. H., Lee, Y. L., King, P. C., Hou, H. S., Chen, H. W., Young, P. Y., & Chao, H. W. (2021, Jan 28). Hyperpolyploidization of hepatocyte initiates preneoplastic lesion formation in the liver. *Nat Commun, 12*(1), 645. https://doi.org/10.1038/s41467-020-20572-8

Lin, S., Staahl, B. T., Alla, R. K., & Doudna, J. A. (2014a, Dec 15). Enhanced homology-directed human genome engineering by controlled timing of CRISPR/Cas9 delivery. *Elife, 3*, e04766. https://doi.org/10.7554/eLife.04766

Lin, Y. C., Boone, M., Meuris, L., Lemmens, I., Van Roy, N., Soete, A., Reumers, J., Moisse, M., Plaisance, S., Drmanac, R., Chen, J., Speleman, F., Lambrechts, D., Van de Peer, Y., Tavernier, J., & Callewaert, N. (2014b, Sep 3). Genome dynamics of the human embryonic kidney 293 lineage in response to cell biology manipulations. *Nat Commun, 5*, 4767. https://doi.org/10.1038/ncomms5767

Liu, M., Zhang, W., Xin, C., Yin, J., Shang, Y., Ai, C., Li, J., Meng, F. L., & Hu, J. (2021, Sep 7). Global detection of DNA repair outcomes induced by CRISPR-Cas9. *Nucleic Acids Res, 49*(15), 8732-8742. https://doi.org/10.1093/nar/gkab686

Liu, Y., Mi, Y., Mueller, T., Kreibich, S., Williams, E. G., Van Drogen, A., Borel, C., Frank, M., Germain, P. L., Bludau, I., Mehnert, M., Seifert, M., Emmenlauer, M., Sorg, I., Bezrukov, F., Bena, F. S., Zhou, H., Dehio, C., Testa, G., Saez-Rodriguez, J., Antonarakis, S. E., Hardt, W. D., & Aebersold, R. (2019, Mar). Multi-omic measurements of heterogeneity in HeLa cells across laboratories. *Nat Biotechnol, 37*(3), 314-322. https://doi.org/10.1038/s41587-019-0037-y

Luo, Y., Liu, C., Cerbini, T., San, H., Lin, Y., Chen, G., Rao, M. S., & Zou, J. (2014, Jul). Stable enhanced green fluorescent protein expression after differentiation and transplantation of reporter human induced pluripotent stem cells generated by AAVS1 transcription activator-like effector nucleases. *Stem Cells Transl Med, 3*(7), 821-835. https://doi.org/10.5966/sctm.2013-0212

Maddox, A. S., Habermann, B., Desai, A., & Oegema, K. (2005, Jun). Distinct roles for two C. elegans anillins in the gonad and early embryo. *Development, 132*(12), 2837-2848. https://doi.org/10.1242/dev.01828

Maddox, A. S., Lewellyn, L., Desai, A., & Oegema, K. (2007, May). Anillin and the septins promote asymmetric ingression of the cytokinetic furrow. *Dev Cell, 12*(5), 827-835. https://doi.org/10.1016/j.devcel.2007.02.018

Mahdessian, D., Cesnik, A. J., Gnann, C., Danielsson, F., Stenstrom, L., Arif, M., Zhang, C., Le, T., Johansson, F., Schutten, R., Backstrom, A., Axelsson, U., Thul, P., Cho, N. H., Carja, O., Uhlen, M., Mardinoglu, A., Stadler, C., Lindskog, C., Ayoglu, B., Leonetti, M. D., Ponten, F., Sullivan, D. P., & Lundberg, E. (2021, Feb). Spatiotemporal dissection of the cell cycle with single-cell proteogenomics. *Nature, 590*(7847), 649-654. https://doi.org/10.1038/s41586-021-03232-9

Mahen, R., Koch, B., Wachsmuth, M., Politi, A. Z., Perez-Gonzalez, A., Mergenthaler, J., Cai, Y., & Ellenberg, J. (2014, Nov 5). Comparative assessment of fluorescent transgene methods for quantitative imaging in human cells. *Mol Biol Cell, 25*(22), 3610-3618. https://doi.org/10.1091/mbc.E14-06-1091

Mahlandt, E. K., Arts, J. J. G., van der Meer, W. J., van der Linden, F. H., Tol, S., van Buul, J. D., Gadella, T. W. J., & Goedhart, J. (2021, Sep 1). Visualizing endogenous Rho activity with an improved localization-based, genetically encoded biosensor. *J Cell Sci, 134*(17). https://doi.org/10.1242/jcs.258823

Makarova, K. S., Wolf, Y. I., Iranzo, J., Shmakov, S. A., Alkhnbashi, O. S., Brouns, S. J. J., Charpentier, E., Cheng, D., Haft, D. H., Horvath, P., Moineau, S., Mojica, F. J. M., Scott, D., Shah, S. A., Siksnys, V., Terns, M. P., Venclovas, C., White, M. F., Yakunin, A. F., Yan, W., Zhang, F., Garrett, R. A., Backofen, R., van der Oost, J., Barrangou, R., & Koonin, E. V. (2020, Feb). Evolutionary classification of CRISPR-Cas systems: a burst of class 2 and derived variants. *Nat Rev Microbiol, 18*(2), 67-83. https://doi.org/10.1038/s41579-019-0299-x

Mali, P., Yang, L., Esvelt, K. M., Aach, J., Guell, M., DiCarlo, J. E., Norville, J. E., & Church, G. M. (2013, Feb 15). RNA-guided human genome engineering via Cas9. *Science, 339*(6121), 823-826. https://doi.org/10.1126/science.1232033

Mangal, S., Sacher, J., Kim, T., Osorio, D. S., Motegi, F., Carvalho, A. X., Oegema, K., & Zanin, E. (2018, Mar 5). TPXL-1 activates Aurora A to clear contractile ring components from the polar cortex during cytokinesis. *J Cell Biol, 217*(3), 837-848. https://doi.org/10.1083/jcb.201706021

Mann, B. J., & Wadsworth, P. (2018, Dec). Distribution of Eg5 and TPX2 in mitosis: Insight from CRISPR tagged cells. *Cytoskeleton (Hoboken), 75*(12), 508-521. https://doi.org/10.1002/cm.21486

Manna, P. T., Davis, L. J., & Robinson, M. S. (2019, Dec). Fast and cloning-free CRISPR/Cas9-mediated genomic editing in mammalian cells. *Traffic, 20*(12), 974-982. https://doi.org/10.1111/tra.12696

Manukyan, A., Ludwig, K., Sanchez-Manchinelly, S., Parsons, S. J., & Stukenberg, P. T. (2015, Jan 1). A complex of p190RhoGAP-A and anillin modulates RhoA-GTP and the cytokinetic furrow in human cells. *J Cell Sci, 128*(1), 50-60. https://doi.org/10.1242/jcs.151647

Mao, Z., Bozzella, M., Seluanov, A., & Gorbunova, V. (2008, Oct 1). Comparison of nonhomologous end joining and homologous recombination in human cells. *DNA Repair (Amst), 7*(10), 1765-1771. https://doi.org/10.1016/j.dnarep.2008.06.018

Margall-Ducos, G., Celton-Morizur, S., Couton, D., Bregerie, O., & Desdouets, C. (2007, Oct 15). Liver tetraploidization is controlled by a new process of incomplete cytokinesis. *J Cell Sci, 120*(Pt 20), 3633-3639. https://doi.org/10.1242/jcs.016907

Maruyama, T., Dougan, S. K., Truttmann, M. C., Bilate, A. M., Ingram, J. R., & Ploegh, H. L. (2015, May). Increasing the efficiency of precise genome editing with CRISPR-Cas9 by inhibition of nonhomologous end joining. *Nat Biotechnol, 33*(5), 538-542. https://doi.org/10.1038/nbt.3190

Masters, J. R. (2002, Apr). HeLa cells 50 years on: the good, the bad and the ugly. *Nat Rev Cancer, 2*(4), 315-319. https://doi.org/10.1038/nrc775

Mastop, M., Bindels, D. S., Shaner, N. C., Postma, M., Gadella, T. W. J., Jr., & Goedhart, J. (2017, Sep 20). Characterization of a spectrally diverse set of fluorescent proteins as FRET acceptors for mTurquoise2. *Sci Rep, 7*(1), 11999. https://doi.org/10.1038/s41598-017-12212-x

Matsumoto, D., Tamamura, H., & Nomura, W. (2020, Oct 23). A cell cycle-dependent CRISPR-Cas9 activation system based on an anti-CRISPR protein shows improved genome editing accuracy. *Commun Biol, 3*(1), 601. https://doi.org/10.1038/s42003-020-01340-2

Maurissen, T. L., & Woltjen, K. (2020, Jun 8). Synergistic gene editing in human iPS cells via cell cycle and DNA repair modulation. *Nat Commun, 11*(1), 2876. https://doi.org/10.1038/s41467-020-16643-5

Medert, R., Thumberger, T., Tavhelidse-Suck, T., Hub, T., Kellner, T., Oguchi, Y., Dlugosz, S., Zimmermann, F., Wittbrodt, J., & Freichel, M. (2023, Feb 22). Efficient single copy integration via homology-directed repair (scHDR) by 5'modification of large DNA donor fragments in mice. *Nucleic Acids Res, 51*(3), e14. https://doi.org/10.1093/nar/gkac1150

Mefferd, A. L., Kornepati, A. V., Bogerd, H. P., Kennedy, E. M., & Cullen, B. R. (2015, Sep). Expression of CRISPR/Cas single guide RNAs using small tRNA promoters. *RNA, 21*(9), 1683-1689. https://doi.org/10.1261/rna.051631.115

Melak, M., Plessner, M., & Grosse, R. (2017, Feb 1). Actin visualization at a glance. *J Cell Sci, 130*(3), 525-530. https://doi.org/10.1242/jcs.189068

Mierzwa, B., & Gerlich, D. W. (2014, Dec 8). Cytokinetic abscission: molecular mechanisms and temporal control. *Dev Cell, 31*(5), 525-538. https://doi.org/10.1016/j.devcel.2014.11.006

Mishima, M., Kaitna, S., & Glotzer, M. (2002, Jan). Central spindle assembly and cytokinesis require a kinesin-like protein/RhoGAP complex with microtubule bundling activity. *Dev Cell, 2*(1), 41-54. https://doi.org/10.1016/s1534-5807(01)00110-1

Mishima, M., Pavicic, V., Gruneberg, U., Nigg, E. A., & Glotzer, M. (2004, Aug 19). Cell cycle regulation of central spindle assembly. *Nature, 430*(7002), 908-913. https://doi.org/10.1038/nature02767

Mittal, N., Dave, J., Harakalova, M., van Tintelen, J. P., Asselbergs, F. W., Doevendans, P. A., Costa, K. D., Turnbull, I. C., & Stillitano, F. (2022, Apr). Generation of human induced pluripotent stem cell (iPSC) lines derived from five patients carrying the pathogenic phospholamban-R14del (PLN-R14del) variant and three non-carrier family members. *Stem Cell Res, 60*, 102737. https://doi.org/10.1016/j.scr.2022.102737

Miyaoka, Y., Chan, A. H., Judge, L. M., Yoo, J., Huang, M., Nguyen, T. D., Lizarraga, P. P., So, P. L., & Conklin, B. R. (2014, Mar). Isolation of single-base genome-edited human iPS cells without antibiotic selection. *Nat Methods, 11*(3), 291-293. https://doi.org/10.1038/nmeth.2840

Mollinari, C., Kleman, J. P., Saoudi, Y., Jablonski, S. A., Perard, J., Yen, T. J., & Margolis, R. L. (2005, Mar). Ablation of PRC1 by small interfering RNA demonstrates that cytokinetic abscission requires a central spindle bundle in mammalian cells, whereas completion of furrowing does not. *Mol Biol Cell, 16*(3), 1043-1055. https://doi.org/10.1091/mbc.e04-04-0346

Morais-de-Sa, E., & Sunkel, C. (2013, Aug). Adherens junctions determine the apical position of the midbody during follicular epithelial cell division. *EMBO Rep, 14*(8), 696-703. https://doi.org/10.1038/embor.2013.85

Nakade, S., Mochida, K., Kunii, A., Nakamae, K., Aida, T., Tanaka, K., Sakamoto, N., Sakuma, T., & Yamamoto, T. (2018, Aug 16). Biased genome editing using the local accumulation of DSB repair molecules system. *Nat Commun, 9*(1), 3270. https://doi.org/10.1038/s41467-018-05773-6

Nambiar, T. S., Billon, P., Diedenhofen, G., Hayward, S. B., Taglialatela, A., Cai, K., Huang, J. W., Leuzzi, G., Cuella-Martin, R., Palacios, A., Gupta, A., Egli, D., & Ciccia, A. (2019, Jul 30). Stimulation of CRISPR-mediated homology-directed repair by an engineered RAD18 variant. *Nat Commun, 10*(1), 3395. https://doi.org/10.1038/s41467-019-11105-z

Niiya, F., Tatsumoto, T., Lee, K. S., & Miki, T. (2006, Feb 9). Phosphorylation of the cytokinesis regulator ECT2 at G2/M phase stimulates association of the mitotic kinase Plk1 and accumulation of GTP-bound RhoA. *Oncogene, 25*(6), 827-837. https://doi.org/10.1038/sj.onc.1209124

Nishimura, Y., & Yonemura, S. (2006, Jan 1). Centralspindlin regulates ECT2 and RhoA accumulation at the equatorial cortex during cytokinesis. *J Cell Sci, 119*(Pt 1), 104-114. https://doi.org/10.1242/jcs.02737

O'Hagan, D., Kruger, R. E., Gu, B., & Ralston, A. (2021, Jul 1). Efficient generation of endogenous protein reporters for mouse development. *Development, 148*(13). https://doi.org/10.1242/dev.197418

Oceguera-Yanez, F., Avila-Robinson, A., & Woltjen, K. (2022). Differentiation of pluripotent stem cells for modeling human skin development and potential applications. *Front Cell Dev Biol, 10*, 1030339. https://doi.org/10.3389/fcell.2022.1030339

Oceguera-Yanez, F., Kim, S. I., Matsumoto, T., Tan, G. W., Xiang, L., Hatani, T., Kondo, T., Ikeya, M., Yoshida, Y., Inoue, H., & Woltjen, K. (2016, May 15). Engineering the AAVS1 locus for consistent and scalable transgene expression in human iPSCs and their differentiated derivatives. *Methods, 101*, 43-55. https://doi.org/10.1016/j.ymeth.2015.12.012

Oegema, K., Savoian, M. S., Mitchison, T. J., & Field, C. M. (2000). Functional analysis of a human homologue of the Drosophila actin binding protein Anillin suggests a role in cytokinesis. *Journal of Cell Biology, 150*(3), 539-551.

Ogata, T., Kozuka, T., & Kanda, T. (2003, Aug). Identification of an insulator in AAVS1, a preferred region for integration of adeno-associated virus DNA. *J Virol, 77*(16), 9000-9007. https://doi.org/10.1128/jvi.77.16.9000-9007.2003

Okumura, M., Natsume, T., Kanemaki, M. T., & Kiyomitsu, T. (2018, May 31). Dynein-Dynactin-NuMA clusters generate cortical spindle-pulling forces as a multi-arm ensemble. *Elife, 7*. https://doi.org/10.7554/eLife.36559

Osorio, D. S., Chan, F. Y., Saramago, J., Leite, J., Silva, A. M., Sobral, A. F., Gassmann, R., & Carvalho, A. X. (2019, Nov 12). Crosslinking activity of non-muscle myosin II is not sufficient for embryonic cytokinesis in C. elegans. *Development, 146*(21). https://doi.org/10.1242/dev.179150

Osório, D. S., Chan, F. Y., Saramago, J., Leite, J., Silva, A. M., Sobral, A. F., Gassmann, R., & Carvalho, A. X. (2019, Nov 12). Crosslinking activity of non-muscle myosin II is not sufficient for embryonic cytokinesis in C. elegans. *Development, 146*(21). https://doi.org/10.1242/dev.179150

Owens, D. D. G., Caulder, A., Frontera, V., Harman, J. R., Allan, A. J., Bucakci, A., Greder, L., Codner, G. F., Hublitz, P., McHugh, P. J., Teboul, L., & de Bruijn, M. (2019, Aug 22). Microhomologies are prevalent at Cas9-induced larger deletions. *Nucleic Acids Res, 47*(14), 7402-7417. https://doi.org/10.1093/nar/gkz459

Ozugergin, I., Mastronardi, K., Law, C., & Piekny, A. (2022a, Jan 13). Diverse mechanisms regulate contractile ring assembly for cytokinesis in the two-cell C. elegans embryo. *J Cell Sci*. https://doi.org/10.1242/jcs.258921

Ozugergin, I., Mastronardi, K., Law, C., & Piekny, A. (2022b, Feb 1). Diverse mechanisms regulate contractile ring assembly for cytokinesis in the two-cell Caenorhabditis elegans embryo. *J Cell Sci, 135*(3). https://doi.org/10.1242/jcs.258921

Ozugergin, I., & Piekny, A. (2020, Feb 14). Complementary functions for the Ran gradient during division. *Small GTPases*, 1-11. https://doi.org/10.1080/21541248.2020.1725371

Ozugergin, I., & Piekny, A. (2021, May). Complementary functions for the Ran gradient during division. *Small GTPases, 12*(3), 177-187. https://doi.org/10.1080/21541248.2020.1725371

Ozugergin, I., & Piekny, A. (2022). Diversity is the spice of life: An overview of how cytokinesis regulation varies with cell type. *Front Cell Dev Biol, 10*, 1007614. https://doi.org/10.3389/fcell.2022.1007614

Paim, L. M. G., & FitzHarris, G. (2022, Mar 22). Cell size and polarization determine cytokinesis furrow ingression dynamics in mouse embryos. *Proc Natl Acad Sci U S A, 119*(12), e2119381119. https://doi.org/10.1073/pnas.2119381119

Paquet, D., Kwart, D., Chen, A., Sproul, A., Jacob, S., Teo, S., Olsen, K. M., Gregg, A., Noggle, S., & Tessier-Lavigne, M. (2016, May 5). Efficient introduction of specific homozygous and heterozygous mutations using CRISPR/Cas9. *Nature, 533*(7601), 125-129. https://doi.org/10.1038/nature17664

Park, S. H., Cao, M., Pan, Y., Davis, T. H., Saxena, L., Deshmukh, H., Fu, Y., Treangen, T., Sheehan, V. A., & Bao, G. (2022, Oct 21). Comprehensive analysis and accurate quantification of unintended large gene modifications induced by CRISPR-Cas9 gene editing. *Sci Adv, 8*(42), eabo7676. https://doi.org/10.1126/sciadv.abo7676

Paul, B., & Montoya, G. (2020, Feb). CRISPR-Cas12a: Functional overview and applications. *Biomed J, 43*(1), 8-17. https://doi.org/10.1016/j.bj.2019.10.005

Paull, D., Sevilla, A., Zhou, H., Hahn, A. K., Kim, H., Napolitano, C., Tsankov, A., Shang, L., Krumholz, K., Jagadeesan, P., Woodard, C. M., Sun, B., Vilboux, T., Zimmer, M., Forero, E., Moroziewicz, D. N., Martinez, H., Malicdan, M. C., Weiss, K. A., Vensand, L. B., Dusenberry, C. R., Polus, H., Sy, K. T., Kahler, D. J., Gahl, W. A., Solomon, S. L., Chang, S., Meissner, A., Eggan, K., & Noggle, S. A. (2015, Sep). Automated, high-throughput derivation, characterization and differentiation of induced pluripotent stem cells. *Nat Methods, 12*(9), 885-892. https://doi.org/10.1038/nmeth.3507

Paulsen, B. S., Mandal, P. K., Frock, R. L., Boyraz, B., Yadav, R., Upadhyayula, S., Gutierrez-Martinez, P., Ebina, W., Fasth, A., Kirchhausen, T., Talkowski, M. E., Agarwal, S., Alt, F. W., & Rossi, D. J. (2017, Nov). Ectopic expression of RAD52 and dn53BP1 improves homology-directed repair during CRISPR-Cas9 genome editing. *Nat Biomed Eng, 1*(11), 878-888. https://doi.org/10.1038/s41551-017-0145-2

Pavani, G., & Amendola, M. (2020). Targeted Gene Delivery: Where to Land. *Front Genome Ed, 2*, 609650. https://doi.org/10.3389/fgeed.2020.609650

Pellenz, S., Phelps, M., Tang, W., Hovde, B. T., Sinit, R. B., Fu, W., Li, H., Chen, E., & Monnat, R. J., Jr. (2019, Jul). New Human Chromosomal Sites with "Safe Harbor" Potential for Targeted Transgene Insertion. *Hum Gene Ther, 30*(7), 814-828. https://doi.org/10.1089/hum.2018.169

Perez-Leal, O., Nixon-Abell, J., Barrero, C. A., Gordon, J. C., Oesterling, J., & Rico, M. C. (2021, Dec). Multiplex Gene Tagging with CRISPR-Cas9 for Live-Cell Microscopy and Application to Study the Role of SARS-CoV-2 Proteins in Autophagy, Mitochondrial Dynamics, and Cell Growth. *CRISPR J, 4*(6), 854-871. https://doi.org/10.1089/crispr.2021.0041

Peterman, E., Valius, M., & Prekeris, R. (2020, May 14). CLIC4 is a cytokinetic cleavage furrow protein that regulates cortical cytoskeleton stability during cell division. *J Cell Sci, 133*(9). https://doi.org/10.1242/jcs.241117

Petronczki, M., Glotzer, M., Kraut, N., & Peters, J. M. (2007, May). Polo-like kinase 1 triggers the initiation of cytokinesis in human cells by promoting recruitment of the RhoGEF Ect2 to the central spindle. *Dev Cell, 12*(5), 713-725. https://doi.org/10.1016/j.devcel.2007.03.013

Pickar-Oliver, A., & Gersbach, C. A. (2019, Aug). The next generation of CRISPR-Cas technologies and applications. *Nat Rev Mol Cell Biol, 20*(8), 490-507. https://doi.org/10.1038/s41580-019-0131-5

Piekny, A., Werner, M., & Glotzer, M. (2005, Dec). Cytokinesis: welcome to the Rho zone. *Trends Cell Biol, 15*(12), 651-658. https://doi.org/10.1016/j.tcb.2005.10.006

Piekny, A. J., & Glotzer, M. (2008, Jan 8). Anillin is a scaffold protein that links RhoA, actin, and myosin during cytokinesis. *Curr Biol, 18*(1), 30-36. https://doi.org/10.1016/j.cub.2007.11.068

Piekny, A. J., & Maddox, A. S. (2010, Dec). The myriad roles of Anillin during cytokinesis. *Semin Cell Dev Biol, 21*(9), 881-891. https://doi.org/10.1016/j.semcdb.2010.08.002

Pina, R., Santos-Diaz, A. I., Orta-Salazar, E., Aguilar-Vazquez, A. R., Mantellero, C. A., Acosta-Galeana, I., Estrada-Mondragon, A., Prior-Gonzalez, M., Martinez-Cruz, J. I., & Rosas-Arellano, A. (2022, Jan 26). Ten Approaches That Improve Immunostaining: A Review of the Latest Advances for the Optimization of Immunofluorescence. *Int J Mol Sci, 23*(3). https://doi.org/10.3390/ijms23031426

Pinder, J., Salsman, J., & Dellaire, G. (2015, Oct 30). Nuclear domain 'knock-in' screen for the evaluation and identification of small molecule enhancers of CRISPR-based genome editing. *Nucleic Acids Res, 43*(19), 9379-9392. https://doi.org/10.1093/nar/gkv993

Pollard, T. D., & O'Shaughnessy, B. (2019, Jun 20). Molecular Mechanism of Cytokinesis. *Annu Rev Biochem, 88*, 661-689. https://doi.org/10.1146/annurev-biochem-062917-012530

Puri, M. C., & Nagy, A. (2012, Jan). Concise review: Embryonic stem cells versus induced pluripotent stem cells: the game is on. *Stem Cells, 30*(1), 10-14. https://doi.org/10.1002/stem.788

Ran, F. A., Hsu, P. D., Lin, C. Y., Gootenberg, J. S., Konermann, S., Trevino, A. E., Scott, D. A., Inoue, A., Matoba, S., Zhang, Y., & Zhang, F. (2013a, Sep 12). Double nicking by RNA-guided CRISPR Cas9 for enhanced genome editing specificity. *Cell, 154*(6), 1380-1389. https://doi.org/10.1016/j.cell.2013.08.021

Ran, F. A., Hsu, P. D., Wright, J., Agarwala, V., Scott, D. A., & Zhang, F. (2013b, Nov). Genome engineering using the CRISPR-Cas9 system. *Nat Protoc, 8*(11), 2281-2308. https://doi.org/10.1038/nprot.2013.143

Rappaport, R. (1985, Apr). Repeated furrow formation from a single mitotic apparatus in cylindrical sand dollar eggs. *J Exp Zool, 234*(1), 167-171. https://doi.org/10.1002/jez.1402340120

Ratz, M., Testa, I., Hell, S. W., & Jakobs, S. (2015, Apr 20). CRISPR/Cas9-mediated endogenous protein tagging for RESOLFT super-resolution microscopy of living human cells. *Sci Rep, 5*, 9592. https://doi.org/10.1038/srep09592

Reymann, A. C., Staniscia, F., Erzberger, A., Salbreux, G., & Grill, S. W. (2016, Oct 10). Cortical flow aligns actin filaments to form a furrow. *Elife, 5*. https://doi.org/10.7554/eLife.17807

Richardson, C. D., Ray, G. J., DeWitt, M. A., Curie, G. L., & Corn, J. E. (2016, Mar). Enhancing homology-directed genome editing by catalytically active and inactive CRISPR-Cas9 using asymmetric donor DNA. *Nat Biotechnol, 34*(3), 339-344. https://doi.org/10.1038/nbt.3481

Riesenberg, S., Kanis, P., Macak, D., Wollny, D., Dusterhoft, D., Kowalewski, J., Helmbrecht, N., Maricic, T., & Paabo, S. (2023, Jul 20). Efficient high-precision homology-directed repair-dependent genome editing by HDRobust. *Nat Methods*. https://doi.org/10.1038/s41592-023-01949-1

Rizzo, M. A., Davidson, M. W., & Piston, D. W. (2009, Dec). Fluorescent protein tracking and detection: applications using fluorescent proteins in living cells. *Cold Spring Harb Protoc, 2009*(12), pdb top64. https://doi.org/10.1101/pdb.top64

Robert, F., Barbeau, M., Ethier, S., Dostie, J., & Pelletier, J. (2015, Aug 27). Pharmacological inhibition of DNA-PK stimulates Cas9-mediated genome editing. *Genome Med, 7*(1), 93. https://doi.org/10.1186/s13073-015-0215-6

Roberts, B., Haupt, A., Tucker, A., Grancharova, T., Arakaki, J., Fuqua, M. A., Nelson, A., Hookway, C., Ludmann, S. A., Mueller, I. A., Yang, R., Horwitz, R., Rafelski, S. M., & Gunawardane, R. N. (2017, Oct 15). Systematic gene tagging using CRISPR/Cas9 in human stem cells to illuminate cell organization. *Mol Biol Cell, 28*(21), 2854-2874. https://doi.org/10.1091/mbc.E17-03-0209

Roberts, B., Hendershott, M. C., Arakaki, J., Gerbin, K. A., Malik, H., Nelson, A., Gehring, J., Hookway, C., Ludmann, S. A., Yang, R., Haupt, A., Grancharova, T., Valencia, V., Fuqua, M. A., Tucker, A., Rafelski, S. M., & Gunawardane, R. N. (2019, May 14). Fluorescent Gene Tagging of Transcriptionally Silent Genes in hiPSCs. *Stem Cell Reports, 12*(5), 1145-1158. https://doi.org/10.1016/j.stemcr.2019.03.001

Rodrigues, N. T., Lekomtsev, S., Jananji, S., Kriston-Vizi, J., Hickson, G. R., & Baum, B. (2015, Aug 27). Kinetochore-localized PP1-Sds22 couples chromosome segregation to polar relaxation. *Nature, 524*(7566), 489-492. https://doi.org/10.1038/nature14496

Saito, S., Maeda, R., & Adachi, N. (2017, Jul 11). Dual loss of human POLQ and LIG4 abolishes random integration. *Nat Commun, 8*, 16112. https://doi.org/10.1038/ncomms16112

Sakuma, T., Nakade, S., Sakane, Y., Suzuki, K. T., & Yamamoto, T. (2016, Jan). MMEJ-assisted gene knock-in using TALENs and CRISPR-Cas9 with the PITCh systems. *Nat Protoc, 11*(1), 118-133. https://doi.org/10.1038/nprot.2015.140

Savic, D., Partridge, E. C., Newberry, K. M., Smith, S. B., Meadows, S. K., Roberts, B. S., Mackiewicz, M., Mendenhall, E. M., & Myers, R. M. (2015, Oct). CETCh-seq: CRISPR epitope tagging ChIP-seq of DNA-binding proteins. *Genome Res, 25*(10), 1581-1589. https://doi.org/10.1101/gr.193540.115

Sawatsubashi, S., Joko, Y., Fukumoto, S., Matsumoto, T., & Sugano, S. S. (2018, Jan 12). Development of versatile non-homologous end joining-based knock-in module for genome editing. *Sci Rep, 8*(1), 593. https://doi.org/10.1038/s41598-017-18911-9

Schimmel, J., Munoz-Subirana, N., Kool, H., van Schendel, R., van der Vlies, S., Kamp, J. A., de Vrij, F., Kushner, S. A., Smith, G. C. M., Boulton, S. J., & Tijsterman, M. (2023, Jan 25). Modulating mutational outcomes and improving precise gene editing at CRISPR-Cas9-induced breaks by chemical inhibition of end-joining pathways. *Cell Rep, 42*(2), 112019. https://doi.org/10.1016/j.celrep.2023.112019

Schjeide, B. M., & Puschel, G. P. (2023, Jan). Determining On-Target, Off-Target, and Copy Number Status of Transgenic Events After CRISPR/Cas9 Targeted AAVS1 Safe-Harbor Modification of iPSCs Using Double-Control Quantitative Copy Number PCR. *Curr Protoc, 3*(1), e635. https://doi.org/10.1002/cpz1.635

Schneid, S., Wolff, F., Buchner, K., Bertram, N., Baygun, S., Barbosa, P., Mangal, S., & Zanin, E. (2021, Mar 2). The BRCT domains of ECT2 have distinct functions during cytokinesis. *Cell Rep, 34*(9), 108805. https://doi.org/10.1016/j.celrep.2021.108805

Scully, R., Panday, A., Elango, R., & Willis, N. A. (2019, Nov). DNA double-strand break repair-pathway choice in somatic mammalian cells. *Nat Rev Mol Cell Biol, 20*(11), 698-714. https://doi.org/10.1038/s41580-019-0152-0

Sentmanat, M. F., Peters, S. T., Florian, C. P., Connelly, J. P., & Pruett-Miller, S. M. (2018, Jan 17). A Survey of Validation Strategies for CRISPR-Cas9 Editing. *Sci Rep, 8*(1), 888. https://doi.org/10.1038/s41598-018-19441-8

Shams, F., Bayat, H., Mohammadian, O., Mahboudi, S., Vahidnezhad, H., Soosanabadi, M., & Rahimpour, A. (2022). Advance trends in targeting homology-directed repair for accurate gene editing: An inclusive review of small molecules and modified CRISPR-Cas9 systems. *Bioimpacts, 12*(4), 371-391. https://doi.org/10.34172/bi.2022.23871

Shi, Y., Inoue, H., Wu, J. C., & Yamanaka, S. (2017, Feb). Induced pluripotent stem cell technology: a decade of progress. *Nat Rev Drug Discov, 16*(2), 115-130. https://doi.org/10.1038/nrd.2016.245

Shi, Y., Kirwan, P., & Livesey, F. J. (2012, Oct). Directed differentiation of human pluripotent stem cells to cerebral cortex neurons and neural networks. *Nat Protoc, 7*(10), 1836-1846. https://doi.org/10.1038/nprot.2012.116

Shi, Y., Kopparapu, N., Ohler, L., & Dickinson, D. J. (2023, May 15). Efficient and rapid fluorescent protein knock-in with universal donors in mouse embryonic stem cells. *Development, 150*(10). https://doi.org/10.1242/dev.201367

Shibata, A. (2017, Oct). Regulation of repair pathway choice at two-ended DNA double-strand breaks. *Mutat Res, 803-805*, 51-55. https://doi.org/10.1016/j.mrfmmm.2017.07.011

Shin, S., Kim, S. H., Shin, S. W., Grav, L. M., Pedersen, L. E., Lee, J. S., & Lee, G. M. (2020, Jun 19). Comprehensive Analysis of Genomic Safe Harbors as Target Sites for Stable Expression of

the Heterologous Gene in HEK293 Cells. *ACS Synth Biol, 9*(6), 1263-1269. https://doi.org/10.1021/acssynbio.0c00097

Silva, A. M., Osorio, D. S., Pereira, A. J., Maiato, H., Pinto, I. M., Rubinstein, B., Gassmann, R., Telley, I. A., & Carvalho, A. X. (2016, Dec 19). Robust gap repair in the contractile ring ensures timely completion of cytokinesis. *J Cell Biol, 215*(6), 789-799. https://doi.org/10.1083/jcb.201605080

Simpson, J. C., Wellenreuther, R., Poustka, A., Pepperkok, R., & Wiemann, S. (2000, Sep). Systematic subcellular localization of novel proteins identified by large-scale cDNA sequencing. *EMBO Rep, 1*(3), 287-292. https://doi.org/10.1093/embo-reports/kvd058

Sinclair, F., Begum, A. A., Dai, C. C., Toth, I., & Moyle, P. M. (2023, May). Recent advances in the delivery and applications of nonviral CRISPR/Cas9 gene editing. *Drug Deliv Transl Res, 13*(5), 1500-1519. https://doi.org/10.1007/s13346-023-01320-z

Singh, A. M. (2019). An Efficient Protocol for Single-Cell Cloning Human Pluripotent Stem Cells. *Front Cell Dev Biol, 7*, 11. https://doi.org/10.3389/fcell.2019.00011

Singh, D., Odedra, D., Dutta, P., & Pohl, C. (2019, Oct 9). Mechanical stress induces a scalable switch in cortical flow polarization during cytokinesis. *J Cell Sci, 132*(19). https://doi.org/10.1242/jcs.231357

Singh, D., & Pohl, C. (2014, Feb 10). Coupling of rotational cortical flow, asymmetric midbody positioning, and spindle rotation mediates dorsoventral axis formation in C. elegans. *Dev Cell, 28*(3), 253-267. https://doi.org/10.1016/j.devcel.2014.01.002

Skryabin, B. V., Kummerfeld, D. M., Gubar, L., Seeger, B., Kaiser, H., Stegemann, A., Roth, J., Meuth, S. G., Pavenstadt, H., Sherwood, J., Pap, T., Wedlich-Soldner, R., Sunderkotter, C., Schwartz, Y. B., Brosius, J., & Rozhdestvensky, T. S. (2020, Feb). Pervasive head-to-tail insertions of DNA templates mask desired CRISPR-Cas9-mediated genome editing events. *Sci Adv, 6*(7), eaax2941. https://doi.org/10.1126/sciadv.aax2941

Slaymaker, I. M., & Gaudelli, N. M. (2021, Aug). Engineering Cas9 for human genome editing. *Curr Opin Struct Biol, 69*, 86-98. https://doi.org/10.1016/j.sbi.2021.03.004

Smith, J. R., Maguire, S., Davis, L. A., Alexander, M., Yang, F., Chandran, S., ffrench-Constant, C., & Pedersen, R. A. (2008, Feb). Robust, persistent transgene expression in human embryonic stem cells is achieved with AAVS1-targeted integration. *Stem Cells, 26*(2), 496-504. https://doi.org/10.1634/stemcells.2007-0039

Sobral, A. F., Chan, F. Y., Norman, M. J., Osorio, D. S., Dias, A. B., Ferreira, V., Barbosa, D. J., Cheerambathur, D., Gassmann, R., Belmonte, J. M., & Carvalho, A. X. (2021, Dec 20). Plastin and spectrin cooperate to stabilize the actomyosin cortex during cytokinesis. *Curr Biol, 31*(24), 5415-5428 e5410. https://doi.org/10.1016/j.cub.2021.09.055

Spector, D. L., & Goldman, R. D. (2010, Nov 1). Transfection of mammalian cells with fluorescent protein fusions. *Cold Spring Harb Protoc, 2010*(11), pdb prot5517. https://doi.org/10.1101/pdb.prot5517

Spira, F., Cuylen-Haering, S., Mehta, S., Samwer, M., Reversat, A., Verma, A., Oldenbourg, R., Sixt, M., & Gerlich, D. W. (2017, Nov 6). Cytokinesis in vertebrate cells initiates by contraction of an equatorial actomyosin network composed of randomly oriented filaments. *Elife, 6*. https://doi.org/10.7554/eLife.30867

Spitzer, J., Landthaler, M., & Tuschl, T. (2013). Rapid creation of stable mammalian cell lines for regulated expression of proteins using the Gateway(R) recombination cloning technology and Flp-In T-REx(R) lines. *Methods Enzymol, 529*, 99-124. https://doi.org/10.1016/B978-0-12-418687-3.00008-2

Stellon, D., Tran, M. T. N., Talbot, J., Chear, S., Khalid, M., Pebay, A., Vickers, J. C., King, A. E., Hewitt, A. W., & Cook, A. L. (2022). CRISPR/Cas-Mediated Knock-in of Genetically Encoded Fluorescent Biosensors into the AAVS1 Locus of Human-Induced Pluripotent Stem Cells. *Methods Mol Biol, 2549*, 379-398. https://doi.org/10.1007/7651_2021_422

Stemmer, M., Thumberger, T., Del Sol Keyer, M., Wittbrodt, J., & Mateo, J. L. (2015). CCTop: An Intuitive, Flexible and Reliable CRISPR/Cas9 Target Prediction Tool. *PLoS One, 10*(4), e0124633. https://doi.org/10.1371/journal.pone.0124633

Strohmeier, K., Hofmann, M., Hauser, F., Sivun, D., Puthukodan, S., Karner, A., Sandner, G., Le Renard, P. E., Jacak, J., & Mairhofer, M. (2021, Dec 28). CRISPR/Cas9 Genome Editing vs. Over-Expression for Fluorescent Extracellular Vesicle-Labeling: A Quantitative Analysis. *Int J Mol Sci, 23*(1). https://doi.org/10.3390/ijms23010282

Su, K. C., Takaki, T., & Petronczki, M. (2011, Dec 13). Targeting of the RhoGEF Ect2 to the equatorial membrane controls cleavage furrow formation during cytokinesis. *Dev Cell, 21*(6), 1104-1115. https://doi.org/10.1016/j.devcel.2011.11.003

Sugioka, K. (2022, Jul). Symmetry-breaking of animal cytokinesis. *Semin Cell Dev Biol, 127*, 100-109. https://doi.org/10.1016/j.semcdb.2021.12.008

Sumer, S. A., Hoffmann, S., Laue, S., Campbell, B., Raedecke, K., Frajs, V., Clauss, S., Kaab, S., Janssen, J. W. G., Jauch, A., Laugwitz, K. L., Dorn, T., Moretti, A., & Rappold, G. A. (2020, Oct 13). Precise Correction of Heterozygous SHOX2 Mutations in hiPSCs Derived from Patients with Atrial Fibrillation via Genome Editing and Sib Selection. *Stem Cell Reports, 15*(4), 999-1013. https://doi.org/10.1016/j.stemcr.2020.08.015

Sun, D., Evans, L., Perrone, F., Sokleva, V., Lim, K., Rezakhani, S., Lutolf, M., Zilbauer, M., & Rawlins, E. L. (2021, Oct 6). A functional genetic toolbox for human tissue-derived organoids. *Elife, 10*. https://doi.org/10.7554/eLife.67886

Sun, L., Guan, R., Lee, I. J., Liu, Y., Chen, M., Wang, J., Wu, J. Q., & Chen, Z. (2015, May 26). Mechanistic insights into the anchorage of the contractile ring by anillin and Mid1. *Dev Cell, 33*(4), 413-426. https://doi.org/10.1016/j.devcel.2015.03.003

Suzuki, K., Tsunekawa, Y., Hernandez-Benitez, R., Wu, J., Zhu, J., Kim, E. J., Hatanaka, F., Yamamoto, M., Araoka, T., Li, Z., Kurita, M., Hishida, T., Li, M., Aizawa, E., Guo, S., Chen, S., Goebl, A., Soligalla, R. D., Qu, J., Jiang, T., Fu, X., Jafari, M., Esteban, C. R., Berggren, W. T., Lajara, J., Nunez-Delicado, E., Guillen, P., Campistol, J. M., Matsuzaki, F., Liu, G. H., Magistretti, P., Zhang, K., Callaway, E. M., Zhang, K., & Belmonte, J. C. (2016, Dec 1). In vivo genome editing via CRISPR/Cas9 mediated homology-independent targeted integration. *Nature, 540*(7631), 144-149. https://doi.org/10.1038/nature20565

Takahashi, G., & Miyaoka, Y. (2023, Jun 16). Large-scale single-cell cloning of genome-edited cultured human cells by On-chip SPiS. *STAR Protoc, 4*(3), 102364. https://doi.org/10.1016/j.xpro.2023.102364

Takahashi, K., Tanabe, K., Ohnuki, M., Narita, M., Ichisaka, T., Tomoda, K., & Yamanaka, S. (2007, Nov 30). Induction of pluripotent stem cells from adult human fibroblasts by defined factors. *Cell, 131*(5), 861-872. https://doi.org/10.1016/j.cell.2007.11.019

Tamura, R., Jiang, F., Xie, J., & Kamiyama, D. (2021, Feb 26). Multiplexed labeling of cellular proteins with split fluorescent protein tags. *Commun Biol, 4*(1), 257. https://doi.org/10.1038/s42003-021-01780-4

Tanaka, M., Yokoyama, K., Hayashi, H., Isaki, S., Kitatani, K., Wang, T., Kawata, H., Matsuzawa, H., Gurumurthy, C. B., Miura, H., & Ohtsuka, M. (2022, Oct 25). CRISPR-KRISPR: a method to identify on-target and random insertion of donor DNAs and their characterization in knock-in mice. *Genome Biol, 23*(1), 228. https://doi.org/10.1186/s13059-022-02779-8

Tedeschi, A., Almagro, J., Renshaw, M. J., Messal, H. A., Behrens, A., & Petronczki, M. (2020, Apr 8). Cep55 promotes cytokinesis of neural progenitors but is dispensable for most mammalian cell divisions. *Nat Commun, 11*(1), 1746. https://doi.org/10.1038/s41467-020-15359-w

Thieleke-Matos, C., Osorio, D. S., Carvalho, A. X., & Morais-de-Sa, E. (2017). Emerging Mechanisms and Roles for Asymmetric Cytokinesis. *Int Rev Cell Mol Biol, 332*, 297-345. https://doi.org/10.1016/bs.ircmb.2017.01.004

Thorvaldsdottir, H., Robinson, J. T., & Mesirov, J. P. (2013, Mar). Integrative Genomics Viewer (IGV): high-performance genomics data visualization and exploration. *Brief Bioinform, 14*(2), 178-192. https://doi.org/10.1093/bib/bbs017

Thul, P. J., & Lindskog, C. (2018, Jan). The human protein atlas: A spatial map of the human proteome. *Protein Sci, 27*(1), 233-244. https://doi.org/10.1002/pro.3307

Tormos, A. M., Talens-Visconti, R., & Sastre, J. (2015). Regulation of cytokinesis and its clinical significance. *Crit Rev Clin Lab Sci, 52*(4), 159-167. https://doi.org/10.3109/10408363.2015.1012191

Tristan, C. A., Hong, H., Jethmalani, Y., Chen, Y., Weber, C., Chu, P. H., Ryu, S., Jovanovic, V. M., Hur, I., Voss, T. C., Simeonov, A., & Singec, I. (2023, Jan). Efficient and safe single-cell cloning of human pluripotent stem cells using the CEPT cocktail. *Nat Protoc, 18*(1), 58-80. https://doi.org/10.1038/s41596-022-00753-z

Tristan, C. A., Ormanoglu, P., Slamecka, J., Malley, C., Chu, P. H., Jovanovic, V. M., Gedik, Y., Jethmalani, Y., Bonney, C., Barnaeva, E., Braisted, J., Mallanna, S. K., Dorjsuren, D., Iannotti, M. J., Voss, T. C., Michael, S., Simeonov, A., & Singec, I. (2021, Dec 14). Robotic high-throughput biomanufacturing and functional differentiation of human pluripotent stem cells. *Stem Cell Reports, 16*(12), 3076-3092. https://doi.org/10.1016/j.stemcr.2021.11.004

Truong, V., Viken, K., Geng, Z., Barkan, S., Johnson, B., Ebeling, M. C., Montezuma, S. R., Ferrington, D. A., & Dutton, J. R. (2021, Jun). Automating Human Induced Pluripotent Stem Cell Culture and Differentiation of iPSC-Derived Retinal Pigment Epithelium for Personalized Drug Testing. *SLAS Technol, 26*(3), 287-299. https://doi.org/10.1177/2472630320972110

Tse, Y. C., Piekny, A., & Glotzer, M. (2011, Sep). Anillin promotes astral microtubule-directed cortical myosin polarization. *Mol Biol Cell, 22*(17), 3165-3175. https://doi.org/10.1091/mbc.E11-05-0399

Vakulskas, C. A., Dever, D. P., Rettig, G. R., Turk, R., Jacobi, A. M., Collingwood, M. A., Bode, N. M., McNeill, M. S., Yan, S., Camarena, J., Lee, C. M., Park, S. H., Wiebking, V., Bak, R. O., Gomez-Ospina, N., Pavel-Dinu, M., Sun, W., Bao, G., Porteus, M. H., & Behlke, M. A. (2018, Aug). A high-fidelity Cas9 mutant delivered as a ribonucleoprotein complex enables efficient gene editing in human hematopoietic stem and progenitor cells. *Nat Med, 24*(8), 1216-1224. https://doi.org/10.1038/s41591-018-0137-0

van Oostende Triplet, C., Jaramillo Garcia, M., Haji Bik, H., Beaudet, D., & Piekny, A. (2014, Sep 1). Anillin interacts with microtubules and is part of the astral pathway that defines cortical domains. *J Cell Sci, 127*(Pt 17), 3699-3710. https://doi.org/10.1242/jcs.147504

Vandemoortele, G., De Sutter, D., Moliere, A., Pauwels, J., Gevaert, K., & Eyckerman, S. (2019, Jan 4). A Well-Controlled BioID Design for Endogenous Bait Proteins. *J Proteome Res, 18*(1), 95-106. https://doi.org/10.1021/acs.jproteome.8b00367

Verma, N., Zhu, Z., & Huangfu, D. (2017). CRISPR/Cas-Mediated Knockin in Human Pluripotent Stem Cells. *Methods Mol Biol, 1513*, 119-140. https://doi.org/10.1007/978-1-4939-6539-7_9

Viana, M. P., Chen, J., Knijnenburg, T. A., Vasan, R., Yan, C., Arakaki, J. E., Bailey, M., Berry, B., Borensztejn, A., Brown, E. M., Carlson, S., Cass, J. A., Chaudhuri, B., Cordes Metzler, K. R., Coston, M. E., Crabtree, Z. J., Davidson, S., DeLizo, C. M., Dhaka, S., Dinh, S. Q., Do, T. P., Domingus, J., Donovan-Maiye, R. M., Ferrante, A. J., Foster, T. J., Frick, C. L., Fujioka, G.,

Fuqua, M. A., Gehring, J. L., Gerbin, K. A., Grancharova, T., Gregor, B. W., Harrylock, L. J., Haupt, A., Hendershott, M. C., Hookway, C., Horwitz, A. R., Hughes, H. C., Isaac, E. J., Johnson, G. R., Kim, B., Leonard, A. N., Leung, W. W., Lucas, J. J., Ludmann, S. A., Lyons, B. M., Malik, H., McGregor, R., Medrash, G. E., Meharry, S. L., Mitcham, K., Mueller, I. A., Murphy-Stevens, T. L., Nath, A., Nelson, A. M., Oluoch, S. A., Paleologu, L., Popiel, T. A., Riel-Mehan, M. M., Roberts, B., Schaefbauer, L. M., Schwarzl, M., Sherman, J., Slaton, S., Sluzewski, M. F., Smith, J. E., Sul, Y., Swain-Bowden, M. J., Tang, W. J., Thirstrup, D. J., Toloudis, D. M., Tucker, A. P., Valencia, V., Wiegraebe, W., Wijeratna, T., Yang, R., Zaunbrecher, R. J., Labitigan, R. L. D., Sanborn, A. L., Johnson, G. T., Gunawardane, R. N., Gaudreault, N., Theriot, J. A., & Rafelski, S. M. (2023, Jan). Integrated intracellular organization and its variations in human iPS cells. *Nature, 613*(7943), 345-354. https://doi.org/10.1038/s41586-022-05563-7

von Dassow, G., Verbrugghe, K. J., Miller, A. L., Sider, J. R., & Bement, W. M. (2009, Dec 14). Action at a distance during cytokinesis. *J Cell Biol, 187*(6), 831-845. https://doi.org/10.1083/jcb.200907090

Wang, H., La Russa, M., & Qi, L. S. (2016, Jun 2). CRISPR/Cas9 in Genome Editing and Beyond. *Annu Rev Biochem, 85*, 227-264. https://doi.org/10.1146/annurev-biochem-060815-014607

Wang, H., Li, Y., Yang, J., Duan, X., Kalab, P., Sun, S. X., & Li, R. (2020, Apr). Symmetry breaking in hydrodynamic forces drives meiotic spindle rotation in mammalian oocytes. *Sci Adv, 6*(14), eaaz5004. https://doi.org/10.1126/sciadv.aaz5004

Wang, M. J., Chen, F., Lau, J. T. Y., & Hu, Y. P. (2017, May 18). Hepatocyte polyploidization and its association with pathophysiological processes. *Cell Death Dis, 8*(5), e2805. https://doi.org/10.1038/cddis.2017.167

Wang, T., Wei, J. J., Sabatini, D. M., & Lander, E. S. (2014, Jan 3). Genetic screens in human cells using the CRISPR-Cas9 system. *Science, 343*(6166), 80-84. https://doi.org/10.1126/science.1246981

Wang, X., Lin, G., Martins-Taylor, K., Zeng, H., & Xu, R. H. (2009, Dec 4). Inhibition of caspase-mediated anoikis is critical for basic fibroblast growth factor-sustained culture of human pluripotent stem cells. *J Biol Chem, 284*(49), 34054-34064. https://doi.org/10.1074/jbc.M109.052290

Watanabe, K., Ueno, M., Kamiya, D., Nishiyama, A., Matsumura, M., Wataya, T., Takahashi, J. B., Nishikawa, S., Nishikawa, S., Muguruma, K., & Sasai, Y. (2007, Jun). A ROCK inhibitor permits survival of dissociated human embryonic stem cells. *Nat Biotechnol, 25*(6), 681-686. https://doi.org/10.1038/nbt1310

Weigert, M., Schmidt, U., Boothe, T., Muller, A., Dibrov, A., Jain, A., Wilhelm, B., Schmidt, D., Broaddus, C., Culley, S., Rocha-Martins, M., Segovia-Miranda, F., Norden, C., Henriques, R., Zerial, M., Solimena, M., Rink, J., Tomancak, P., Royer, L., Jug, F., & Myers, E. W. (2018, Dec). Content-aware image restoration: pushing the limits of fluorescence microscopy. *Nat Methods, 15*(12), 1090-1097. https://doi.org/10.1038/s41592-018-0216-7

Weisheit, I., Kroeger, J. A., Malik, R., Klimmt, J., Crusius, D., Dannert, A., Dichgans, M., & Paquet, D. (2020, May 26). Detection of Deleterious On-Target Effects after HDR-Mediated CRISPR Editing. *Cell Rep, 31*(8), 107689. https://doi.org/10.1016/j.celrep.2020.107689

Wernike, D., Chen, Y., Mastronardi, K., Makil, N., & Piekny, A. (2016, Apr 15). Mechanical forces drive neuroblast morphogenesis and are required for epidermal closure. *Dev Biol, 412*(2), 261-277. https://doi.org/10.1016/j.ydbio.2016.02.023

Whitford, W., Hawkins, V., Moodley, K. S., Grant, M. J., Lehnert, K., Snell, R. G., & Jacobsen, J. C. (2022, May 20). Proof of concept for multiplex amplicon sequencing for mutation identification using the MinION nanopore sequencer. *Sci Rep, 12*(1), 8572. https://doi.org/10.1038/s41598-022-12613-7

Wiedenheft, B., Sternberg, S. H., & Doudna, J. A. (2012, Feb 15). RNA-guided genetic silencing systems in bacteria and archaea. *Nature, 482*(7385), 331-338. https://doi.org/10.1038/nature10886

Williams, L. A., Davis-Dusenbery, B. N., & Eggan, K. C. (2012, May 25). SnapShot: directed differentiation of pluripotent stem cells. *Cell, 149*(5), 1174-1174 e1171. https://doi.org/10.1016/j.cell.2012.05.015

Wolfe, B. A., Takaki, T., Petronczki, M., & Glotzer, M. (2009, May 5). Polo-like kinase 1 directs assembly of the HsCyk-4 RhoGAP/Ect2 RhoGEF complex to initiate cleavage furrow formation. *PLoS Biol, 7*(5), e1000110. https://doi.org/10.1371/journal.pbio.1000110

Wright, W. D., Shah, S. S., & Heyer, W. D. (2018, Jul 6). Homologous recombination and the repair of DNA double-strand breaks. *J Biol Chem, 293*(27), 10524-10535. https://doi.org/10.1074/jbc.TM118.000372

Wu, X., Scott, D. A., Kriz, A. J., Chiu, A. C., Hsu, P. D., Dadon, D. B., Cheng, A. W., Trevino, A. E., Konermann, S., Chen, S., Jaenisch, R., Zhang, F., & Sharp, P. A. (2014, Jul). Genome-wide binding of the CRISPR endonuclease Cas9 in mammalian cells. *Nat Biotechnol, 32*(7), 670-676. https://doi.org/10.1038/nbt.2889

Xu, H., Kita, Y., Bang, U., Gee, P., & Hotta, A. (2021, Dec 17). Optimized electroporation of CRISPR-Cas9/gRNA ribonucleoprotein complex for selection-free homologous recombination in human pluripotent stem cells. *STAR Protoc, 2*(4), 100965. https://doi.org/10.1016/j.xpro.2021.100965

Xu, H., Xiao, T., Chen, C. H., Li, W., Meyer, C. A., Wu, Q., Wu, D., Cong, L., Zhang, F., Liu, J. S., Brown, M., & Liu, X. S. (2015, Aug). Sequence determinants of improved CRISPR sgRNA design. *Genome Res, 25*(8), 1147-1157. https://doi.org/10.1101/gr.191452.115

Xu, L., & Massague, J. (2004, Mar). Nucleocytoplasmic shuttling of signal transducers. *Nat Rev Mol Cell Biol, 5*(3), 209-219. https://doi.org/10.1038/nrm1331

Yamamoto, K., Miura, H., Ishida, M., Mii, Y., Kinoshita, N., Takada, S., Ueno, N., Sawai, S., Kondo, Y., & Aoki, K. (2021, Dec 8). Optogenetic relaxation of actomyosin contractility uncovers mechanistic roles of cortical tension during cytokinesis. *Nat Commun, 12*(1), 7145. https://doi.org/10.1038/s41467-021-27458-3

Yan, N., Sun, Y., Fang, Y., Deng, J., Mu, L., Xu, K., Mymryk, J. S., & Zhang, Z. (2020, Mar 6). A Universal Surrogate Reporter for Efficient Enrichment of CRISPR/Cas9-Mediated Homology-Directed Repair in Mammalian Cells. *Mol Ther Nucleic Acids, 19*, 775-789. https://doi.org/10.1016/j.omtn.2019.12.021

Yang, D., Scavuzzo, M. A., Chmielowiec, J., Sharp, R., Bajic, A., & Borowiak, M. (2016, Feb 18). Enrichment of G2/M cell cycle phase in human pluripotent stem cells enhances HDR-mediated gene repair with customizable endonucleases. *Sci Rep, 6*, 21264. https://doi.org/10.1038/srep21264

Yang, L., Guell, M., Byrne, S., Yang, J. L., De Los Angeles, A., Mali, P., Aach, J., Kim-Kiselak, C., Briggs, A. W., Rios, X., Huang, P. Y., Daley, G., & Church, G. (2013, Oct). Optimization of scarless human stem cell genome editing. *Nucleic Acids Res, 41*(19), 9049-9061. https://doi.org/10.1093/nar/gkt555

Ye, J., Coulouris, G., Zaretskaya, I., Cutcutache, I., Rozen, S., & Madden, T. L. (2012, Jun 18). Primer-BLAST: a tool to design target-specific primers for polymerase chain reaction. *BMC Bioinformatics, 13*, 134. https://doi.org/10.1186/1471-2105-13-134

Ye, M., Wilhelm, M., Gentschev, I., & Szalay, A. (2021, Feb 20). A Modified Limiting Dilution Method for Monoclonal Stable Cell Line Selection Using a Real-Time Fluorescence Imaging System: A Practical Workflow and Advanced Applications. *Methods Protoc, 4*(1). https://doi.org/10.3390/mps4010016

Yeh, C. D., Richardson, C. D., & Corn, J. E. (2019, Dec). Advances in genome editing through control of DNA repair pathways. *Nat Cell Biol, 21*(12), 1468-1478. https://doi.org/10.1038/s41556-019-0425-z

Yonemura, S., Hirao-Minakuchi, K., & Nishimura, Y. (2004, May 1). Rho localization in cells and tissues. *Exp Cell Res, 295*(2), 300-314. https://doi.org/10.1016/j.yexcr.2004.01.005

Yu, J., Vodyanik, M. A., Smuga-Otto, K., Antosiewicz-Bourget, J., Frane, J. L., Tian, S., Nie, J., Jonsdottir, G. A., Ruotti, V., Stewart, R., Slukvin, II, & Thomson, J. A. (2007, Dec 21). Induced pluripotent stem cell lines derived from human somatic cells. *Science, 318*(5858), 1917-1920. https://doi.org/10.1126/science.1151526

Yu, L., Lei, Y., Ma, Y., Liu, M., Zheng, J., Dan, D., & Gao, P. (2021, 2021-April-12). A Comprehensive Review of Fluorescence Correlation Spectroscopy [Review]. *Frontiers in Physics, 9*. https://doi.org/10.3389/fphy.2021.644450

Yu, X., Liang, X., Xie, H., Kumar, S., Ravinder, N., Potter, J., de Mollerat du Jeu, X., & Chesnut, J. D. (2016, Jun). Improved delivery of Cas9 protein/gRNA complexes using lipofectamine CRISPRMAX. *Biotechnol Lett, 38*(6), 919-929. https://doi.org/10.1007/s10529-016-2064-9

Yuan, M., Zhang, J., Gao, Y., Yuan, Z., Zhu, Z., Wei, Y., Wu, T., Han, J., & Zhang, Y. (2021, Jan-Jun). HMEJ-based safe-harbor genome editing enables efficient generation of cattle with increased resistance to tuberculosis. *J Biol Chem, 296*, 100497. https://doi.org/10.1016/j.jbc.2021.100497

Yuce, O., Piekny, A., & Glotzer, M. (2005, Aug 15). An ECT2-centralspindlin complex regulates the localization and function of RhoA. *J Cell Biol, 170*(4), 571-582. https://doi.org/10.1083/jcb.200501097

Zanin, E., Desai, A., Poser, I., Toyoda, Y., Andree, C., Moebius, C., Bickle, M., Conradt, B., Piekny, A., & Oegema, K. (2013, Sep 16). A conserved RhoGAP limits M phase contractility and coordinates with microtubule asters to confine RhoA during cytokinesis. *Dev Cell, 26*(5), 496-510. https://doi.org/10.1016/j.devcel.2013.08.005

Zelensky, A. N., Schimmel, J., Kool, H., Kanaar, R., & Tijsterman, M. (2017, Jul 7). Inactivation of Pol theta and C-NHEJ eliminates off-target integration of exogenous DNA. *Nat Commun, 8*(1), 66. https://doi.org/10.1038/s41467-017-00124-3

Zeng, F., Beck, V., Schuierer, S., Garnier, I., Manneville, C., Agarinis, C., Morelli, L., Quinn, L., Knehr, J., Roma, G., Bassilana, F., & Nash, M. (2020, Dec 5). A Simple and Efficient CRISPR Technique for Protein Tagging. *Cells, 9*(12). https://doi.org/10.3390/cells9122618

Zhang, J. P., Li, X. L., Li, G. H., Chen, W., Arakaki, C., Botimer, G. D., Baylink, D., Zhang, L., Wen, W., Fu, Y. W., Xu, J., Chun, N., Yuan, W., Cheng, T., & Zhang, X. B. (2017, Feb 20). Efficient precise knockin with a double cut HDR donor after CRISPR/Cas9-mediated double-stranded DNA cleavage. *Genome Biol, 18*(1), 35. https://doi.org/10.1186/s13059-017-1164-8

Zhang, S., Nguyen, L. H., Zhou, K., Tu, H. C., Sehgal, A., Nassour, I., Li, L., Gopal, P., Goodman, J., Singal, A. G., Yopp, A., Zhang, Y., Siegwart, D. J., & Zhu, H. (2018a, Apr). Knockdown of Anillin Actin Binding Protein Blocks Cytokinesis in Hepatocytes and Reduces Liver Tumor Development in Mice Without Affecting Regeneration. *Gastroenterology, 154*(5), 1421-1434. https://doi.org/10.1053/j.gastro.2017.12.013

Zhang, S., Zhou, K., Luo, X., Li, L., Tu, H. C., Sehgal, A., Nguyen, L. H., Zhang, Y., Gopal, P., Tarlow, B. D., Siegwart, D. J., & Zhu, H. (2018b, Feb 26). The Polyploid State Plays a Tumor-Suppressive Role in the Liver. *Dev Cell, 44*(4), 447-459 e445. https://doi.org/10.1016/j.devcel.2018.01.010

Zhang, X. H., Tee, L. Y., Wang, X. G., Huang, Q. S., & Yang, S. H. (2015, Nov 17). Off-target Effects in CRISPR/Cas9-mediated Genome Engineering. *Mol Ther Nucleic Acids, 4*(11), e264. https://doi.org/10.1038/mtna.2015.37

Zhao, W. M., & Fang, G. (2005, Sep 13). MgcRacGAP controls the assembly of the contractile ring and the initiation of cytokinesis. *Proc Natl Acad Sci U S A, 102*(37), 13158-13163. https://doi.org/10.1073/pnas.0504145102

Zhou, S., Feng, S., Brown, D., & Huang, B. (2020). Improved yellow-green split fluorescent proteins for protein labeling and signal amplification. *PLoS One, 15*(11), e0242592. https://doi.org/10.1371/journal.pone.0242592

Zhou, X. X., Chung, H. K., Lam, A. J., & Lin, M. Z. (2012, Nov 9). Optical control of protein activity by fluorescent protein domains. *Science, 338*(6108), 810-814. https://doi.org/10.1126/science.1226854

Zuccaro, M. V., Xu, J., Mitchell, C., Marin, D., Zimmerman, R., Rana, B., Weinstein, E., King, R. T., Palmerola, K. L., Smith, M. E., Tsang, S. H., Goland, R., Jasin, M., Lobo, R., Treff, N., & Egli, D. (2020, Dec 10). Allele-Specific Chromosome Removal after Cas9 Cleavage in Human Embryos. *Cell, 183*(6), 1650-1664 e1615. https://doi.org/10.1016/j.cell.2020.10.025